3D Plasma Edge Transport and Radiative Power Exhaust in Wendelstein 7-X Limiter and Island Divertor Scenarios

by

Florian Effenberg

A dissertation submitted in partial fulfillment of

the requirements for the degree of

Doctor of Philosophy

(Nuclear Engineering & Engineering Physics)

at the

University of Wisconsin–Madison

2018

Date of final oral examination: 07/12/2018

The dissertation is approved by the following members of the Final Oral Committee:

David T. Anderson, Professor, Electrical and Computer Engineering
Chris C. Hegna, Professor, Nuclear Engineering & Engineering Physics
Oliver Schmitz, Professor, Nuclear Engineering & Engineering Physics
Carl R. Sovinec, Professor, Nuclear Engineering & Engineering Physics
Amy E. Wendt, Professor, Electrical and Computer Engineering
Thomas Sunn Pedersen, Professor, Physics*

* Ernst-Moritz-Arndt-Universität Greifswald & Max-Planck-Institut für Plasmaphysik, Germany

Abstract

A first-time numerical exploration of radiative power exhaust in limiter startup and island divertor scenarios has been performed at the new optimized quasi-isodynamic stellarator Wendelstein 7-X (W7-X). The experiments conducted in this study confirm the main transport features predicted by simulations with the 3D plasma fluid and kinetic neutral edge transport Monte Carlo Code EMC3-EIRENE and the feasibility of radiative power dissipation with impurity seeding in the W7-X island divertor for the first time. The heat and particle transport in the limiter scenarios is found to be governed by the 3D helical magnetic geometry and well characterized by the simple scrape-off layer (SOL) model. The correlation between heat fluxes and connection lengths predicted by 3D modeling has been confirmed with experimental IR camera measurements. Reduction of the limiter heat fluxes was predicted to be very effective with Neon (Ne) seeding because it enhances the radiation (P_{rad}) at the upstream location while Nitrogen (N_2) radiates deeper in the SOL. Experiments confirmed this, but the limiter plasmas are shown to be more frequently terminated by radiative instabilities in case of Ne seeding. The internal shear of the magnetic islands creates much longer and more complex heat and particle transport channels in the parallel and perpendicular direction in the island divertor scenarios. Ne and N_2 seeding in the island divertor demonstrates stable power exhaust substantially reducing T_e, and $q_{\parallel,div}$. Ne seeding generally features P_{rad} enhancement with slow decay over several seconds after termination of the puff suggesting high recycling. N_2 seeding shows fast recovery of P_{rad}, T_e and $q_{\parallel,div}$ after injection termination indicating low recycling. The feasibility of impurity exhaust control has been demonstrated by manipulation of the island geometry with control coils. 3D modeling provides evidence for reduced overall Ne impurity dwell times with increased islands and reduced connection lengths. The potential impact of equilibrium effects on the edge island geometry and plasma transport has been anticipated based on a high β scenario calculated with the 3D MHD code HINT.

Acknowledgments

First, I like to thank the committee members Prof. Oliver Schmitz, Prof. David Anderson, Prof. Chris Hegna, Prof. Carl Sovinec, Prof. Amy Wendt and Prof. Thomas Sunn Pedersen for taking the time to review this work and providing helpful feedback.

In particular, I am profoundly grateful to my advisor Prof. Oliver Schmitz for providing the opportunities and challenges to work on interesting topics in exciting environments. I highly appreciate his guidance, support, and enthusiasm.

I am genuinely thankful to Dr. Yühe Feng for co-advising, for the introduction into his very useful numerical methods and tools and moreover for all the patient and valuable physics discussions and constructive feedback.

I have to thank my very conscientious collaborators Dr. Ralf König and Dr. Maciej Krychowiak for all their crucial support during the preparation and execution of experiments. Special thanks go to the task force leaders Dr. Marcin Jakubowski and Dr. Sebastijan Brezinsek for being very supportive of my proposals.

Holger Niemann deserves particular thanks for being remarkable reliable and fast with providing data and helpful explanations about the IR measurements. I desire to thank Dr. Daihong Zhang for the collaboration and providing essential bolometer data. Also, I like to thank Dr. Joachim Geiger and Dr. Rainer Burhenn for their patient explanations and helpful feedback. I am very thankful to Dr. Aaron Bader for reading parts of this thesis, providing useful feedback and being always very helpful concerning issues with the numerical tools. I thank Dr. Heinke Frerichs for his support, bug-fixing and providing many valuable tools which were very helpful for the numerical assessment during this work. I like to thank Dr. Glen A. Wurden, Dr. Tullio Barbui and Dr. Laurie Ann Stephey, Dr. Yasuhiro Suzuki for providing essential data and having fruitful collaborations.

Furthermore, I have to thank Dr. Christoph Biedermann, Dr. Andreas Dinklage, Dr. Boyd D. Blackwell, Dr. John C. Schmitt, Dr. Dorothea Gradic, Valeria Perseo, Victoria Winters, Adnan Ali

for their support and collaborations. I want to thank Dr. Matthias Otte for being very helpful with programming the experiments. Thanks to the many other colleagues from E-4 for support during experiments and for providing a trustful and open work environment. Thanks to the whole W7-X team for contributing to the success of the operation.

I'm thankful to the teachers from the UW Colleges of Nuclear, Electrical and Mechanical Engineering for the education received.

Special thanks to the colleagues and friends from HSX for their support, openness and making daily life on and off-campus an enjoyable time. I am immensely grateful to my loyal old and new friends for all their support during the time of this thesis.

I am deeply thankful to my grandfather Werner Andersch† who has taught me endurance and discipline by example.

Finally, I have to thank the United States Department of Energy (DoE) and the College of Nuclear Engineering at the University of Wisconsin - Madison for the financial support of this work.

This work was supported in part by the U.S. Department of Energy (DoE) under grant DE-SC0014210 and by start-up funds of the Department of Engineering Physics and of the College of Nuclear Engineering at the University of Wisconsin - Madison, USA.

This work has been carried out within the framework of the EUROfusion Consortium and has received funding from the Euratom research and training programme 2014-2018 under grant agreement No 633053. The views and opinions expressed herein do not necessarily reflect those of the European Commission.

This research was performed using the computer resources and assistance of the UW-Madison Center For High Throughput Computing (CHTC) and the high performance computing systems Hydra and Draco of the Max-Planck-Gesellschaft at Rechenzentrum Garching (RZG).

TABLE OF CONTENTS

Page

Page

LIST OF FIGURES

Figure Page

Figure Page

Figure Page

Figure Page

Figure Page

Figure Page

Figure Page

Figure Page

Figure Page

Chapter 1

Introduction

1.1 Nuclear fusion

The release of binding energy between nuclei during fusion of light elements is one of the most promising options for a safe, clean and sustainable energy production. The high energy density in the fusion processes compared to burning fossil fuels is a result of the fact that nuclear binding energies and forces are on the order of a million times greater than the atomic binding energies.

In space, nuclear fusion is established as the most common nuclear energy source. The stars are natural nuclear fusion power plants and the released energy produced by the Sun is already used for terrestrial generation of electricity by solar energy conversion with mostly silicon-based semiconductors. However, this indirect usage of nuclear energy is less efficient due to the low photon flux densities, their weather and day time-varying intensities and also due to the comparably low conversion efficiency of photo-electric energy generation.

Realization of a nuclear fusion energy source on earth would allow for a more controllable and efficient way of energy production and usage. However, the proton-proton fusion process that starts the fusion cycle in the Sun has a rather small cross-section and is not applicable on Earth.

Therefore, various alternative nuclear fusion reactions are considered. The most promising process based on currently accessible fuels is the fusion of the hydrogen isotopes Deuterium and

Tritium according to the following nuclear reaction:

$$ {}^{2}_{1}D + {}^{3}_{1}T \rightarrow {}^{4}_{2}He + n^{0} + 17.6\,\text{MeV} \tag{1.1} $$

Nuclear fission of heavy elements is currently the most advanced and already established approach for nuclear energy production. Generation IV power plant concepts [19, 20] are expected to reduce or overcome issues of older generations of reactors related to the production of nuclear waste, the potential risk of accidental radioactive contamination of environments or proliferation. Fission reactors have the advantage of already being established and proven and have the potential to contribute significantly to the address the issue of increasing worldwide energy demand and provide a solution for clean [21], sustainable and long-term stable energy production.

Nuclear fusion has a high potential to contribute to these unsolved problems. It is about one order of magnitude more efficient due to the energy density of its fuel compared to nuclear fission. Nuclear fusion has the advantage that it features strong inherent safety due to physics constraints and does not require additional nuclear waste cycles. It has the big advantage that its light element based fuels are nearly unlimited and uniformly distributed on Earth and in Space.

Demonstration of economic feasibility of fusion power generation (ITER, DEMO) [22, 23] is expected to happen on a similar time scale as the development of Generation IV fission power plants [20]. Fusion is also considered to be highly suitable or even required for effective nuclear space propulsion and planetary defense [24, 25].

Magnetic confinement fusion is the most advanced approach to generate thermonuclear fusion energy. Past and current leading experiments rely either on the tokamak [26] or the stellarator [27, 28]. Tokamaks are axisymmetric toroidal devices that need an additional toroidal plasma current to create a field for stable confinement. Recent, current and near future leading tokamak experiments are TEXTOR, ASDEX-U, JET, DIII-D, EAST, and ITER. Stellarators are inherently 3D toroidal devices which generate the confining magnetic field exclusively by a set of multiple

helical or modular coils. Recent and current relevant stellarator experiments are W7-AS, TJ-II, Heliotron J, HSX, LHD, and W7-X.

The performance of nuclear fusion reactors is commonly measured based on the triple product of density n, energy confinement time τ_E, and plasma temperature T. The condition for ignition, that is, that the energy gain balances all energy losses through fusion processes without external power input is defined by the Lawson criterion [29]:

$$nT\tau_E \leq 3 \cdot 10^{21}\ \text{keVsm}^{-3} \tag{1.2}$$

An overview of the fusion performance relative to ignition is shown in the diagram in figure 1.1 for different experiments. Currently, the tokamak JET is the experiment in operation achieving the highest performance.

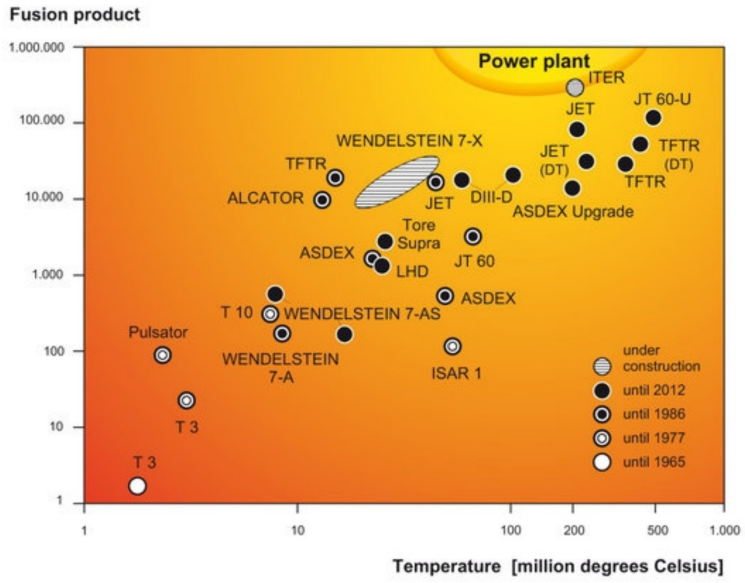

Figure 1.1 This ignition diagram shows the progress of fusion based on the triple product $nT\tau_E$ (www.ipp.mpg.de).

The present study was conducted at the stellarator W7-X. The technical details and properties of this experimental reactor will be described in section 1.3.

1.2 The role of the plasma edge transport and plasma surface interactions

Plasma edge transport and plasma surface interactions (PSI) strongly impact both the performance of fusion plasmas and the lifetime of plasma facing components (PFCs) of present and next step fusion experiments. Here, the parallel heat fluxes $q_{\|}$ within the SOL which are determined by the input power entering the SOL P_{SOL} and the heat flux channel width $\lambda_{q\|}$ are of concern. One key challenge is to remove most of the thermal power coming from the main plasma while in the scrape-off layer (SOL) and before it reaches the PFCs. This is crucial for achieving long pulse steady state operation and demonstrating the reactor feasibility of various magnetic confinement based fusion energy concepts. Therefore a particular focus of this study will be on the parallel heat fluxes within the SOL which are determined by the input power and the heat flux channel width: $q_{\|} \sim \frac{P_{SOL}}{\lambda_{q\|}}$.

For tokamaks, it was found that the heat flux channel width scales with the poloidal magnetic field. Remarkable short power widths $\lambda_{q||}$ in the order of a few millimeters were reported in recent studies for tokamaks causing an intense concentration of heat loads on divertor target tiles [30, 31]. The technically feasible target heat flux limits are $q_{\|,target,max}$ ≈5-10 MWm^{-2} in advanced current devices. The same limits will - from the present state of knowledge - hold for ITER and DEMO [32, 33] which will operate at maximum heating powers of 150 MW and 500 MW respectively and where also the excess heat from the fusion reaction which enters the SOL has to be handled. In DEMO a minimum separatrix power of 100-200MW required for H-mode operation would result in a 5-10 GWm^{-2} heat flux at the mid-plane [34]. This can be mitigated by geometrical means (through the incident angle of field lines on the target) and by turbulent broadening [35]. However, the power flux must be reduced by an additional factor of 10-20 before it reaches the target.

For stellarators, no generic scaling about the power deposition is available so far. Just the contrary, because of the longer connection length in the SOL of stellarators and the 3D nature of

the SOL flux channels, developing metrics to characterize the heat flux deposition and transport characteristics is a current and crucial field of stellarator edge research. It is assumed that the much longer connection length will result in a significant broadening of the heat flux channel width. The helical SOL of the W7-X startup scenario allows initial assessment of this hypothesis, though, in the limiter configuration, the magnetic connection lengths are in a range close to those in a tokamak SOL as will be shown in this study.

To avoid damage of the PFCs (in particular for divertors with metal target plate materials) due to excessive heat fluxes and material erosion, additional means to control and mitigate the heat flux issue are under investigation. One approach is the reduction of power fluxes by radiative edge cooling. Here, dedicated low and medium atomic charge Z impurity species are used to radiate significant amounts of the power entering the SOL by impurity line emission. The impurity radiation acts as an additional power loss channel. For steady state, long pulse operation it is desired to use this line radiation to cool the plasma edge such that the temperatures downstream near the main PFCs are reduced and reliably controlled at levels of a few eV. Therefore, radiative power exhaust is widely under investigation at tokamaks [36, 37, 38, 39, 1, 40, 41, 42, 43, 44] and stellarators [45, 46, 47, 48].

Having low temperatures and high densities (with a high neutral fraction close to the pumping gap) is desired to achieve divertor conditions in which on the one side good neutral pumping for stable density control is provided, and on the other side, the heat fluxes onto the divertor targets are below the technically critical limits. An ideal regime is the so-called 'detached divertor' regime [49] in which is also characterized by enhanced radiation and reduced recycling flux. The main fraction of the parallel heat flux is dissipated in the high density, recombining plasma in front of the plates in this regime. Detachment in tokamaks requires recombining plasmas at electron temperatures of T_e <1 eV in the divertor. The stellarator promises the feasibility of power detachment at higher temperatures (10 eV) due to increased momentum losses by counter-streaming flows

[6]. The friction between these flows can cause a significant pressure drop without the intensive ion-neutral collisions. This has the advantage of a reduced instability likelihood from atomic and molecular processes and enables to operate at low heat fluxes with still substantial, but cold, particle fluxes. This combination is essential to maintain good neutral exhaust during the detachment and might be a unique regime for volumetric divertors like the island divertor under considerations. Impurity radiation strongly determines the SOL power balance under these conditions. The work in this thesis aims at understanding how actively injected radiator gases can aid and yield stable control of this scenario.

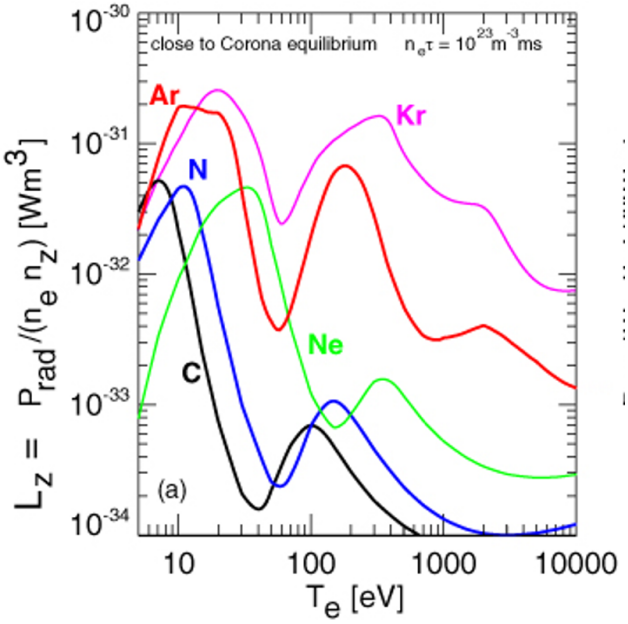

Figure 1.2 Cooling function from [1].

For ITER and DEMO high power loss fractions of $\frac{P_{rad}}{P_{heat}} \approx 0.5$ and 0.9, respectively, are aimed for. However, the radiative losses are required to be located in the plasma edge avoiding impurity accumulation in the core plasma which needs to maintain sufficiently high temperatures for fusion reactions ($T_{core} \sim 20 - 30$ keV). Therefore gases (mostly noble gases) must be chosen that have a strong cooling capacity in the target range of plasma parameters for cold divertor solutions, i.e.,

at roughly 20 eV and below. In figure 1.2 the nonlinear cooling functions of the radiation potential L_Z of a collection of low and medium Z species are shown. Lower Z species such as carbon and nitrogen are advantageous because they are most efficient radiators at low temperatures and therefore act as energy loss channel mainly in the SOL while higher Z species like krypton cool efficiently even up to 2000 eV.

In [50], island divertor scenarios were identified that allow for detached high-performance operation in Wendelstein 7-X [51] that are entirely based on carbon impurities as edge radiators. However, for plasma operation beyond these optimal high-performance conditions, it is desired to have additional means of power dissipation by external impurity seeding. In particular specific MHD effects such as current formation during the transient ($\sim$10s time scale) pressure build-up phase in the later quasi-stationary discharges of W7-X are of concern. Before reaching the equilibrium state of operation, internal plasma currents are evolving on the time scale of seconds that change the magnetic edge topology significantly and cause critically high heat loads onto leading edges of the divertor modules [52]. This required for the development of additional plasma facing components, so-called scraper elements, which are installed such that they can reduce the heat loads on the critical components, but are also predicted to reduce the pumping efficiency. Radiative edge cooling might be an alternative or at least supporting means to address this issue. The island divertor at W7-X is hence also in regards of edge cooling physics a new territory. Exploration of radiative cooling as possible means for power dissipation requires an understanding of the basics of heat and particle transport in the island divertor topology and based on this also on impurity transport. These studies can be conducted with carbon as wall material as they are off generic nature.

However, in view on operational aspects for future fusion devices, radiative edge cooling by impurity seeding might be of critical importance. W7-X is currently fully equipped with graphite PFCs, but as a long-term goal and for a potential W7 reactor [53, 54] it is planned to replace

graphite PFCs and probably make use of tungsten, advanced tungsten alloys or other metallic elements as the first wall material. This means that carbon as an intrinsic radiator is missing and hence a form of self-regulated power load control by enhanced sputtering at higher temperatures which reduces the divertor temperature back to acceptable values is lost. Controlled impurity seeding will then be the only, and therefore essential means for power dissipation in the edge to prevent melting and achieve detached operation. Therefore it is crucial to investigate impurity seeding, transport, and the related PSI physics in the 3D environment of current stellarators. In this thesis, particular focus will be on the effects of the 3D edge magnetic topology of dedicated scenarios provided by the considerable flexibility of the configuration space [5]. Potential magnetic field changes that stem from the plasma response itself [55, 56] are briefly discussed and will have more relevance in future studies of high-performance scenarios. Therefore this study contributes to the high-level requirements for a next-step stellarator towards a HELIAS power plant as specified in [54].

The definition of accurate measures for the characterization of SOL transport such as cross-field plasma profile widths is a challenge and mostly unexplored territory in 3D devices (see discussion below). Understanding the governing SOL physics and developing simplified analytical models similar to the simple SOL model [4] is required to enable reliable predictions in particular for the scaling of downstream power widths $\lambda_{q||}$ with upstream parameters (e.g., density and temperature profile widths). This is also essential for the incorporation of plasma surface interactions into stellarator optimization schemes like STELLOPT [57].

For the validation of methods for edge optimization based on simple SOL models and predictive modeling, the more complex 3D plasma edge transport code EMC3-EIRENE is commonly used [58, 59, 60, 61]. Even more, its purpose is the interpretation of experimental results and development of a comprehensive description of 3D transport.

The work discussed in this thesis was conducted at the Wendelstein 7-X stellarator, located in Greifswald Germany. The primary physics goals and device specifications of W7-X will be discussed in the next section. Based on the general motivation on the relevance of edge transport here and this overview on W7-X, the specific physics questions addressed in this thesis are described in section 1.4.

1.3 Device properties and physics goals of W7-X

Wendelstein 7-X is an optimized quasi-isodynamic stellarator [62, 63] developed and constructed by the Max-Planck-Institut für Plasmaphysik in Germany, to demonstrate the capacity of this specific stellarator optimization for good ion confinement at high plasma pressures combined with the island divertor as innovative exhaust component. This also involves assessing if this integrated approach of a core/edge solution is scalable to stellarator reactor concepts. Stellarators produce the full magnetic field by 3D shaped external magnetic coils. Ideally, the modular coils provide the helical and toroidal components to create the full confining magnetic field that allows for net current-free plasma operation. This allows for steady state operation and eliminates the problem of current disruption which is a great concern for tokamaks.

The HELIAS-type concept underlying W7-X is promising because it features in general inherent capability of stationary operation, absence of current disruptions, sufficiently small loss cones for particles, good energy confinement, negligible bootstrap currents, no need for current drive, no need for feedback position control, no (hard) density limit [64, 62].

W7-X is optimized with respect to drifts and improved neoclassical confinement of thermal plasma and fast ions, sufficiently high stability and equilibrium limits and a feasible exhaust concept, the so-called island divertor [65]. This is considered being required to achieve steady-state operation at high normalized plasma pressure ($\beta = 2\mu_0(p_e + p_i)/B^2$) with values of the volume averaged $< \beta >$ up to 5%, ion temperatures of several keV and plasma densities of 10^{20} m^{-3} and higher. Plasma exhaust relies on a resonant island divertor which requires, as far as possible, a magnetic equilibrium configuration which is not sensitive to the plasma β. This means that the Shafranov shift and bootstrap current have to remain small.

With the 5-fold periodicity of the machine, a low-shear rotational transform profile with a boundary value of 5/5 (toroidal to poloidal mode number) generates the large magnetic islands for

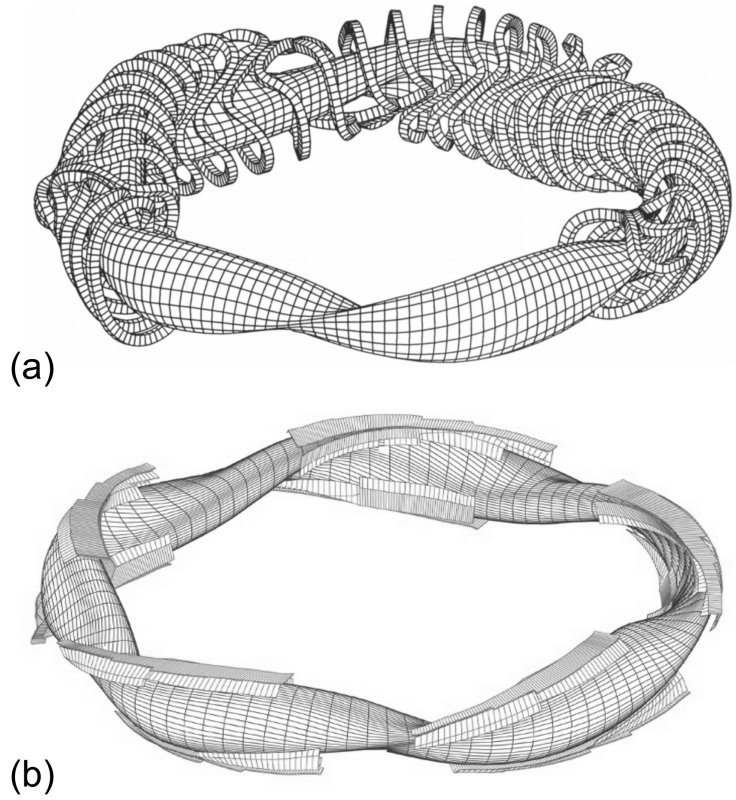

Figure 1.3 (a) Main W7-X coils and confined plasma [2]. (b) Divertor plates around the plasma domain (10 modules) [www.ipp.mpg.de].

the island divertor, while avoiding major resonances in the plasma. Flexibility in the coil system also allows boundary ι values of 5/6 and 5/4 with corresponding island chains.

70 superconducting coils realize the magnetic field configurations. 50 non-planar modular coils provide the necessary rotational transform. 20 planar coils allow us to vary the rotational transform and to adjust the radial position of the plasma. Ten normally conducting divertor coils facilitate sweeping of the divertor strike lines. Besides, five normally conducting trim coils are introduced outside the cryostat vessel for plasma edge control and error field correction. The maximum achievable magnetic field is 3 T. A major radius of R=5.5 m and an average minor

radius of a = 0.55 m correspond to a plasma volume of about 30 m^3. The coil geometry and characteristic plasma shape of W7-X are shown in figure 1.3(a).

W7-X started the first plasma operation (OP1.1) in a limiter configuration [66, 67]. In this field configuration, the SOL was defined by five poloidal graphite limiters located at the bean-shaped symmetry planes. The limiters defined the last closed flux surface and were positioned such that they prevent high heat fluxes onto the unprotected main chamber wall and metallic frame structures of the divertor targets not included during OP1.1.

After the limiter campaign, the uncooled, graphite test divertor units (TDUs) were installed for the first island divertor operation (OP1.2). The divertor plates are shown in figure 1.3(b). They consist of 10 modules matching with the average shape of the plasma. Each module can be separated into various components.

W7-X will eventually strive for 30 min continuous plasmas operation at heating powers of 10 MW. This is supposed to cover all time scales relevant for steady-state operation. Main prerequisites for this long pulse discharges are actively cooled plasma-facing components. An analysis of the expected plasma scenarios shows that technical or physics solutions have to be prepared to allow safe operation of the actively cooled high heat flux divertor.

1.4 Outline of main questions addressed in this work

This work contributes to the topic of heat and particle exhaust and plasma-surface interactions in 3D plasma edge geometries in general and the understanding of this topic in the limiter and island divertor configuration at Wendelstein 7-X. It is closely related to actual experiments conducted at the W7-X stellarator addressing central aspects of the high-level physics goal "Divertor optimization and detachment".

For the numerical analysis, the 3D plasma edge fluid and kinetic neutral transport Monte Carlo code EMC3-EIRENE is used [68, 69].

The following questions are motivated and addressed in this work.

(1) What is the role of 3D edge geometry on heat and particle transport and plasma surface interactions at W7-X?

Here, the significant geometric properties of the limiter and island divertor configurations considered were analyzed. The following analysis focuses on two limiter and two divertor configurations. Dedicated and well-defined changes of the edge magnetic geometry were realized in limiter and island divertor configurations to investigate their impact on the plasma edge transport and PSI in detail. For one divertor configuration also the effects of pressure driven equilibrium changes due to finite values of the volume averaged ratio of thermal pressure to the magnetic field will be included in the assessment.

The limiter configurations will show a nicely defined 3D edge geometry, which serves as a testbed for concepts of 3D plasma edge analysis with both, the EMC3-EIRENE model as well as with simplified analytical descriptions.

The transition from limiter to island configurations comes along with an increase of the parallel transport length scales, the target-to-target connection lengths L_C, by one order of magnitude. This increase of the parallel path length of plasma particles or plasma fluid packages to the surface

enhances the probability of effective outward transport and hence is a fundamental parameter for the transport studies. It will be discussed which primary geometry parameters will determine the plasma transport and local deposition of heat and particles.

(2) What are the main characteristics of limiter and divertor edge plasmas?

In this study, the characteristic properties of the plasma edge regimes will be investigated by 3D modeling. Systematic scans of the input parameters to the modeling are performed to identify general trends in the divertor conditions in dependence on the main plasma scenario and regime. This allows for a more systematic physics analysis and interpretation of first limiter plasmas which were sparsely diagnosed or did, e.g., not allow access to higher density regimes in many cases. The main parameters in these scans were the upstream densities and heating power.

One crucial question is in how far the level of perpendicular transport and its ratio to the parallel transport affects the transport and plasma-surface interactions. The radial transport coefficients are a priori unknown and can be difficult to estimate in complex 3D geometries. The model uses the anomalous transport coefficients as free parameters. The scan of these parameters allows determining their effects on the major heat and particle transport channels and the heat and particle loads onto plasma facing components. Under fixed radial transport, increasing density affects the downstream recycling. Hence, by this assessment, the aim is to investigate the question under which conditions high recycling and detached plasma regimes can be established.

Eventually, it is essential to relate the conditions at the divertor target to the conditions in the main plasma. Scaling laws between the upstream to the downstream position are required to project main plasma performance on divertor regimes and the assessment performed addressing this central questions will help to identify suitable scaling metrics.

(3) Can radiative power exhaust by low Z impurity line emission be used to reduce downstream heat and particle fluxes at the divertor target plate?

The capability of power dissipation in the volume in front of the divertor target tiles is an attractive option to reduce the divertor heat loads and protect the physical integrity of the first wall. To address this, first, the role of transport of intrinsic impurities has to be investigated. Carbon is the major impurity released by erosion processes since the plasma facing components consist mostly of graphite. Furthermore, oxygen will be briefly considered as second most important intrinsic impurity since it may be stored in the walls.

Beyond the radiative energy losses by these intrinsic impurities, which can be considered as a form of self-protection of the divertor targets, deliberate injection of impurities at well-selected positions is an attractive option. The technique of radiative edge cooling mandates a general and primary assessment of several physics aspects. First, the position of the injection point with respect to the magnetic geometry has to be studied to provide optimization approaches and check if the method can work in such a geometry altogether. For the given injection location [14], various species can be injected, and it is important to assess the capability of features of the typical radiation species discussed before in this 3D boundary structure.

The transport of intrinsic and extrinsic impurities in limiter and divertor configurations will be characterized. Here, the dependence on significant transport parameters and the geometry will be considered, which determine the strength of friction and thermal forces.

Eventually, the impact of line radiation of low Z impurities on heat and particle exhaust is addressed. The most relevant and promising light impurity species introduced in section 1.2 are compared in their power exhaust efficiency (Z-dependence), and the role of the source location (low vs. high recycling) is assessed. The feasibility of impurity seeding is investigated in limiter and divertor configurations, and initial qualitative comparisons to experimental trends will be presented.

Chapter 2

Models for plasma edge transport and plasma surface interactions

In this chapter, the 3D model and numerical representation of the magnetic configurations and plasma scenarios will be introduced first. The view on the complete 3D distributions of plasma parameters obtained by simulations, however, requires further analysis by simpler analytical models (preferably 1D or 0D) in order to gain a physics understanding of the complex 3D transport processes.

2.1 3D fluid edge plasma and kinetic neutral transport modeling with EMC3-EIRENE

2.1.1 Background

Non-axisymmetric geometries of stellarators or axisymmetric systems with resonant magnetic perturbations require self-consistent 3D modeling of plasma edge and neutral transport and plasma surface interactions including recycling and impurity sources. The fully 3D coupled fluid plasma edge and kinetic neutral transport Monte Carlo code EMC3-EIRENE [70, 71] is presently the most advanced numerical physics model and used in this study.

EMC3 was initially developed for helical devices and mostly motived by the physics of the stellarator W7-AS at the Max-Planck-Institut für Plasmaphysik in Garching (Germany). It solves a set of reduced time-independent Braginskii fluid equations [72] for particles, parallel momentum,

and energies for electrons and ions in a magnetic mesh representing the 3D geometry of the considered configuration [68]. This geometry may contain open and closed field lines. The open field lines are field lines intersected by wall components, limiters or divertor targets. The closed field lines are found on magnetic flux surfaces. Furthermore, the configuration may contain perturbed flux surfaces, islands, and regions with strong stochasticity. The parallel heat transport is classical while the perpendicular transport of particles and heat is assumed to be anomalous and has to be set as input parameters $D_\perp$ and $\chi_{\perp,e,i}$. The effects of drifts, electrical currents, and volumetric recombination are not included in the present code version, yet. Substantial effort is presently being spent on the implementation of $E \times B$ drifts [73].

EIRENE was developed at the Institut für Plasmaphysik of Forschungszentrum Jülich (Germany). It solves the kinetic transport equations for neutral atoms and molecules including collisional processes [69, 74]. It provides ionization sources, momentum and energy sources and sinks from the atomic and molecular processes such as charge exchange and ionization.

The structure of the coupled codes and the required input is shown in figure 2.1. A field aligned grid, a representation of main PFCs and a set of boundary conditions and parameters represent the main input to both codes. Solutions are iterated based on a Monte Carlo technique. The details of the models and the input will be described in the following.

2.1.2 Equations for the main plasma transport

The most fundamental and simplified description of transport within a magnetized plasma is provided by the single particle description. The motion of charged particles, e.g. electrons and hydrogen ions is determined by the Lorentz force:

$$\vec{F}_L = m\frac{d\vec{v}}{dt} = q(\vec{E} + \vec{v} \times \vec{B}) \tag{2.1}$$

The solution of this equation of motion describes particles of mass m and charge q that move in a circular orbit with cyclotron frequency $\omega_c = \frac{|q|B}{m}$ and Larmor Radius $\rho_l = \frac{v_\perp}{\omega_c}$ along the field lines.

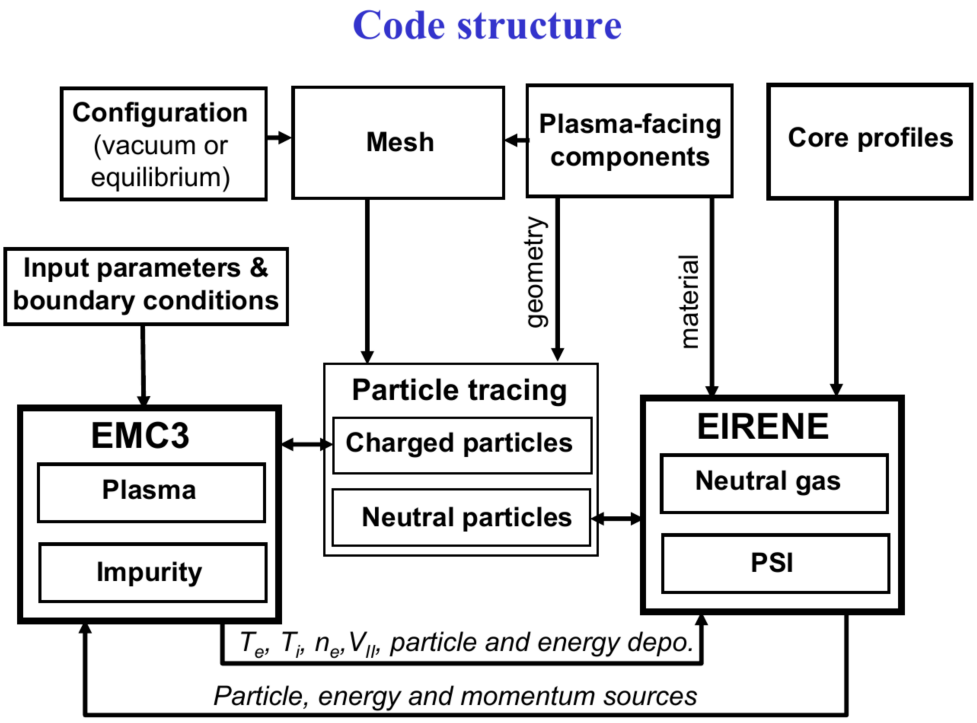

Figure 2.1 Structure of EMC3-EIRENE code [3].

Additional forces $\vec{F}$ acting perpendicular to the $\vec{B}$ will induce drift velocities according to

$$\vec{v}_f = \frac{1}{q}\frac{\vec{F}\times\vec{B}}{B^2} \tag{2.2}$$

This description neglects interactions with other particles.

The kinetic theory provides a more fundamental approach to describe the plasma as a N-particle system. Here, the plasma state is described by a set of one-particle probability functions $f_\alpha(\vec{r},\vec{v},t)$ for each point $(\vec{r},\vec{v})$ in phase space for particle species α . The time evolution of the plasma state is given by the Boltzmann equation:

$$\frac{\partial f_\alpha}{\partial t} + \vec{v}\cdot\nabla f_\alpha + \frac{\vec{F}_L}{m_\alpha}\cdot\nabla_{\vec{v}} f_\alpha = (\frac{\partial f_\alpha}{\partial t})_{coll.} \tag{2.3}$$

The collisional operator $C_\alpha = (\frac{\partial f_\alpha}{\partial t})_{coll.}$ describes the microscopic properties of collisional particle interactions.

The fluid description of the plasma requires macroscopic measures for particle density n_α, flow Γ_α and energy E_α. Those are obtained by calculating the respective moments of the particle distributions functions:

$$n_\alpha = \int d^3v f_\alpha \tag{2.4}$$

$$\Gamma_\alpha = n_\alpha V_\alpha = \int d^3v \vec{v} f_\alpha \tag{2.5}$$

$$E_\alpha = \frac{3}{2} n_\alpha T_\alpha = \int d^3v \frac{m_\alpha}{2} (\vec{v} - \vec{V}_\alpha)^2 f_\alpha \tag{2.6}$$

To define the fluid transport appropriately by particle, momentum, and energy balance equations one has to calculate these three moments from the Boltzmann equation (2.3). However, this results in a set of equations that depends on higher moments and cannot be closed, yet. Closure is achieved by relating the higher moments to gradients of lower order moments assuming that the edge plasma is collisional. The following description assumes that effective length-scales for collisions and particle gyro-radii are smaller than the length scales for variations of fields and that effective collision times are smaller than dynamical time scales. This allows to approximate the viscosity tensor and the heat conduction with a Diffusionansatz as such:

$$\vec{\Pi}_\alpha = \eta_\alpha \nabla \vec{V}_\alpha \tag{2.7}$$

$$q_\alpha = \kappa_\alpha \nabla T_\alpha \tag{2.8}$$

with the transport coefficients η_α and κ_α. The parallel components are approximate based on the classical transport theory [72] including Coulomb collisions and neglecting effects of micro turbulence. A more detailed derivation of this closure can be found in [75].

Assumption of steady state, quasi-neutrality, and vanishing plasma currents are made, which allow for various simplifications and eventually result in a solvable set of fluid balance equations. The EMC3 equations for mass, momentum, and energy for electrons and ions [68]:

$$\nabla_{||} \cdot (nV_{||}) + \nabla_{\perp} \cdot (-D_{\perp} \nabla_{\perp} n) = S_P \tag{2.9}$$

$$\nabla_{||} \cdot (m_i n V_{||} V_{||} - \eta_{||} \nabla_{||} V_{||}) + \nabla_{\perp} \cdot (-m_i V_{||} D_{\perp} \nabla_{\perp} n - \eta_{\perp} \nabla_{\perp} V_{||}) = -\nabla_{||} n(T_e + T_i) + S_m \tag{2.10}$$

$$\nabla_{||} \cdot (-\kappa_{||}^e \nabla_{||} T_e + \frac{5}{2} n T_e V_{||}) + \nabla_{\perp} \cdot (-\chi_{\perp}^e n \nabla_{\perp} T_e - \frac{5}{2} T_e D_{\perp} \nabla_{\perp} n) = -k(T_e - T_i) + S_{ee} + S_{e,imp} \tag{2.11}$$

$$\nabla_{||} \cdot (-\kappa_{||}^i \nabla_{||} T_i + \frac{5}{2} n T_i V_{||}) + \nabla_{\perp} \cdot (-\chi_{\perp}^i n \nabla_{\perp} T_i - \frac{5}{2} T_i D_{\perp} \nabla_{\perp} n) = -k(T_e - T_i) + S_{ei} \tag{2.12}$$

where $V_{||}$, $\kappa_{||}^{e,i}$, $\eta_{||,\perp}$ and k are the parallel plasma velocity, the classical parallel heat conductivity of electron/ion, the viscosity and the equilibration coefficient. S_p , S_m , S_{ee} and S_{ei} are the ionization source, momentum source/loss and energy source/loss via atomic/molecular processes, e.g., charge exchange (CX) and ionization, which are calculated by EIRENE. $S_{e,imp}$ represents an energy loss term due to excitation and ionization of impurities described in the fluid approach below. The coefficients for anomalous particle transport $D_{\perp}$ and anomalous electron and ion heat transport $\chi_{\perp,e,i}$ are free model parameters which are in general unknown and can be inferred experimentally [76]. Edge plasma heating is defined by setting the electron and ion heating power across the inner simulation boundary. Finite decay lengths are set at the outermost boundary for density, momentum, and energy. The decay lengths in the outer boundary are not the same as the decay lengths at the last closed flux surface. The latter define e.g. the SOL width and are a result of the self-consistent transport simulation.

Further plasma parameters have to be set for the neutral transport by EIRENE in the peripheral vacuum region and the core region. The plasma temperatures and densities prescribed in these domains determine in particular the energy of neutrals released into the plasma transport domain.

A more detailed description of the theory and assumptions summarized above is, e.g., provided in [75].

2.1.3 Model for impurity sourcing and transport

Impurities are either sourced from defined wall elements or plasma facing components according to sputtering and recycling processes or from a defined point source according to local outgassing or impurity injection. The start energy of the impurities $E_{0,imp}$ is typically approximated by the surface temperature in case of erosion or by the valve temperature in case of thermal gas injection. The start distribution f_{imp} can be assumed isotropic or according to a parametrized angle-dependent distribution $f_{imp}(\nu) \propto sin(\nu)^{\alpha} cos(\nu)^{\beta}$ for sputtering by setting α and β. The standard choice used in this work is $\alpha = \beta = 1$. The source strengths determining the influx Γ_{imp} of impurities can be set in different ways. One option is to set the total radiated power losses $P_{rad,imp}$ by impurity line emission. In this case, the source strength is rescaled after an impurity iteration to match the requested power loss.

Sputtering or recycling of impurities can be set by a sputtering coefficient $C_{sputter}$. In this case, the present model treats the impurity generation similar to chemical sputtering. That is, impurities are sourced proportional to the local main ion recycling flux Γ_{rec} strengths and distributions:

$$\Gamma_{imp} \approx \Gamma_{imp,chem} = C_{sputter,chem} \Gamma_{rec} \tag{2.13}$$

This is however a simplification of the actual energy and flux dependent chemical erosion according to the Roth formula [77]:

$$Y_{chem}(E, T, \Phi) = \frac{Y_{low}(E, T)}{1 + (\Phi / 6 \cdot 10^{21})^{0.54}} \tag{2.14}$$

where Φ is the ion flux density, Y_{low} is a low yield (< 0.08) obtained from low flux ion beam data. On the other hand, physical sputtering is neglected completely. The physical sputtering yield for normal incidence of a ion on a target is calculated with the Bohdansky formula [78]:

$$Y_{phys}(E_0) = Q S_n(\epsilon)(1 - (\frac{E_{th}}{E_0})^{\frac{2}{3}})(1 - (\frac{E_{th}}{E_0}))^2 \tag{2.15}$$

where Q is the yield factor, S_ϵ is the nuclear stopping cross-section:

$$S_n(\epsilon) = \frac{3.441\sqrt{\epsilon}ln(\epsilon + 2.718)}{1 + 6.355\sqrt{\epsilon} + \epsilon(6.882\sqrt{\epsilon} - 1.708)} \tag{2.16}$$

and $\epsilon = {}^{E_0}/_{E_{TF}}$ with the Thomas-Fermi energy E_{TF}. Note that the threshold energy E_{th} defines a value for onset of physical sputtering: $Y \to 0$ for $E_0 \to E_{th}$.

Although self-sputtering and physical sputtering are not included in the impurity fluid model, it has to be mentioned that EIRENE provides more options to simulate physical sputtering and self-sputtering (TRIMSP).

For the simulation of local impurity injection point sources are defined. The strengths of the injected impurity fluxes are either determined by P_{rad} or directly by the total influx rate Γ_{imp}.

Once the neutral impurities are released and ionized their transport is modeled by a trace fluid approach. A simplified fluid momentum balance equation is solved and the impurities impact the main plasma species only by ionization and excitation through a loss term in the energy balance equation [79]. The following continuity and momentum equations are solved:

$$\nabla_\parallel \cdot (n_z V_{z\parallel}) + \nabla_\perp \cdot (-D_{imp}\nabla_\perp n_z) = S_z \tag{2.17}$$

$$\begin{aligned} 0 = -\frac{1}{n_z}\frac{dp_z}{ds} + ZeE_\parallel + m_z\frac{V_\parallel - V_{z\parallel}}{\tau_{zi}} + 0.71Z^2\frac{dT_e}{ds} + 2.6Z^2\frac{dT_i}{ds} \\ = F_P + F_E + F_{fr} + F_{th,e} + F_{th,i} \end{aligned} \tag{2.18}$$

where S_z represents the impurity ionization and recombination balance of adjacent charge states, and D_{imp} is the anomalous particle diffusivity. τ_{zi} is the collision time between impurities and background main ions[4]:

$$\tau_{zi} = \frac{1.47 \cdot 10^{13} m_z ({}^{T_i^3}/_{m_i})^{0.5}}{(1 + {}^{m_i}/_{m_z}) n_i Z^2 ln\Lambda} \tag{2.19}$$

with $ln\Lambda \approx 15$. The terms in equation 2.18 correspond to pressure force F_P, electric force F_E, friction force F_{fr} and electron and ion thermal force $F_{th,e}$ and $F_{th,i}$, respectively. The impurity ion temperatures are assumed to be equal to the background main ion temperature ($T_z = T_i$).

The usual directions and relative strengths of the different forces parallel to the magnetic field within the SOL are shown in figure 2.2. The parallel electric field component $E_\parallel$ and the parallel ion flow velocity $v_{i,\parallel}$ are directed towards the target.

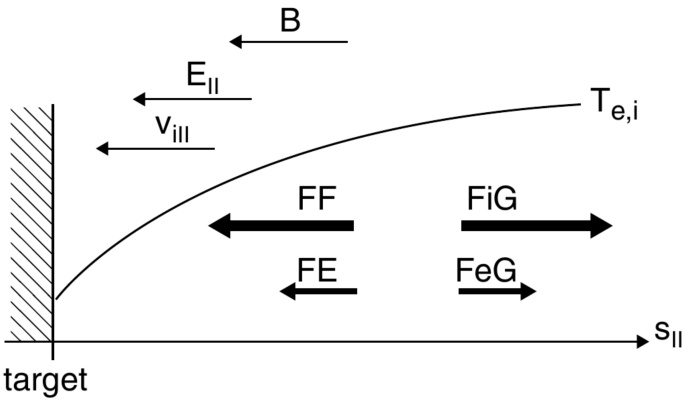

Figure 2.2 The parallel forces acting on impurity ions: the friction force FF, the electrostatic force FE, and the electron and ion-temperature gradient forces FeG, FiG. [4].

The thermal forces $F_{th,e}$ and $F_{th,i}$ result from parallel temperature gradients and are directed to the higher temperature regions. This means thermal forces generally draw impurities upstream. The friction force F_{fr} drives impurities in the direction of the main plasma flow (see figure 2.2).

The impurity force balance in equation 2.18 can in a steady state be directly expressed in terms of the resulting parallel impurity flow velocity:

$$V_{z\parallel} = V_\parallel + \frac{\tau_{zi} Z^2}{m_z}\left(0.71\frac{dT_e}{ds} + 2.6\frac{dT_i}{ds}\right) + \frac{\tau_{zi} Ze}{m_z}E_\parallel - \frac{\tau_{zi}}{n_z m_z}\frac{T_i}{ds}n_z \tag{2.20}$$

It is shown that electrostatic force and pressure force can be neglected in general [4, 6] (see also relative force strengths indicated by the thickness of vector arrows in figure 2.2). This simplifies

equation 2.20 with $\tau_{zi} \propto Z^{-2}$ to a force balance that is determined by the friction and ion thermal forces only and that is not dependent on the charge state Z anymore:

$$V_{z\parallel} \approx V_{\parallel} - \alpha \frac{dT_i}{ds} = V_{fr} - V_{i-th} \tag{2.21}$$

with the characteristic velocities V_{fr} and V_{i-th} induced by F_{fr} and F_{i-th}, respectively. The impurity force balances will be discussed based on the simple impurity flow expression inferred in equation 2.21 for the W7-X scenarios considered in this work.

The trace impurity fluid model is valid for light impurities at small concentrations, $Z_I^2 n_I \ll n_e$. Impurities contribute to the main plasma transport equations only by ionization and radiation losses in the electron energy balance equation 2.11:

$$S_{e,imp} = P_{rad} + S_{ion,imp} = \Sigma_{z=0}^{Z-1} P_{rad,z} + \Sigma_{z=0}^{Z-1} E_z R_{z\rightarrow z+1}^{ion} \tag{2.22}$$

with E_z, $R_{z\rightarrow z+1}^{ion}$ being the ionization energy and ionization rate coefficients.

The boundary condition at the core interface is set such that impurities can either be reflected with the same charge state at the inner simulation boundary (i.e. the net flux for each impurity ion charge state is zero) or they pass through and are subject to a 1D core transport model [80]. This model allows for further ionization of impurities inside the core plasma based on prescribed density and temperature profiles.

Despite its simplifications, the fluid approach with chemical-like sputtering is chosen for this study. Here, the focus is on general features of the impurity transport and their cooling effects. The ADAS database [81] provides the atomic data, namely effective rate coefficients for ionization, recombination and charge exchange and relevant line emission.

2.1.4 Synthetic diagnostics and line emission modeling

Measurements from the experiment on the other hand usually provide only a very localized view of the plasma. The values obtained by experimental measurement may not correspond to the real target measure due to limitations, bias, interfering physics processes or systematic errors within the measurement. The advantage of the 3D modeling is that it allows for a self-consistent comparison between the 'true' plasma state and the plasma state according to the measurement performed within the simulation. This requires modeling of the considered measurement technique, also called a 'synthetic diagnostic'. Synthetic diagnostic modeling can help to analyze and evaluate the physics of the measurement technique. Synthetic diagnostics are generally implemented as post-processing routines applied to the converged plasma and neutral transport calculations.

An essential component of many synthetic spectroscopy measurements is the local line emission integrated along a line of sight (LoS). Versatile post-processing routines have been developed [82] and were extended based on motivations arising from the physics questions in the present study [83, 84]. Photoemission coefficients (PECs) in the ADF15 format provided by ADAS [81] or collisional radiative models (CRMs) are used to model the emission at specific wavelengths. The local line emission for a wavelength λ of emitted light from ions of species α with charge state z is calculated as such:

$$I_\lambda(n_e, n_{\alpha,z}, T_e) = PEC(\lambda, n_e, T_e) n_e n_{\alpha,z} \tag{2.23}$$

Integration along single or a set of lines of sight of length L provides signal strength S_λ. It is determined by the local emission I_λ along the path length l captured by a local synthetic spectroscopic view or a camera:

$$S_\lambda = \int_{l=0}^{L} I_\lambda(n_e, n_{\alpha,z}, T_e) dl \tag{2.24}$$

The calculation of line emission and its integration along lines of sight was in particular used for comparisons of modeling data with helium beam measurements based on CRM, particle flux

measurements based on H_α, coherence imaging spectroscopy (CIS) based on line emission from carbon ions, impurity line emission captured with video diagnostics or the bolometer. Examples will be discussed in this work.

2.1.5 Field geometry and grid generation

The application of the numerical method to solve the model equations requires a computational grid. The grid generation starts with the choice of magnetic field configuration. The characteristics and physics of the prescribed ideal vacuum configuration space are reported in [85] and further reviewed in certain physics aspects in [5]. The vacuum magnetic field of a configuration is created with Biot-Savart law according to the sets of coil currents provided in [85]. The set of coils of one field period is shown in figure 2.3. The five types of non-planar coils are shown in red, and the planar coils are shown in blue. The small rectangular coils are the island control coils.

Mostly four vacuum field configurations are considered in this study. The standard divertor configuration (SDC) requires the following setup of normalized coil currents: $I_1 = I_2 = ... = I_5 = 1$ and $I_A = I_B = 0$. The OP1.1 standard limiter configuration requires $I_1 = I_2 = ... = I_5 = 1$ and $I_A = I_B = 0.13$ [66]. The OP1.1 limiter configuration with increased rotational transform was modified by reducing the current in the second planar coil: $I_A = 0.13$ and $I_B = 0$. The narrow high mirror configuration (NHM) uses the following arrangement of coil currents: $I_1 = 1.0$, $I_2 = 1.02$, $= I_3 = 1.08$, $= I_4 = 0.93$, $= I_5 = 0.843$ and $I_A = I_B = 0$. The OP1.1 limiter configurations and the narrow high mirror island divertor configuration are recent designs that are not listed in the original canonical set of configurations [85].

Taking into account the five-fold periodicity and the stellarator symmetry of W7-X [2] a simulation grid covering a toroidal extension of $\Delta\phi_{tor} = \frac{1}{2} \cdot \frac{360^\circ}{5} = 36^\circ$ may be sufficient to cover the complete plasma transport and PSI with EMC3-EIRENE. A minimally sized grid capturing the full geometry is always desired to save computational time and storage. Depending on the magnetic

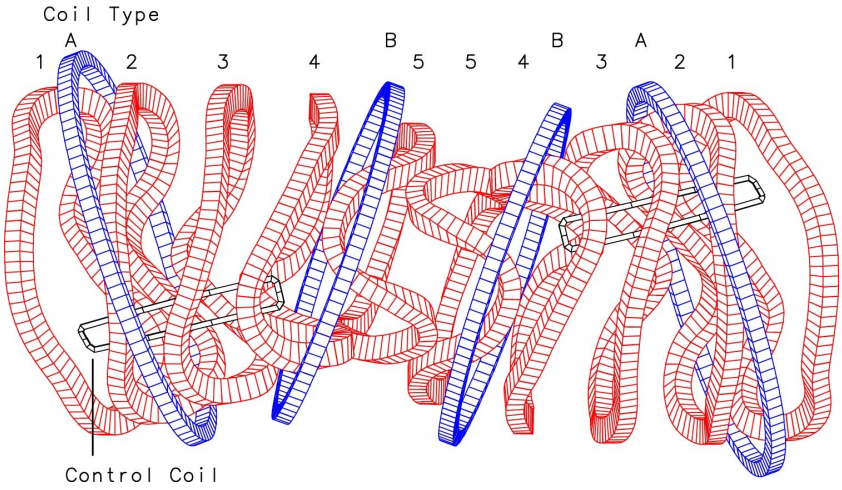

Figure 2.3 Set of coils for one field period [5].

field geometry and physics aspects to be resolved a minimum spatial resolution and grid extension is set e.g. by the size of boundary magnetic islands and the ionization lengths of neutrals released into the plasma.

Ideally, flux surfaces are chosen for the definition of the computational mesh to allow for an optimum approximation of the magnetic field structure. This is mostly feasible within the core and confinement region. Interpolated flux surfaces are used where necessary to ignore resonances or stochastic domains. The particular geometry of the limiter configuration allows matching surfaces of the magnetic field with the computational grid surfaces even in the boundary domain.

A relatively regular grid structure is required to establish 3D flux tubes based on adjacent grid cells. The field lines within islands and stochastic domains are then reconstructed and interpolated within the 3D flux tube grid [86].

The choice and extension of the computational domain are shown in figure 2.4 for the standard limiter configuration. In figure 2.4(a) the Poincaré plot (blue) is depicted in the bean-shaped symmetry cross-section. Flux core and boundary flux surfaces (red and magenta) are extracted from the vacuum magnetic field. The outermost core surface will serve as inner simulation boundary in this case. Further flux surfaces are interpolated between the inner simulation boundary and the outermost flux surface used for the plasma transport domain.

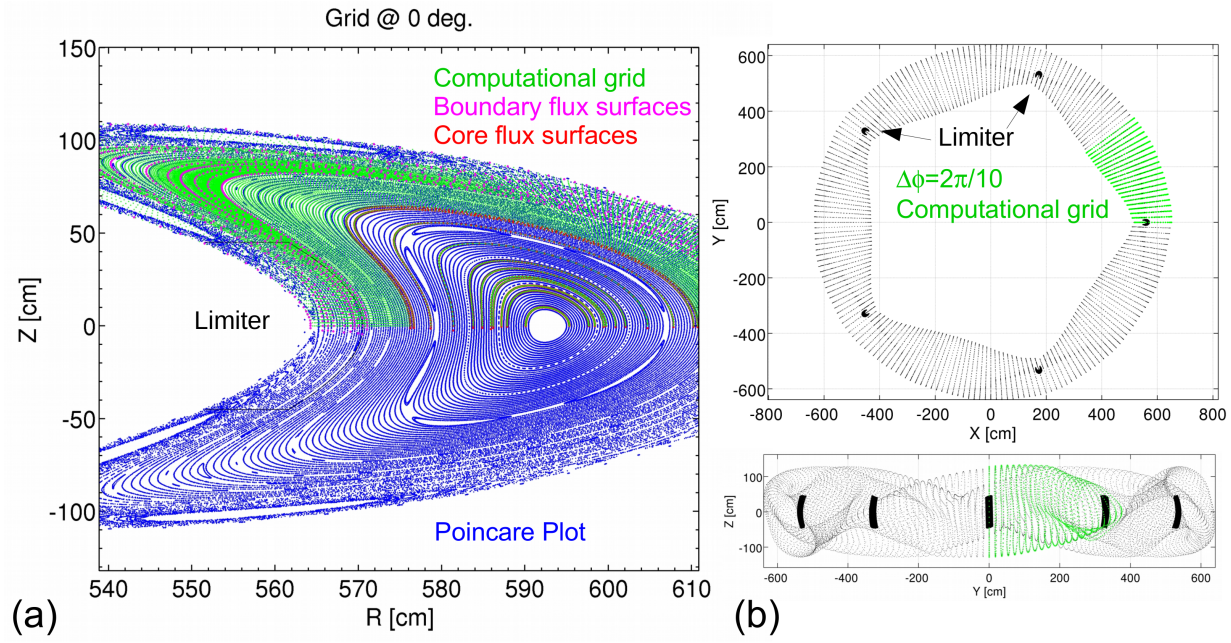

Figure 2.4 Grid generation. (a) Poincaré plot (blue) combined with choice of core (red) and boundary surfaces (magenta) used for interpolation of computational grid (green). (b) top down and side view on full grid (black) and choice of computational domain (green).

Once the radial and poloidal extension of the computational domain is defined in one toroidal cross section, it is used as a 2D base grid. This base grid is then extended in toroidal direction by following the field lines. The present grid extends from $\phi = 0°$ to $\phi = 36°$.

The interpolated domain used for the computational mesh is shown in green. The outermost flux surface corresponds to the vessel and encloses the vacuum domain between plasma transport

domain and vessel for neutral transport. The innermost core flux surfaces serve for the core neutral transport as well. These outermost and innermost domains serve therefore as neutral cells mostly for EIRENE only.

For orientation a top-down and a side view are shown in the global Cartesian coordinate system in figure 2.4(b). The full 360° grid structure is shown in black (including the limiters as main PFCs). The computational domain is shown in green. A symmetry operation maps all diagnostics or additional gas sources into the green computational domain in the present study. Main PFCs such as the limiters or divertor targets are modeled in the simulation domain.

Plasma surface interactions such as recycling or erosion are defined based on their geometric representation in additional input files.

In the present study, the limiter and divertor geometry is provided in a cylinder format like representation, also called 'Kisslinger format'. Wall, limiters, and divertors have a somewhat complicated shape adjusted to the field geometry. The helically extend divertor structures are not optimized for a specific configuration while the limiters were optimized to fit precisely to the shape of the limiter magnetic field configuration [66].

The symmetry used may be violated by field asymmetries in reality [87]. Transport of impurities released from single point sources may justify full 360° simulations. However, due to the limited diagnostic coverage and for the present more general transport questions addressed in this work the symmetry assumptions are considered to be sufficient. More details about the grid generation in general can be found in [86, 75].

In case of higher β-scenarios, the plasma response may significantly change the magnetic field geometry. For this purpose solutions provided by the 3D magnetohydrodynamic (MHD) equilibrium solver HINT [88] code are considered. The HINT code uses a relaxation method based on the dynamic equations of the magnetic field and pressure. The first step consists of a relaxation process of the plasma pressure satisfying the condition $\boldsymbol{B}\cdot\nabla p = 0$ for a fixed $\boldsymbol{B}$. The second step

is a relaxation process of the magnetic field for a fixed p, where an equation of motion (neglecting the nonlinear convective term) and the induction law are solved towards steady state. The final equilibrium state corresponds almost to a stable steady-state satisfying force balance. One scenario based on a HINT calculation will be discussed in this study.

Eventually experimental equilibrium reconstruction with V3FIT [89, 90] will be used to provide fields directly from the experimental scenarios as input for grid generation or comparison with implemented configurations.

2.1.6 Iterative scheme and input parameter

The general structure of the EMC3-EIRENE code is shown in figure 2.5. The code calculates the time-independent solutions of the simplified Braginskii equations by an iterative procedure employing the plasma, impurity and neutral main modules. The fluid equations introduced above can be generalized into a convective-diffusive Fokker-Planck form:

$$\nabla \cdot (\vec{V} f - \vec{D} \cdot \nabla f) = S \tag{2.25}$$

with the fluid quantity f, the transport coefficients $\vec{D}$, $\vec{V}$ and the source S. This equation represents conservation of either mass, energy or momentum during convective and diffusive processes. It can be treated like a stochastic (Markov) process and simulated with a Monte Carlo technique. The Monte Carlo particles are randomly generated according to a provided source distribution on the computational mesh. They are followed in a random walk steps Δr determined by a time step $\Delta \tau$ and scored until they are lost to defined targets or sinks. A more detailed description and derivation of the Monte Carlo scheme are provided in [68, 91, 75]. The computational scheme is shown in figure 2.1. Generally, the computation is initialized with constant densities and temperatures with the 'ENERGY' module. In following steps, momentum and particle transport are included with 'STREAMING' and 'NEUTRAL' modules. Relaxation factors f have to be chosen carefully to achieve a stable solution under the constraint of limited computational resources. The general

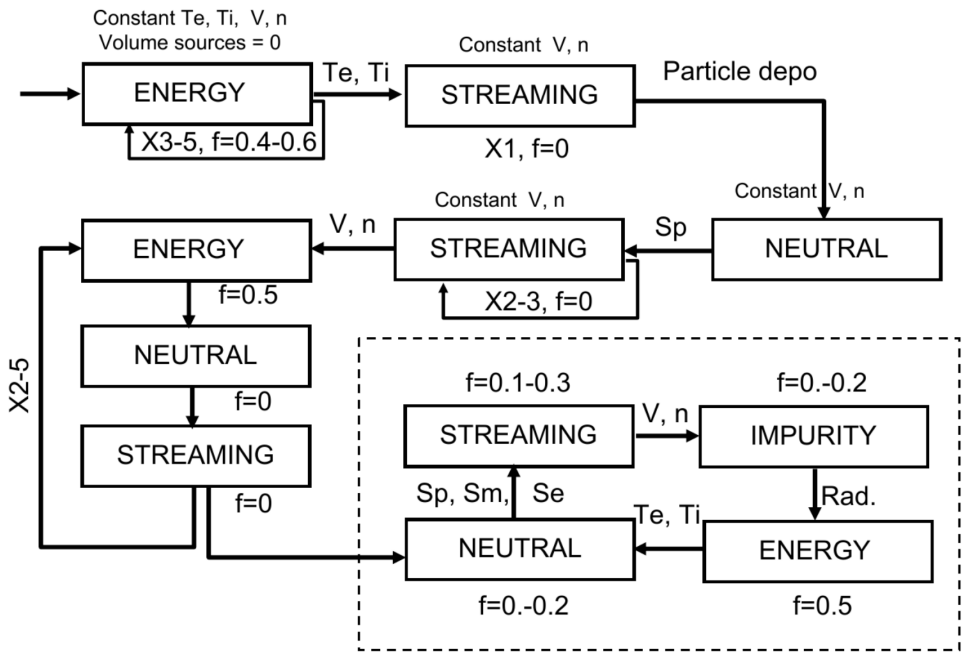

Figure 2.5 Pre-computation, iteration and relaxation scheme of EMC3-EIRENE [3].

procedure is to first produce a stable solution for a reference plasma before introducing impurities by the 'IMPURITY' module (dashed box in figure 2.5). If one or more impurity species are added the iteration has to be continued until a stationary solution is found. Some systematic convergence studies are, e.g., reported in [92, 75].

The code is parallelized. Depending on the grid size and resolution, transport coefficients and plasma regime it may be run on a standard PC or clusters of high-performance facilities. The simulations of this work were mostly performed at the HYRDA and DRACO Clusters of Rechenzentrum Garching (RZG) and the UW-Madison Center for High Throughput Computing (CHTC).

2.2 Analytical modeling of edge transport

2.2.1 Simple SOL description for limiter scenarios

Basic understanding of plasma edge transport requires simplified analytical models. Most advancements were made in tokamak research where simple models have been developed based on slab geometries as an approximation for ideal, high aspect ratio, axisymmetric configurations. The plasma boundary in earlier configurations was commonly defined by stationary limiting objects inserted into the plasma. Those limiters serve as heat and particle sinks and divide the main plasma transport domain into a confinement region with closed field lines and flux surfaces and an open field line domain, the so-called 'scrape-off layer' (SOL).

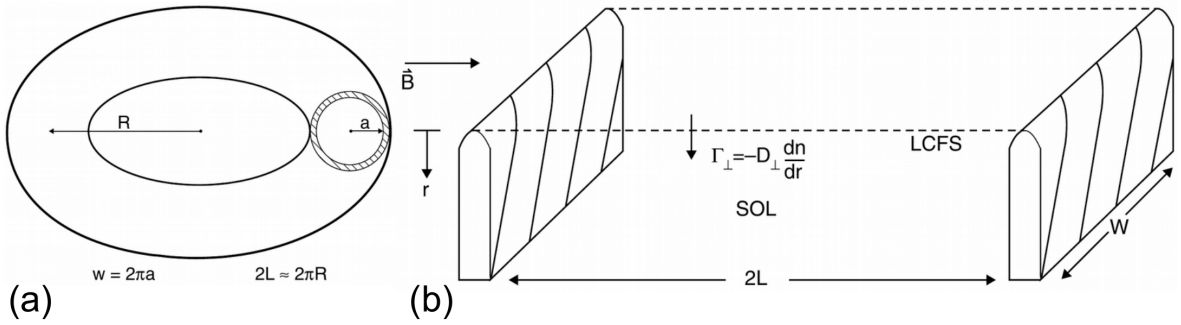

Figure 2.6 Sketch of an ideal limiter SOL. (a) full poloidal limiter. (b) Simple SOL defined by limiter [4]

This is shown in figure 2.6 (a). Here, the complete poloidal circumference of the limiter ($w = 2\pi a$) guarantees a homogeneous SOL of open field lines of lengths $2L = 2\frac{\pi R}{\iota} = L_C$. L_C is according to this definition the target-to-target connection length and ι is the rotational transform accounting for the pitch angle of the field lines (and inverse to the safety factor commonly used in the tokamak theory: $\iota = q^{-1}$). The resulting SOL is shown in figure 2.6 (b) straightened out. The dashed lines marks the last closed flux surface (LCFS) which is the border between confinement and SOL. Radial cross field transport of particles is directed into the SOL. Its strength is determined

by the diffusive transport coefficient $D_\perp$ and can be expressed as such:

$$\Gamma_\perp = -D_\perp \frac{dn}{dr} \tag{2.26}$$

This simplified picture establishes a simple path for a basic transport analysis. The perpendicular fluxes entering the SOL are transported parallel to $\vec{B}$ towards the target plates. To calculate radial and parallel profiles, the following assumptions are made within the so called 'Sheath-Limited Simple SOL' [4]:

- Ionization source located within LCFS, no ionization in the SOL, no volumetric recombination.
- Perpendicular transport is driven by diffusion ($\Gamma_\perp = -D_\perp \frac{\partial n}{\partial r}$) and provides the only particle source in the SOL.
- Power is released into the SOL by cross-field convection and conduction from the main plasma power source.
- Isothermal SOL ($\nabla_\parallel T_e = \nabla_\parallel T_i = 0$).
- T_e and T_i are thermally de-coupled.
- Bohm boundary condition, i.e. flow velocity is ion sound speed at the target (downstream) ($v_\parallel = c_s = \sqrt{\frac{k(T_e+T_i)}{m_i}}$).
- The limiter and divertor target sheaths are the only particle and heat sinks.
- No neutral friction, no radiative or charge-exchange cooling.

It will be demonstrated that these assumptions may serve as an analysis approach in many SOL scenarios of the W7-X limiter configuration despite its 3D SOL geometry. Following the

argumentation above one can infer the radial SOL plasma profile and width. Define λ_n to be the characteristic density fall-off length:

$$\lambda_n = -\left(\frac{1}{n}\frac{dn}{dr}\right)^{-1} \tag{2.27}$$

The total particle out-flow from the confined plasma into the SOL is:

$$\begin{aligned} \phi_\perp = \Gamma_\perp A_{LCFS} = -D_\perp \left(\frac{dn}{dr}\right)_{r=r_{LCFS}} 2Lw \\ \Rightarrow \phi_\perp = D_\perp \left(\frac{n_{LCFS}}{\lambda_n}\right) 2Lw \end{aligned} \tag{2.28}$$

The total particle flux to the left and right target in figure 2.6(b) is then:

$$\Phi_\parallel = 2w \int_{r=r_{LCFS}}^{\infty} nc_s dr \approx 2w\lambda_n nc_s \tag{2.29}$$

under the Bohm sheath criteria with a wetted area of $A_{wetted} \approx w\lambda_n$. Based on the experimental experience the assumption of an exponential density profile holds approximately:

$$n(r) = n_{LCFS} e^{-r/\lambda_n} \tag{2.30}$$

Without any particle sources or sinks within the SOL the simple particle balance $\phi_\perp = \phi_\parallel$ gives:

$$\lambda_n = \sqrt{\frac{D_\perp L}{0.5 c_s}} \tag{2.31}$$

The factor 0.5 is related to the drop of density in parallel direction as the flow is accelerated to ion sound speed. λ_n represents the characteristic width of the parallel particle transport channel and is closely related to the widths of the convective heat flux channel.

Similarly, exponentials can be defined for electron and ion temperature T_e and T_i with characteristic decay lengths λ_{T_e} and λ_{T_i}:

$$T_{e,i}(r) = T_{e,LCFS} e^{-r/\lambda_{T_{e,i}}} \tag{2.32}$$

This implies exponential decays for electron and ion pressures, particle and heat fluxes:

$$p_{e,i}(r) = nkT_{e,i} \tag{2.33}$$

$$\Gamma_{e,i}(r) = 0.5nc_s \tag{2.34}$$

$$q_{\parallel,e,i}(r) = \gamma_{e,i} k T_{e,i} \Gamma_{e,i}(r) \tag{2.35}$$

where $\gamma_{e,i}$ are the electron and ion sheath heat transmission coefficients. The characteristic decay lengths of these exponentials are related to the density and temperature decays as follows:

$$\frac{1}{\lambda_{p_{e,i}}} = \frac{1}{\lambda_n} + \frac{1}{\lambda_{T_{e,i}}} \tag{2.36}$$

$$\frac{1}{\lambda_{\Gamma_{e,i}}} = \frac{1}{\lambda_n} + \frac{1}{2\lambda_{T_{e,i}}} \tag{2.37}$$

$$\frac{1}{\lambda_{q_{\parallel,e,i}}} = \frac{1}{\lambda_n} + \frac{3}{2\lambda_{T_{e,i}}} \tag{2.38}$$

The latter requires constant $T_e = T_i = T$ in the entire SOL. Actually, typical SOL conditions obey rather $T_e < T_i$. Assuming $\lambda_{T_i} \to \infty$ one has approximately

$$\frac{1}{\lambda_{q_{\parallel,e}}} = \frac{1}{\lambda_n} + \frac{1}{\lambda_{T_e}} \tag{2.39}$$

$$\frac{1}{\lambda_{q_{\parallel,i}}} = \frac{1}{\lambda_n} \tag{2.40}$$

A more complex description has also to include the effects of neutrals and impurities. The limiters (and any PFCs considered in the following) act in general also a main recycling and erosion sources. Additionally, neutral particles may be released into the SOL plasma by fueling or impurity seeding. Their penetration depths are characterized by an ionization length:

$$\lambda_{iz} = \frac{v_n}{n_e < \sigma_I v_e >} \tag{2.41}$$

where v_n is the thermal velocity of the neutrals, n_e the electron density, and $< \sigma_I v_e >$ is the rate coefficient for electron impact ionization.

The simple sheath limited SOL model and its characteristic decay lengths will be used in the following for the transport analysis of the 3D helical limiter SOL.

2.2.2 Simplified models for island transport

The divertor concept is fundamentally different from the limiter configuration. Here, the SOL does not require deep insertion of a solid limiting object. The idea is rather to increase the distance between PFCs and confinement region. Thereby the SOL can act as a protective layer between the core and plasma-surface interaction region preventing the release of recycling neutrals and sputtered impurities into the core. The general divertor concept is sketched in figure 2.7 (adapted from [6]). On the left and in the center the poloidal field divertor commonly used in tokamaks is shown. On the right side, the stellarator island divertor concept is shown as it is used in W7-X and W7-AS ($n = 8$ was realized in W7-AS).

Heat and particles leave the confinement region as indicated by the perpendicular fluxes $q_\perp$ and $\Gamma_\perp$ in figure 2.7 and are guided parallel to open magnetic field lines ($q_\parallel$ and $\Gamma_\parallel$) to the targets (blue) distant from the core plasma. This requires in tokamak single and double-null configurations additional poloidal fields which tear the nested flux surfaces apart by creating a separatrix. Low-shear stellarators such as W7-AS and W7-X have an inherent separatrix and magnetic islands.

The inherent magnetic islands in the boundary layer open due to their internal shear an additional radial transport channel in parallel direction. This is approximated by the rotational transform:

$$\iota = \frac{m}{n} + r_i \iota' \tag{2.42}$$

where m and n are the toroidal and poloidal mode numbers, r_i is the radial island width and $\iota' = \frac{d\iota}{dr}$ is the shear of the m/n resonance. The internal rotational transform $\iota_i = r_i \iota'$ around the island O-point is responsible for the termination of field lines on the targets. The island connection lengths are determined by the internal shear of the islands:

$$L_C = \frac{2\pi R}{N \iota'} \tag{2.43}$$

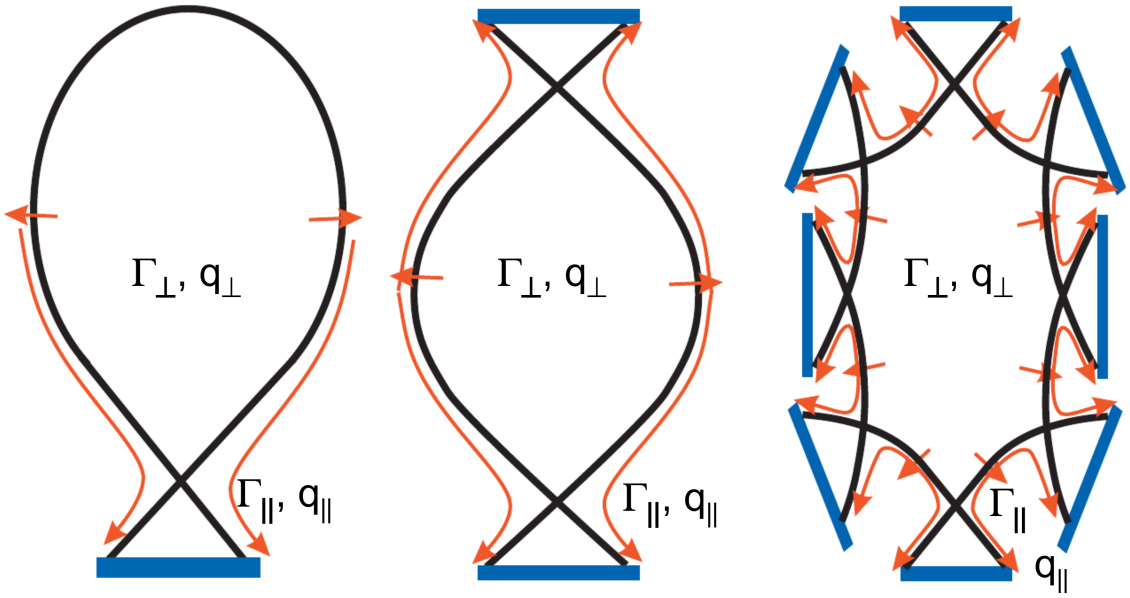

Figure 2.7 The divertor concept. Left and center: single and double-null poloidal field divertor (tokamak). Right: n =8 island divertor [6].

where N is the null number or number of islands. The width of the island scales as $r_i \propto \sqrt{Rb_{mn}/n\iota'}$ where b_{mn} is the resonant radial perturbation field normalized to the toroidal field. The connection lengths in stellarators with island divertors is generally much longer than in tokamaks due to their low shear.

The field line pitch is defined as $\Theta = \iota_i a/R$ and reaches in the present low shear stellarator a value of about 0.001[6].

The perpendicular to parallel transport ratio of heat conduction is a measure of interest. In order to obey dominant parallel against perpendicular heat flux conduction the following relation has to be satisfied [91]:

$$T_e > \left(\frac{\chi n_e}{\Theta^2 \kappa_e}\right)^{\frac{2}{5}} \tag{2.44}$$

In general, the cross-field transport competes and sometimes even dominates in the island divertor.

To relate downstream plasma parameter to (ideally) controllable upstream parameter 0D two-point models are typically used.

In a first step consider the basic Two-Point-Model of a divertor SOL [4]. The upstream position indicates the midpoint of a connection length or flux tube in the divertor geometry. Any ionization sources, friction or viscous effects are neglected. Thus the total pressure consisting of static and dynamic pressure is conserved along the flux tube:

$$p + nmv^2 = constant. \tag{2.45}$$

Assume $T_e = T_i$

$$p = nkT_e + nkT_i = 2nkT \tag{2.46}$$

The flux tube is characterized by $v = 0$ along almost the entire flux tube while and Bohm Boundary condition is applied at the target (t): $v_t = c_s = (\frac{2kT_t}{m_i})^{0.5}$. This results in the following simpler relation between upstream (u) and downstream/target (t):

$$n_t(2kT_t + mv_t^2) = 2n_u kT_u \tag{2.47}$$

$\rightarrow$

$$2n_t T_t = n_u kT_u \tag{2.48}$$

Conductive heat transport is assumed since the there is no flow:

$$T_u^{\frac{7}{2}} = T_t^{\frac{7}{2}} + \frac{7}{2} q_{\parallel} \frac{L}{\kappa_{0e}} \tag{2.49}$$

with electron parallel conductivity coefficient κ_{0e} for thermally coupled electrons and ions, neglecting parallel ion heat conductivity and $L = 0.5L_C$ The heat flux at the target or, more precisely, at the sheath entrance is

$$q_{\parallel} = q_t = \gamma n_t kT_t c_s \tag{2.50}$$

with sheat heat transmission coefficient $\gamma = 7$.

The complexity of the geometry of the island SOL and the various additional particle and heat sources and sinks, additional transport channels and plasma surface interactions may require more sophisticated and extended models in general [91]. In this study, it is one goal to characterize the 3D heat and particle transport based on relatively simple models.

Chapter 3

Analysis of limiter plasmas

3.1 Characterization of SOL heat and particle transport

3.1.1 Main geometrical properties of the limiter SOL

For initial operation (OP1.1) a limiter configuration was designed based on the field line diffusion method (FLD) [66, 93] and supported by EMC3-EIRENE calculations [7]. The magnetic field configuration and the shape of five inboard graphite limiters were chosen such that significant power loads to the metallic in-vessel components are avoided, and a limiter heat load distribution is achieved, which is as homogeneous as possible. The design process was iterative. A color-coded L_C plot with a Poincaré plot for an early design for limiter field configuration is shown in figure 3.1. The example shown has already the main geometric features of the finally designed configuration discussed in further detail below. Resonances including the m=6, n=5 resonance appear only in the confinement region. The limiters are inserted into the boundary layers and define the open field line domain. The contour plot shows a poloidally modulated pattern. This early limiter configuration was implemented in EMC3-EIRENE in order to assess the behavior of the limiter configuration based on a more sophisticated physics model, as compared to the faster and simpler FLD rather suitable for optimization. Initial EMC3-EIRENE results indicated the possibility of higher residual heat fluxes onto metallic in-vessel components shadowed by the limiter than what was predicted by FLD. Therefore, the configuration was adjusted by shifting the limiters 5cm deeper into the plasma. The following analysis is based on results published in [7].

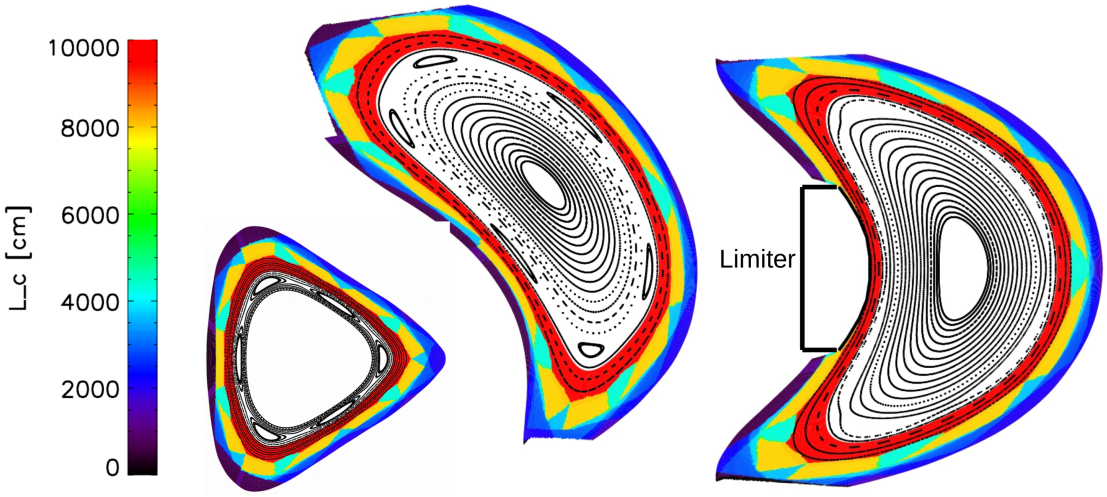

Figure 3.1 Earlier limiter design and field configuration: Poincaré plot combined with target-to-target connection lengths (L_C) for the vacuum magnetic field at toroidal angles $\phi_{tor} = 0°$, $\phi_{tor} = 12.3°$ and $\phi_{tor} = 36°$.

For the final configuration a complete vacuum Poincaré plot calculated at the bean shaped symmetry cross section (toroidal angle, ϕ_{tor} = 0°) is shown in figure 3.2a. In figure 3.2b the impact of the limiters is visualized by overlaying the color map of $L_c(R, Z)$. The limiters have a vertical extension of about ΔZ ≈90cm and and toroidal extension of ΔY ≈18cm ($\Delta\phi_{tor}$ ≈1.9°).

They define the magnetic SOL topology by cutting the field lines in a domain featuring mostly closed magnetic flux surfaces. The resulting poloidally alternating pattern in the L_C profile shown in figure 3.2b represents the open field lines which form the 3D scrape-off layer. Three different L_C length scales can be separated: L_C =36m, 43m, and 79m. The $\iota = 5/5$ divertor islands are shifted far outside of the limiter radius (not included in the Poincaré plot), while the $\iota = 5/6$ resonance is located within the LCFS. As a result, any short-circuiting within the edge transport region by fast transport around island separatrices is avoided.

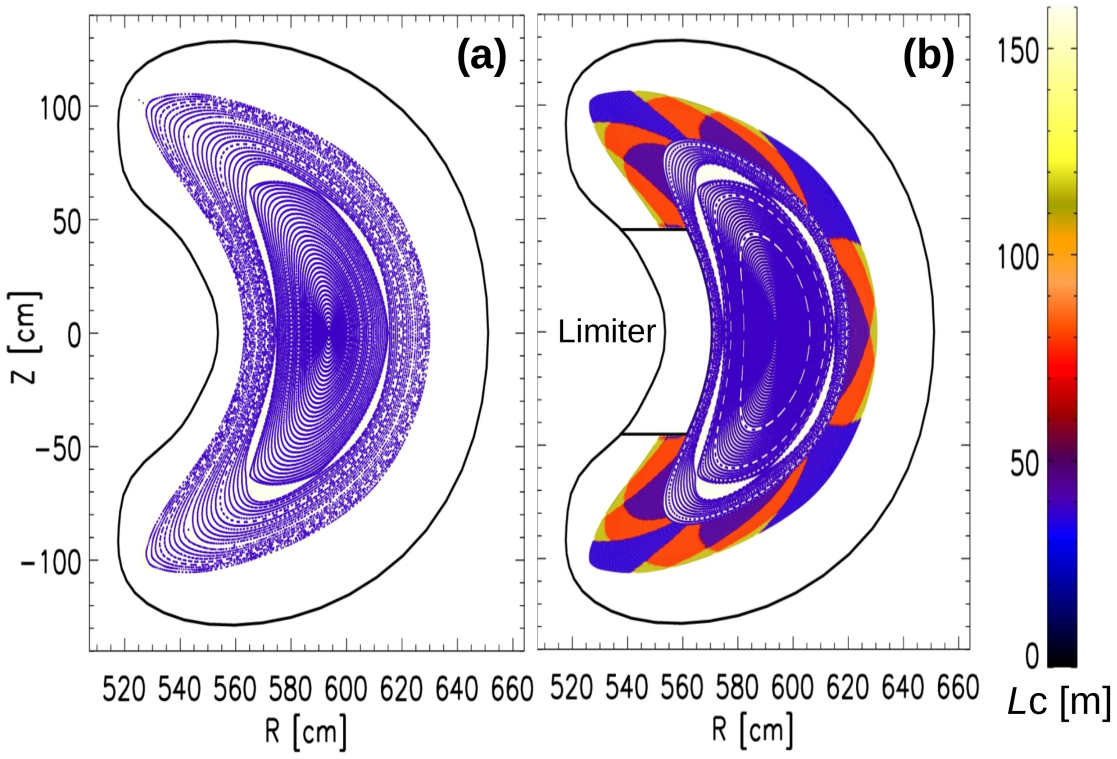

Figure 3.2 (a) Poincaré plot of the vacuum magnetic field at the bean shaped symmetry plane ($\phi_{tor} = 0°$). (b) Limiter and resulting target-to-target connection lengths (L_C) profile [7].

The magnetic topology is analyzed by calculating the target-to-target field line connection lengths L_C which define characteristic parallel transport length scales of the helical flux channels. The 3D spatial trace of the magnetic flux tubes which form the SOL are shown in figure 3.3 as 2D connection length profiles $L_C = L_C(R, Z)$ at four toroidal cross sections. In figure 3.3a the up/down-symmetric bean shaped section at ϕ_{tor} = 0° is shown, where the limiter is located. The cross section including the location of the gas injection system at ϕ_{tor} = 12.3° is shown in figure 3.3b. A further loaction at ϕ_{tor} = 24° is shown in figure 3.3c. The triangle shaped symmetry section at ϕ_{tor} = 36° is shown in figure 3.3d.

An evident poloidal variation of L_C is seen, which results from the intersection of the limiters with helical field lines at low magnetic shear. It is found that the magnetic SOL geometry

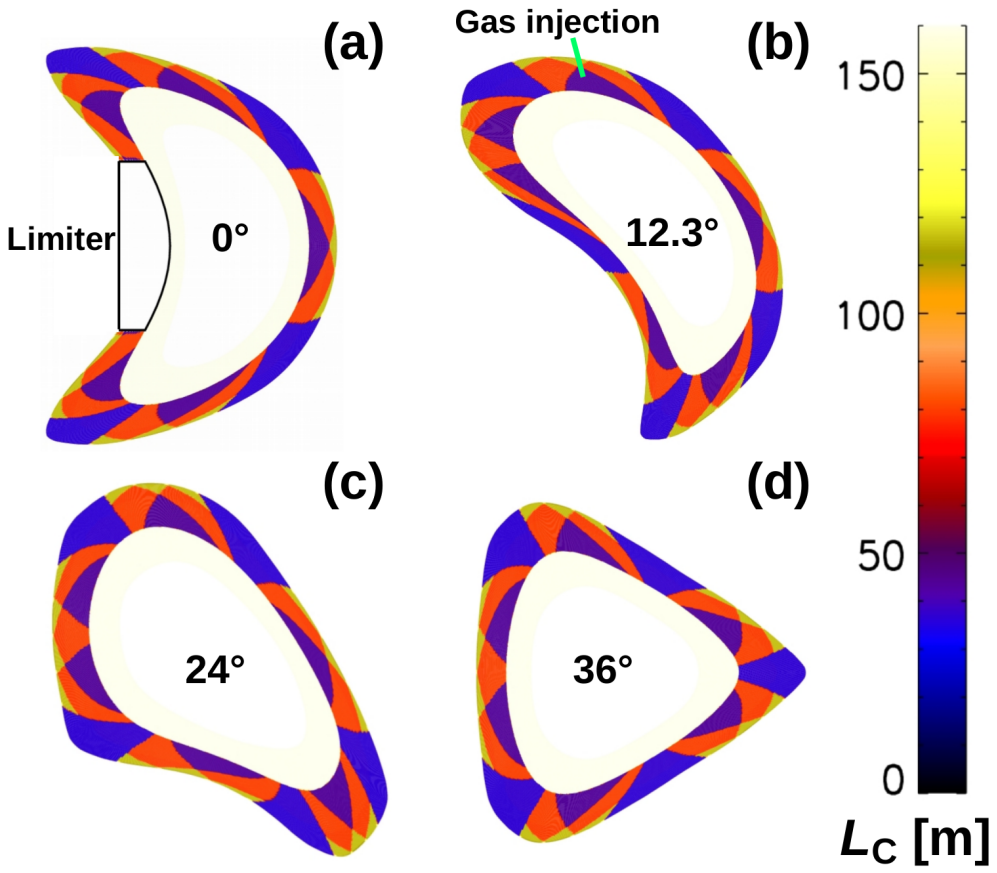

Figure 3.3 Target-to-target connection lengths (L_C) profiles covering a half field period ($\Delta\phi_{tor} = \frac{1}{2} \cdot \frac{360°}{5} = 36°$) (a) at the bean shaped symmetry plane ($\phi_{tor} = 0°$, including the limiter), (b) the cross section of the impurity seeding source ($\phi_{tor} = 12.3°$, green mark: poloidal seeding position), (c) a cross section at $\phi_{tor} = 24°$, (d) the triangular symmetry plane at $\phi_{tor} = 36°$.[7]

is composed out of three types of magnetic flux tubes of different L_C. This geometric feature existed already in the early limiter configuration shown in figure 3.1 and is maintained during slight changes of the rotational transform as discussed below.

The reason for the formation of these different length scale magnetic flux tubes is explained based on figure 3.4 (left). Here, the 3D paths of three single field lines, each representative of one magnetic flux tube, are shown. In the first case, the field line starts and ends at the same limiter after one toroidal turn (figure 3.4a), corresponding to a length of $L_C \approx$36m. In the second case,

the field line hits after 1.2 toroidal terms the next neighbouring limiter, corresponding to L_C ≈43m (figure 3.4b). In the last case, the field line needs 2.2 toroidal turns (L_C ≈79m) to reach the next neighboring limiter (figure 3.4c). The discrete lengths can be approximated as such:

$$L_C \approx N_{turn} \frac{2\pi R}{5} \tag{3.1}$$

with N_{turn} =5, 6, 11 and major radius R.

On the right side of figure 3.4 the total connection length and shortest connection length distributions are shown. The marks and arrows identify the geometrical stagnation points in the flux tubes (or upstream location in a more simplified model) in the field line plots and the connection lengths distributions. These stagnation points are simply the midpoints of the flux tubes.

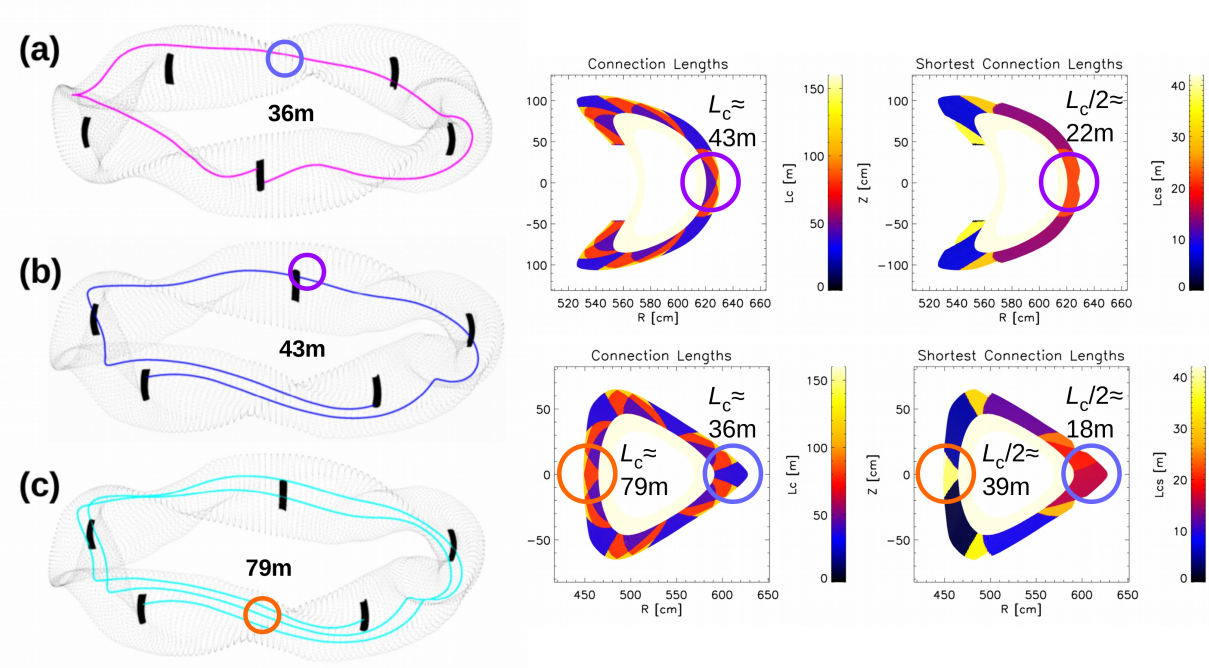

Figure 3.4 Left: Magnetic field lines representing the three different types of magnetic flux bundles in the SOL. (a) 1 turn, L_C ≈ 36m. (b) 1.2 turns, L_C ≈ 43m. (c) 2.2 turns, L_C ≈ 79m [7]. Center: Total connection lengths in toroidal symmetry cross sections. Right: shortest connection lengths in toroidal symmetry cross sections. Circles: exact upstream positions.

From figure 3.4 it is evident that every limiter is connected with itself by the shortest flux tube (36m) and with the next neighboring limiters by the longer ones (43m and 79m). Due to the five-fold symmetry of W7-X, these three flux bundles are formed starting at each limiter. Therefore, the SOL magnetic structure consists of $3 \cdot 5 = 15$ separate regions of magnetic flux tubes.

A characteristic point within such simple SOL geometries is the stagnation point of the flow somewhere in the middle between the limiters connected. To identify the exact upstream and downstream locations the connection lengths and the shortest connection lengths are considered and plotted on the right side of figure 3.4. Both are shown for the symmetry planes for bean shape (top, $\phi_{tor} = 0°$) and triangular shape (bottom, $\phi_{tor} = 36°$). The downstream location merely is at the position of the limiter at the inboard midplane of the bean-shaped toroidal section. The limiter is the central heat and particle sink.

The exact upstream positions are geometrically located at the center of the flux tubes and marked by circles in figure 3.4(right). It turns out that the upstream position for the $L_C = 43$m flux tube is located at the toroidal bean shaped limiter section at the outboard midplane. The upstream locations of the shortest ($L_C = 36$m) and longest ($L_C = 79$m) flux tubes are located outboard and inboard midplane in the toroidal triangular shaped section. These upstream reference points are exactly halfway ($L_C/2$ distant from the limiters in both parallel/toroidal directions. It will be shown later that this geometrically predicted reference points can be recovered within the SOL plasma parameters.

The outermost SOL layers which may contain open field lines with $L_C >>$80m (yellow in figure 3.4(right)) in the very edge has a negligible impact. It lies several density decay lengths radially outward of the real SOL transport domain. As a consequence, the wall and in-vessel components are neglected as targets in this topological analysis and the following transport calculations.

In summary, it is shown that the W7-X start-up topology features a relatively simple discrete distribution of connection lengths due to the low magnetic shear and the way the limiters were

physically mounted. This is in contrast to the island divertor configuration discussed later, which also features a radial magnetic component and in average a factor of 10 longer L_C within the islands (and a factor of 100 longer L_C at the separatrix).

3.1.2 Impact of small rotational transform changes on edge magnetic structure

Small changes to the rotational transform can have a significant impact on the core transport and also to the plasma-wall interactions. Towards the end of the end of OP1.1, a configuration scan was performed by changing the currents in the planar coils which resulted in a slight increase of the ι. The motivation was to investigate if better core confinement can be achieved by, on the one hand impacting the electron root core confinement and on the other hand, by the resulting adjustment of the edge topology and moving the $5/6$ islands further inwards away from the particle source at the limiters. Aspects of core transport and Helium exhaust are discussed in [13, 94, 95]. The maximum ι showed the most substantial differences in plasma transport and PSI compared to the default limiter configuration. Therefore, a second limiter configuration with maximum increased rotational transform ι_{LCFS}=0.91 was implemented in this study.

The connection lengths profiles and vacuum Poincaré plots of the standard and increased ι limiter magnetic field configurations are shown in figure 3.5. The increased ι has a slightly smaller minor radius. In comparison to the standard limiter magnetic field scenario in figure 3.5 the $5/5$ main resonances are shifted further inwards cutting back the domain of smooth closed magnetic flux surfaces in the outer boundary. The $5/6$ resonances are shifted more in-depth into the confinement domain and reduced in size. Near the LCFS the SOL features the same three types of magnetic flux tubes like the standard ι case. However, the volume of the shortest flux tube ($L_C \approx$36 m) is increased at the expense of the other region. The toroidally and poloidally volume averaged radial connection lengths distributions are shown in figure 3.6. Note that the absolute positions

of the LCFS of the two configurations deviate from each other. In both configurations an average value of

$$< L_C >_V \approx 50m \tag{3.2}$$

is found for the main SOL, that is the region between LCFS and far SOL most relevant for transport.

The far edge profile contains domains of infinite L_C corresponding to closed field lines of the $5/5$ islands, that do not intersect with the limiters. In the standard island divertor configuration considered later, these islands will be shifted inwards and define the main SOL. However, in the limiter configuration, they are located several radial decay lengths of plasma parameters distant from the LCFS deep in the limiter shadow and probably also limited by in-vessel structures neglected in the modeling. Therefore it is not expected that these islands are relevant for the plasma transport and PSI in the main SOL.

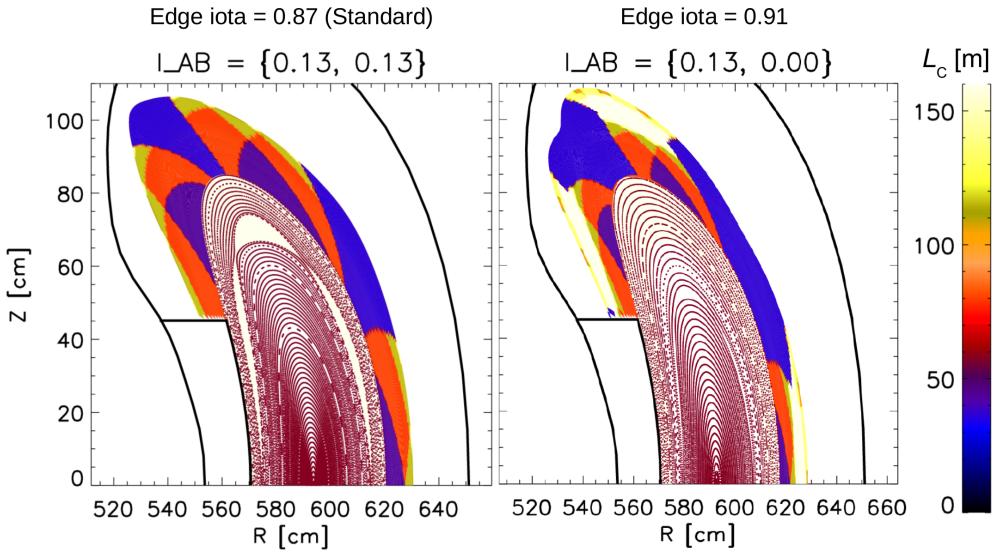

Figure 3.5 Connection lengths profiles overlaid and Poincaré plots for both the standard and increased iota configurations [8].

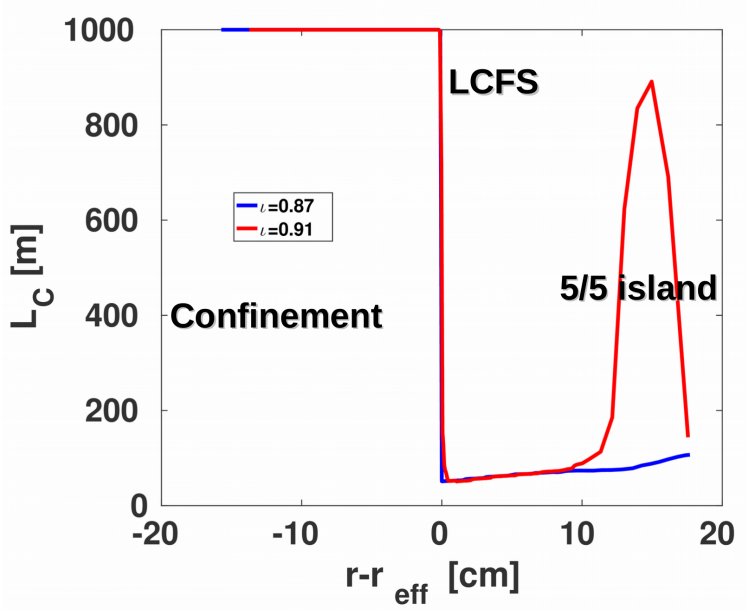

Figure 3.6 Flux surface averaged connection lengths profiles of both limiter configurations considered.

A perpendicular view onto the SOL allows a more intuitive understanding of the qualitative changes between the two configurations. The toroidal and poloidal distribution of L_C is shown on the left of figure 3.7. The dark center stripe represents the limiter. The red stripes correspond to the long (79m) connection lengths flux tubes. The mapping of the connection lengths onto the limiter is shown on the right of figure 3.7. A comparison of top and bottom plots clearly shows that the long (red) flux tubes are shifted towards the midplane in the high ι configuration. As will be shown in the following chapters, this has consequences for the local heat and particle patterns and consequently on the location of erosion and deposition zones. It is seen, that the relative poloidal widths of the flux tubes differ between the two configurations. The shorter flux tubes will collect more particles in the poloidal direction in case of increased transform because their cross-section is enlarged poloidally. However, this hardly affects the average $\parallel$ to $\perp$ transport ratios, which are mostly depended on the parallel and radial transport parameters.

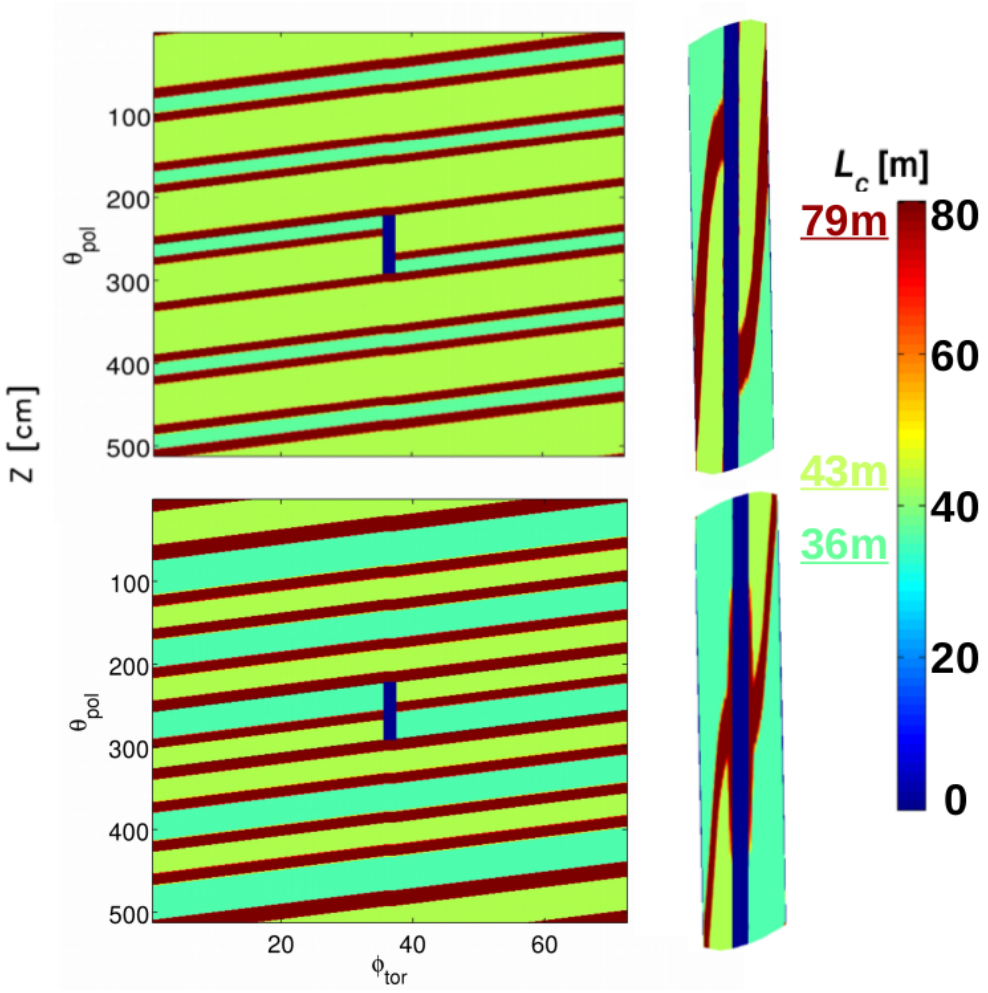

Figure 3.7 Flux surface connection lengths profiles (left) and limiter mappings (right) onto the limiters for standard (top) and increased ι (bottom) configurations.

In summary, it is stated that the moderate increase of rotational transform shows local changes and shifts of connection lengths, change of flux tube volumes and L_C pattern on the limiters. The significant geometrical properties, such as the type and number of flux tubes and the average connection lengths are conserved. The volume of the confined domain reduces slightly, and the $5/5$ islands remain in the remote SOL. In the following chapters, the correlation between connection lengths distribution and 3D plasma transport and PWI will be discussed.

3.1.3 Correlation between limiter SOL geometry and counter streaming flows

In this section, the main transport features in the previously analyzed 3D structure are investigated with EMC3-EIRENE modeling and analyzed based on the sheath limited simple SOL model introduced earlier (section 2.2.1). Part of the results of this first time systematic study of the limiter plasmas scenarios is published in [7]. The findings helped to shape and interpret experiments in the first campaign. General assessment was undertaken to explore edge physics phenomena of interest accessible by edge diagnostics. One goal was to explore the operation space with a focus on input powers and densities which may potentially cause high local heat fluxes onto the limiters. A particular goal was to initiate development of controlled radiative power exhaust to prevent or reduce such loads. The transport results in this section will be used to understand the downstream PSI discussed in following sections.

EMC3-EIRENE simulations were carried out for pure hydrogen plasmas at spatially fixed perpendicular transport coefficients ($D_\perp$=1 m^{2}s^{-1}, $\chi_{\perp,e,i}$=3$D_\perp$). An example is shown in figure 3.8 for a scenario with n_{LCFS} =7·10^{18} m^{-3} at P_{in} =4 MW. The 2D profile of the thermal plasma pressure ($p = n(T_e + T_i)$) is shown in figure 3.8a as color coded contour plot at $\phi = 12.3°$ toroidally. Clear oscillations of the pressure are seen in the plasma edge, which become directly visible in figure 3.8b, where a poloidal profile of the pressure on a SOL flux surface is shown.

The comparison with the SOL topology in figure 3.3b indicates the dented shape of the isobars is linked to the connection length modulation in poloidal direction. Poloidal scans of plasma data and connection lengths along poloidal surfaces of constant effective radii show a clear correlation between plasma transport and magnetic edge topology. In figure 3.8b such a 1D poloidal profile is shown for SOL pressure (red) and L_C (blue). The maxima and minima of the pressure match with the maxima and minima of the connection lengths.

The lower pressure in the regions of short connection length is a result of the faster parallel transport along shorter L_C to the limiters ($\tau_p \propto \frac{L_C}{v_\parallel}$). The parallel flow has been built up already to a finite level in this region of the simple SOL flux channel, which causes a directly enhanced parallel loss. It is relatively overweighting the incoming radial flux. A detailed analysis of this situation was also discussed at the TEXTOR-DED tokamak along direct measurements of this pressure drop inside of the short L_C flux tubes [96].

This modulated pressure (figure 3.8a,b) drives flows, which is seen in the 2D Mach number profile in figure 3.8c. This poloidal modulation represents counter streaming flows in adjacent flux channels (alternating blue and red domains in figure 3.8c). The local flow strengths depend on their distance to the limiters. The flow approaches stagnation at the upstream position and accelerates closer to downstream positions. Additionally, there is flow stagnation in the small layers between counter streaming flows due to viscous friction. This is shown in the 1D poloidal SOL profiles in figure 3.8d. The Mach number (green) shows clear modulation and stagnation between flows in negative and positive parallel direction. Maxima and minima are determined by the shortest distance to the next limiter at the respective poloidal position because particles will take the shortest path to a limiter and accelerate to ion sound speed near the surface.

The counter streaming flows at a given toroidal location (here $\phi_{tor} = 12.3°$) arise because the adjacent helical transport channels are of different connection lengths (L_C) and they are partly connected to different limiters. The midpoints ($l_\parallel = 0.5 L_C$) of the open field lines or flux tubes are in the simple SOL model [4] the locations of the stagnation points ($v_\parallel$ =0 ms^{-1} and M =0). Within a single flux tube, the flow strength increases once one leaves the stagnation point along the open field line in either positive or negative direction towards the connected limiters. The direction and level of sonic flow depend on the distance to the closest limiter where it reaches ion sound speed (M=1) - in EMC3-EIRENE, the Bohm velocity is used as the boundary condition at the target. This was experimentally also seen in the TEXTOR-DED tokamak, which also featured a

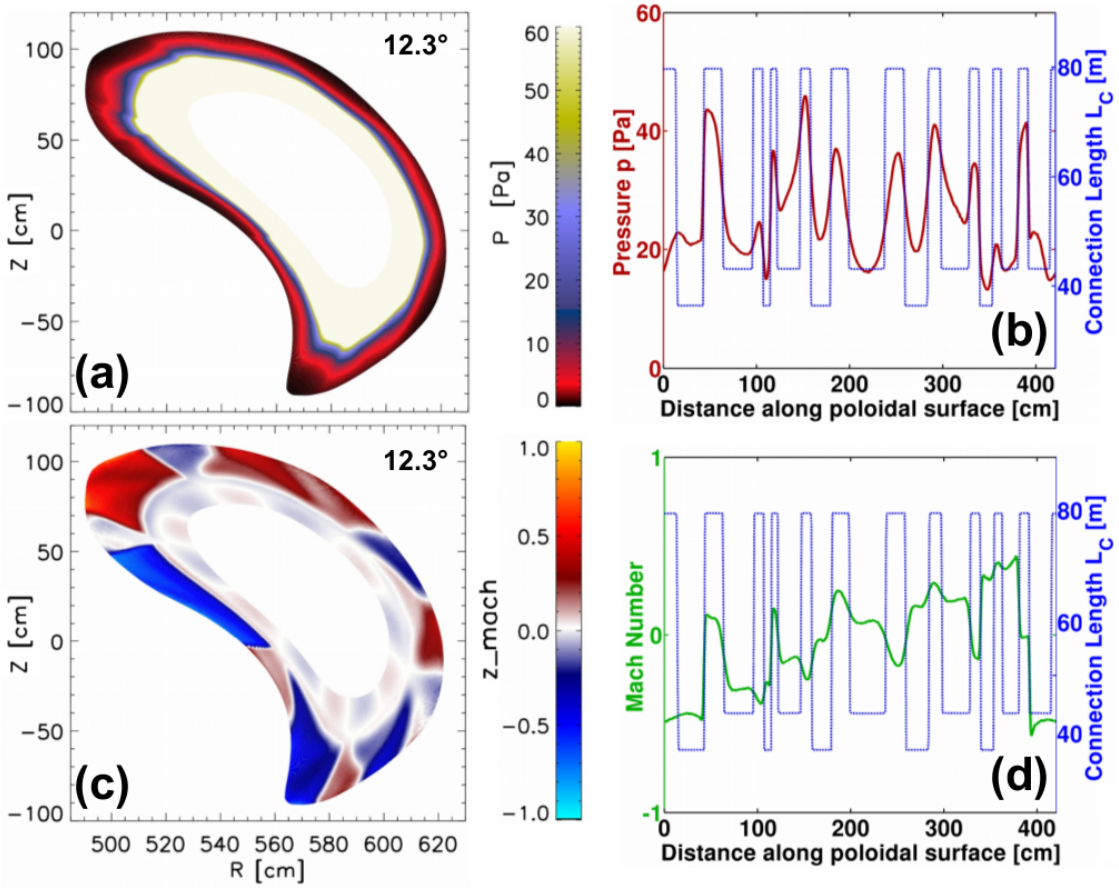

Figure 3.8 Plasma profiles for $n_{LCFS} = 7{\cdot}10^{18}$ m^{-3}, $P_{in} = 4MW$ at ϕ_{tor} =12.3°: (a) 2D Pressure profile. (b) 1D poloidal pressure and connection lengths profile. (c) 2D Mach number profile. (d) 1D poloidal Mach number and connection lengths profile.[7]

comparable helical SOL structure [96] and more recently in the more complex SOL geometry of HSX [97]. Flow measurements were recently conducted for the first time at W7-X in the island divertor and will be discussed later. The link between topology and the non-axisymmetric, highly complex flow pattern is important because it might impact on the momentum balance and hence introduces physics aspects not known from tokamak detachment physics [98]. It is particularly important for the edge impurity transport and the related feasibility of radiative power exhaust by intrinsic and extrinsic impurities discussed later.

3.1.4 Impact of field geometry changes on plasma edge transport

The analysis before showed the direct link between the connection length and the actual plasma parameters inside of the SOL. In order to address the impact of changes to the geometry induced by an increase of the rotational transform ι on the plasma edge structure, further plasma transport modeling with EMC3-EIRENE was undertaken. Plasma scenarios in both configurations were simulated. The results are shown in figure 3.9. Boundary conditions for hydrogen plasma closer to actual experimental conditions are used, a LCFS density of n_{LCFS} ≈5.5·10^{18} m^{-3} and ECRH heating of P_{ECRH} =1 MW. The configuration with edge rotational transforms of $\iota_{LCFS} = 0.87$ (1-D: dashed lines) and $\iota_{LCFS} = 0.91$ (1D: solid lines) are compared.

The analysis of the change to the magnetic structure showed that the SOL flux bundles were compressed poloidally and extended somewhat further out into the SOL domain - when ι was increased. Also, the $5/5$ island chain was moved into the modeling domain, however, at a far distance of about 15cm away radially from the LCFS. In the pressure profile, this manipulation results in a change of the isobar structures. The comparison of the 2D pressure profiles in figure 3.9(a) and (b) with the 2D L_C profiles in figure 3.5(left) and figure 3.5(right) shows that the poloidal pressure distribution changes in correlation with the the re-distribution of connection lengths [9]. Regions with higher pressure are always located in the regions with longer connection lengths because they receive more heat and particles by cross fueling.

The 1D flux surface averaged profiles for temperatures, and densities (figure 3.9(c,d)) almost match between the different configurations for an anomalous diffusion coefficient of $D_\perp = 1.0$ m^2s^{-1} within the SOL. For $D_\perp = 0.4$ m^2s^{-1} the 5/6-islands within the LFCS appear as a clear effect in the temperature of the standard limiter configuration profile (green) ($\iota_{LCFS} = 0.87$). The local flattening of the radial temperature profile is a result of the magnetic field line displacement across the island width, which causes fast parallel convection of heat around the island. This yields

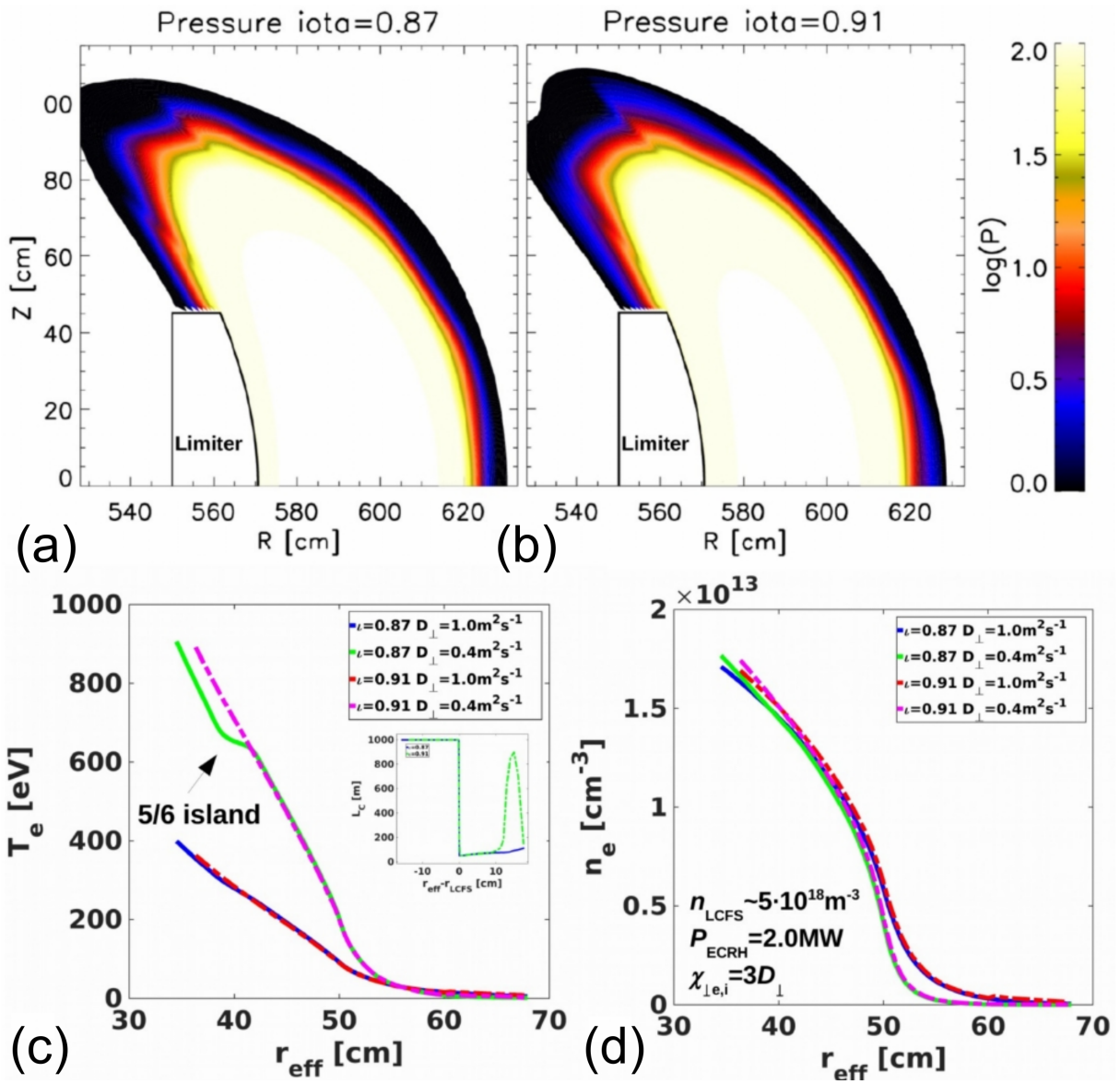

Figure 3.9 Comparison of limiter scenarios with $n_{LCFS} \approx 5.5 \cdot 10^{18}$ m^{-3}, $P_{ECRH} = 1$ MW. 2D pressure profiles for (a) $\iota_{LCFS} = 0.87$ and (b) $\iota_{LCFS} = 0.91$. 1D temperature and density profiles for (c) $\iota_{LCFS} = 0.87$ and (d) $\iota_{LCFS} = 0.91$ [9]

an effectively enhanced radial transport at fixed perpendicular energy influx into the domain. A reduced radial temperature gradient across the $5/6$ island is established at sufficiently low perpendicular heat diffusivity. In this case, the parallel transport along field lines within the island is faster than the perpendicular diffusive transport across the island. This effect is seen here for the standard limiter configuration only because the 5/6 islands are shifted inwards (beyond the inner simulation boundary) in the increased ι configuration (see figure 3.5). Such effects are of relevance in the island SOL discussed later.

According to EMC3-EIRENE modeling, the change of the magnetic geometry mostly causes a poloidal redistribution of SOL plasma parameters. However, the geometry properties in the main SOL do not change between the two limiter configurations compared. Both vacuum magnetic fields show mostly closed flux surfaces in the transport relevant boundary and three types of flux tubes. Although the connection length distributions change locally, the poloidally and toroidally average connection length is almost equal ($< L_C > \approx 50$m). Therefore the parallel to perpendicular transport ratio does not change overall.

Estimates of fueling and exhaust based on the present simulation results suggest that the global particle confinement times between the scenarios are comparable. In the experiment, however, increased confinement times have been measured for both the main hydrogen species and injected helium during transport experiments. Here, the helium and hydrogen confinement times increase for the increased ι configuration and an enhanced release of neutral pressure after the discharge is measured which indicated higher retention of the fueling term in this alternate 3D edge topology [13, 99, 94]. The reason for this deviation is beyond the scope of this thesis. However, the results of the redistribution of plasma parameters in correlation with the change of the magnetic edge topology will have an impact on the PSI as discussed in the following sections.

3.1.5 Parallel edge transport in flux tubes

For the analysis of the parallel plasma profiles, the quasi-discretization of the SOL geometry is used to distinguish the 3D distributions of plasma parameters based on the flux tube lengths L_C. For this purpose parallel profiles of densities n_e, electron and ion temperatures $T_{e,i}$, Mach number and particle source S_p are extracted from the three flux tubes and plotted in figure 3.10 (a-d) over a parallel length coordinate $l_\parallel$. The three colors represent the short and long L_C (blue: 36m, green 43m, red: 79m). The temperature profiles T_e as solid and T_i as dashed lines. These typical profiles recover the properties of the simple SOL discussed in the previous section.

The profiles are extracted at the same (magnetic) radial distance. The highest density is reached in the longest flux tube (red, figure 3.10(a)). From pressure conservation, Bohm boundary condition and assumption of an approximately isothermal SOL it follows from equation 2.48 that the downstream density at the limiters located at the ends of the profiles in parallel direction must drop to $n_{down} = 0.5 n_{up}$ [4].

The parallel temperature gradients almost vanish, in particular for the electron temperature. The Mach number converges to $M = \frac{v_\parallel}{c_S} = \pm 1$ at the limiters. The particle source strengths are shown in a logarithmic scale in figure 3.10(d) and peak only near the limiter due to the localized release of recycling neutrals. The small-scale oscillations in the S_p profile occur when field lines pass a toroidal domain with a limiter, where the neutral concentration is higher than in the rest of the torus.

These profiles show in summary typical isothermal and flow profiles of the simple SOL despite the presence of a particle source at the downstream location. Scenarios with higher densities deviating from the simple SOL description will be discussed later.

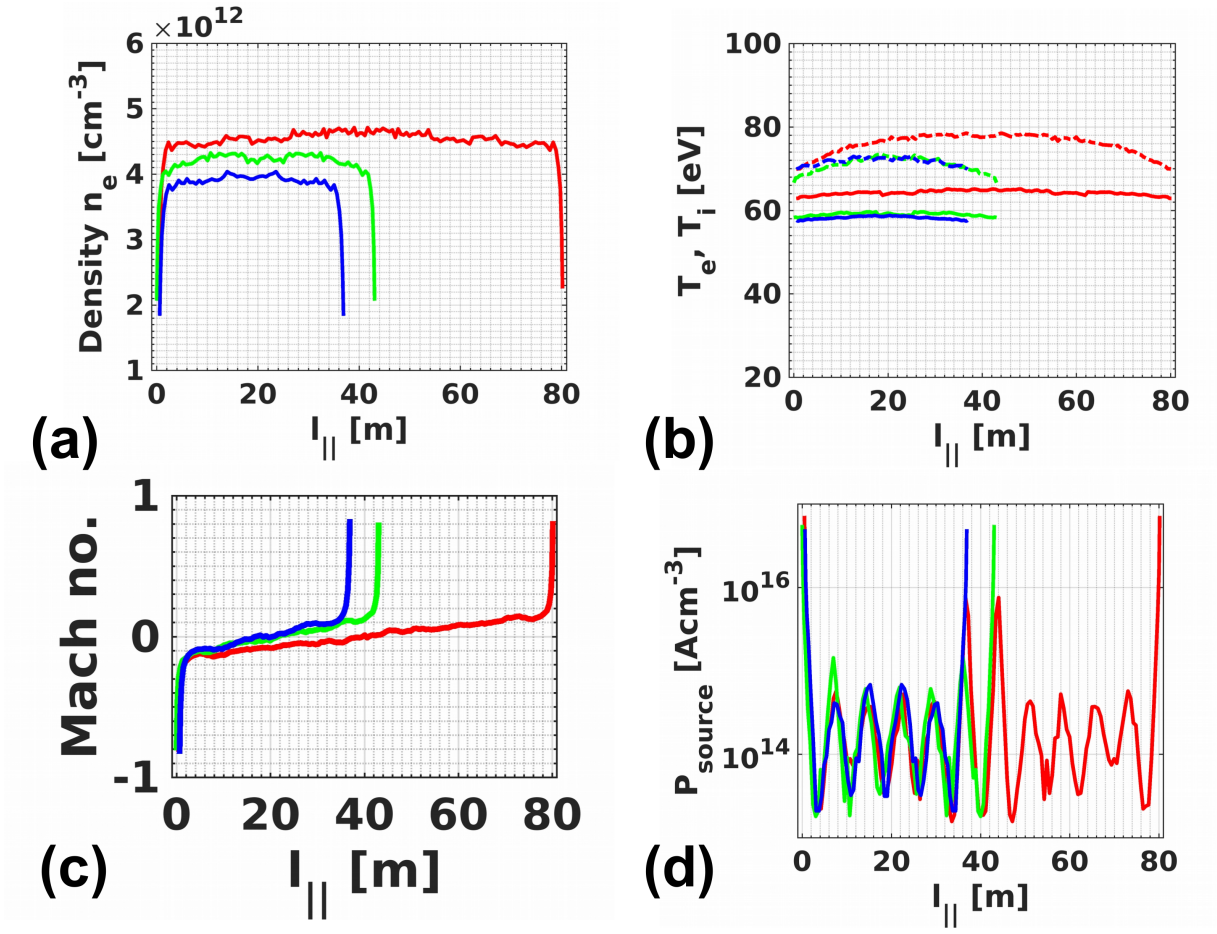

Figure 3.10 Parallel profiles of (a) densities, (b) electron and ion temperatures, (c) Mach number and (d) particle sources in the flux tubes. The data are plotted along field lines of lengths $L_C =$ 36m, 43m and 79m

3.1.6 Correlation between plasma decay lengths and edge geometry

As introduced in section 2.2.1 the sheath limited simple SOL assumes ideal exponential decay within the SOL. The decay length is a crucial parameter, that determines the SOL width, the plasma wetted area and in particular the heat flux channel widths. Here, the decay lengths are considered for each connection length region.

For the analysis, the poloidally and toroidally averaged radial edge density profiles are plotted in figure 3.11 for (a) standard limiter configuration and (b) increased ι limiter configuration. The

solid black line represents the average over all flux tubes and the full domain. The blue line represents the SOL averaged density profile (for consistency, it has to match with the black one beyond the LCFS). Green, red and magenta represent the radial densities in the short (36m and 43m)and long flux tubes (79m). The dashed line marks the radial location of the LCFS.

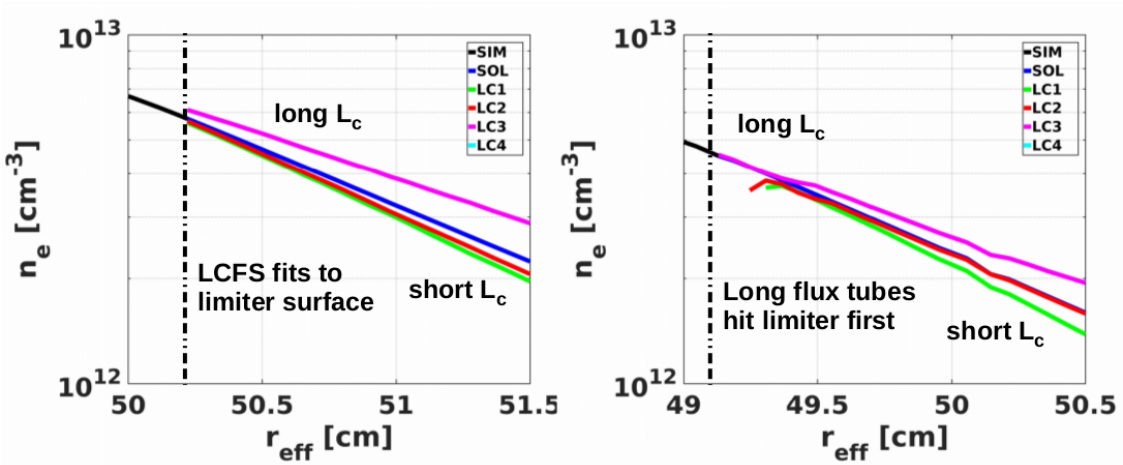

Figure 3.11 Density profiles for limiter scenarios. (a) standard limiter configuration. (b) increased ι configuration. (Black: full simulation domain, blue: SOL, green, red, magenta: $L_{C1,2,3} = 36$m, 43m and 79m).

The flux tube densities are adjacent to the LCFS in the standard limiter configuration (figure 3.11(a)). The longest flux tube (magenta) shows the highest density and also a slower decay compared to the shorter flux tubes. Green clearly shows the fastest decay. The averaged SOL density is closer to the density profiles in the shorter L_C regions. The same profiles are shown in figure 3.11(b) for the increased ι configuration. Here, some small-scale effects can be recovered within a few millimeters outside the LCFS. The flux tubes in the shorter L_C region (green and red) are not adjacent to the LCFS. Only the long connection length channel (magenta) is adjacent to the LCFS. The shorter channels are therefore fueled from the longer L_C channels. This effect is due to the mismatch of the magnetic field geometry and the limiter shape.

The limiter was designed for the specific shape of the flux surfaces within the standard limiter configuration. The LCFS, therefore, does not match with the limiter shape in the other configurations of an increased rotational transform. This mismatch will also be noticeable in the in the limiter deposition patterns. There may also be a mismatch in the standard limiter configuration under experimental conditions. Slight imperfections related to the magnetic field or displacement of the limiters may result in a deviation from the ideal geometry assumptions based on the design study.

The main result is that despite differences in the magnetic configuration radial distribution of plasma parameters is quite similar between both configurations. The plasma density is in both scenarios higher in the longer flux tubes. The density decay lengths λ_n can measure the SOL widths. The width depends on the SOL geometry and scales in both configurations as such:

$$\lambda_n \propto L_C^{\frac{1}{2}} \tag{3.3}$$

The faster transport in shorter connection lengths regions ($\tau_{\|} \propto \frac{L_C}{c_S}$) results in steeper gradients of the plasma profiles. In the following, the impact of this 3D geometry on PSI will be examined in a few example scenarios.

3.1.7 Correlation between the 3D SOL geometry and limiter heat and particle fluxes

In the following, the limiter heat loads of hydrogen plasmas are analyzed with a particular focus on the correlation of the flux pattern with the magnetic footprint on the limiters as well as the impact of the actual geometry of the limiter surface. This discussion is a summary with some extension of the results published in [7].

As a first step, the magnetic footprint and the limiter heat loads q_{depo} are calculated with EMC3-EIRENE and plotted in figure 3.12. The 2D L_C and the deposited heat load are shown on the left and right, respectively. The example considered corresponds to a scenario with case with

n_{LCFS} =1·10^{18} m^{-3} at an input power of P_{in} =4 MW. The connection lengths pattern consists of diagonal red stripes corresponding to the long (79m) magnetic flux tubes. The dark blue center stripe represents a region without a magnetic connection because of the flat top of the limiter. Here the field lines of the LCFS proceed tangential along the limiter. The size of the unexposed area might be slightly overestimated in the modeling because of the finite radial resolution of the numerical grid used for the L_C mapping. The dark blue unwetted region and the red stripes enclose the domain of 43m long connection lengths (green). The outer (turquoise) area corresponds to the shortest length scale (36m).

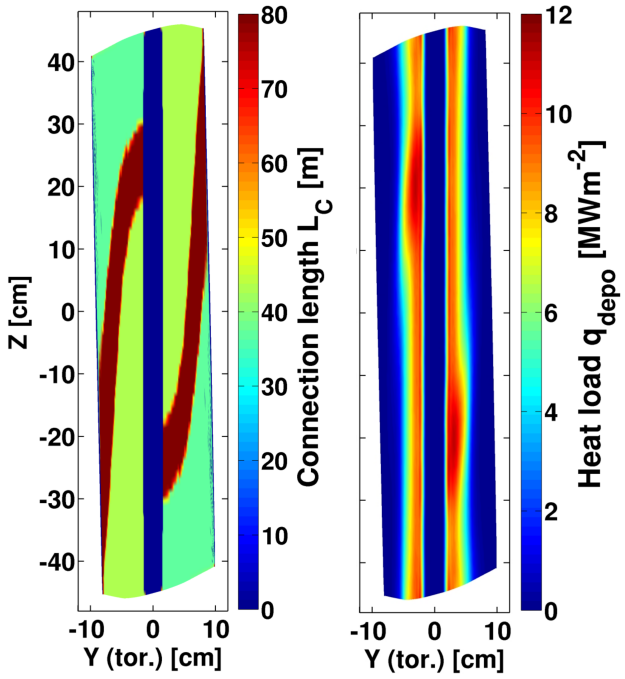

Figure 3.12 Left: Target-to-target connection length L_C mapped on the limiter. Right: 2-D limiter heat flux deposition for a hydrogen plasma at P_{in} =4 MW and $n_{LCFS} = 1 \cdot 10^{18}$ m^{-3} [7].

A characteristic feature of the heat flux pattern shown in figure 3.12 (left) are the vertical stripes with maxima $P_{peak} = max(q_{depo})$ on the upper left and lower right part of the limiters ($Z \approx +/- 0.2$m). These striation patterns are a result of a combined effect of magnetic flux

tube topology, target geometry, incident angles of the field lines and the radial decay of plasma transport. The heat loads reduce towards the outer part of the limiters, as the parallel heat fluxes decay exponentially in the radial direction.

The heat flux to the tip of the limiter is small, because there is no direct parallel heat transport but only the much smaller radial heat diffusion onto this area.

Electrons and ions lost along the open field lines towards the limiters can establish parallel temperature and density gradients in the code (using ambipolarity condition), which cause convective (through the particle flux due to the parallel pressure gradient) and conductive heat fluxes onto the limiters. According to the correlation between plasma parameter and magnetic length scales L_C, the P_{peak} appear at positions where the long flux tubes connect to the limiters close to the LCFS (at $Z \approx +/-0.2$m in figure 3.12). As in the case of the pressure and flow modulations correlated to L_C before, this is because the long magnetic flux tube receives more cross field fueling of particles and energy. This correlation, however, is effective only in the near SOL region where the flux tubes touch the LCFS and receive cross field fueling from the confinement region. In the far SOL, this correlation gets diluted, since the perpendicular transport reduces and flux tubes overlap in the radial direction in the outer SOL and exchange particles and heat among each other.

The limiters of the W7-X startup configuration have a 3D shape such that effects of the target geometry, this means the local angles of incidence (also referred to as 'geometry function' in the following), on the deposited heat fluxes, have to be considered carefully. To define a measure for the heat load decay linked to the SOL heat flux channel width, a description of the deposited heat flux distributions and explanation of governing mechanisms is summarized in the following. The details can be found in [7].

The parallel heat flux reaching the limiter is defined as:

$$q_{\parallel} = nc_s(\gamma_e T_e + \gamma_i T_i) + q_{rec} \tag{3.4}$$

where γ_e =4.5 and γ_i =2.5 represent the sheath heat transmission coefficients for electrons and ions and $c_s \approx \sqrt{\frac{T_e+T_i}{m_i}}$ is the ion sound speed. The additional term q_{rec} =(13.6 eV +2 eV)nc_s accounts for a small heat flux contribution due to atomic and molecular recombination on the limiter surface. The parallel heat flux $q_\parallel$ is assumed to decay radially as:

$$q_\parallel = q_{\parallel,0} e^{-(r-r_{LCFS})/\lambda_{q_\parallel}} \tag{3.5}$$

where $\lambda_{q_\parallel}$ is a characteristic decay length and r is the effective radius. As derived in [7] the deposited heat flux is determined by the target geometry:

$$q_{depo} = q_\parallel \sin(\alpha) = q_{\parallel,0} e^{-(r-r_{LCFS})/\lambda_{q_\parallel}} \sin(\alpha) \tag{3.6}$$

where α is the incident angle of a field line on the limiter. An explicit representation of $q_\parallel$ in flux surface coordinates is usually not possible in stellarators because of the presence of islands and ergodic regions present in the boundary magnetic field. A first attempt in this study and experimentally was made to measure local q_{depo}-profiles as functions of the surface coordinate s or local absolute radius.

$$q_{depo} = q_{depo,0} e^{-r/\lambda_{q_{sf}}} \tag{3.7}$$

whith the surface heat load profile width

$$\lambda_{sf} := -\frac{q_{depo}}{\frac{dq_{depo}}{ds}} \approx \lambda_{q_\parallel} \frac{ds}{dr} \tag{3.8}$$

The heat load width λ_{sf} and the maxima of q_{depo} are used as effective measures to characterize the limiter heat fluxes. During the present study, both the effective heat loads modified by the local angles of incidence on the limiter surface and the downstream heat fluxes not modified by the limiter surface geometry, are considered. The latter allows for a more general analysis. The definition of heat flux measures in this 3D limiter configuration is relatively simple compared to the more complex island divertor configurations discussed later in this study.

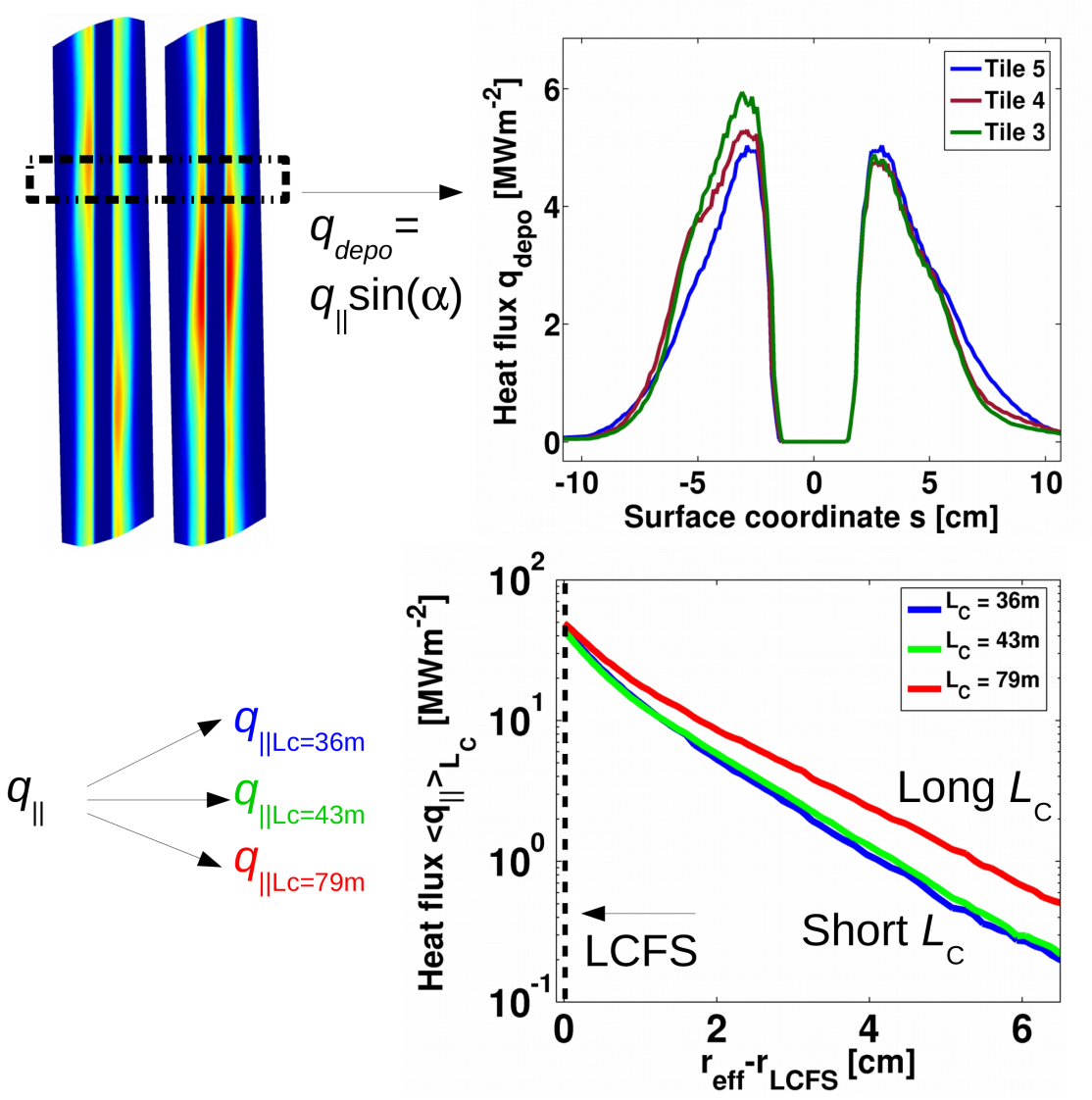

Figure 3.13 Analysis of the effective heat loads q_{depo}. (a) 2D (left) and 1D (right) profiles of the deposited heat fluxes. (b) three downstream heat flux profiles for short and long L_C.

The relatively simple magnetic field structure of the limiter plasmas and its alignment with the limiter geometry allow for separate analysis of downstream heat fluxes $q_{\parallel}$ and effective heat fluxes q_{depo}. The analysis method is shown in figure 3.13. Here, the deposited heat fluxes are shown for the standard limiter configurations on the top left. On the top right, the profiles of deposited heat flux on the surface are shown. On the bottom, the downstream heat flux $q_{\parallel}$ is shown averaged over domains of equal L_C like the SOL densities and temperatures discussed above. The longest flux tube (red) carries a higher level of heat flux and shows a flatter decay than the shorter ones (green and blue).

The heat and particle fluxes are both expected to follow a decay according to $\frac{1}{\lambda_{q\parallel}} = \frac{1}{\lambda_{n_e}} + \frac{3}{2\lambda_{T_e}}$ and $\frac{1}{\lambda_{\Gamma\parallel}} = \frac{1}{\lambda_{n_e}} + \frac{1}{2\lambda_{T_e}}$ as introduced in section 2.2.1. It will be shown in the following that in most scenarios the temperature decay is rather slow. Therefore, the heat flux channel scales rather like λ_n.

Since the limiter plasma regime is dominated by convective transport, heat and particle fluxes are expected to show similar distributions and parametric dependencies to each other. The actual quantitative value of the flux and the decay are both determined by L_C. The modeled heat loads onto the limiter center are expected due to the assumption that only $q_{\parallel}$ contributes to q_{depo}. As discussed in [100, 101] loads up to 10% of $q_{\parallel}$ can appear on PFCs oriented parallel to B in tokamak experiments. They depend strongly on the cross-field transport which will be discussed in the next section.

3.1.8 Impact of anomalous transport on edge transport and heat and particle fluxes

The anomalous transport coefficients for energy and particles are diffusion coefficients in the EMC3-EIRENE model equations. They are free parameters for the solution and determining them

experimentally is difficult. Hence, a sensitivity study of the various SOL physics characteristics on these transport coefficients is presented.

In this survey, partially based on publication [7], a transport coefficient scan at a fixed ratio of $\chi_{\perp,i,e} = 3D_{\perp}$ is performed. The density at the LCFS was set to n_{LCFS}=9·10^{18} m^{-3} and two heating scenarios, one at low and one at higher power (P_{in} =2 MW and 4 MW) were addressed.

The resulting 2D limiter heat loads for $D_{\perp}$ = 0.5 m^{2}s^{-1}, 1.0 m^{2}s^{-1} and 2 m^{2}s^{-1} are shown in figure 3.14(left) for P_{in} =2 MW. The corresponding 1D profiles are shown in figure 3.14 (right) for both heating scenarios. The blue, cyan and green curves correspond to increasing transport coefficients at P_{in} =4 MW while magenta, red and yellow correspond to the same coefficients at P_{in} =2 MW. The reduction of the input power by a factor of 2 causes a reduction of the maximum peak heat fluxes by almost a factor of two. However, in both input power cases P_{peak} strongly varies with $D_{\perp}$ as well.

The dependence of the peak heat fluxes on the transport coefficients is shown in figure 3.15. Here, the drop of P_{peak} as a result of reduced input power and the decay with increasing $D_{\perp}$ is seen. Green symbols represent the high input power (P_{in} =4 MW) maximum peaks and effective λ_{sf} obtained from left and right peaks by fitting the profiles. The blue symbols correspond to the same data obtained at P_{in} =2 MW. The evolution shows very clearly a broadening of the heat channel and a decay of the maximum peak in the two heating scenarios. The perpendicular convective and conductive heat flux in equation **??** increases with increasing $\chi_{\perp,e,i}$ and $D_{\perp}$ respectively.

The decay of the right peak maximum P_{peak} by ≈40% and the increase of the related λ_{sf} by a factor of 2-3 for increasing $D_{\perp}$ emphasizes the importance of carefully choosing the perpendicular transport parameters. The transport coefficients $D_{\perp}$ and $\chi_{perp,e,i}$ must be inferred by matching the experimental profiles with the modeled profiles.

Based on these overall dependencies, a more detailed analysis with a specifically optimized grid was conducted. This grid decomposes the SOL into the different flux channels and relates

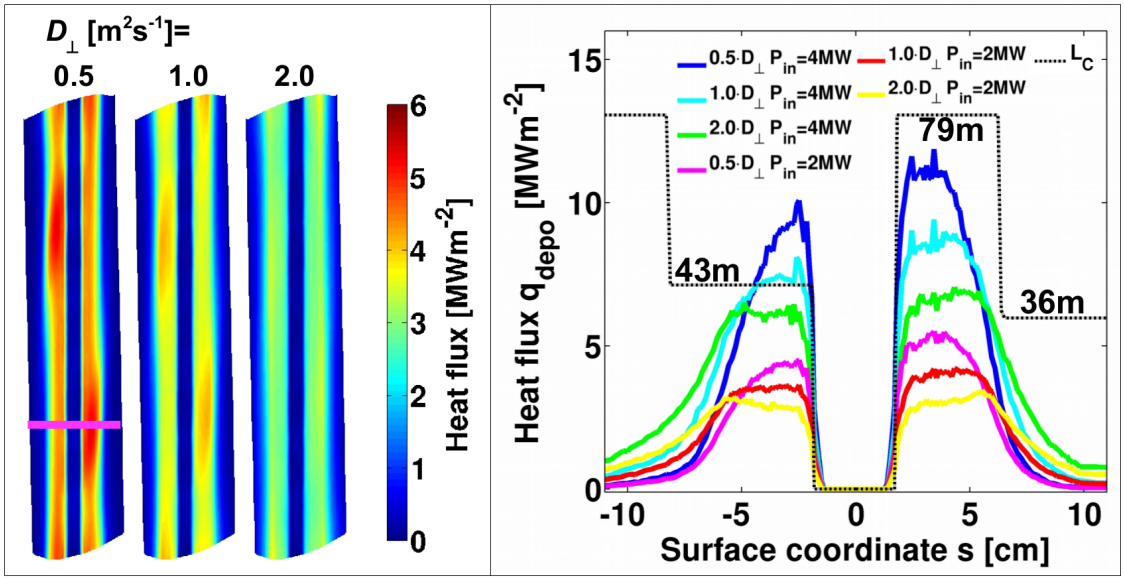

Figure 3.14 Left: 2-D limiter heat flux deposition for a transport parameter scan for a pure hydrogen plasma at $n_{LCFS} = 9 \cdot 10^{18}$ m^{-3}, $P_{in} = 2MW$, $D_\perp = 0.5$, 1.0, 2.0 m^{2}s^{-1}, $\chi_{\perp,e,i} = 3D_\perp$. Right: 1-D surface scan of the deposited heat flux at $Z = -0.2$m for a transport and power parameter scan at $n_{LCFS} = 9 \cdot 10^{18}$ m^{-3}, P_{in} =2 MW, 4 MW, $D_\perp$ =0.5, 1.0, 2.0 m^{2}s^{-1}, $\chi_{\perp,e,i} = 3D_\perp$ extracted at $Z = -0.2$m, magenta mark, left [7].

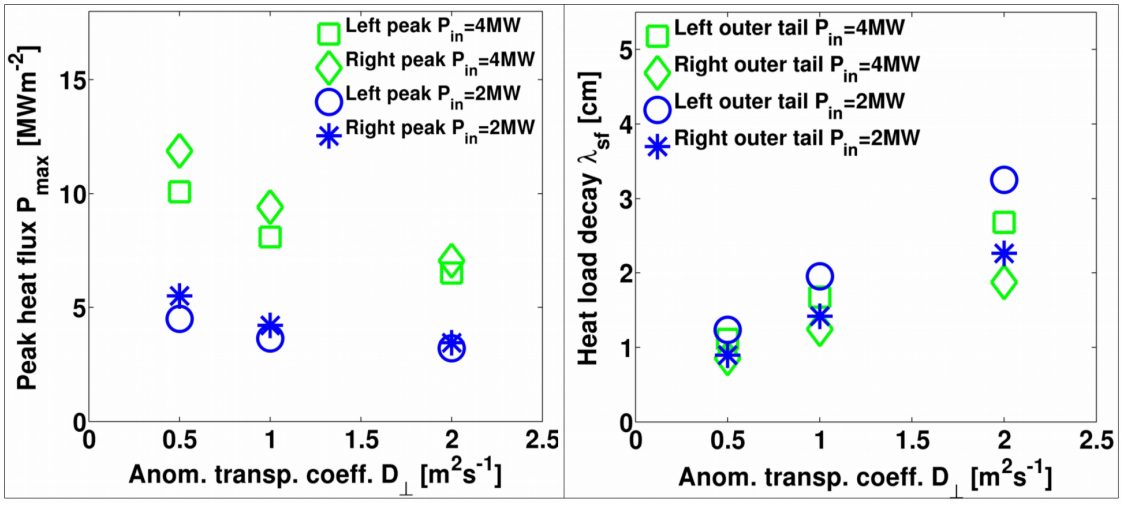

Figure 3.15 Left: Maximum deposited peak heat fluxes P_{peak} and right: limiter surface deposition decay lengths λ_{sf} for three different spatially fixed anomalous transport coefficients $D_\perp$ ($\chi_{perp,e,i} = 3D_\perp$) for $n_{LCFS} = 9 \cdot 10^{18}$ m^{-3} at $P_{in} = 2$ MW, 4 MW respectively, inferred from the 1D profiles in figure 3.14 [7].

upstream to downstream parameters inside of the flux tube geometry. Here, $D_\perp = 0.25 - 2.0$ m^2s^{-1} ($\chi_{perp} = 3D_\perp$) are considered. Two typical scenarios are addressed in this scan as shown in figure 3.16. The top plots show results for a low density and low power case, that is $n_{LCFS} = 2 \cdot 10^{18}$ m^{-3} at $P = 1$ MW. The bottom plots represent a case with medium density and power of $n_{LCFS} = 4 \cdot 10^{18}$ m^{-3} and $P = 2$ MW, respectively.

The left plots show the downstream densities n_d averaged at the limiter targets The center plots show the limiter recycling fluxes Φ_{rec} and the right plots show the downstream electron and ion temperatures $T_{e,i,d}$. The increase of $D_\perp$ by a factor of 4 causes a drop in the downstream density by 10% which means that particles were removed from the simulation when hitting the outermost boundary. This is a consistent result within the modeling. However, under experimental conditions, a high perpendicular particle flux to the walls would result in additional recycling, back-fueling and sputtering.

The recycling flux follows a weaker than linear increase with increasing anomalous transport. Since it is proportional to a surface integral of the limiter particle flux it scales with the density decay $\propto D_\perp^{0.5}$. Similarly, the increase of SOL width with rising $D_\perp$ causes a drop in the average downstream temperatures. The increase of diffusive energy transport across flux surfaces causes reductions of temperatures by 30-60%.

The local changes of downstream fluxes caused by different levels of anomalous cross field transport are shown in figure 3.17 for scenarios with $n_{LCFS} = 4 \cdot 10^{18}$ m^{-3} at $P = 2$ MW for standard (left) and increased ι (right) field configurations.

The fluxes are normalized to their peak maximum within each mapping in order to elucidate changes within the deposition patterns. The heat fluxes ($q_{||,depo}/max(q_{||,depo})$) are shown on the top and the particle fluxes ($\Gamma_{||,depo}/max(\Gamma_{||,depo})$) are shown on the bottom. At first glance, heat and particle fluxes follow the strike line distributions with maximum fluxes within the domain of longest L_C (see figure 3.7 and figure 3.12). The SOL widths increase with increasing cross field diffusive

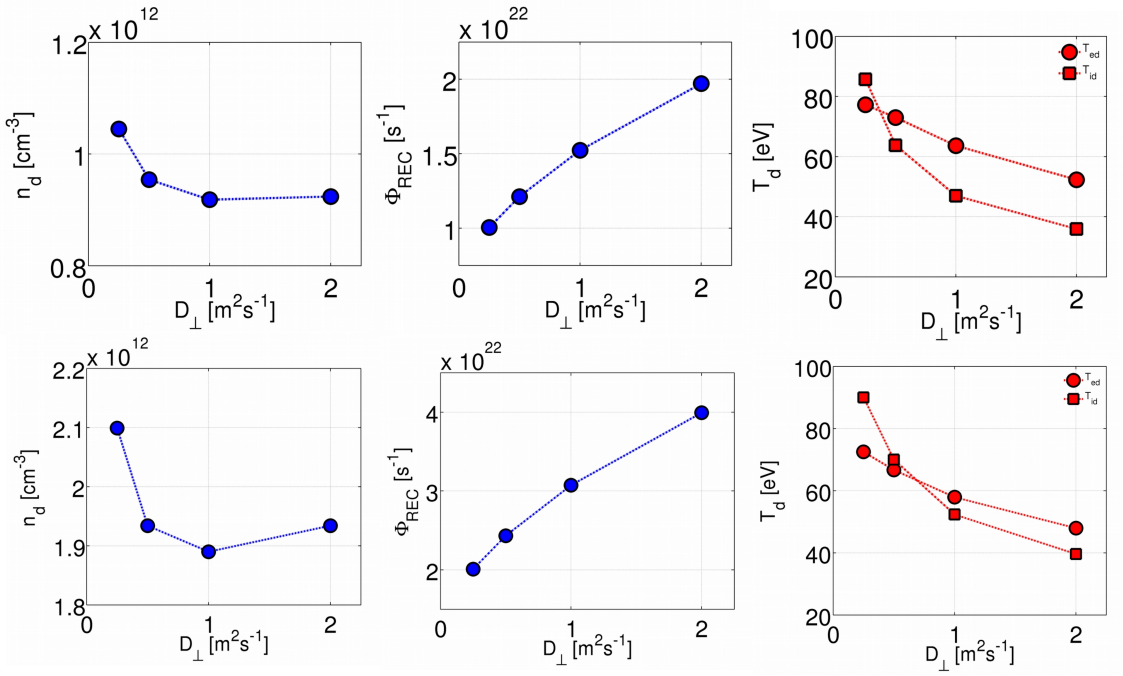

Figure 3.16 Downstream parameters versus anomalous transport coefficients $D_\perp$ ($\chi_{perp} = 3D_\perp$). Top: scenario with $n_{LCFS} = 2 \cdot 10^{18}$ m^{-3} at $P = 1$ MW. Bottom: scenario with $n_{LCFS} = 4 \cdot 10^{18}$ m^{-3} at $P = 2$ MW. Left: downstream density n_d at the limiters. Center: recycling flux Φ_{rec} at the limiters. Right: Downstream electron and ion temperatures (circles: T_e, squares: T_i).

heat and particle transport causing wider deposition stripes on the limiters (modified by the local geometry according to equation 3.8). The maximum peak heat fluxes that are shown in the top plots of figure 3.17 tend to remain in position for all levels of $D_\perp$, while the peak particle fluxes on the bottom of figure 3.17 move radially/toroidally/horizontally and vertically away from the limiter center. This follows from the e-folding lengths of heat and particles inferred in equations **??** and **??**. The higher weight of the inverse temperature decay ($\frac{3}{2\lambda_{Te}}$) causes a narrower heat flux channel and makes it less sensitive to changes of cross-field transport.

The widths of different SOL transport channels are shown in figure 3.18 for an extended scan of transport coefficients. The downstream heat decay lengths $\lambda_{q||}$ and particle decay lengths $\lambda_{\Gamma||}$ are shown in figure 3.18(a). The three colors represent the three different connection lengths L_C. The

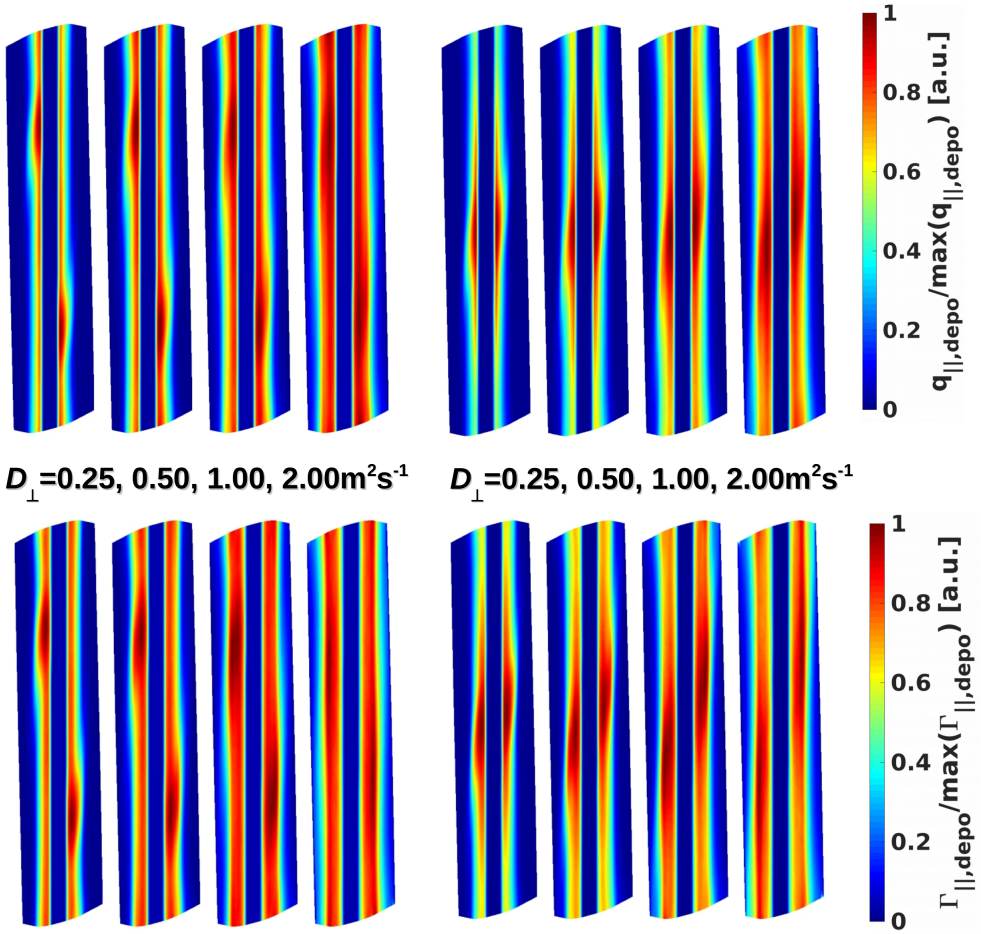

Figure 3.17 Overview of change of limiter fluxes with different anomalous transport coefficients for heat (top) and particle loads (bottom) for standard (left) and increased iota (right) configuration for $n_{LCFS} = 4 \cdot 10$ m^{-3} at $P = 2$ MW.

related density, temperature and pressure decay lengths are shown in the figure 3.18(b). The heat and particle flux channel widths increase by a factor of 2-3 if $D_\perp$ is increased by a factor of 6. They show similar scaling to the density and pressure e-folding lengths shown on the right, while the electron decay lengths are 2-4 times larger. The ion temperature decay is not shown since the ion temperature profiles tend to be very flat and do not modify the heat flux channel widths. The widths inferred here define the deposition widths shown in figure 3.17. The contribution from convective transport is dominant since parallel temperature gradients vanish over the short distances along L_C.

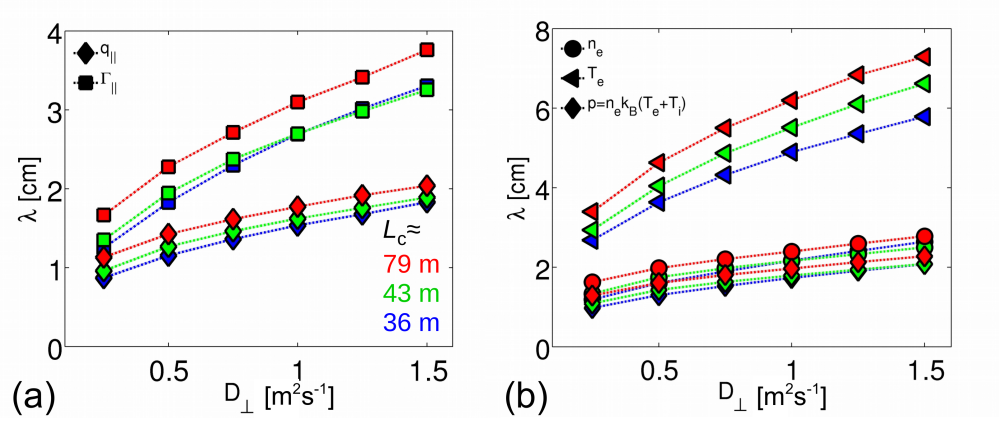

Figure 3.18 (a) Downstream and particle decay lengths within the flux bundles of three different lengths L_C and (b) related density, temperature and pressure decay lengths for $n_{LCFS} = 4 \cdot 10^{18}$ m^{-3} at $P = 2$ MW.

Additionally, the static pressure $p = n_e k_B (T_e + T_i)$ is depicted, in order to provide an upstream measure correlated to the energy.

Assuming cold ions ([4]. p. 161, (4.26)) one can approximate the scaling of λ_{T_e} based on its dependence on λ_{ne}:

$$\left(1 + \frac{\lambda_{n_e}}{\lambda_{T_e}}\right)\left(\frac{5}{2} + \frac{\chi_\perp^e}{D_\perp}\frac{\lambda_{n_e}}{\lambda_{T_e}}\right) = \gamma_e \tag{3.9}$$

With the fixed relation $\chi_\perp = 3D_\perp$ this reduces to $\lambda_{Te} \propto \lambda_{n_e} \propto D_\perp^\delta$, with $\delta \approx 0.5$.

This scan of transport coefficients demonstrates that plasma edge transport and the heat and particle fluxes are very sensitive to assumptions about anomalous transport.

Furthermore, the particle and heat transport channel widths of the 3D helical flux tubes can still be well described and characterized by simple SOL models. Deviations from ideal assumptions are likely due to the 3D shape of the field structures. The toroidally and poloidally varying flux expansion and compression may cause anisotropic cross-fueling between confinement and SOL. Cross-fueling between neighboring flux tubes of different lengths sometimes featuring opposite flows may cause further deviation from the description of simple SOL description of geometrically uniform flux tubes.

3.1.9 Dependence of heat and particle transport on upstream power

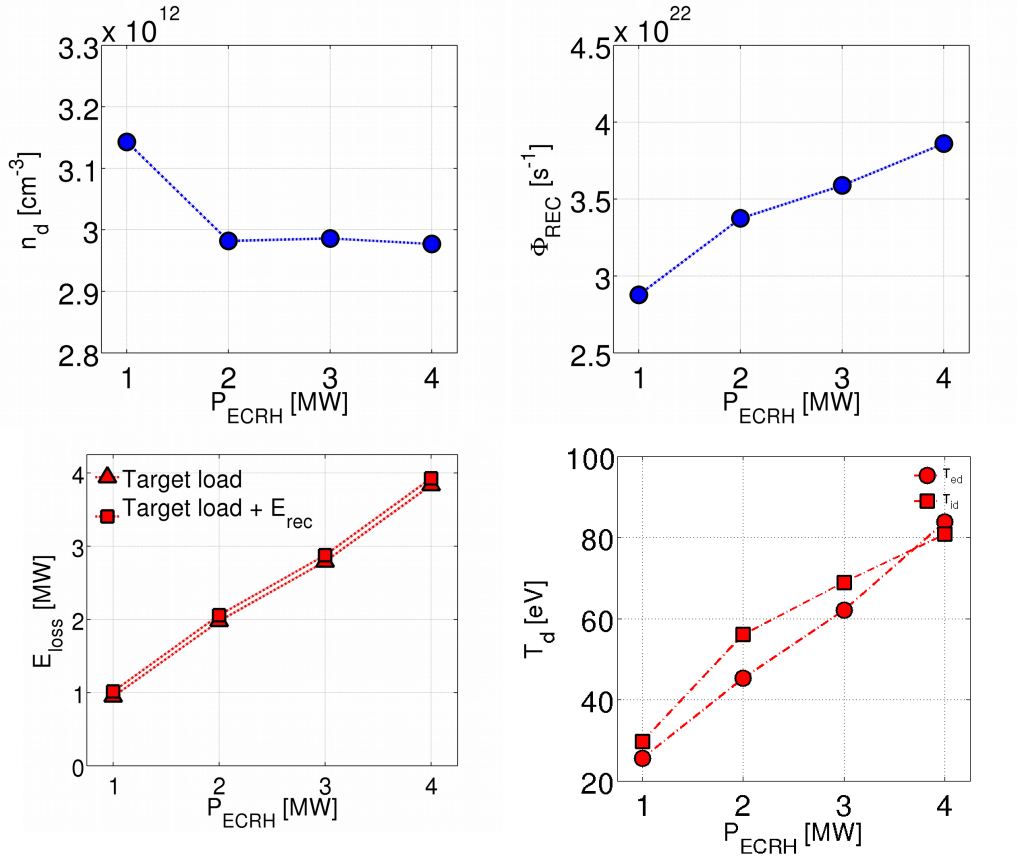

Figure 3.19 Downstream heat and particle parameters with varying input power for $n_{LCFS} = 6 \cdot 10\ \mathrm{m}^{-3}$.

A power scan was performed in order to evaluate the effects of power entering the SOL on characteristic up- and downstream parameters of heat and particle transport. With respect to the power entering the SOL, this can be considered to be equivalent to either variation of heating power or ionization and radiation losses of impurities in the confinement region. In particular higher Z impurities, e.g., iron, tungsten, copper, aluminum predominantly cause power losses in the core region. However, in the case of limiter scenarios also light and medium Z impurities can significantly reduce the power before it enters the SOL as will be discussed later.

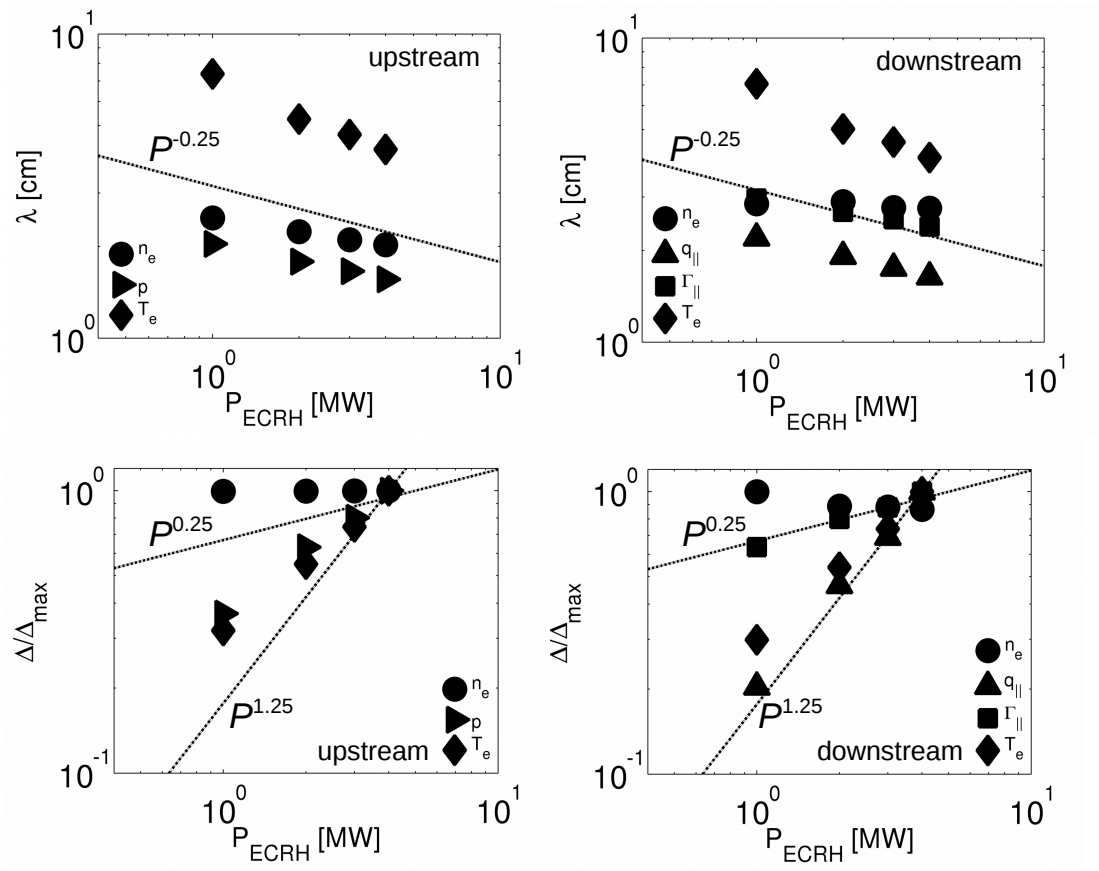

Figure 3.20 Upstream (left) and downstream (right) heat- and particle transport decays (top) and levels (bottom) for power scan of input power for $n_{LCFS} = 6 \cdot 10^{18}$ m^{-3}.

The edge density was set to $n_{LCFS} \approx 6 \cdot 10^{18}$ m^{-3} and transport coefficients were fixed to $D_\perp = 0.5$ m^2 m^{-1}. The power was varied over a range of P_{ECRH} =1.0 - 4.0 MW corresponding to experimentally realized conditions. The characteristic parameters are shown in figure 3.19 and 3.20. The downstream density and recycling flux are shown on the top of figure 3.19. The density slightly drops when power is increased from 1 MW to 2 MW. The recycling flux increases almost linearly with rising power. The downstream energy fluxes and downstream temperatures shown on the bottom of figure 3.19 increase linearly with the input power, that is:

$$E_{target} \propto T_d \propto P_{SOL} \tag{3.10}$$

The upstream pressure rises at a fixed upstream density and reaches during the four power steps 83.22, 146.9, 190.4 and 241.2 Pa, respectively. This drives stronger heat and particle flows. The energy deposited on the target rises.

The characteristic widths λ of the different parallel transport channels for heat and particles and their normalized levels (normalized to their maxima, Δ/Δ_{max}) are measured and depicted in figure 3.20 for upstream (left) and downstream (right). For upstream the characteristic values for density, electron temperature and pressure are shown. For downstream the characteristic values for density, electron temperature and heat and particle fluxes are also included in figure 3.20. The dashed lines indicate different power scalings used in the discussion below.

In general, heat and particle transport channel widths λ decrease with rising heating power due to the increase of fast parallel losses to the limiters. The temperature decay length λ_{Te} decreases from 7cm to 4cm between low and high power. This changes at the upstream and downstream location almost equally as no temperature gradients are present and therefore the energy transport is mostly convective.

The upstream density decays λ_n decrease only slightly with rising power and remains almost constant at the downstream position. The local density levels show an opposite trend of staying constant at the upstream location and slightly reducing at the downstream location between the power steps. This is due to the parallel conservation of total pressure enforcing dropping downstream density in case of rising momentum.

The power scan is most effective concerning energy-related plasma parameters. Here, it is worth to consider the parallel energy transport time scale for limiter plasma conditions [4]:

$$\tau_{E||} \propto \frac{L_C}{c_S} \tag{3.11}$$

The parallel transport time reduces in the short flux tubes ($L_C = 36$m) from $\tau_{E||} \approx 217\mu$s to 130μs and in the long ones ($L_C = 79$m) from $\tau_{E||} \approx 482\mu$s to 290μs. Similar to the particle transport decay length, the width of parallel the energy transport channels is in general determined by:

$$\lambda_E \propto \sqrt{\chi_{i,e}\tau_{E||}} \tag{3.12}$$

The pressure decay upstream and the heat flux decay downstream show similar scaling. In particular, the scaling of the power decay λ_q and downstream flux levels Δ_q can be approximated as follows:

$$\lambda_{q||} \propto \lambda_{Te} \propto \tau_{E||}^{0.5} \propto c_S^{-0.5} \propto T_e^{-0.25} \propto P_{ECRH}^{-0.25} \tag{3.13}$$

From this it can be further approximated for the peak heat flux level:

$$\Delta_q \propto \frac{P_{ECRH}}{\lambda_{q||}} \propto \frac{P_{ECRH}}{P_{ECRH}^{-0.25}} = P_{ECRH}^{\frac{5}{4}} \tag{3.14}$$

These relations are also included by the dashed lines in figure 3.20. The downstream Δ_q and λ_q are close to these scaling.

In summary, this scan of input power shows that heat fluxes, but also pressures and temperatures are not only sensitive to SOL power concerning their absolute values, but also with respect to their SOL e-folding lengths. The level of heat and particle fluxes depends strongly, almost linearly, on the heating power. The power entering the SOL determines the widths of parallel energy-related transport channels. An increase of power yields both, higher heat fluxes and smaller deposition widths due to decreasing λ_q.

The scaling of the power channel widths can be approximated based on simple SOL assumptions as long no significant particle sources in addition to the limiters are present. This scan shows, that reduction of the power before it enters the SOL would be a safer way in order to decrease the downstream power flux and increase the wetted area. In particular, such a limiter scenario with short L_C and fast energy transport has not much capacity within the SOL for power dissipation at lower densities. The feasibility of power reduction within the SOL will be discussed in the following.

3.1.10 Energy dilution by density increase on plasma transport

The ionization behavior inside of the SOL flux channels defines much of the parallel pressure drive term of the flows as well as the parallel gradients. At higher densities, conductive energy transport may contribute to the convective ones. Therefore, a sensitivity study of the impact of different plasma densities on the parallel profiles and the transport phenomena driven by those is presented. The discussion is partly based on results reported in [7]. This also investigates cooling effects by power dilution purely through the increase of particle density number.

The first dependent plasma parameter investigated is the deposited heat flux. In figure 3.21(left) the resulting 2-D heat flux distributions on the limiter surface are shown for densities at the LCFS in the range of n_{LCFS} =1·10^{18}-1.9·10^{19} m^{-3} at a fixed input power of P_{in} =4 MW.

Profiles along the limiter surface path length s in horizontal direction are extracted at the position of the peak value in the right deposition stripe ($Z \approx -0.2$m) for the different values of n_{LCFS}. These 1D surface heat flux profiles $q_{depo}(s)$ are overlaid with the connection lengths L_C as shown in figure 3.21(right). Due to the geometry effects discussed above, the 1D profiles exhibit steep decay towards the limiter center and shallower decay in the outer part of the limiter.

This analysis shows as an overall trend that increasing density yields a broadening of the heat flux profiles and hence an overall reduction of the locally deposited heat flux. In order to analyze

the impact on peak heat flux and the decay length, those parameters were extracted from the profiles shown in figure 3.21(b) and they are depicted in figure 3.22.

The heat flux characteristics for the density scan are shown in figure 3.22. The heat load maxima (P_{peak}) obtained from the left and right peak profiles (figure 3.21) are plotted for the different densities in figure 3.22(left). The effective λ_{sf} of the tails of the left and right peaks are shown in figure 3.22 (right). In order to reduce the effects of the target geometry and keep them separated by the magnetic connection lengths L_C as discussed above, the λ_{sf} are determined by exponential fits of the left and right 1-D peak profile tails marked in red, (figure 3.21 (right). The left tail features a slightly higher λ_{sf} than the right tail (a factor of ≈1.3) as seen in figure 3.22(right).

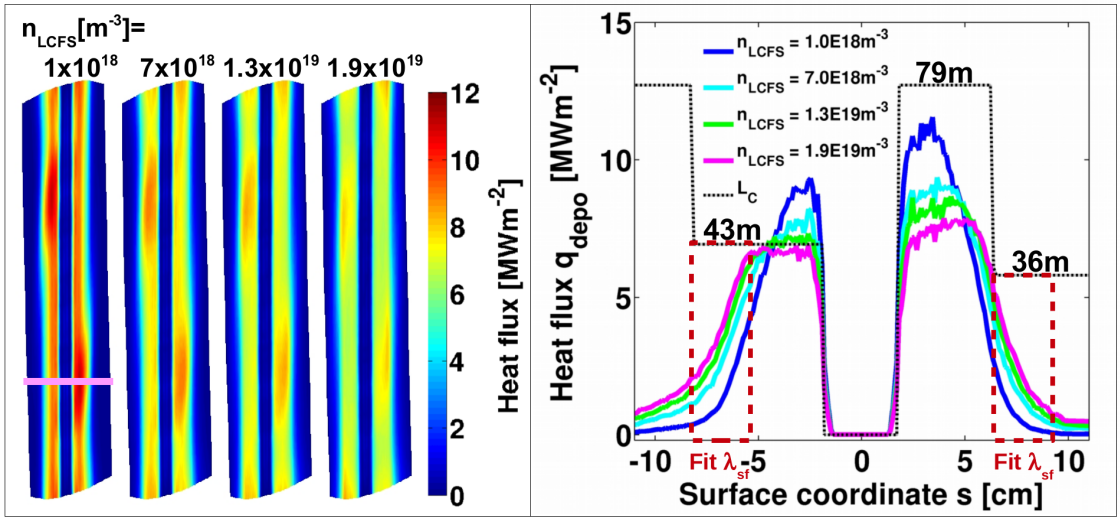

Figure 3.21 Left: 2-D limiter heat flux deposition for a density scan with pure hydrogen for a density range $n_{LCFS} = 1 \cdot 10^{18}$ m^{-3} to 1.9·10^{19} m^{-3} at P_{in} =4 MW. Right: 1-D surface profile of the deposited heat loads extracted at $Z = -0.2$m, magenta mark, left. The overlaid black dotted line corresponds to the local L_C. The red dotted box indicates the fit domain for λ_{sf} [7].

With an increase in n_{LCFS} of approximately a factor of 20 from 1·10^{18} m^{-3} to 1.9·10^{19} m^{-3}, the maximum peak loads reduce from P_{peak} ≈12.5 MW to ≈7.5 MW on the right profile and

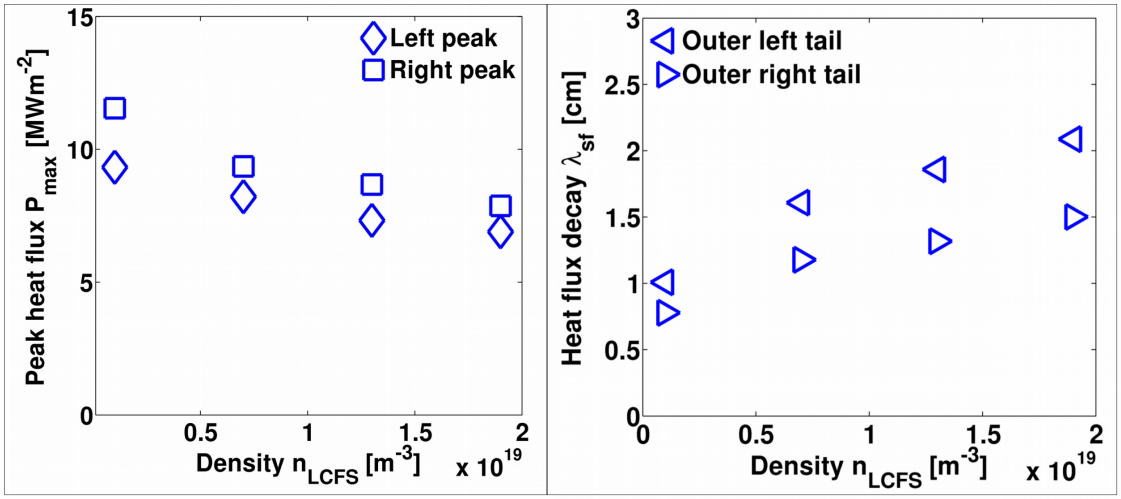

Figure 3.22 Left: Maximum deposited peak heat fluxes P_{peak} and right: limiter surface deposition decay lengths λ_{sf} for four different density cases $n_{LCFS} = 1 \cdot 10^{18}$, $7 \cdot 10^{18}$, $1.3 \cdot 10^{19}$ and $1.9 \cdot 10^{19}$ m^{-3} at $P_{in} = 4MW$ inferred from the 1D profiles in figure 3.21 [7].

from P_{peak} ≈9.5 MW to P_{peak} ≈7MW on the left profile. The decay length increases for the right profile tail by a factor of two from λ_{sf} ≈0.75cm to ≈1.5cm. The left profile tail increases by approximately the same factor from λ_{sf} ≈1cm to ≈2.1cm. This is because with rising density the fixed input power is distributed among more plasma particles and perpendicular fueling of the flux tubes is increased.

This is a result of the linear density scaling of the conductive term in the radial heat flux equation as shown in equation 3.15. The conductive term increases linearly with the density while the convective term is dependent on the perpendicular density gradient. The increase in density is expected to broaden the heat flux profiles from the conductive term related to a finite gradient in the radial temperature profile.

$$q_{\perp} = \chi_{\perp,e,i} n \nabla_{\perp} T_{e,i} + \frac{5}{2} T_{e,i} D_{\perp} \nabla_{\perp} n \tag{3.15}$$

In addition to the increasing density, an effect of reduced temperature under fixed power input is expected from the convective and conductive terms in equation 3.15. While the density is increased by one order of magnitude at the upstream position, the temperature is only reduced by 16%. This results in the decay of P_{peak} (figure 3.22,left) and broadening of $\lambda_{q_{\parallel}}$ (figure 3.22, right). However, the change of maximum peak levels and distribution widths in the deposition profiles in figure 3.21 and the heat flux characteristics in figure 3.22 decreases with further increasing n_{LCFS}.

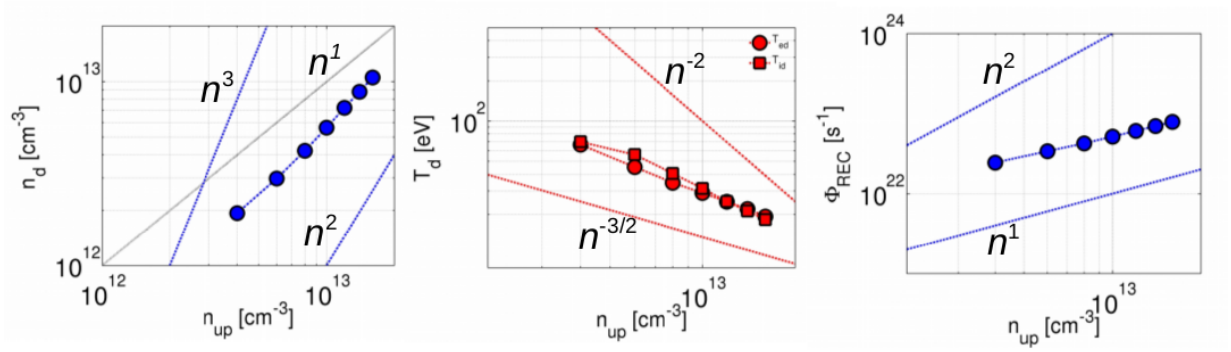

Figure 3.23 Downstream parameters versus upstream density n_{up} set at LCFS. Left: downstream density n_d at the limiters. Center: recycling flux Φ_{rec} at the limiters. Right: Downstream electron and ion temperatures (circles: T_e, squares: T_i).

The complex interplay of radial and parallel gradients as drive terms for the outward energy and particle transport and the eventual deposition onto plasma facing components is usually referred to as scaling behavior between the upstream and downstream positions. Such scalings enable to predict downstream conditions for specific upstream conditions, i.e., to link the plasma core domain to the divertor or limiter surface conditions. Also, such scalings enable to define the recycling regime of the plasma situation, an important element to understand the fueling, recirculation, and heat dissipation capacity of the edge plasma.

The scaling of downstream density, temperature and recycling flux with the upstream density is a required assessment for the limiter scenario at W7-X with a specially refined grid. This grid enables a precise resolution of the different SOL flux channels and unambiguous definition of

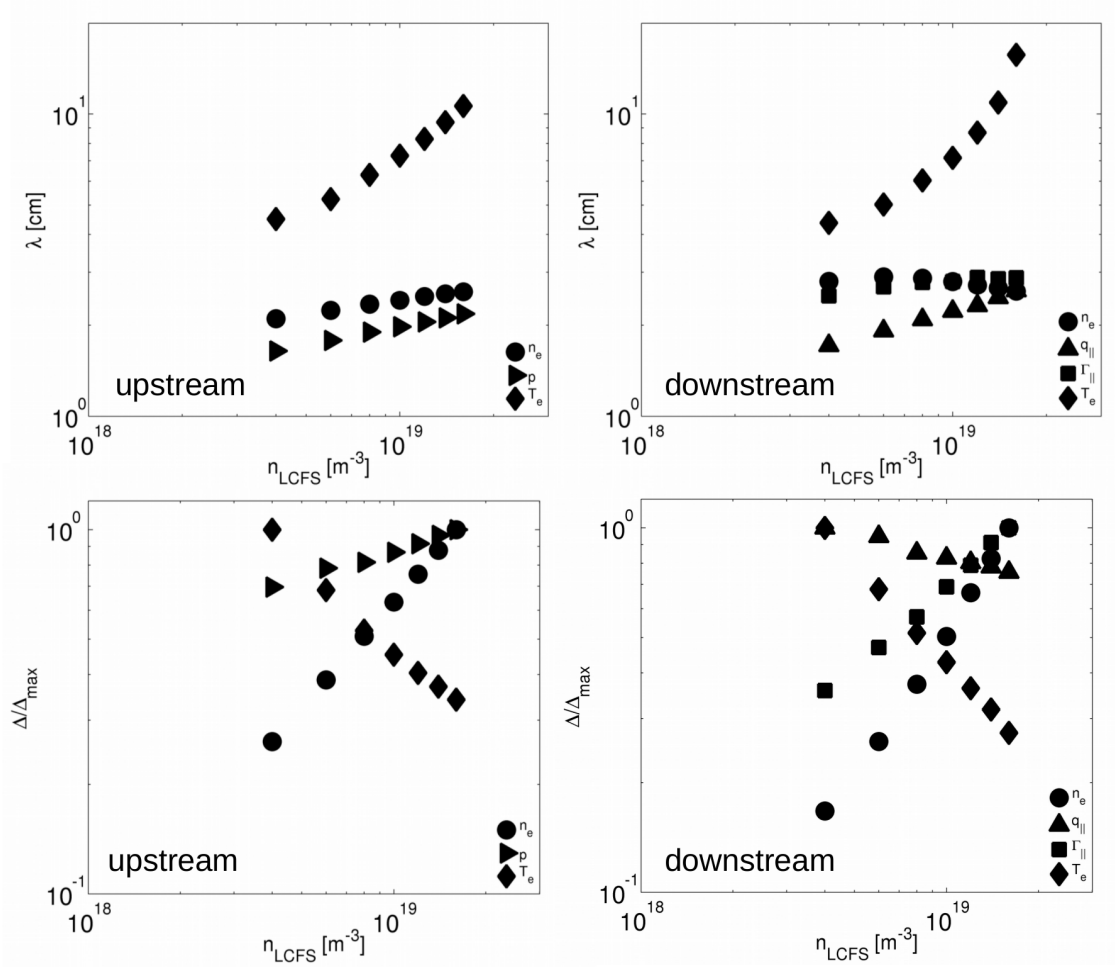

Figure 3.24 Upstream (left) and downstream (right) decay lengths (top) and peak values (bottom) versus upstream density n_{LCFS} set at LCFS.

upstream and downstream positions in these SOL flux channels. Also, the refinement allows for more precise measurement of upstream and downstream gradient lengths, which can serve as an estimation for the terms in 3.15.

The input power was fixed at P_{ECRH} =2.0 MW and transport coefficients set to $D_\perp = 0.5$ m^2 m^{-1} ($\chi_{\perp,e,i} = 3D_\perp$). The density was raised from $n_{LCFS} \approx 4 \cdot 10^{18}$ m^{-3} to $1.6 \cdot 10^{19}$ m^{-3} in steps of $\Delta n_{LCFS} = 2.0 \cdot 10^{18}$ m^{-3}. This is higher than usually established in the experiment

The results for the global scaling are shown in the figure 3.23(a-c). The dashed lines are used to mark the scaling of linear and potential non-linear regimes. The results of downstream density n_d, downstream electron and ion temperature $T_{d,e,i}$ and recycling flux Φ_{REC} show almost linear growths and decays, respectively in the considered density range. The averaged downstream density reaches $\approx 10^{13}$ cm^{-3}. The dilution of energy among increasing number of particles is obvious when considering the averaged downstream temperatures in figure 3.23(b). They drop from $T_{d,e,i} \approx 60 - 70$ eV to $T_{d,e,i} \approx 20$ eV.

The decay lengths λ and the normalize levels Δ of the upstream and downstream parameters are depicted in figure 3.24(a-d). Temperature, density and pressure are considered at the upstream position (3.24(a ,c)). The corresponding downstream values for heat, particle, density and temperatures are depicted in 3.24(b ,d). The rise of density causes a moderate increase of the upstream density decay from λ_n ≈2.1cm to 2.8cm. The pressure decay λ_p increases almost at the same growth rate, while the rise of temperature decay is more dramatic. It rises from $\lambda_{T_{d,e}}$ ≈4.4cm to 11cm. The ion temperature decay is not depicted since it is much larger and thereby hardly contributes to the pressure, heat and flux decay lengths. The heat flux level drops by $\approx 30\%$ over the range of densities considered.

The downstream heat flux decay λ_q can be well approximated by the upstream pressure decay λ_p while the particle flux channel widths λ_Γ increases only weakly and eventually saturates. The downstream density decay λ_n saturates and slightly drops while the downstream temperature decay λ_{Te} eventually increases stronger than the upstream decay. This is due to the increasing particle source at the downstream location, which introduces significant ionization within the SOL in front of the limiter. The local rise in density causes locally steeper gradients in the radial direction and thereby a reduction of the density decay λ_n. The sheath limited simple SOL description is not valid anymore when higher densities introduce a significant particle source into the SOL. Then, heat conduction becomes more relevant.

It is useful to consider the parallel SOL plasma profiles to understand the changes of the characteristic parameters of SOL heat and particle transport with rising density. The parallel densities n_e, electron and ion temperatures T_e, T_i, the Mach number, the particle source S_p and the downstream to upstream ratios of n_e and $T_{e,i}$ are depicted in figure 3.25(a-f). Here the dotted and dashed lines represent the short flux bundles (L_C ≈36m, 43m), while the solid lines represent the longest flux bundles (L_C ≈79m). Profiles were extracted within a density range $n_{up} = 2\dot{1}0^{18}$to$1.2\dot{1}0^{19}$ m^{-3}.

At the higher upstream densities the SOL density shows 'shoulders' near the downstream location at the limiters (figure 3.25(a)). The temperature profiles feature increasing gradients (figure 3.25(b,c)). This indicates a deviation from the simple SOL towards the complex SOL [4] with stronger ionization sources within the SOL and additional fueling at the downstream location. The rise of S_p is plotted in figure 3.25(e). It causes a stronger cooling at the downstream position and thereby increase of temperature decay with respect to the upstream position. The T_e and even more T_i show parallel gradients in case of higher n_{up}. The conservation of total pressure slightly de-accelerates flows as seen in the Mach number. Therefore the static pressure is increased at the downstream location by a local increase in density. The deviations from the simple SOL can be demonstrated by the downstream to upstream ratios in figure 3.25(f). This ratio increases for the density due to the increase in the downstream particle source and localized cross field fueling since the density is strongly increased in front of the limiter in the confinement. This toroidally localized rise in density causes a steeper decay of the radial density profile at the downstream location. This explains the drop of λ_n at higher densities shown in figure 3.24(b). The fact that λ_q growths although λ_n decreases cannot be explained with the simple SOL and convective transport only, anymore. The particle flux channel widths λ_Γ saturates, the heat flux decay is then determined also by the conductive parallel heat flux.

In summary, the density scan showed, that it is possible to increase critical transport channel widths such as λ_q by the increase of density. The lower LCFS densities of $2 - 4 \cdot 10^{19}$ m^{-3} were

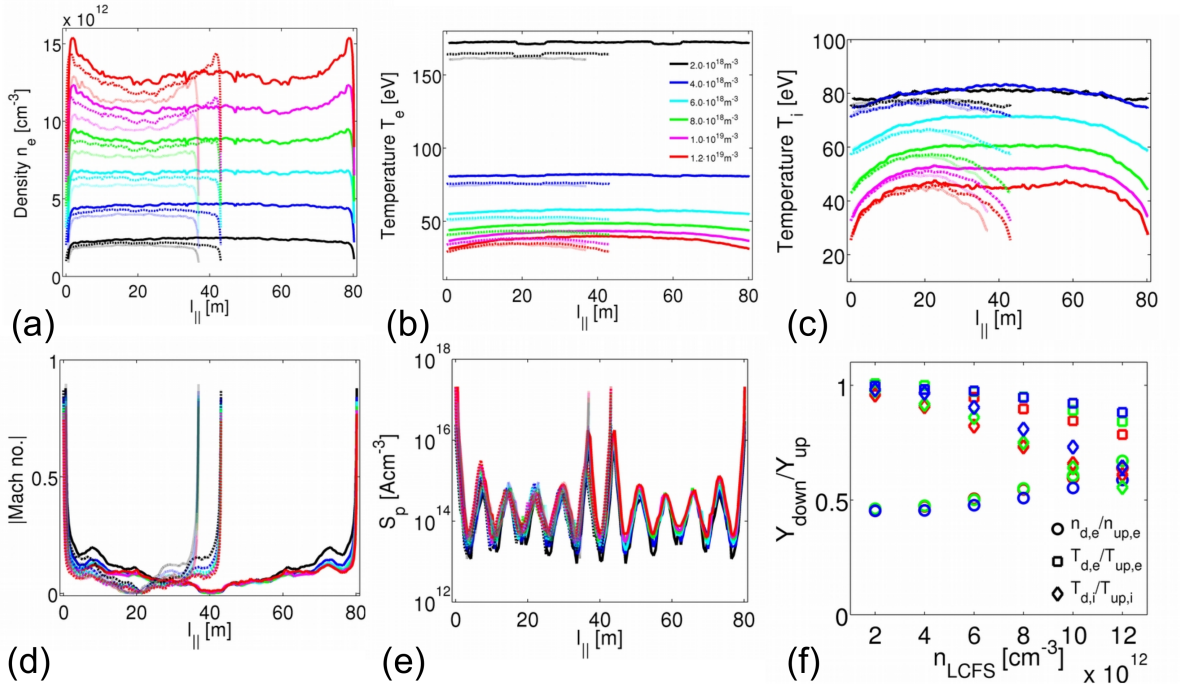

Figure 3.25 Parallel SOL profiles of (a) density n_e (b) electron temperature T_e (c) ion temperature T_i (d) Mach number (e) particle source S_p (f) down stream to upstream ratios of n_e, T_e, T_i.

more relevant for experimental limiter plasma regimes. Here, the sheath limited simple SOL is still a good approximation. In case of higher densities, energy is diluted by enhanced perpendicular energy transport. The simple SOL description is not applicable anymore.

3.1.11 Comparison with experimental measurements

Some suitable experimental measurements exist from the limiter campaign at W7-X, which in general was rather sparsely diagnosed. In this section, direct comparisons are presented which focus on providing support for the actual heat and particle flux distribution and how they compare to the modeling results.

For the scenarios discussed in the previous sections, the heat fluxes calculated with EMC3-EIRENE are considered and compared with IR camera measurements. In order to investigate how the limiter heat load distribution is related to the magnetic flux tube topology, the deposition of the parallel heat fluxes (q_{depo}) and a mapping of the connection lengths on the limiter surface are calculated for the standard limiter scenario and the higher ι scenario.

The comparison is shown in figure 3.26. The L_C distributions is shown in figure 3.26a. The surface temperature distributions from IR thermography measurement in figure 3.26b and the resulting 2D distributions of the modeled heat loads for both scenarios are shown in figure 3.26c [9, 102].

The diagonal red stripes in the L_C distributions in figure 3.26a correspond to the domain where the long magnetic flux tubes (79 m) connect to the limiters. The remaining surface area connects to the transport channels of short L_C (36m, 43m). The raw surface temperature distributions from IR thermography measurement [102] in figure 3.26b shows clearly a pattern, that matches with the modeled heat fluxes in figure 3.26c. As described in the sections above already for the standard limiter scenario the peak heat loads re-distribute during an increase of rotational transform according to the re-distribution of L_C. The measured T_{surf}-maxima and the maxima of the modeled heat loads shift in correlation to the long L_C at the limiter center towards the midplane ($Z = 0$ cm). This good agreement of surface temperature and modeled heat fluxes confirms that the 3D SOL

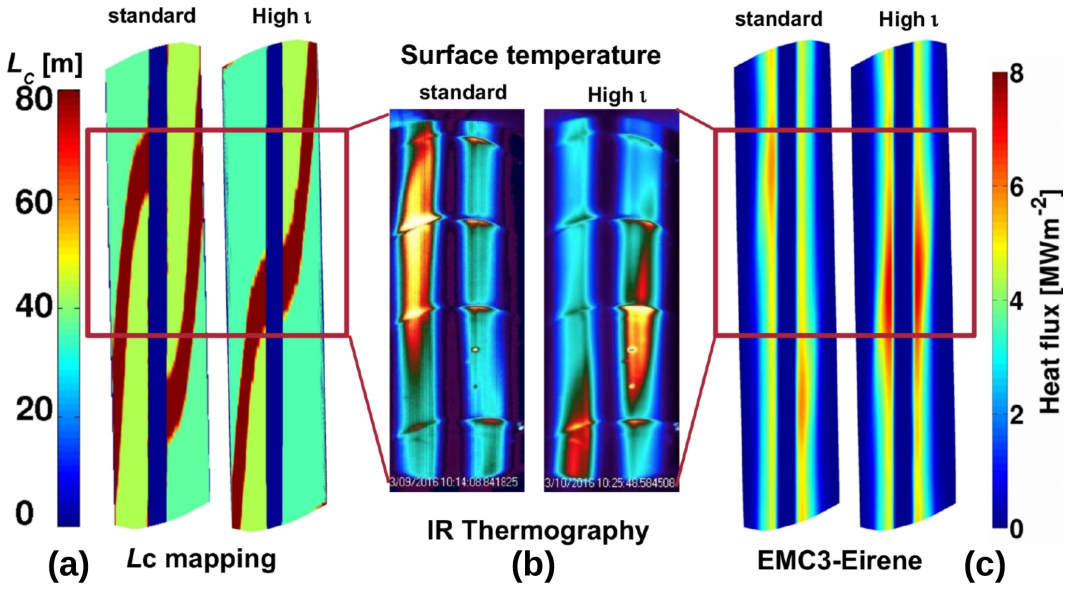

Figure 3.26 Comparison of EMC3-EIRENE calculations with IR tomography. The red frames represent the observation domain covered by the camera view. (a) Mapping of the target to target connection lengths L_C onto the limiters for ι_{LCFS} =0.87 (left) and ι_{LCFS} =0.91 configuration (right). (b) Front view of limiters by IR tomography. The colored patterns represent the surface temperature. Left: ι_{LCFS} =0.87, right: ι_{LCFS} =0.91 (c) Calculated limiter heat loads with EMC3-EIRENE for ι_{LCFS} =0.87 (left) and ι_{LCFS} =0.91 (right) shown at IAEA FEC 2016 [9] and published in [10].

geometry plays an important role in the transport and is recovered as clear imprint in both, model and measurement.

These surface temperature data were further processed in order to obtain the actual heat fluxes [103]. For this, the THEODOR code was used, which takes the measured time evolution of the surface temperature as input and performs a numerical 2D heat transport calculation inside of the material based on the temperature dependent heat diffusion coefficients (graphite) [104].

A comparison between the measured and modeled heat fluxes is shown in figure 3.27. The normalized heat fluxes from 3D modeling are shown on the left and the processed heat fluxes obtained from the experiment are shown on the right. The black lines mark the borders of the different connection lengths flux tubes enclosing the longest heat flux channel. The distributions

show good agreement. Deviations may result from higher diffusive transport than used in the depicted modeling scenario and from the presence of error fields induced by misalignment and deformations of the superconducting coils [105]. The level of anomalous transport can shift the maximum vertically and in the diagonal direction along the limiter surface as shown in figure 3.17 in section 3.1.8. A small mismatch between ideal configuration and actual realized magnetic fields might change the actual distribution of L_C as well.

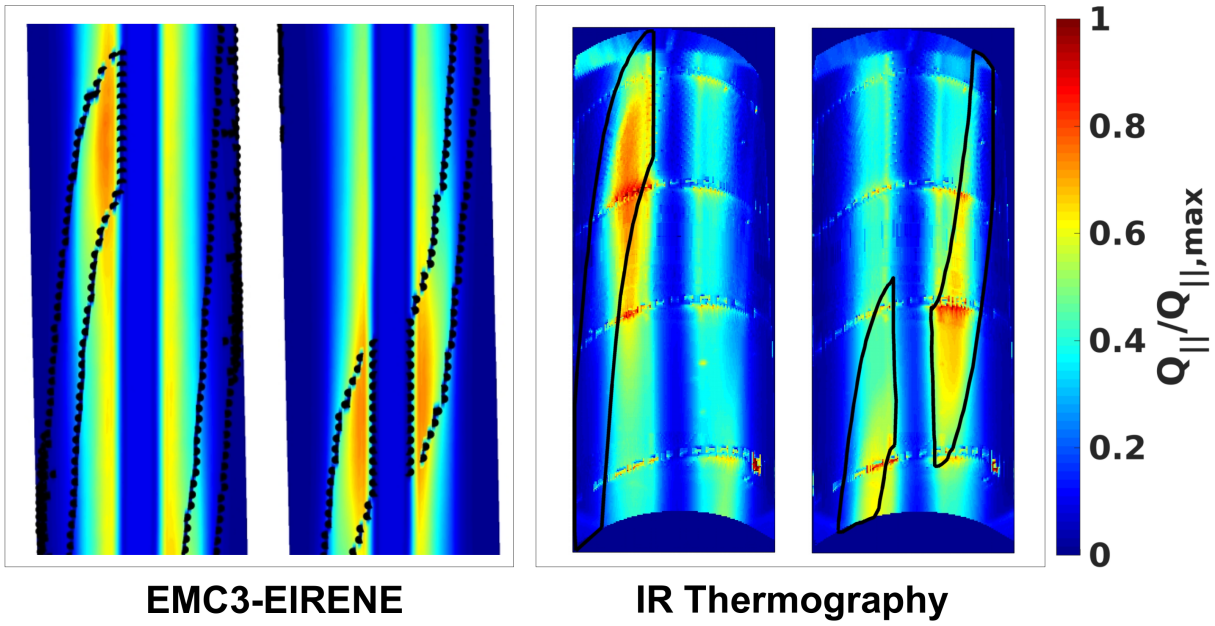

Figure 3.27 (Left) Predicted heat flux distributions with EMC3-EIRENE for standard and increased ι scenario. (Right) Heat fluxes based on IR measurements. The heat fluxes obtained with the THEODOR code follow the structure of the raw surface temperature shown.

Processed experimental heat flux data were related to local magnetic coordinates and connection lengths on the limiter surface based on magnetic fields calculated with VMEC. Here, effects of forces acting on coils during the experiment are taken into account in order to achieve best possible matching. Sorting of the local heat flux values according to the local L_C allows to recover a discrete distribution function. This distribution is shown in figure 3.28 for one example case.

It confirms (within uncertainties not yet resolved), that the maximum heat fluxes are found in the domain of longest L_C. The details of this analysis are reported in [11].

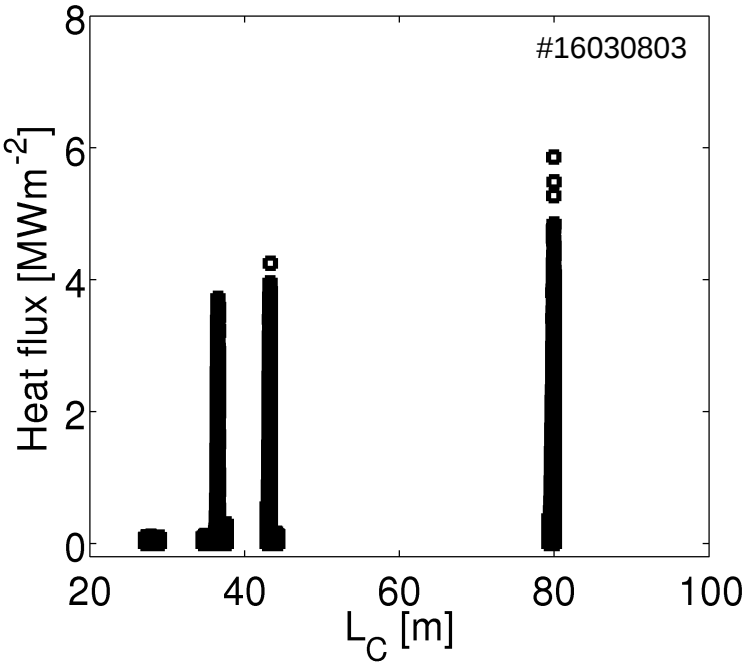

Figure 3.28 Distribution of heat fluxes in flux tubes. Heat flux is sampled over time in distinct flux tubes at the limiter during discharge 160308039.

Experimentally inferred 1D heat flux profiles are shown [11] in figure 3.29. The heat flux profiles have been measured locally in domains of the distinct connection lengths L_C attempting to recover geometry dependence of heat flux channel widths λ_q resolved in the modeling. However, effects of fluctuations, details of camera resolution and uncertainties of local incidence angles based on various assumptions about field imperfections are still under investigation. The predicted decay lengths of 'far' power decay λ_{qf} $\approx$2.0-2.5cm is in the range of predictions by EMC3-EIRENE modeling in the main SOL. Unfortunately, no precise SOL density and temperature measurements are available in order to narrow the range of transport coefficients.

Furthermore, the experimentally observed narrow heat flux component (λ_{qn}) is still under investigation. This domain needs careful treatment by numerical modeling. The code reproduces a similar steep decay of heat flux near the LCFS at the limiter. However, this is due to the enforced drop of density according to $n_d = 0.5 n_u$. The finite toroidal resolution of grid cells causes a steep, but continues decay instead a step function. These results will be further analysed and published elsewhere.

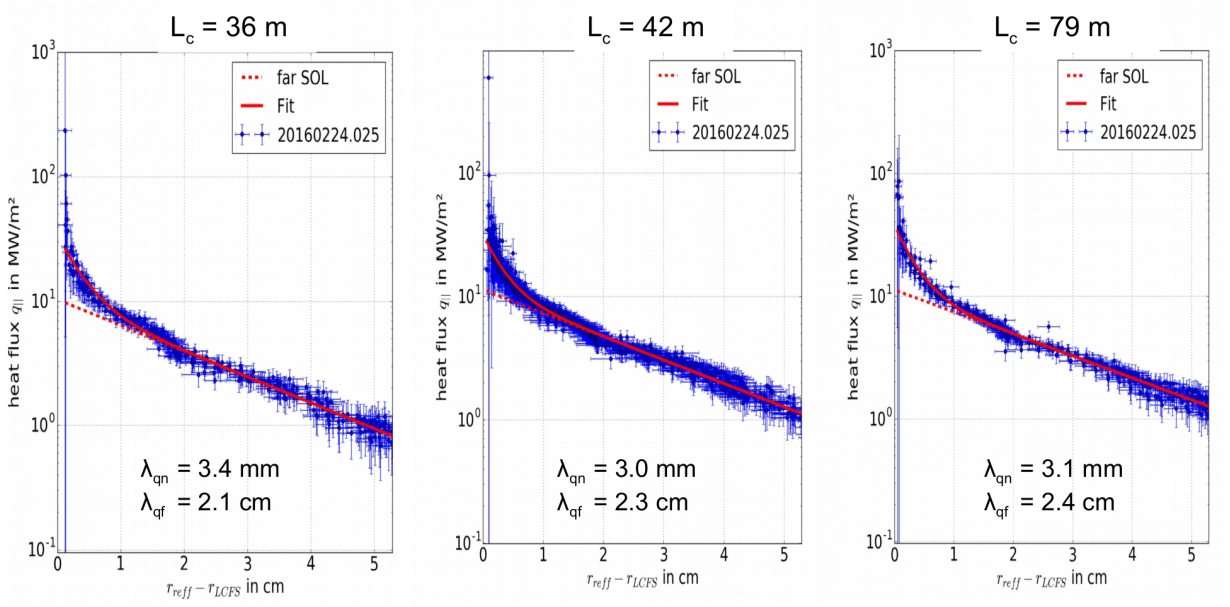

Figure 3.29 Experimentally extracted radial heat flux profiles within the three SOL heat flux channels [11]. Red lines indicate fit functions used to infer near and far heat flux decay $\lambda_{qn,f}$.

The scaling of main SOL heat flux decays λ_{qf} with L_C, ECRH heating P and density is shown in figure 3.30. The measured heat flux decay lengths scatter mostly in a range between 2.0cm and 3cm. This may indicate a higher diffusivity than $D_\perp = 0.5$ m^{-s}s^{-1} mostly assumed in the modeling (compare with $D_\perp$-scan data in figure 3.18 in section 3.1.8). It confirms for various discharges within error bars, that the decays lengths increase with L_C. It confirms the decrease of heat flux channel widths with rising power (see figure 3.20 in section 3.1.9). The scaling of

experimentally measured $\lambda_q f$ with upstream density taken from Thomson Scattering measurement deviates from the modeling (see data in figure 3.24 in section 3.1.10). However, no density was possible during the experiment. Density increase was mostly achieved in correlation to increase of heating. Increase of power and density have opposite effects on the heat transport. Dependence on heating power could dominate here. A more sophisticated analysis will have to take the power balance for each density step into account. L_C and P should allow for most robust comparisons.

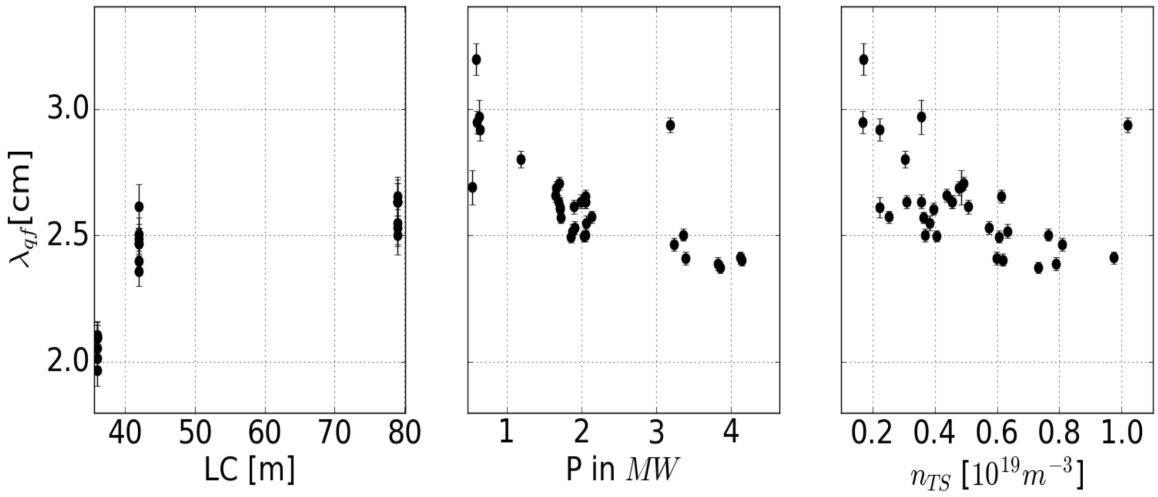

Figure 3.30 Scaling of experimentally inferred heat flux e-folding lengths λ_{qf} with connection lengths L_C, ECRH heating power P and upstream density n_{TS} obtained from Thomson Scattering [12].

Comparison of modeling and experimental results were performed using the set of synthetic diagnostics introduced in section 2.1.4.

This new synthetic diagnostic capability [83] enables to exploit the EMC3-EIRENE data base for interpretation of spectroscopic diagnostics, which suffer from line of sight integration effects. One example is the CCD camera, which observed the limiter through an H_α filter.

Here, comparisons between modeling and particle flux measurements used for estimation of eroded carbon flux show were made. The results are shown in figure 3.31. The top left figure

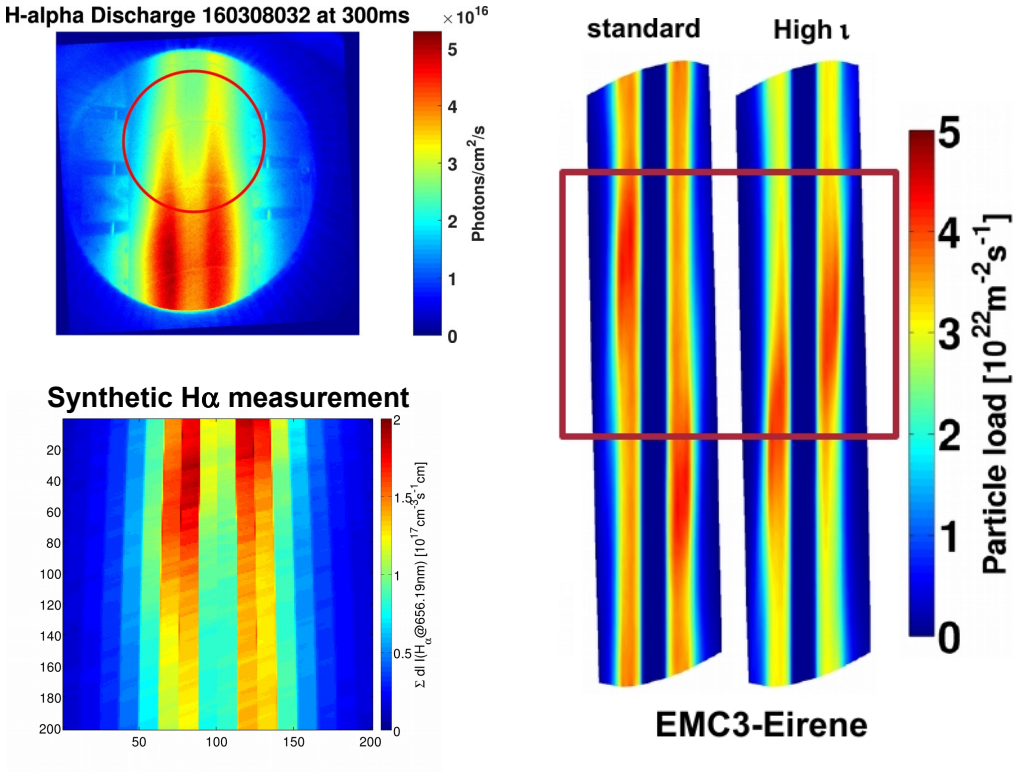

Figure 3.31 Experimentally observed particle flux based on H_α [13] and particle fluxes modeled with EMC3-EIRENE.

shows actual particle flux measurement reported in [106] and [107]. The right plot of figure 3.31 shows the deposited particle fluxes $\Gamma_{\parallel,depo}$ from modeling for both limiter configurations. The patterns of the modeled and the measured particle fluxes do not agree at all. Application of the synthetic H_α camera shows in addition a pattern with highest intensity on the top of the camera observation plane. The experimenttal H_α measurement, however, shows emission concentrated at the limiter center not in agreement mit modeling or IR heat flux distribution. It also does not change if significant changes to the local PSI are induced by increase of rotational transform. A change of SOL geometry would according to modeling and IR measurement result in a change of particle

flux distributions as shown on the left side of figure 3.31. Since the more reliable IR measurement of mostly convective heat fluxes agrees with the modeling a further analysis of the particle flux measurement, basically H_α measurement, was undertaken. Synthetic modeling revealed some principal uncertainties with respect to the role of molecular dissociation and geometry of lines of sight as reported in [84]. Furthermore, misalignment and wavelength range of the filters may have introduced some systematic errors. This demonstrated that 3D simulations can help to refine the measurement techniques. These initial steps and discussion will contribute to the more challenging analysis of particle fluxes and erosion in the island divertor campaign. Similar comparisons between 3D modeling and particle flux measurements are also in preparation for limiter scenarios at HSX [108].

This ansatz now allows to better understand the particle fluxes and facilitates depending assessments, like the reconstruction of the intrsinic carbon source from chemical sputtering as discussed in [106] and [107].

3.2 Impurity transport and radiative power exhaust

3.2.1 Impurity transport and power losses in the 3D helical SOL

The helical SOL transport scenarios discussed so far did not include effects of impurities. The impurity transport is addressed in the following with the particular focus on the impact of impurity radiation on the limiter heat loads. The experience gathered will be used for the proposed investigations of this topic in the topologically more challenging island divertor scenarios. During these studies, only the most relevant intrinsic impurities and impurities used for seeding are considered.

Carbon and Oxygen are found as dominant impurity species in the edge of magnetic confinement experiments with graphite wall materials, and hence they are usually the most significant contributors to intrinsic edge radiation.

The power loss fraction may vary based on the plasma regime. Here, a power loss fraction of $f_{rad} \approx 25\%$ is usually assumed for intrinsic radiators according to bolometer measurements in some reference scenarios [109]. Nitrogen (N) and Neon (Ne) are often used as extrinsic coolant gases and depending or their recycling behavior, sourced from the valve locations or the limiters. Another impurity considered for diagnostic purposes and exhaust studies is Helium [110, 94].

In this chapter, the distribution of these impurities in the 3D helical SOL will be analyzed for the first time in order to understand the resulting radiation distribution and the capacity of radiative edge cooling in this edge geometry. First, the intrinsic radiation from Carbon eroded by sputtering will be discussed and compared to the role of the actively injected coolant gases N and Ne.

The 2D profiles of the total impurity radiation distribution for a density scenario of $n_{LCFS} = 7.0 \cdot 10^{19}$ m^{-3} at P_{in} =4 MW at the toroidal cross-section of the gas inlet are shown in figure 3.33. In figure 3.33a only the integrated carbon impurity radiation is shown, while figures 3.33b and c contain the total radiation during nitrogen and neon seeding scenarios. The carbon radiation is primarily located near the LCFS, peaking within the SOL. In figure 3.33a the radiation pattern contains a stripe-shaped domain of high intensity corresponding to the shadow of a limiter, from where the carbon originates. The 2-D radiation patterns in case of additional nitrogen and neon seeding are shown in figure 3.33b, c. The radiation distribution of the seeded impurities reveals strong accumulation behavior inside of topological domains of the helical SOL, i.e., the different flux bundles. This is because the impurities are injected into the L_C =79m and 43m flux tubes, which overlap in the radial direction along the injection path. This is shown in figurefig:Seedinglocation. The neutral impurities are released in the far SOL into the L_C =79m flux tubes and may also fuel the L_C =43m ones. Ionized impurities may mostly remain trapped in the flux tubes close to their source location.

The resulting localization of the impurity line radiation in the vicinity of the seeded magnetic flux bundle could be disadvantageous for the desired uniform heat load mitigation if the toroidal

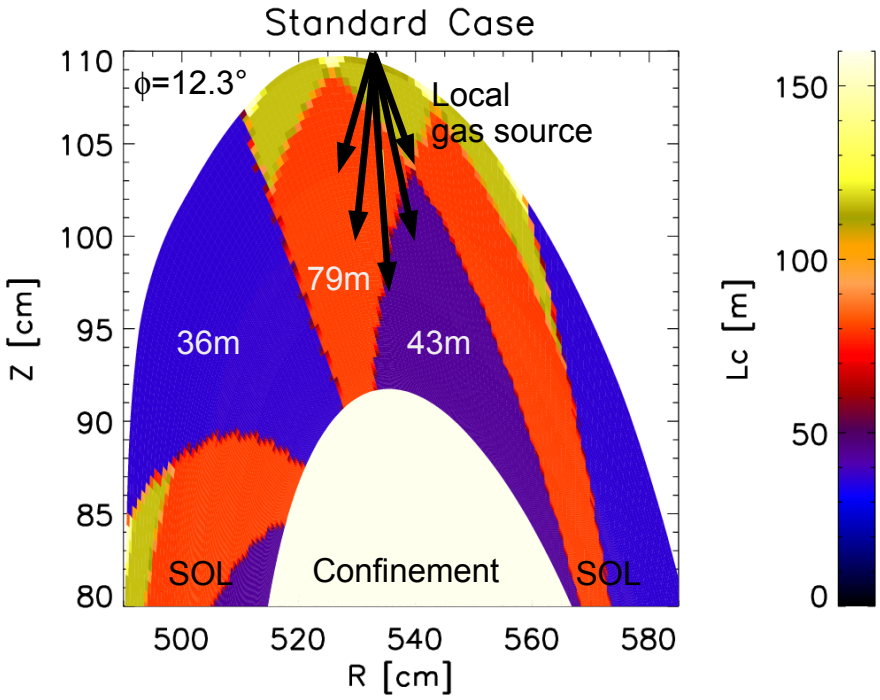

Figure 3.32 Connection lengths plot with source location for impurity seeding in the standard limiter configuration. Impurities are mostly released into the L_C =79m and 43m flux bundles.

distribution of local seeding sources is limited and does not match with the periodicity of the helical magnetic topology. During the initial limiter operation scenarios, two of the later planned ten toroidally symmetric distributed gas injection systems (one in each divertor module) is used for testing controlled impurity seeding for radiative edge cooling and for a thermal helium beam system to measure radial profiles of electron density and temperature [14]. Such local seeding of a magnetic flux tube by a single gas source allows for investigation of the SOL flux tube geometry and possible local source effects. Comparisons of experimental results to the modeling results presented here are ongoing.

The 3D distribution of power losses within the SOL is determined by the toroidal and poloidal migration of carbon impurities. The impurity transport described by equations 2.17-2.19 changes in particular in different SOL density scenarios, due to the impact of plasma density on both, the

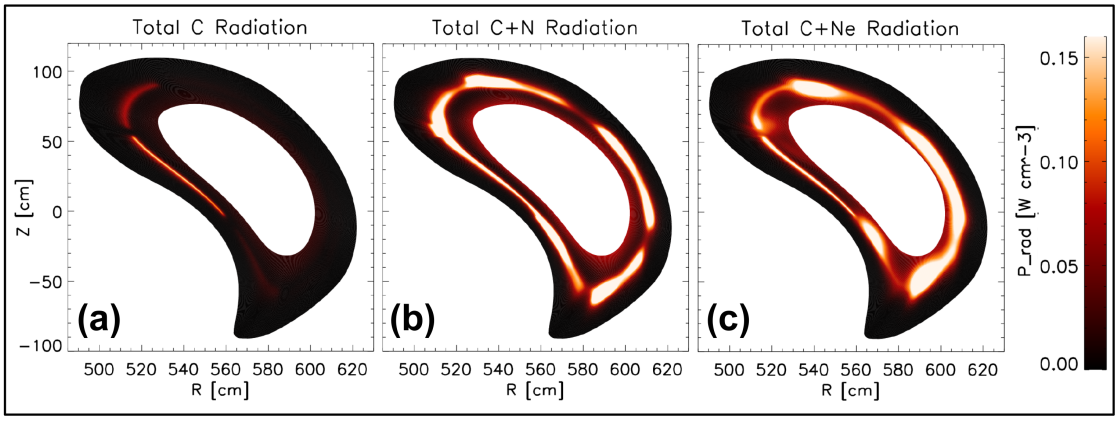

Figure 3.33 2D total impurity radiation profiles at $\phi_{tor} = 12.3°$ for (a) intrinsic carbon eroded from the limiter, (b) seeded nitrogen (including intrinsic carbon), (c) seeded neon (including intrinsic carbon) at $n_{LCFS} = 7{\cdot}10^{18}$ m^{-3} at P_{in} =4 MW. Nitrogen and neon are injected at the top (compare with figure 3.3b) [7].

friction force and the thermal force in the impurity transport equation (see section 2.1.3). This is investigated by a systematic variation of the plasma density. In figure 3.34, the 2D toroidal and poloidal distribution of the total carbon impurity radiation and the total carbon density for a three-step density scan are shown for the following input parameter and boundary conditions: P_{in} =2 MW, $n_{LCFS} = 4{\cdot}10^{18}$ m^{-3}, $8{\cdot}10^{18}$ m^{-3} and $1.2{\cdot}10^{19}$ m^{-3}. The coordinates (ϕ, θ) in x and y-direction correspond to the grid cell indices in poloidal and toroidal direction. The small darks tripes in the center of the plots are the limiter. The plots cover a poloidal domain of $\Delta\theta = 360°$ and toroidal domain of $\Delta\phi = 72°$ with the limiter in the center according to one field period. In this scan of the plasma density, it is seen that the total carbon radiation $P_{rad,C}$ (figure 3.34, top) spreads out in the toroidal direction at low density, but increases and concentrates near the limiter with rising density. Correspondingly, the total impurity density $n_C = \Sigma_Z n_{C+Z}$ concentrates with increasing density downstream at the limiter targets (figure 3.34, bottom). This is due to the enhanced friction force and reduced ionization lengths in case of higher background plasma densities.

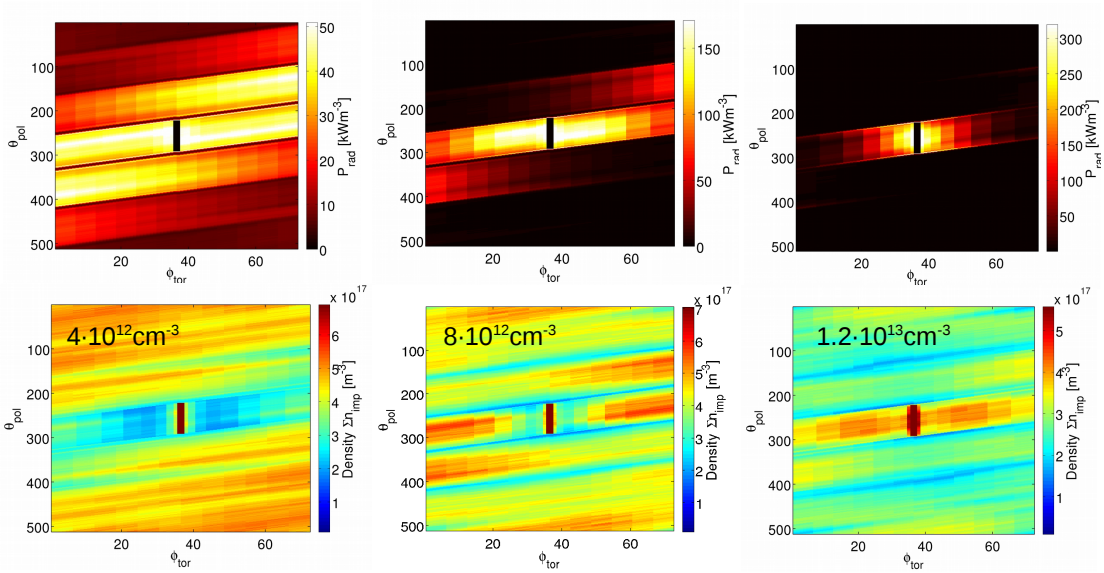

Figure 3.34 Density scan for assumption of constant $f_{rad,C} = \frac{P_{rad}}{P_{ECRH}}$ =25%. Top: total carbon impurity radiation within the SOL. Bottom: total impurity density within the SOL. The local impurity source and the friction force determine the impurity particle and radiation distributions in the limiter plasma regimes considered.

A corresponding case is shown for nitrogen seeding in figure 3.35. The impurities are released into the SOL further upstream away from the limiters. However, rising density results in a stronger toroidal localization of $P_{rad,N}$ and total nitrogen density $n_N = \Sigma_Z n_{N+Z}$ due to shorter ionization lengths as discussed in the following.

This analysis suggests that the radiation of light impurities may dominate near the downstream position. This may lead to the conclusion that upstream measurements of the radiation with a Bolometer may underestimate the power losses systematically. This may be in particular true if

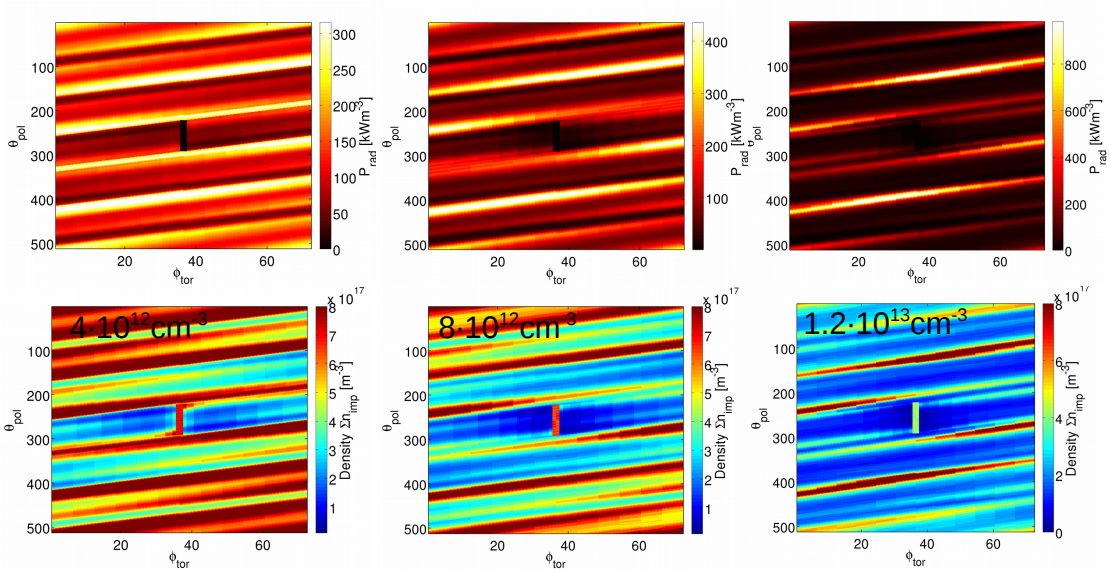

Figure 3.35 Nitrogen seeding for different densities at $P = 2$ MW. Top: $P_{rad,N}$ for $frad, N = 40\%$. Bottom: Σn_{N+Z}.

one considers light impurities and SOL radiation only. As shown previously, significant radiation contribution is located within the confinement region.

Here, the transport is defined by purely radial transport across concentric flux surfaces and hence more isotropic and not confined in separated sub-volumes like the SOL flux tubes. The radial and poloidal integrated radiation values are analyzed as a function $P_{rad}(\phi)$ of the toroidal angle ϕ to investigate the toroidal distribution of the radiation. This is shown in figure 3.36(left) for the three density cases. The solid lines represent the total radiation in the full simulation domain, including part of the confinement, i.e., all the way to the inner simulation boundary. The dashed lines represent the SOL radiation only. This analysis shows a negligible toroidal variation

of carbon radiation for the lower density case which is typical for limiter scenarios. The peak of radiated power is seen at the limiter at $\phi = 0°$ for higher densities. The ionization of eroded carbon neutrals occurs closer to the limiter in scenarios with higher density, which will be discussed in the following. The ratios of minimum to maximum toroidal $P_{rad,C}$ are shown on the right side of figure 3.36.

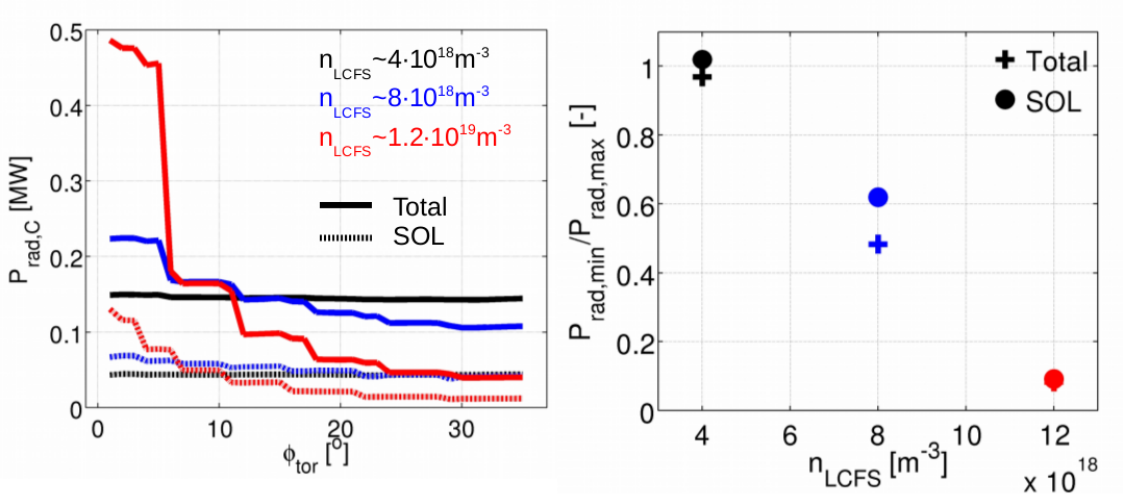

Figure 3.36 Left: toroidal distribution of poloidally and radially integrated total and SOL carbon radiation $P_{rad,C}(\phi)$ for low, medium and high density. Right: ratio of minimum to maximum $P_{rad,C}(\phi)$ for low, medium and high density.

This finding demonstrates an essential and intuitive feature of the distribution of the carbon radiation as intrinsic impurity born at the limiter, and it also has an important diagnostic implication. Toroidally localized measurements suggest that radiative losses may under or overestimate the global radiation losses if the assumption of a toroidally uniform distribution is made.

Without additional diagnostics, 3D modeling might help to close gaps in the 3D power balance. The current Bolometer system is located only at one triangular cross-section [109]. This location is farthest away from the main plasma facing components ($\Delta\phi_{tor} = 36^o$) in any configuration. The limiters as discrete main impurity and recycling sources are centered at the bean-shaped cross

section ($\phi_{tor} = 0^o$). Also, the divertors, although toroidally more continuous and extended, are centered at the bean-shaped cross-section and do not cover the triangular cross section. Extension of the Bolometer system is planned in the future in order to obtain a better toroidal distribution of the radiation measurement.

A view with a more complete poloidal and a wider toroidal coverage of radiation can be obtained by the video diagnostic capturing the emission in the full visible spectrum or employing filters for certain spectral lines [111, 14]. The set of post-processing routines in EMC3-EIRENE [83] is used to obtain more direct comparison to the modeling results. A scenario based on the following modeling input was analysed: P_{in} =2 MW, $n_{LCFS} = 4{\cdot}10^{18}$ m^{-3}, $D_\perp = 0.5$ m^{2}s^{-1} and $f_{rad,C} = 25\%$.

In figure 3.37, such a direct comparison is shown, based on a tangentially viewing video diagnostic, with a line of sight into the triangular plane. Therefore, this view integrates a significant length along the toroidal direction, enabling to see the helicity of the device and the helical radiation distribution. On the left side synthetic camera plots of H_α (656.19nm) (top) and CIII (465nm) (bottom) are shown. On the right side, typical radiation structures observed in the visible range are depicted.

The lines emissions in the modeling are chosen from the visible range and are calculated based on photoemission coefficients (PECs) provided by the ADAS database [81]. The H_α radiation is concentrated at the limiter location in the background since it is the dominant recycling source. The CIII, however, is determined by double ionized carbon which may also radiate at toroidal positions at some distance from the limiters. Line emission from neutral hydrogen and carbon impurities are assumed to be significant fractions of the radiating boundary layer captured with experimental video diagnostics. The structures may allow identification of the LCFS and widths of the radiating boundaries. The modeling suggests a strong localization of H_α and helical stripes in case of carbon impurity radiation. The latter corresponds to a clear limiter imprint, corresponding

to a projection of the C source localized at the limiter along the connected flux channel. It is found that higher anomalous transport coefficients cause more blurred patterns, which may fit better with the observed radiation layer widths.

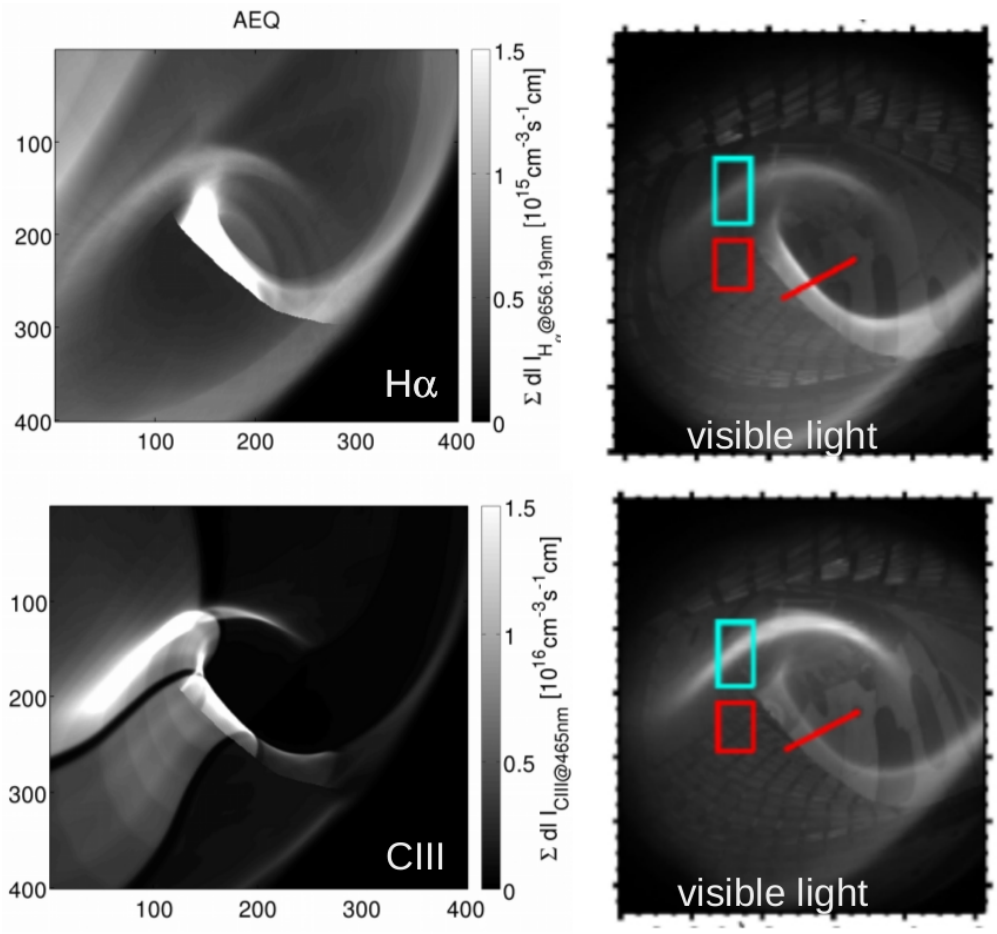

Figure 3.37 Left: Modeled H_α (656.19nm) and CIII (465.01nm). Right: visible light captured by videodiagnostic.

This tangential overview observation is accompanied by a tangential view with a higher resolution around the limiter surface. Examples of the observed line emission recovered with the EMC3-EIRENE synthetic video diagnostics for this view is shown in figure 3.38 for H_α(656.19nm), CII(514nm) and CIII(465nm) on the left and with images from experimental image data on the

right. Here, the qualitative most comparable radiation pattern was obtained for carbon line emission was with P_{in} =2 MW, $n_{LCFS} = 1.2{\cdot}10^{19}$ m^{-3}, $D_{\perp} = 0.5$ m^{2}s^{-1} and $f_{rad,C} = 25\%$. For lower density, the line emission is seen to be less concentrated at the limiters and rather spread out in toroidal direction.

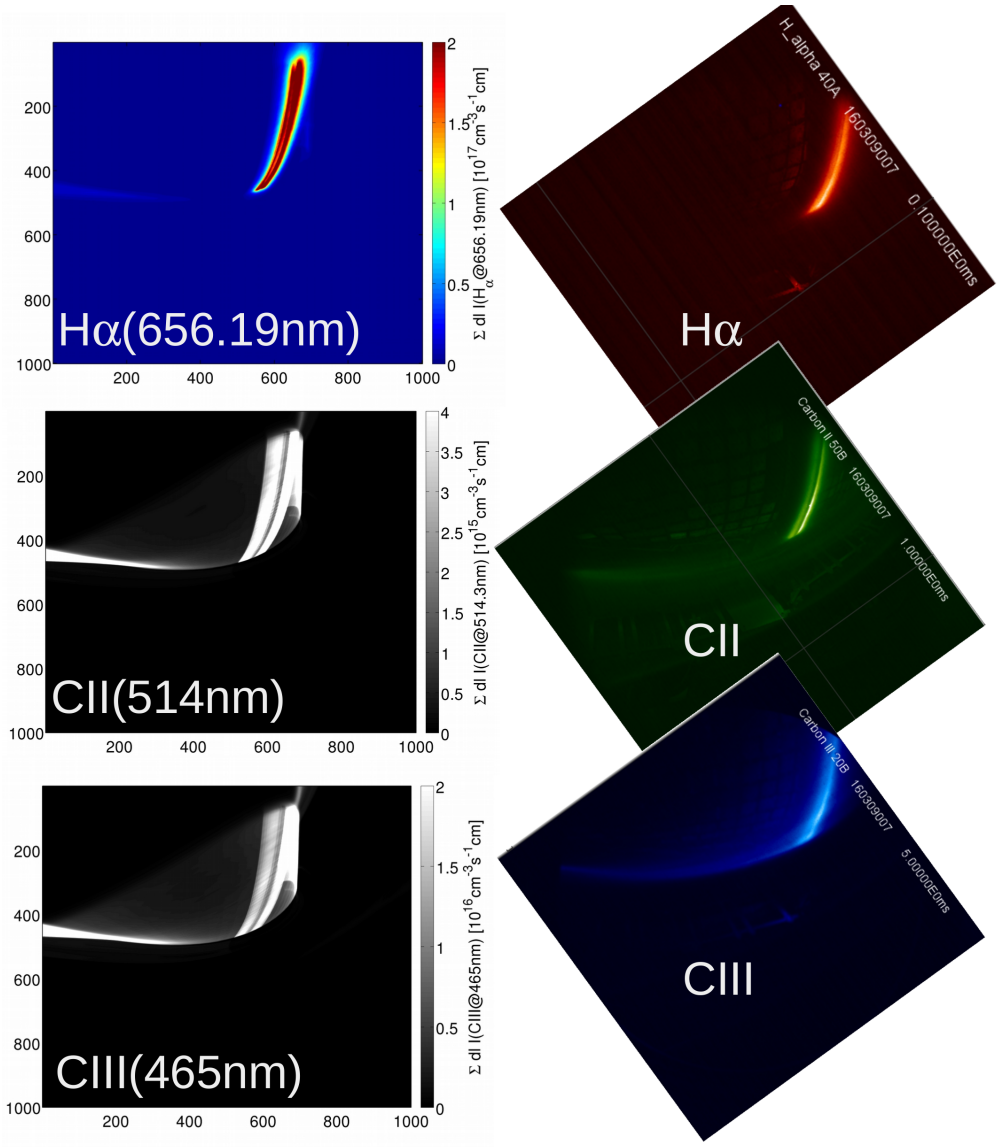

Figure 3.38 Comparison of video diagnostic and modeled line emission from H_α and CI-CIII. The experimental measurement used a filter for a range of 467±5 nm [14]. The modeling shows strong sensitivity to local plasma parameter.

In order to visualize the distribution of injected impurities, a final example is shown in 3.39 of the distribution of Ne radiation as seen in a synthetic image of a tangential view from the upper region of the device into the vacuum chamber. The NeVIII(694.12nm) is chosen for a scenario with P_{in} =2 MW, $n_{LCFS} = 4.0{\cdot}10^{18}$ m^{-3}, $D_{\perp} = 0.5$ m^{2}s^{-1} and $f_{rad,Ne} = 40\%$. A more detailed discussion of the link between impurity transport and the radiation pattern is provided in the following sections. Here, consider only the general structure of the neon radiation. Two cases are distinguished: sourcing from the point source and sourcing from the limiters in order to distinguish and approximate a low and a high recycling case for neon. Zero recycling is modeled by sourcing Neon only from the gas valve and fully absorbing it by the wall and limiters. The edge line emission is shown in figure 3.39 (left). Single radiating structures in the vicinity of the seeded flux tubes are identified within the boundary radiation. The recycling case is approximated by sourcing the Neon from the limiters only. It is shown figure 3.39 (right). The radiation is distributed much more homogeneously and does not feature any bundle structures. Although line emission from higher charge states is chosen, a clear difference in radiation patterns is found, which demonstrates the strong dependence of these patterns on the recycling assumptions of the seeded impurities. Neon is a noble gas and generally expected to feature a high recycling coefficient. Modeling from other devices typically fully neglect the seeding locations and sources Neon from all recycling targets [48].

This overview shows that the 3D edge magnetic geometry can have a substantial effect on the edge radiation. The helical SOL structure of long and short flux bundles together with the discrete intrinsic and extrinsic impurity sources induces complex 3D boundary radiation layers. The underlying impurity transport and sensitivity to assumptions made will be discussed in the following sections. In particular, its potential for radiative power exhaust will be discussed.

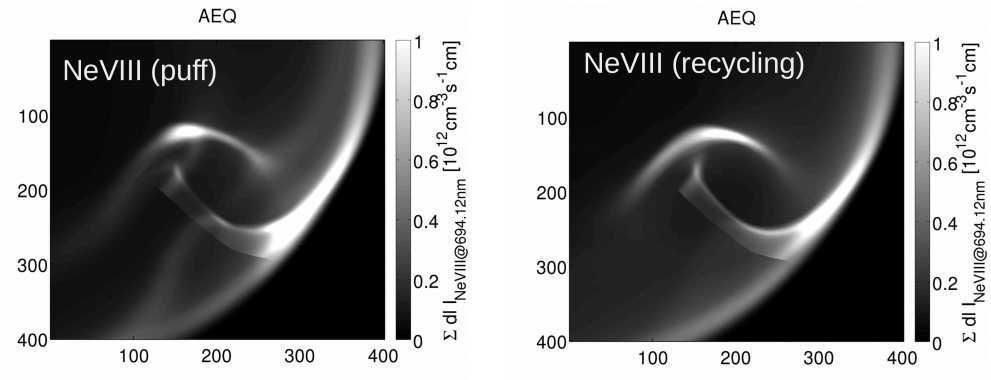

Figure 3.39 Left: Modeled NeVIII (694nm). Left: puff Right: recycling/Limiter sourcing.

3.2.2 Parallel transport analysis of impurities

The overview analysis of the radiation distribution discussed before provided clear evidence for a sensitivity of the radiation distribution on source location and the plasma density. This indicates that the impact of plasma conditions on the impurity transport determines the eventual 3D radiation distribution. Therefore, the parallel profiles and the relation to the impurity distribution is discussed in the following.

The parallel transport of intrinsic impurities is considered for the example of carbon for typical limiter scenarios for a representative case with $n_{LCFS} = 4 \cdot 10^{19}$ m^{-3}, $D_\perp = 0.5$ m^{2}s^{-1} at $P = 2$ MW and with $f_{rad,C} \approx 25\%$. Since the parallel temperature gradients vanish or are only marginal main SOL remains in a friction force dominated impurity transport regime. The main constituents of the force balance according to equation 2.21, the friction force F_{fr} and the ion thermal force F_{i-th} and their difference ΔF are shown in figure 3.40 (left and center). The friction force is equal to the main plasma flow. The profiles shown use the same velocity scale and comparison of F_{fr} and F_{i-th} already indicates that $F_{fr} > F_{i-th}$ in the relevant SOL transport domain. The difference between friction and ion thermal force results again in a distribution mostly determined by the friction force: $\Delta F = F_{fr} - F_{i-th} \approx F_{fr}$ (see figure 3.40, right). This does not change for the

parameter ranges considered in this study covering typical heating and density scenarios realized in the experiments.

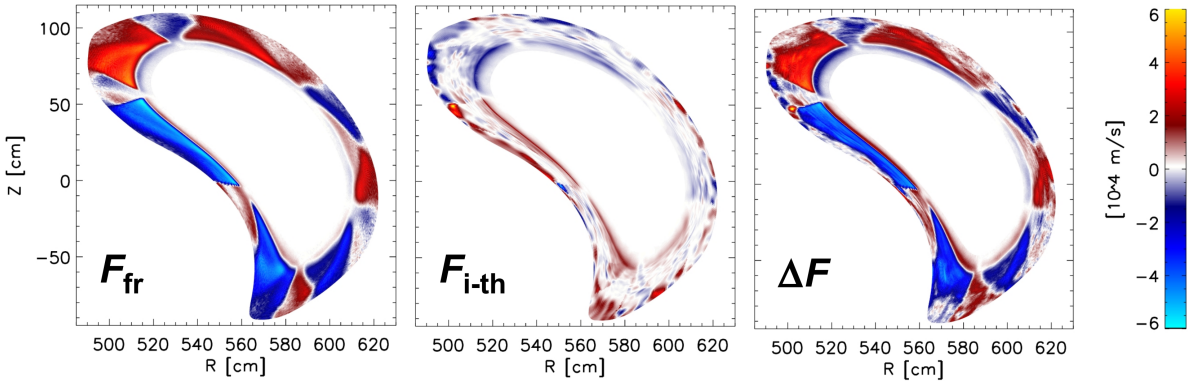

Figure 3.40 Distribution of friction force F_{fr}, ion thermal force F_{i-th} and force balance $\Delta F = F_{fr} - F_{i-th}$ for a typical limiter scenario.

The resulting parallel SOL transport profiles are shown in figure 3.41. The parallel plasma density profiles are shown on the top left. The blue, green and red colors represent profiles from the three types of connection lengths flux bundles described above (L_C ≈36, 43 and 79m). The neutral impurity density n_{C0} at the top center shows an almost discrete distribution peaking downstream at the limiter locations. The plots for n_{I+Z} with are the carbon impurity ion densities for $Z = 1, 2, .., 6$. The resulting total carbon radiation $P_{rad,C}$ is shown on the bottom right.

The lower charge state densities ($Z < +4$) and the $P_{rad,C}$ and peak downstream, close to the limiter. They vary up to one order of magnitude between upstream and downstream, i.e., between the center and boundary values of the profiles. The shape of the radiation peak in parallel direction can be understood by considering the plasma density and the density of lower charge states together. The hydrogen density drops to half of the upstream density while the lower carbon charge states reach their maximum at the limiter. The total carbon radiation is $P_{rad,C} = \Sigma_Z n_e n_{C+Z} L_{n_C+Z}$. The friction force of the plasma flow directed to the limiter holds the eroded impurities back. Impurities of higher charge states ($Z > +3$) are concentrated further upstream. Those impurities are

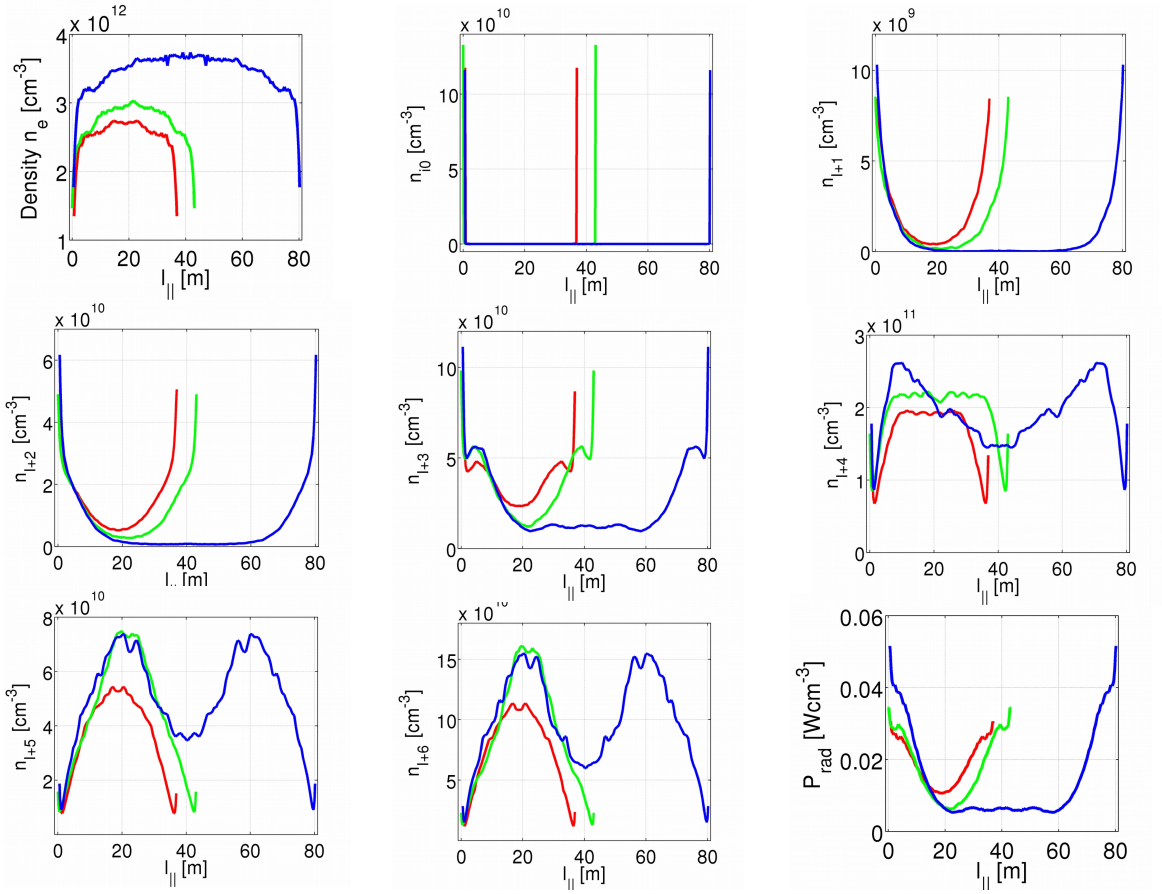

Figure 3.41 Ion densities and $P_{rad,C}$ for a typical limiter case with carbon.

either further ionized within the SOL or fueled back into the SOL once they got ionized in the confinement. $P_{rad,C}$ is mostly determined by radiation from charge states ($0 < Z < +4$).

The resulting parallel profiles of the main species density n_e, the carbon density for $Z = +3$ and the resulting total radiated carbon power $P_{rad,C}$ are shown for the three densities $n_{LCFS} = 4 \cdot 10^{18}$, $8 \cdot 10^{18}$ and $1.2 \cdot 10^{19}$ m^{-3}, $D_\perp = 0.5$ m^{2}s^{-1} at $P = 2$ MW and with fixed $f_{rad,C} = 25\%$ in figure 3.42. The main plasma density peaks in front of the limiter in higher density cases. The ionization lengths are reduced, and the stronger friction forces press the impurities closer to the target. This is shown for the main radiators, the densities n_{C+3}, in the center row of figure 3.42. Accordingly, the total radiated power shown in figure 3.42(bottom) concentrates near the target.

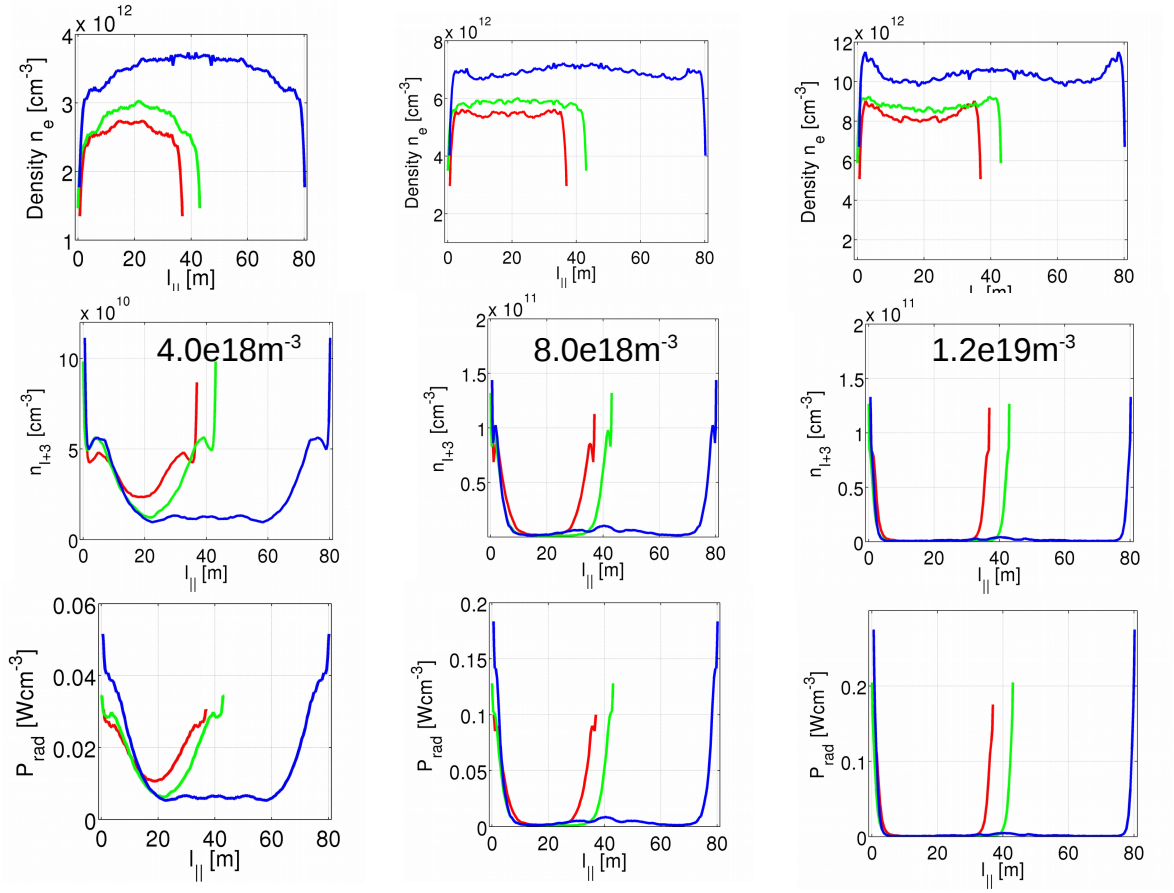

Figure 3.42 Density scan for carbon with fixed power losses of $f_{rad,C} = 25\%$.

This explains the tendency of the toroidal power losses to peak at the bean-shaped limiter cross section as stated in the previous section and shown in figure 3.36. As pointed out before, this has an important implication for the measurements of the total radiated power. A concentration of impurity radiation at the downstream location in higher density friction force dominated regimes may underestimate the global power losses extrapolated based on a measurement at the triangular cross section.

Parallel profiles are extracted for nitrogen and neon seeding seeding scenarios with $n_{LCFS} = 4{\cdot}10^{18}$, $D_\perp = 0.5\,\mathrm{m^2 s^{-1}}$ at $P = 2\,\mathrm{MW}$ and with fixed $f_{rad,N,Ne} = 40\%$ and depicted in figure 3.43. For neon both, local seeding and sourcing from the limiters are considered, in order to compare

effects from seeding and approximated recycling effects. The top row shows the neutral nitrogen and neon impurity density distributions. The parallel profiles for impurity ion densities n_{I+Z} and P_{rad} are plotted underneath. The discrete stellarator symmetry in use also determines the source locations. For Neon, the center plots show the case with seeding only, and the right plots show the case with recycling only. In the latter case, the neon is sourced from the limiter. Because of its high recycling coefficient, the latter approximation is expected to be the more realistic one and, as such, is also used for similar studies at LHD [48].

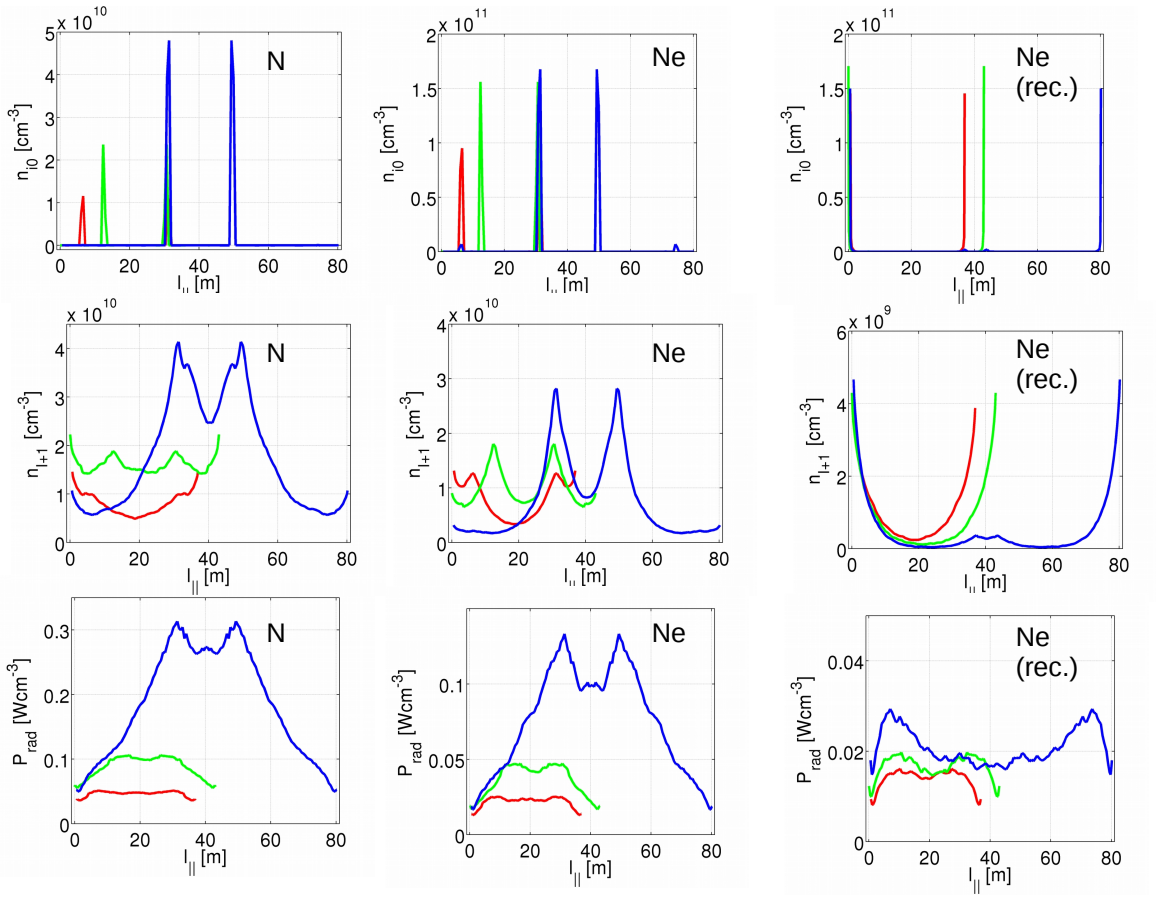

Figure 3.43 Left: Nitrogen injected. Center: Neon injected. Right: Neon recycled (sourced from the limiter).

The parallel profiles of nitrogen and neon show similar density and radiation distributions in case of seeding. It shall be noted that each flux tube is seeded twice since stellarator symmetry is used in order to save computational resources and since only about the principal effects are discussed here. The results show that one may approximate a single gas source within a flux tube by shifting the point sources to the ideal upstream locations at the midplanes identified previously.

The most extended flux tube accumulates most of the impurities since it is directly exposed to the source (see figure 3.32) and the shorter ones less. The shortest (36m) flux tube shows the smallest impurity concentration from seeding because it is most distant from the source location as explained in previous sections. The radiation peaks somewhat upstream and is a factor of ≈3-4 higher than downstream. This indicates a more inhomogeneous distribution of SOL radiation. For neon, the case with full recycling shows an entirely different radiation pattern. If recycling comes into play, the peaking zone of the radiation shifts downstream towards the limiters as shown in the left plots of figure 3.43 .

Simulations for higher density scenarios show for the discussed Nitrogen and Neon cases a similar tendency as discussed above for carbon. With rising density, the friction force drives the main radiators further downwards. The radiation peaks are shifted somewhat away from the source location. However, the effects are less strong.

In summary, these findings indicated that the friction force at higher density results in an increase of the impurity transport towards the limiters. The radiation zone may be shifted or concentrated according to the actual magnitude of the resulting impurity flow towards the limiter surface. The resulting anisotropy in the distribution of total power losses is likely to result in an underestimation of power losses at the upstream location if impurities are sourced mostly downstream. Impurity seeding is found to introduce an additional uncertainty since the modeling indicates a strong peaking of radiation near the source location.

3.2.3 Perpendicular transport analysis

3.2.3.1 Radial distribution of impurities and radiation

The analysis of the parallel profiles and the link to impurity fluxes before has resolved the basic mechanism of impurity transport away from the surface and towards the surface, based on the ratio of thermal and friction force. Once the impurities enter the main plasma volume, i.e., penetrate inward of the LCFS, they are transported according to equations 2.17 and 2.18 by a radial diffusion parameter and the density gradient of the plasma. In this section, this perpendicular transport of impurities back into the SOL and within the SOL is analyzed.

In figure 3.44 the flux surface averaged radial distributions of the total impurity radiation for four density scenarios are shown. The density dependence of the radial carbon radiation distribution for the four density cases is provided in figure 3.44a. For the densities with n_{LCFS} >7.0·10^{18} m^{-3}, the peak values of the total carbon radiation are located in the SOL at an effective radius of $r_{eff} \approx$ 50 cm, 2-3 cm distant from the LCFS. The highest density (n_{LCFS} =1.9·10^{19} m^{-3}) causes the highest C erosion flux based on the chemical sputtering assumption of a fixed yield. Therefore the highest density scenario results in highest radiation amount (cyan line in figure 3.44a) with a peak value of $P_{rad,C,max}$ ≈0.11Wcm^{-3}.

However, the choice of the transport coefficients and the boundary conditions for the impurities can change the results. In order to assess this sensitivity, both, the boundary conditions at the LCFS and the cross-field transport coefficients are varied for carbon in the following for a fixed n_{LCFS} =9·10^{18} m^{-3} with P_{in} =4 MW. The resulting radial radiation profiles are shown in figure 3.44b. The blue line represents the default scenario with spatial constant $D_{\perp} = 1.0 m s^2 s^{-1}$ for main ions impurities. The red profile represents the application of the 1D core impurity transport

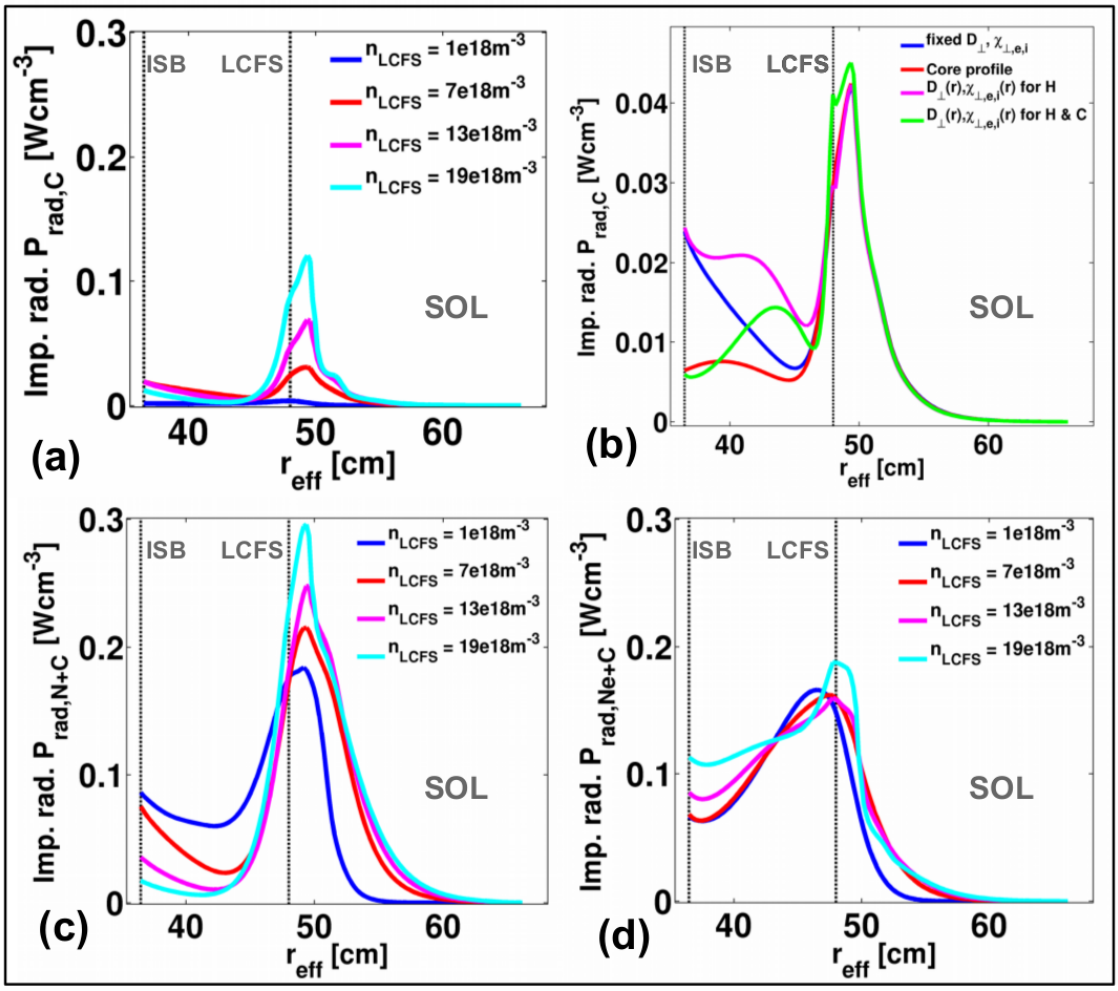

Figure 3.44 Radial distribution of total impurity radiation for the density scan at P_{in} =4 MW. (a) Intrinsic carbon eroded from the limiter, (b) intrinsic carbon for different transport conditions at fixed $n_{LCFS} = 9{\cdot}10^{19}$ m^{-3}, (c) seeded nitrogen (including intrinsic carbon), (d) seeded neon (including intrinsic carbon). The black dotted lines indicate ISB and LCFS (relevant for the boundary conditions)[7].

model allowing for further ionization of impurities crossing the inner simulation boundary. The assumption of low $D_{\perp,core}$ for hydrogen only is represented by the magenta data. Green corresponds to the scenario with reduced $D_{\perp,core}$ for main ions and impurities.

In the previous default cases, the transport parameters were kept spatially constant at $D_\perp = 1.0$ m^2s^1, $\chi_{\perp,e,i} = 3D_\perp$ inside and outside the LCFS and the inner simulation boundary condition is set such that the net impurity ion flux for each charge state is zero. The resulting radiation distribution is shown in figure 3.44b (blue); in this case, about 50% of the total radiative losses occur in the confinement region. This is because the intermediate charge states are not further ionized within the domain enclosed by the ISB, but they penetrate deeper into the plasma core, which is not modeled here. Therefore, the boundary condition of impurity ion reflection and the charge change in which they are returned into the modeling domain are essential parameters.

To explore the dependency of the impurity transport results on the boundary conditions, a 1D impurity transport core model [80] is applied assuming a flat core profile of $n_{core} = 5.0\times10^{19}$ m^{-3}, $T_{e,core} = 2.0$ keV and $D_{\perp,core} = 0.1$ m^2s^{-1}. The resulting profile in figure 3.44b (red) shows a strong reduction of radiated power in the confinement region; in this case, the radiation at the ISB drops from $P_{rad,C}$ ≈0.025Wcm^{-3} to $P_{rad,C}$ ≈0.007Wcm^{-3}. This is because the core transport model allows for further ionization steps to take place, for C^{+5} in particular. In the default case, further ionization of this charge state within the core is neglected which causes an overestimation of its density around the ISB and related contributions to the total impurity radiative losses. However, the peak and the radial distribution of the total impurity radiation within the SOL is not affected by these boundary conditions.

The assumption of reduced transport coefficients within the LCFS may approximate the effects reduced outward impurity fluxes due to a transport barrier. Therefore two further cases (magenta and green in figure 3.44b) are presented assuming different perpendicular transport coefficients for the SOL and confinement region. A radial core transport profile is defined as: $D_\perp(r) =$

0.1 m^2s^{-1} for $r < r_{LCFS}$ and $D_\perp(r) = 1.0$ m^2s^{-1} for $r \geq r_{LCFS}$ ($\chi_{\perp,e,i}(r) = 3D_\perp$(r)). In the first case (magenta) these profiles are assumed for the main hydrogen species only while the coefficients are kept spatially constant for carbon at $D_\perp$ =1 m^2s^{-1}. In the second case (green) these profiles are used for both main hydrogen plasma and carbon impurities. In the first case, the radiation distribution within the SOL hardly deviates from the cases (blue and red) discussed above. However, it features higher radiative losses in the confinement domain than the remaining cases discussed here. In the second case (green) the radiation has another peak in the confinement domain and then reaches at the ISB the level of radiation obtained by applying the core transport model (red) discussed above. Additionally, the sharp transition of the perpendicular transport applied to the impurities causes a further peak in radiation at the LCFS and a slightly increased peak within the SOL. The radiation distribution depends non-linearly on the temperature profile [81] which changes with varying transport conditions as well.

This analysis shows that the SOL radiation is relatively independent of the transport conditions in the confinement and core domain for spatially fixed cross-field transport of the impurities. The last case (green) discussed demonstrates a higher sensitivity of the SOL radiation to changes of the perpendicular transport of the impurities.

3.2.3.2 Species dependence of radial impurity distributions

Because of the different ionization potential of the species under consideration, the radial and poloidal, distributions of the radiation are different for these species. In figure 3.45 the flux surface averaged radial impurity ion density distributions of the four impurity species considered for radiative power exhaust are shown for a typical limiter scenario with $n_{imp,Z} = 4 \cot 10^{18}$ m^{-3}, $P = 2$ MW and $D_\perp = 0.5$ m^2s^{-1}. The solid black lines correspond to the neutral impurity densities $n_{imp,0}$, the different colors correspond to the higher charge states densities $n_{imp,+Z}$. The black dotted line represents the total integrated impurity density $\Sigma_Z n_{imp,+Z}$. Carbon and oxygen are assumed to be

intrinsic radiators and therefore sourced from the limiters (see discussion of these assumptions in section 3.2.1). Their yields are iterated until power loss fractions of $f_{rad,C} = f_{rad,O} = 25\%$ are established (figure 3.45(a) and (b)). Neon is treated similarly and sourced from the limiter in order to approximate its high recycling behavior. Its yield is iterated until its impurity influx establishes a power loss fraction of $f_{rad,Ne} = 40\%$ (figure 3.45(c)). Atomic nitrogen is sourced remotely from a point source, and recycling is neglected. Its yield is iterated until its impurity influx establishes a power loss fraction of $f_{rad,N} = 40\%$ (figure 3.45(d)).

The ionization equilibrium for impurities eroded or recycled at the limiter shows evident peaking of lower charge states around the LCFS. The scenario with nitrogen seeding shows a peaking of lower charge states ($Z < +5$) densities within the SOL, however. Neutral nitrogen (black curve) hardly penetrates into the confinement under the given assumptions. This explains the radial power distributions shown previously. Under the assumption of no recycling, the limiter appears to be very effective for the screening of seeded impurities. Based on these results, it is expected that N will be a dominant radiator in the SOL while Ne is more optimal for radiation around the LCFS.

3.2.3.3 Sensitivity of radial transport to source energy

The dependence of the radial distribution of impurities and radiation distribution on the energy of the penetrating impurities has been investigated by varying the start energy of the sourced particles. The energies selected for this sensitivity study range from thermal speeds - representative for atoms released by a gas valve or at the wall - to energies in the range of typical molecular dissociation energies. The latter is relevant, as a:CH layers will build up on the surface on the limiters and also N may undergo molecular chemical bonds with the C surface material. When these molecules are eroded and break up, parts of the molecular binding energy is provided to the dissociation products, resulting in a higher energy class of impurity atoms.

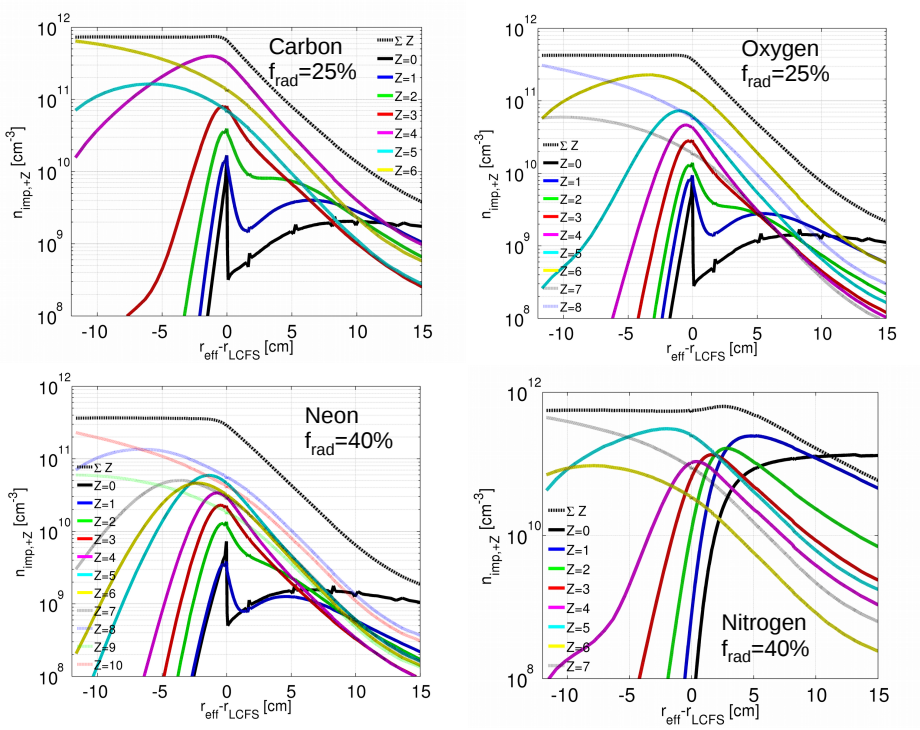

Figure 3.45 Radial profiles of averaged impurity ion densities and for each charge state. Top, left: Carbon, right: Oxygen. Bottom left: Neon sourced from the limiter; right: Nitrogen injected.

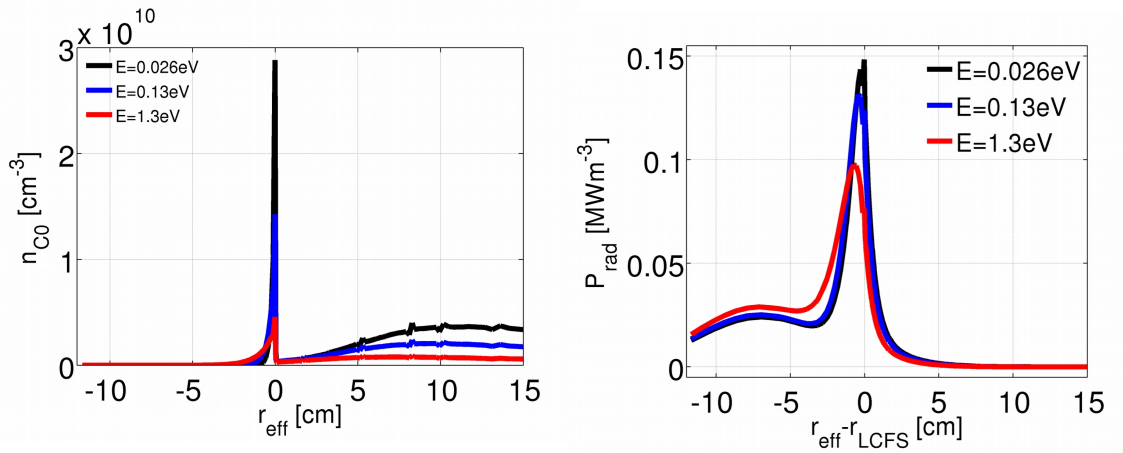

Figure 3.46 Radial distribution of eroded carbon neutrals and total impurity radiation for different energies covering two orders of magnitude (black: $E = 0.026$ eV, blue $E = 0.13$ eV, red: $E = 1.3$ eV) for case with P_{in} =2 MW, $n_{LCFS} = 4{\cdot}10^{19}$ m^{-3}, $D_{\perp}$ =0.5 m^{2}s^{-1}, $f_{rad,C}$ =25%.

The resulting distributions of carbon neutrals and total impurity radiation for case with P_{in} =2 MW, $n_{LCFS} = 4{\cdot}10^{18}$ m^{-3}, $D_{\perp}$ =0.5 m^{2}s^{-1}, $f_{rad,C}$ =25% are shown in figure 3.46 on the left and right, respectively (black: $E = 0.026$ eV, blue $E = 0.13$ eV, red: $E = 1.3$ eV). The $P_{rad,SOL}$ to $P_{rad,tot}$ fraction decrease with increasing energy from 20.3% to 17.2% to 11.1%.

This analysis shows that even for two orders of magnitude increase of the start energy of the impurities, only a marginal shift of the radiation peak slightly inwards and reduce the SOL power losses by a factor of 0.5. The experimentally measured surface temperature stays mostly below a few hundred Kelvin [10], corresponding to the low to medium energies assumed here. E.g. $k_T T_{surf}$ ≈0.07 eV for T_{surf} =800K.

3.2.3.4 Sensitivity of radial transport to anomalous transport coefficients

The impurity transport is expected to depend strongly on the anomalous transport coefficients. Since no measurement for impurity transport coefficients in the SOL (and Core) was available, sensitivity studies with transport modeling are of interest. In addition to the previous survey on the effects of the core-confinement transport (section 3.2.3.1) the diffusive transport has been varied here in three steps, keeping $D_{\perp}$ for main plasma and impurity ions spatially constant in the whole simulation domain. The anomalous heat transport is varied at a fixed ratio with $\chi_{\perp,i,e} = D_{\perp}$. The scans were performed for a scenario with $n_{LCFS} = 4{\cdot}10^{18}$ m^{-3} at input power of P_{in} =2 MW.

The Carbon impurity flux from the limiter is set such that it establishes a power loss fraction of $f_{rad,C} = \frac{P_rad,C}{P_{in}}$ =25%. The transport coefficients are varied in a typical range of $D_{\perp}$ =0.5, 1.0 and 1.5 m^{2}s^{-1}, keeping the ratio $\chi_{\perp,i,e} = 3D_{\perp}$. The results are depicted in figure 3.47. Here, the radial distributions of (top left) main ion density, (top right) integrated carbon ion density, (bottom left) total impurity radiation and (bottom right) temperatures are shown. With increasing perpendicular transport, one obtains flatter profiles for heat and particles. The maximum level of integrated impurity density even reduces since the outer tail features a slower decay. The radiation peak

maximum $P_{rad,max}$ moves only slightly inward. More radiation occurs in the SOL. The ratio of SOL radiation to total radiation $\frac{P_{rad,SOL}}{P_{rad}}$ increases with rising perpendicular transport from 17.2% to 24.5%, to 29.4%. The increase of diffusive transport by a factor of 3 increases the fraction of power losses in the SOL by a factor of 1.7. A higher diffusive transport for impurities only would be beneficial in order to reduce power losses and impurity accumulation in the confinement. This analysis shows again that the transport coefficients will have to be estimated from main plasma parameters and radial profiles in the SOL in order to allow a quantitative analysis of the outward impurity flux at the LCFS and in the SOL.

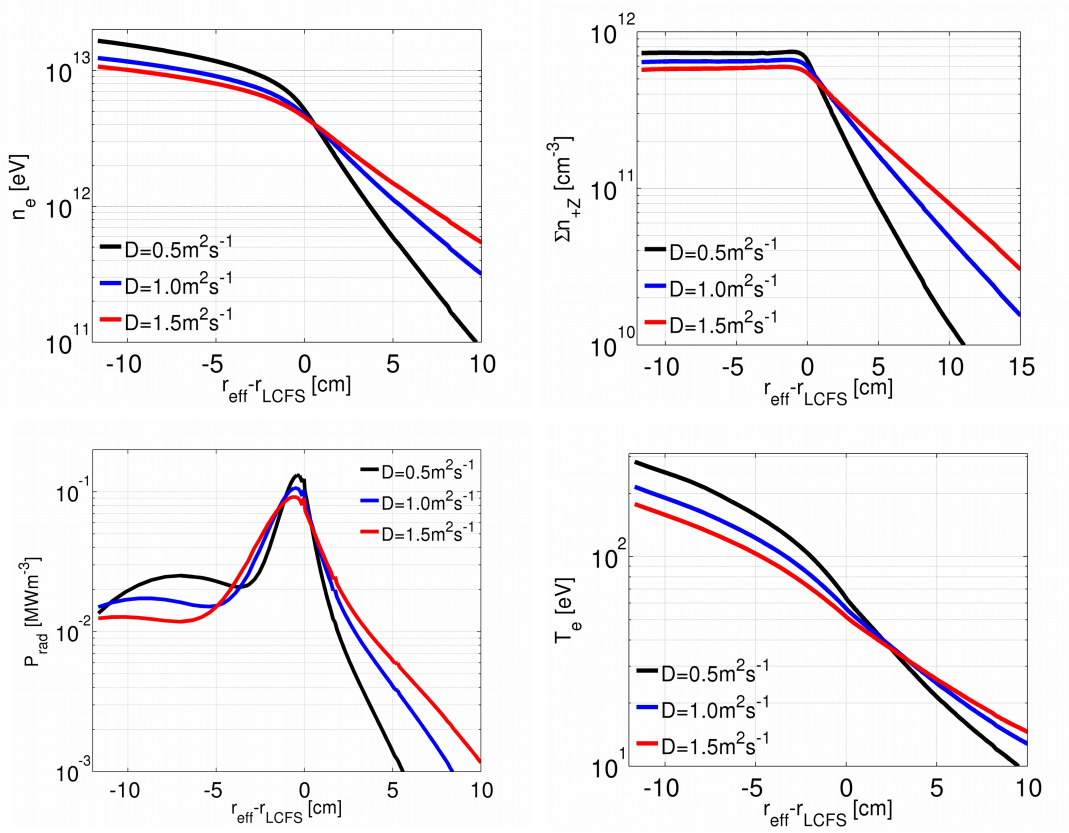

Figure 3.47 Radial distributions of (top left) main ion density, (top right) integrated carbon ion density, (bottom left) total impurity radiation and (bottom right) temperatures for different transport coefficients ($D_\perp$ =0.5, 1.0 and 1.5 m^{2}s^{-1}, $\chi_{\perp,i,e} = 3D_\perp$) for a case with P_{in} =2 MW, $n_{LCFS} = 4{\cdot}10^{18}$ m^{-3}, $f_{rad,C}$ =25%.

3.2.4 Radiative power exhaust by impurities

3.2.4.1 Discussion of radiative cooling by intrinsic sources

The analysis of the basic impurity transport losses before was made to investigate how these features can be utilized for a controlled dissipation of energy before it arrives on the limiter surfaces. One particular question is, if and under what assumptions carbon or oxygen may define radiative density limits for the limiter plasmas [112]. A simple estimation is made by defining a fixed yield for chemical erosion based on a typical power loss fraction of $f_{rad} \approx 0.25$ obtained from the Bolometer system [109]. In a first step simulations have been performed for a scenario with $n_{LCFS} = 4.0 \cdot 10^{18}$ m^{-3}, $P = 2$ MW, $D_\perp = 0.5$ m^{2}s^{-1}, $\chi_\perp = 3D_\perp$ in order to calculate the yields of carbon and oxygen using f_{rad} as input parameter separately. One obtains relatively high yields of $Y_C = 0.12$ and $Y_O = 0.6$. These yields were kept fixed in a second step, where the n_{LCFS} was increased in steps of $n_{LCFS} = 2 \cdot 10^{18}$ m^{-3} until $f_{rad,C,O}$, now being an output parameter, reached $\approx 100\%$, corresponding to power detachment or radiative collapse. The poloidally and toroidally averaged radial profiles for P_{rad} and T_e are shown in figure 3.48 (a-d) for plasmas with carbon and oxygen sourced from the limiters.

For carbon the radiative limit is reached or exceeded for $n_{LCFS} = 1.0 \cdot 10^{19}$ m^{-3}. In this case all power losses (green $P_{rad,C}$ profile in figure 3.48(a)) are concentrated at the inner simulation boundary at the heating source. The electron temperature drops to ≈1 eV in almost the entire simulation domain (green T_e profile in figure 3.48(c)). The same inward shift of the radiation zone happens with oxygen, but the critical density for that is already achieved or exceeded at $n_{LCFS} = 8 \cdot 10^{18}$ m^{-3}.

Such an inward movement of the radiation front approaching radiative collapse was also seen in the experiment. The evolution of such a collapse is recovered with synthetic video images in figure 3.50. Here, the tangential camera view is applied to the simulation data for CIII(465.01nm)

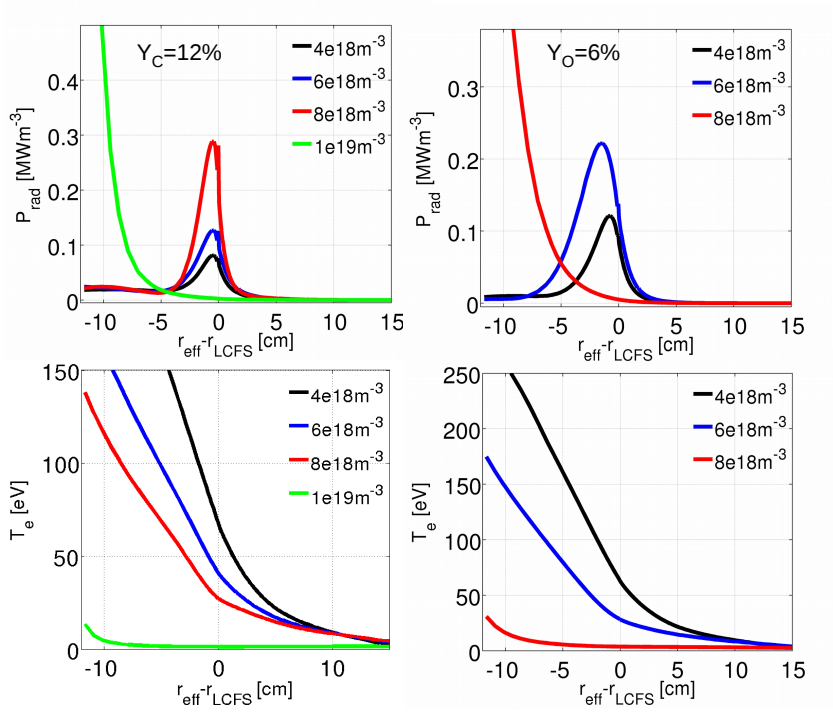

Figure 3.48 Density scan for assumption of Y_C =12% and Y_O =6% corresponding to power loss fraction of 25% by these light impurities at low density. Similar to experimental observation MARFE limit would be crossed at higher densities.

for each density step. For densities of $4 - 10 \cdot 10^{18}$ m^{-3}, radiation belts are present in the edge which correspond to C^{+2} ions which follow the field lines connected to the vicinity of their source locations (the limiters). In case of collapse, the radiation zone is moved inwards, and the belt structures originating from the limiters are dissolved.

The comparison of those two intrinsic radiators shows that oxygen is more than twice as 'efficient' as carbon concerning its radiation potential. This indicates that secondary intrinsic impurities even in smaller concentrations have to be taken into account since they may reduce the critical density for radiative instabilities based on carbon [113]. Here, the discussion is restricted to light impurities relevant for edge radiation. Radiative density limits are mostly discussed based on the bulk radiation of heavier impurities [112].

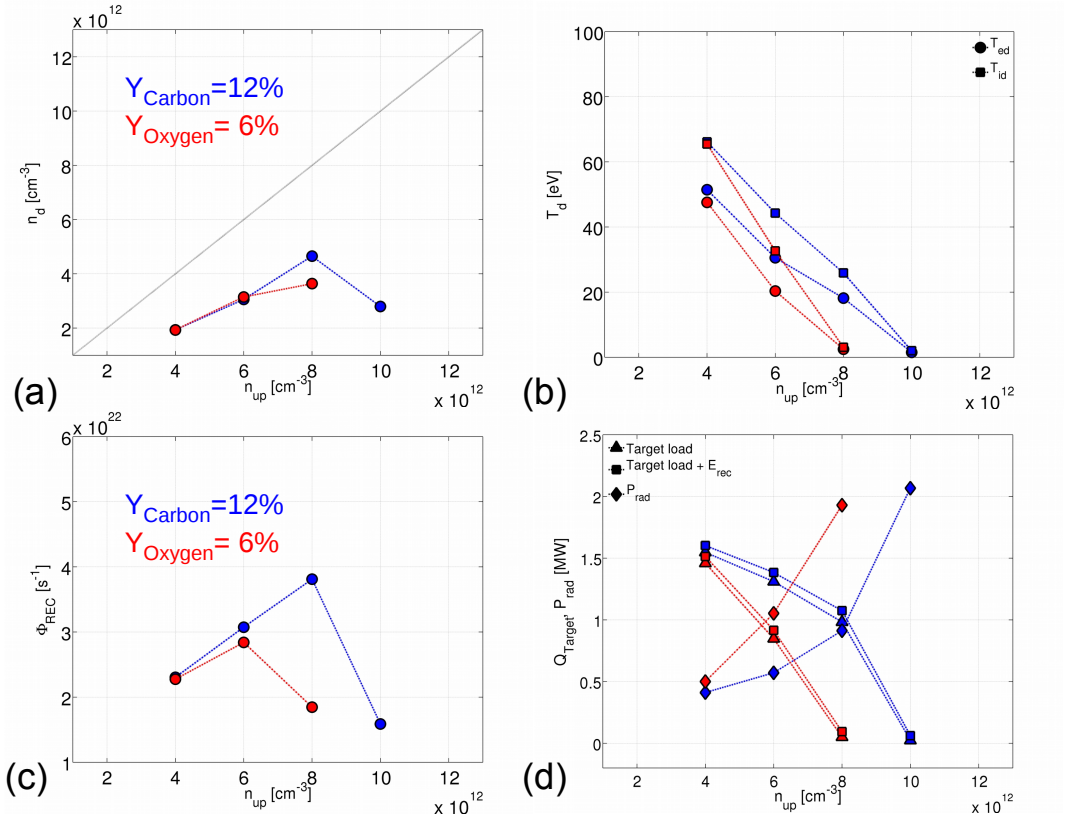

Figure 3.49 Density scan for assumption of Y_C =12% and Y_O =6% corresponding to power loss fraction of 25% by these light impurities at low density. Similar to experimental observation MARFE limit would be crossed at higher densities.

The impact of these impurities on the recycling conditions and the up- as well as downstream conditions, are analyzed. The results are shown in figure 3.49 for carbon (blue) and oxygen (red). Here, in figure 3.49 (a), the relation of upstream to downstream density is shown. The relation between upstream density and downstream temperatures, recycling flux and target power loads are shown in figure 3.49 (b-d).

The downstream density shows roll-over and drop ones a critical power fraction is approached at which 50% of the input power is lost by radiation (compare figure 3.49(d)) and the particle source is reduced near the target. This is related to the drop in reycling flux shown in (figure 3.49(c)). The

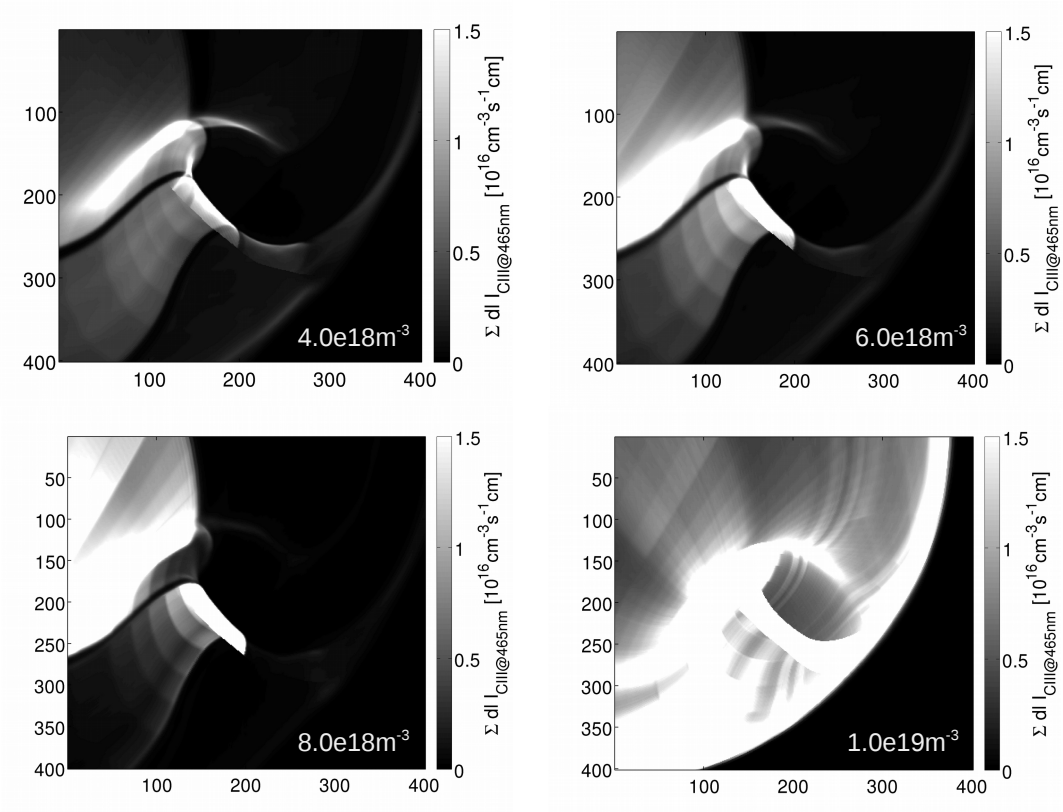

Figure 3.50 CIII (465.01nm) modeled for different densities - at the highest density level considered, the power balance shows a radiative collapse connected to the inward moving of the radiation front.

target heat loads Q_{Target} almost vanish when P_{rad} approaches 2 MW for $n_{LCFS} = 8 \cdot 10^{18}$ m^{-3} in case of oxygen and $n_{LCFS} = 1.0 \cdot 10^{19}$ m^{-3} in case of carbon.

This simple approximation of radiative density limits in a self-consistent manner based base on fixed sputtering yields inferred based on experimental $P_{rad,tot}$ indicates, that in principal power detachment, MARFE formation and collapse could occur due to light edge radiators only, but would require relatively high erosion yields. A recent material analysis also revealed traces of Copper, and Sulfur deposited on the limiter [107]. The role of the medium and high Z intrinsic

radiators is beyond the scope of this study but is anticipated to be necessary for a quantitative match to experiments.

3.2.4.2 Edge cooling by active gas injection

The power balance and radiation distribution for actively injected gas species are studied in the following. Seeding of nitrogen and neon is discussed based on assumptions estimated from experimental data that are shown below (for seeding location consider figure 3.32). The idea is to study the dependence of cooling on the gas species. First, nitrogen and neon have different cooling potentials L_Z (compare figure 1.2). Second, they have different recycling properties. Both aspects will determine the radial position of the edge radiation layer and thereby the radial location of the effective energy sink.

A typical density scenario with an edge density of $n_{LCFS} = 4 \cdot 10^{18}$ m^{-3}, heating power of P=2 MW is considered. The anomalous perpendicular transport for particles is set to $D_\perp = 0.5$m^{2}s^{-1} and for energy a typical relation of $\chi_{\perp,e,i} = 3D_\perp$ is used. The impact of intrinsic and seeded impurities is discussed with respect to their distribution of radiated power and their impact on SOL electron temperatures.

In the following carbon is assumed to be the main intrinsic edge radiator for simplicity. Fractional power losses of $f_{rad} = 25\%$ (0.5 MW) are set as boundary conditions treating the limiter as the primary source for both impurity species according to the discussion above. The calculations for a reference plasma without impurity seeding and with intrinsic impurity radiation yield a carbon impurity fluxes of Γ_C =2.83$\cdot 10^{21}$s^{-1}.

For nitrogen seeding experiments two cases are considered. In the first case, N is injected at through the He beam gas box valve, setting $f_{rad,N} = 40\%$ (0.8 MW), neglecting any other impurities and assuming absorption once nitrogen hits the wall/limiter due to its low recycling properties. The required flux is found to be Γ_N=6.45$\cdot 10^{21}$s^{-1}. In the second case, C background

is set as discussed previously and nitrogen is injected in an amount to account for another 25% of additional power losses, such that total loss by intrinsic C and seeded N add up to $f_{rad} = 50\%$ (1 MW). The carbon and nitrogen fluxes turn out to be Γ_C=2.59·10^{21}s^{-1} and Γ_N=3.89·10^{21}s^{-1}.

The approach is similar for neon but extended by one case. First, neon seeding from the point source is assumed with $f_{rad,Ne} = 40\%$ (0.8 MW) resulting in a flux of Γ_{Ne}=2.63·10^{21}s^{-1}. Second, neon is also sourced from the limiter with $f_{rad,Ne} = 40\%$ (0.8 MW) corresponding to recycling neon only. Here, a reduced flux of Γ_N=9.7·10^{20}s^{-1} is obtained which corresponds to 37% of the remotely seeded amount. In the third case, neon is seeded remotely with $f_{rad,Ne} = 40\%$ (0.8 MW) in combination with C sourced from the limiter with $f_{rad,C} = 25\%$ (0.5 MW) corresponding to a total loss fraction of $f_{rad,C+Ne} = 65\%$ similar to the experimental total losses presented later. The limiter carbon flux and the neon injection rates are in this case Γ_C=2.3·10^{21}s^{-1} and Γ_{Ne}=1.77·10^{21}s^{-1}. Each is slightly reduced compared to above described individual treatments.

The results of these six cases, intrinsic C, N seeding, intrinsic C combined with N injection, Ne injection, Ne sourcing from the limiter and Ne sourcing from the limiter combined with C, are discussed based on the total radiated power P_{rad}, and electron temperatures T_e and shown in figure 3.51. The poloidally and toroidally averaged profiles of total radiation and temperature are shown for N in figure 3.51(a) and (c) and for the scenarios with Ne in figure 3.51(b) and (d). The reference cases with no impurities and with intrinsic carbon source are indicated by black dashed and solid lines, respectively.

The pure nitrogen seeding case (figure 3.51(a), blue) shows peaking of P_{rad} mostly within the near SOL. In the case of combining N and C, the total radiation maximum shifts to the LCFS (figure 3.51(a), red). The T_e profiles show a steeper decay if nitrogen radiates deeper in the SOL (figure 3.51(c), blue). That is assumed to be mostly caused due to the position of the impurity gas source, which is located 12 cm behind the LCFS, causing 56% of the radiation losses to occur within the SOL. The combination of carbon sourced from limiter and nitrogen seeded from the

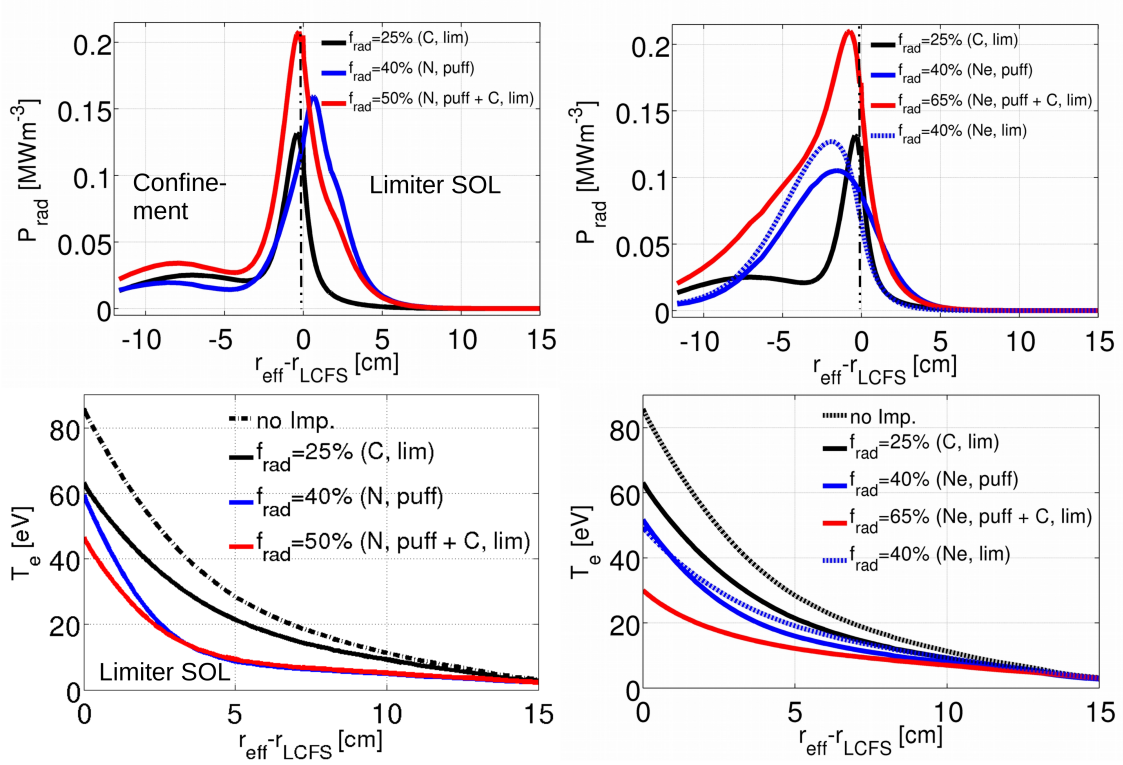

Figure 3.51 Comparison of Nitrogen vs Neon seeding vs intrinsic Carbon radiation. Nitrogen is puffed only, for Neon both puffing and limiter sourcing is compared.

divertor causes a more uniform cooling in near and far SOL (figure 3.51(c), red). This is caused by power losses within the confinement domain, whereas the SOL accounts for 35.6% of the total losses. In case of pure N seeding the T_e drop at the LCFS is only 30% and reaches 40% deeper within the SOL. The position of effective energy sink can be seen in the temperature profiles by comparing the decay of black, blue and red lines respectively (figure 3.51(c)). This shows that the nitrogen alone wouldn't be an effective means for cooling the near SOL without intrinsic radiators, which shift the $P_{rad,C+N}$ further inwards.

The $P_{rad,Ne}$ established by neon seeding from the divertor valve is shown in figure 3.51(b) as solid blue line. The peak maximum and main power losses are located within the confinement, with 21.6% of SOL power losses in contrast to the corresponding N seeding scenario. The distributions

for Ne sourced from the limiters are shown as blue dashed lines for P_{rad} and T_e in figure 3.51(b) and (d). Neon sourced from the limiters shows a shift of the power sink deeper into the confinement, while the SOL losses are only 8.3%. However, the results show that the impurity source location of neon has an only small impact on the cooling effect on edge temperature (figure 3.51(d) solid blue line vs. dashed blue line). This indicates that neon is mostly determined by its cooling potential L_Z, that generally has maxima at higher temperatures within the LCFS. The profiles for the combination of Ne seeding and carbon sourced from the limiter are shown in red in the right plots in figure 3.51(b) and (d). The SOL power loss fraction is now 14.7%, and the maximum is shifted slightly outwards compared to the case with neon only. The effective energy sink is still located within the confinement domain, and the temperature reduction is homogeneous. The temperature drops by almost 55 eV from 85 eV (case without impurities, dashed black line) to 30 eV (red).

In the modeling, they tend to be one order of magnitude higher. The lowest flux is obtained for neon sourced from the limiter idealizing its recycling properties.

The cooling potential of the respective impurity determines the effective radial location of P_{rad}. It is a function of T_e. The P_{rad} maxima of Ne are shifted further inwards compared to C and N because it radiates at a higher T_e (compare figure 1.2). Second, if one combines different impurities, such as C and N or C and Ne, they define new effective cooling potentials different from the individual ones. The results above indicate, e.g., a reduction of individual impurity fluxes in case of combined, still reaching the same radiative power fractions. The combination of their nonlinear cooling potentials may make them more effective and cause more homogeneous inward shifted radiation. Contributions of other impurities neglected in this modeling may further move the radiation further inwards. Furthermore, the modeling indicates, that the location and recycling properties are of vital importance for the cooling efficiency. Nitrogen only released into the far SOL with zero recycling has a lower effect on temperatures around the LCFS and is more efficient

deeper in the SOL. Impurities sourced from the limiter are always more efficient and cause more homogeneous SOL cooling. The recycling and source location of the impurities, therefore, matter for the radial radiation distribution as well. In addition to recycling, self-sputtering may add uncertainty not yet implemented in the 3D model.

Experimental data from the Bolometer system are shown for comparison with the numerical modeling. The distribution of the experimentally observed total radiation obtained by Bolometer is shown in figure 3.52.

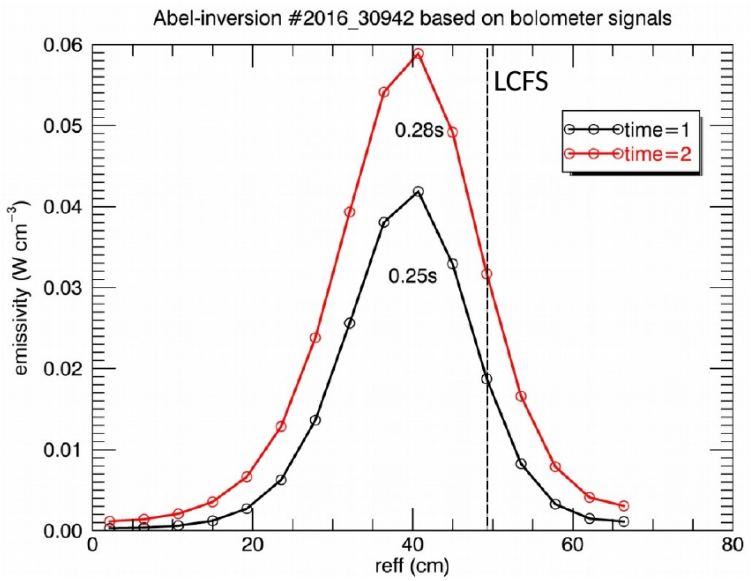

Figure 3.52 Radiation profile from Bolometer measurement. Black curve: radiation profile before N_2 injection. Red curve: radiation profile with additional radiation fraction due to N_2 seeding. The dashed line marks the position of the LCFS [15].

Dedicated experiments were performed to study the general features with active gas injection for power dissipation in more detail. A sequence of systematic discharges was performed for nitrogen and neon. Several nitrogen seeding experiments were successful in the sense that edge cooling could be achieved while the discharge could be maintained. In contrast, neon seeding caused almost every time immediate collapse of the discharge.

A first comparison of modeled radiative edge cooling and experimental results obtained by the various edge and core plasma diagnostics was reported in [14] and [15]. As one extracted highlight from these experiments, the increase of radiated power P_{rad} and the drop in electron temperature T_e measured by Bolometer and Limiter Langmuir probes is shown in figure 3.53 taken from [15].

A clear correlation between the nitrogen injection peaks and the radiation maxima and temperature minima is observed. In addition to the radiation response in the SOL, an even stronger radiation increase is observed in the total power losses dominated by radiation within the LCFS. This is partly in contrast to the predictions and assumptions made so far, which instead showed radiation profiles peaking at the LCFS with dominating radiation fraction within the SOL (figure 3.44).

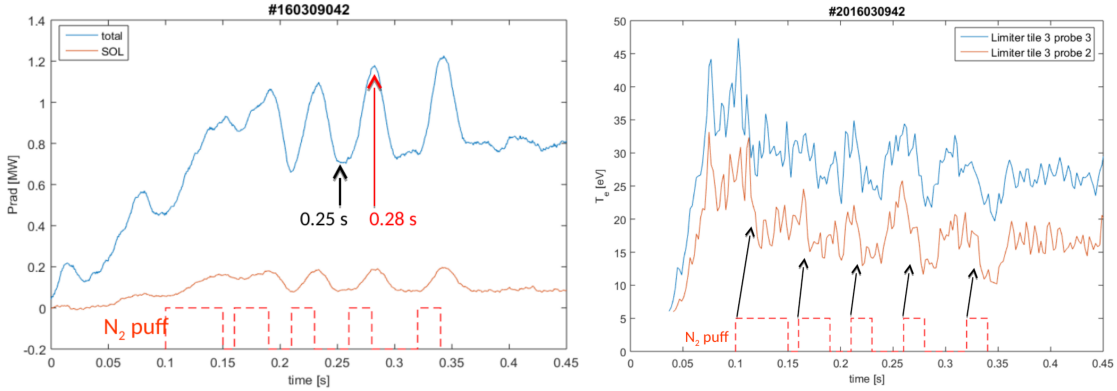

Figure 3.53 Experimental measured correlation between pulsed N_2 injection and response of total radiation P_{rad} (left) and electron temperature T_e (right) [15].

In conclusion, the results provide some general insights within a set of boundary conditions chosen and assumptions concerning the ideal geometry of the problem. In comparison to the experiment one main deviation is found to be the levels of impurity fluxes. Those are in case of seeding well defined. In the modeling, they tend to be one order of magnitude higher. The lowest flux is obtained for neon sourced from the limiter idealizing its recycling properties. Fluxes are lower in the experiment, and radiative power distributions have their maxima 10cm deeper within

the LCFS compared to modeling. The modeling already provides hints for the potential reason for shifts of the radiation peak position.

In the experiment, impurity injection but also general wall out gassing changed the local and global densities dynamically. In particular local density changes may enhance intrinsic impurity sourcing and radiation as well because of enhanced chemical sputtering. Impurities can also cause enhanced sputtering once injected. Mainly, a better resolution of edge impurity content is required before further benchmarking and refinement of the 3D modeling can be performed.

3.2.4.3 Impact of intrinsic cooling on heat loads

The ultimate goal of this study is to qualify impurity seeding for energy dissipation in the plasma edge to reduce surface heat fluxes. The studies discussed before clearly show the interplay of intrinsic and actively injected impurities. In this section, the impact of the various impurity species discussed before on the limiter heat fluxes is investigated.

To examine the impact of carbon erosion on the limiter heat loads, only spatially fixed transport coefficients ($D_\perp = 1.0$ m^{2}s^{-1}) are used. This is performed as a first step as the exact conditions in the experiment are unknown, and the analysis above has shown that impurity transport and the radiation distribution in the SOL and the vicinity of the LCFS is barely affected by the changes of the core transport conditions. In figure 3.54 (left) the 2-D heat flux deposition patterns are shown for the case of pure hydrogen and for cases including impurities at P_{in}=4 MW and n_{LCFS} =7·10^{18} m^{-3}. Comparing the two cases, with and without the effects of eroded carbon show only marginal changes in the 2-D profiles. The corresponding 1-D profiles (blue and cyan) in figure 3.54(right) deviate only slightly in their maximum peak levels. Comparing the surface deposition decay lengths λ_{sf} inferred and the maximum peak loads P_{peak} in the heat flux characteristics in figure 3.56 (blue and green symbols) confirms that the contribution of intrinsic carbon impurities

to heat flux mitigation causes reductions of less than 10% between the peak load maxima while changes of λ_{sf} are almost undetectable.

The modeling results presented within these boundary conditions (carbon yield of 0.02) show that carbon sputtered from the graphite limiters has only a small capacity for self-protection regarding power dissipation. According to these predictive results, the sputtered carbon level in the parameter region assessed does not provide a sufficient energy sink to cause plasma termination before possible heavier impurities sputtered from the main vessel wall become relevant [93]. Furthermore, the results clearly show that the edge impurity transport behavior is, within the assumptions of this study, almost independent of the core transport conditions. The results discussed here are published in and taken from [7].

Experience gained here is valuable also for addressing the transport of intrinsic carbon impurities in the proposed island divertor scenarios. However, in the latter case, the situation is different in the sense that the sputtering occurs remotely in the divertor region. The LCFS will here not directly touch the impurity source region. The separatrix is further away from the impurity source region determined by the widths of the magnetic islands. At the same time, the higher densities and higher fluxes to PFCs will cause much higher levels of erosion of intrinsic carbon.

An example of the 2-D limiter heat load distributions including the mitigation effects of nitrogen and neon impurities (and simultaneous carbon erosion) is shown in figure 3.54 (left), and as 1-D surface scan in figure 3.54 (right, green and magenta) for n_{LCFS}=$7 \cdot 10^{18}$ m^{-3}. The increase of impurity radiation by additional seeding results in a strong mitigation of the peak maxima almost in correlation to the power loss fraction of a factor of $\approx$0.4.

The density dependence of the impurity fluxes achieved by nitrogen and neon puffing is shown in figure 3.55 (left). The cyan triangles represent the nitrogen flux, and the magenta circles correspond to the neon flux. The simultaneous carbon fluxes during nitrogen and neon seeding are given

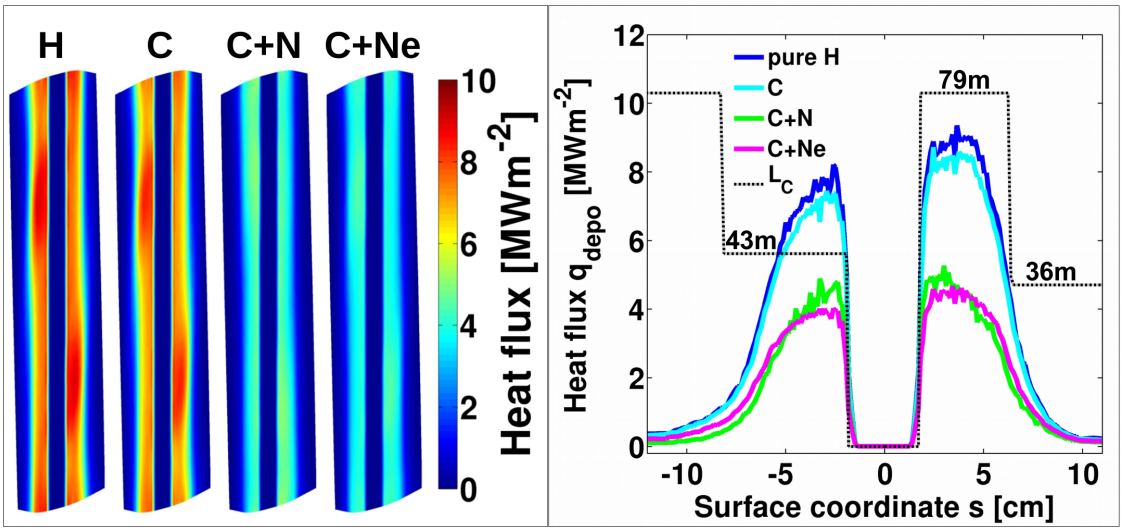

Figure 3.54 Left: 2-D limiter heat loads for $n_{LCFS} = 7 \cdot 10^{19}$ m^{-3}, P_{in} =4 MW for pure hydrogen (H), including power losses due to sputtered carbon (C), additional nitrogen seeding (C+N) and additional neon seeding (C+Ne). Right: the resulting 1-D surface profiles for pure hydrogen and diluted plasmas at $Z = -0.2m$ (compare mark in figure 3.21) [7].

by black triangles and circles, respectively. For comparison, the carbon fluxes for scenarios without seeding are shown as grey squares. During seeding with neon or nitrogen the carbon flux drops by ≈11-12%. The resulting total impurity radiation is shown in figure 3.55 (right) consists of the prescribed 1.6 MW losses (dashed blue line) by impurity seeding and additional radiative losses from sputtered intrinsic carbon which scales with the limiter recycling fluxes of the considered density scenarios.

The results in figure 3.55 (left) show unrealistically high seeding rates required for low density plasmas to achieve the 1.6 MW radiation losses so that the seeded impurity would dominate over the main hydrogen plasma species (e.g. $I_N \approx 100 \cdot I_C \approx 2.8 \cdot 10^{20}$s^{-1} for n_{LCFS}=$1 \cdot 10^{18}$ m^{-3}). Radiative edge cooling with significant power losses appears not to be feasible in the lowest density scenario taken into account here and violates the validity of the trace impurity model applied. With rising n_{LCFS}, the nitrogen fluxes reach the same strength as those from intrinsic carbon.

Even lower seeding rates are needed for neon. For example one finds for n_{LCFS}=1.9 $\cdot$ 10^{19} m^{-3}, $I_N \approx I_C \approx 3.2 \cdot 10^{21}\mathrm{s}^{-1}$ and $I_{Ne} \approx 0.3 \cdot I_C \approx 10^{21}\mathrm{s}^{-1}$. This means that in this relevant regime only moderate amounts of nitrogen and neon are needed for achieving significant radiative power losses.

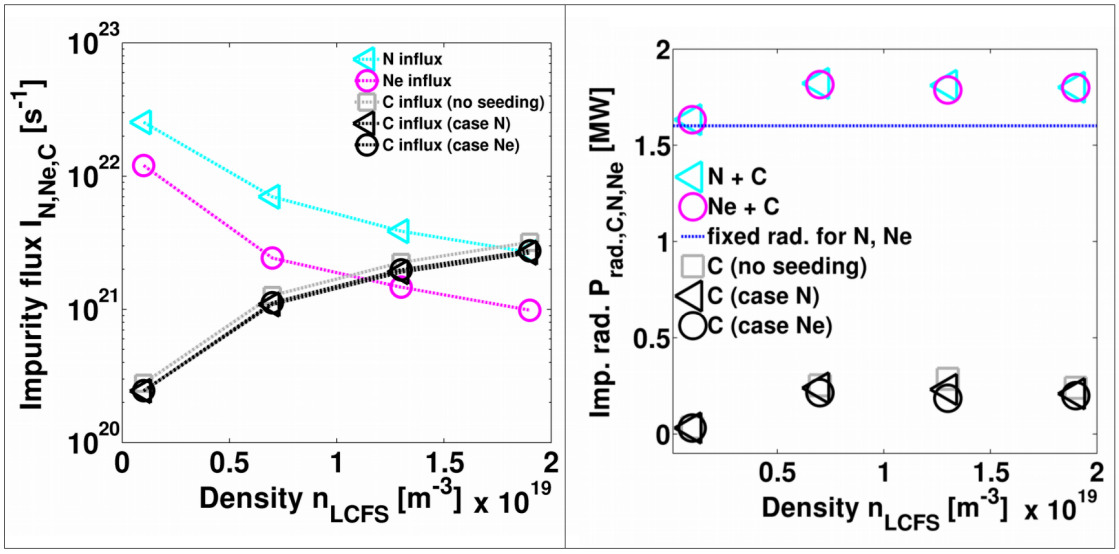

Figure 3.55 Left: impurity influxes for nitrogen (cyan triangles) and simultaneously eroded carbon (black triangles), neon (magenta circles) and simultaneously eroded carbon (black circles) and eroded carbon without seeding (grey squares) for different n_{LCFS}. Right: total impurity radiation caused by the fluxes shown on the left for seeded nitrogen and eroded carbon (cyan triangles), neon and eroded carbon (magenta circles) and impurity losses in case of eroded carbon without seeding (grey squares) and the respective radiation fractions due to carbon erosion only in case of seeded nitrogen (black triangles) and neon (black circles). The blue dotted line marks the fixed radiation fraction of the seeded species [7].

In figure 3.56 the heat flux characteristics are shown for all density scenarios at an input power of 4 MW with and without eroded and seeded impurities. The peak heat maxima of the 1-D surface profiles show for left and right peaks a substantial drop of 40-50% in case of lower densities once nitrogen or neon are injected (figure 3.56, left). However, with increasing density, the peak heat maxima are less affected by the power dissipation through impurities. The local heat flux decays λ_{sf} shown in figure 3.56 (right) are affected even less dramatically by the power dissipation.

Despite the discrete distribution of local gas sources and the helical localization of radiative power losses (figure 3.33b, c) a homogeneously reduced power load is achieved.

Neon is a more effective radiator compared to nitrogen as it provides more energy levels and achieves the same integrated radiation with less concentration such that $I_{Ne} \approx 0.3 \cdot I_N$. However, it is shown in figure 3.44d that neon radiation also expands more in-depth into the confinement region where a change of transport conditions, as demonstrated above for carbon, might also change the SOL radiation fraction $P_{rad,Ne}(r < r_{LCFS})$ significantly. In contrast, nitrogen radiates for the higher densities predominantly in the SOL and the vicinity of the LCFS (figure 3.44c). Thus, the arguments made for carbon in the previous section regarding the uncertainties in core transport should hold for nitrogen in no small extent. A more massive amount of core nitrogen radiation occurs for the lowest density case (figure 3.44c), but the seeding flux, in this case, reaches the order of magnitude of the recycling flux of the background hydrogen. As discussed above such scenarios with high impurity content are not desired.

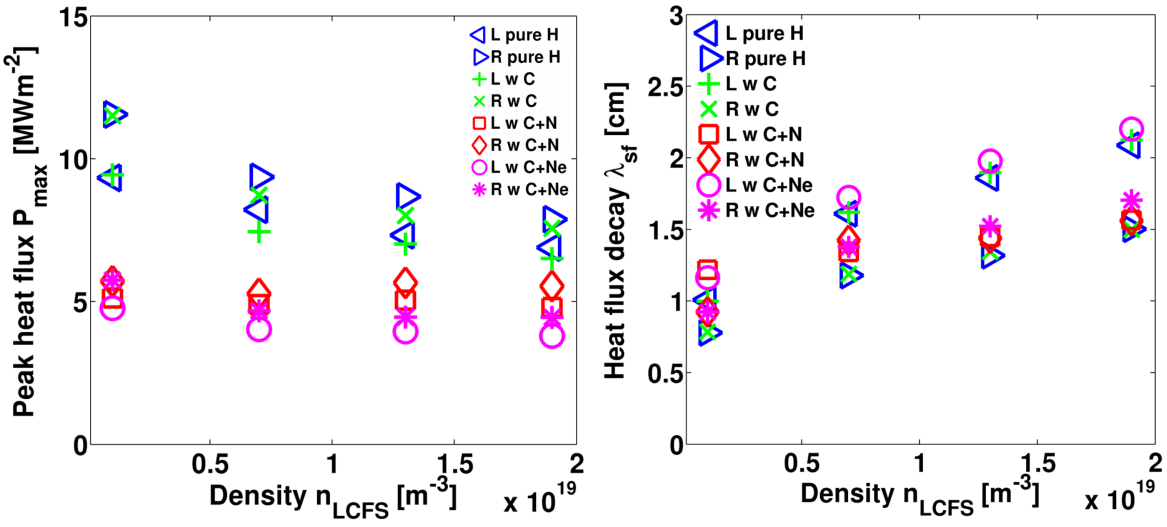

Figure 3.56 Left: Peak heat fluxes P_{peak} and right: limiter surface deposition decay lengths λ_{sf} for different n_{LCFS} for hydrogen plasmas (blue triangles), including intrinsic sputtered carbon impurities (green +- and x-symbols), additional seeding of nitrogen (red diamonds and squares) and neon (magenta circles and stars) [7].

For the proposed island divertor studies the approach here is valuable. Since one has currently to deal with a strong carbon impurity background, the question remains in how far one has the flexibility to achieve detachment by additional gas injection. The total radiation sets a density limit. It has to be investigated if scenarios with sufficiently low background carbon radiation exist allowing for introducing external edge radiators to induce and control the detached divertor operation.

Besides, the modeling data from the scenarios discussed in the previous section are considered again. The reference scenario is a hydrogen plasma with $n_{LCFS} = 4 \cdot 10$ m^{-3} and $P_{in} = 2$ MW, $D_\perp = 0.5$ m^{2}s^{-1}. This reference scenario is compared with cases with C and O sourced from the limiter with $f_{rad,C} = f_{rad,O} = 25\%$, with N injected from the gas box with $f_{rad,N} = 40\%$, with Ne injected from the gas box with $f_{rad,Ne} = 40\%$ and with Ne sourced from the limiter with $f_{rad,Ne} = 40\%$. The resulting changes of downstream electron temperatures T_e, heat fluxes $q_\parallel$ and particle fluxes $\Gamma_\parallel$ and their decay lengths λ_{T_e}, $\lambda_{q_\parallel}$ and $\lambda_{\Gamma_\parallel}$, respectively are shown in figure 3.57(a) and (b). The peak particle fluxes, represented by triangles in figure 3.57(a), show only a drop of 10% or 15% in response to intrinsic impurity radiation or impurity radiation from seeded impurities. Temperatures and heat fluxes (squares and pyramids) show a much stronger drop and reduce by 25% in case of C and O, by 35% in case of N and by 40-45% in case of seeded and sourced Ne. Nitrogen appears to be less effective for cooling. It cools the far SOL and is, therefore, less effective in reducing the power and entering the SOL which determines the strength of the parallel heat fluxes on the main wetted area.

The most robust cooling is achieved by neon sourced from the limiter (case 6 in figure 3.57(a)). In this case, the power is significantly reduced at the LCFS as discussed before.

The decay lengths are shown in figure 3.57(a) remain mostly constant. In case of no recycling and seeding of Ne and N in the far SOL, they show a clear drop. The temperature decay length drops in case of N seeding even bi 50%. A smaller drop is noticed in the case of $\lambda_{q_\parallel}$ with N

seeding. The cooling of the far SOL establishes a steeper decay of the radial temperature and heat flux profiles. The temperature at the LCFS is less affected; therefore a steeper gradient establishes. A slight increase of λ_{T_e} is noticed for Ne sourced from the limiter (figure 3.57(b), case 6). Here, the confinement edge is cooled, and power is removed within the LCFS before it reaches the SOL. Neon causes the most substantial drop in heat and particle fluxes and widening of the energy transport channel in case of sourcing from the limiter. However, is mostly achieved by undesired power losses within the confinement. Nitrogen on the other tends to cool the rear SOL and steepens the radial temperature gradient.

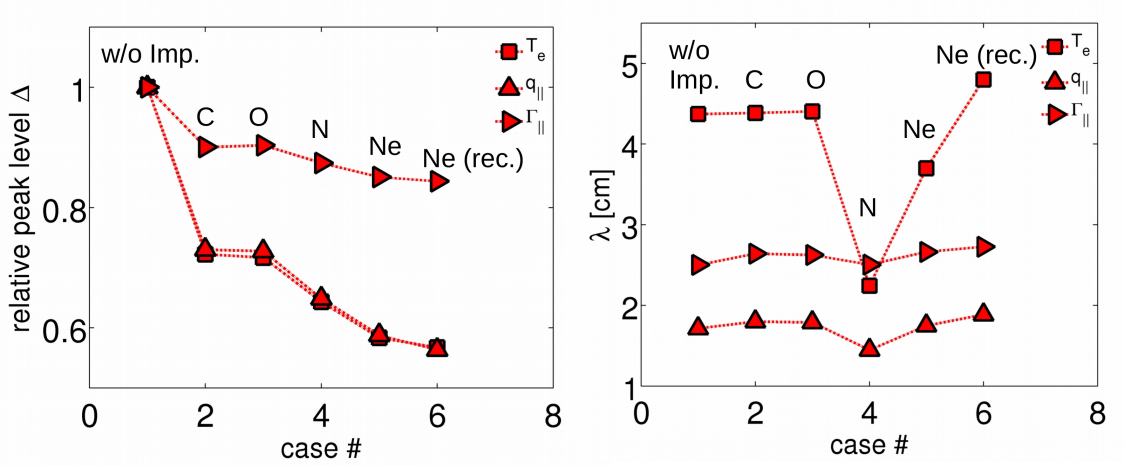

Figure 3.57 Relative changes of peak levels (left) and decay lengths (right) of downstream electron temperature T_e, heat flux $q_{\parallel}$ and particle flux $\Gamma_{\parallel}$ in response to power dissipation by impurity line emission. Case 1-6 represent scenario with $n_{LCFS} = 4 \cdot 10$ m^{-3} and $P_{in} = 2$ MW with (1) no impurities, (2) Carbon sputtering $f_{rad,C} = 25\%$, (3) Oxygen outgassing $f_{rad,O} = 25\%$, (4) nitrogen injection $f_{rad,N} = 40\%$, (5) neon injection $f_{rad,Ne} = 40\%$, (6) neon recycling $f_{rad,N} = 40\%$.

An analysis of the experimental results also showed evidence for power flux mitigation. Results for limiter heat fluxes q_{depo} are shown in figure 3.58 (a) and for the measured carbon and nitrogen line emission in figure 3.58 (b). The heat fluxes in figure 3.58 (a) are measured with the infrared cameras and integrated over tile 2, 5 and 8 of the limiter in module 5. The corresponding data

for CIII(465 nm) and NII (500.5 nm) are shown in figure 3.58 (b). The stars and circles represent discharges without and with N_2 puff, respectively. The discharge-to-discharge evolution shows an apparent reduction of heat fluxes in response to N_2 seeding. After helium cleaning, the heat fluxes are as high as before the sequence of the nitrogen puffs. This suggests a low recycling coefficient and surface dilution of the PFC material by nitrogen leading either to N-containing layers or nitride formation. He-cleaning discharges were performed in between the experimental sequence and led to the removal of nitrogen and recovery of heat fluxes to levels before seeding.

The discharge evolution of CIII (465 nm) and NII (500.5 nm) for a series of N seeded shots followed by some shots without N injection. A high level of N has been observed in consecutive discharges after the N seeded shots until He cleaning discharges have been performed. It is shown in figure 3.58 (b) that C radiation reduces while N radiation increases during the nitrogen injection. This suggests a reduction of C sputtering owing to the lower energy of the impinging ions due to plasma cooling and dilution of the layer surface with impinging nitrogen. C line emission and related C sputtering increase again when the active seeding is stopped as indicated by the enhancement in the CIII line emission.

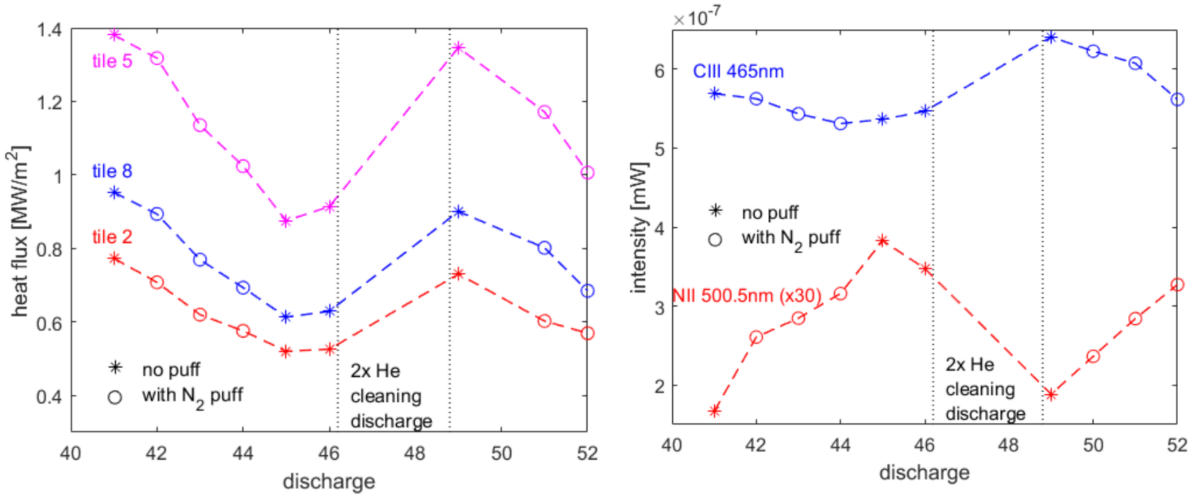

Figure 3.58 Left: heat fluxes measured during N seeding discharges. Right: NII and CIII line emission measured

3.3 Summary for limiter plasmas

The analysis of the limiter edge geometry, the transport therein and the coupling to impurity radiation and the capacity to actively control surface heat fluxes has delivered a systematic overview of these aspects. In the following a brief survey of the main findings is presented:

(1) The W7-X limiter SOL consists of three types of helical magnetic flux bundles of lengths L_C

It was shown that the startup configuration at W7-X features a relatively simple edge topology consisting out of three different length scales regarding the SOL channel structure. The plasma edge transport such as pressure and flow show a strong correlation between plasma transport and magnetic lengths scale L_C. The clear flux tube geometry, and in particular the average target-to-target connection lengths of $L_C \approx$50m is ideal to test simple SOL models from standard tokamak literature and control effects of the 3D structure by cross-fueling ($D_\perp, \chi_\perp$).

(2) The plasma transport within the SOL flux tubes can be described with the sheath limited simple SOL model.

Despite its inherently 3D geometry, the plasma transport within the flux tube is best approximated by the simple SOL due to the low collisionality regime established in most plasmas with $\nu^*_{SOL,e} \leq 10$. Deviations occur, e.g., above $n_{LCFS} > 6 \cdot 10^{18}$ m^{-3}, $P = 2$ MW, $D_\perp = 0.5$ m^{2}s^{-1}, $\chi_{\perp,i,e} = 3D_\perp$.

(3) Limiter heat and particle flux pattern are correlated to connection lengths topology (L_C).

It is demonstrated that the SOL geometry determines the heat and particle load patterns. The long flux tubes receive more heat and particles across the SOL-confinement interface due to the longer parallel path lengths L_C. They obey a higher pressure than the shorter flux tubes and therefore drive stronger heat and particle flows. The maximum loads on the limiter targets occur in domains of the long connection lengths ($L_C = 79$m).

(4) Slight changes of the rotational transform for core confinement optimization may change the heat and particle load pattern significantly, but the general SOL transport characteristics may remain unaffected.

It is shown that the heat and particle load patterns change and shift according to the locations of the strike lines in response to the increase of rotational transform ι. The long flux tubes touch the limiter close to the midplane in the latter case, heat, and particle loads are shifted accordingly.

(5) The sensitivity of up- and downstream parameter based on various input parameter were investigated.

Scaling of up and downstream parameters is inferred based on simple SOL relations. Those are valid to a large extent under low collisionality conditions. Decay lengths show a scaling with L_C^{δ}, with $0.1 < \delta < 0.5$ Deviations are expected to arise generally from the 3D shape of the plasma. The short transport channels may be saturated in case of high anomalous transport coefficients or high upstream densities. In this case, the differences in the load patterns between domains with long and short L_C vanish. In case of high densities and higher collisionality, $\nabla_{\parallel} T_e \neq 0$ and may become significant.

(6) Fast parallel transport governs the SOL transport.

Due to the relatively short L_C, fast transport governs the SOL transport in the typical low collisionality plasmas.

(7) Carbon and oxygen are considered as main intrinsic radiators due to chemical erosion.

Carbon and oxygen are considered to be main intrinsic radiators with $f_{rad,C,O} = 25\%$ for low collisionality plasma. They are considered separately and both sourced from the limiters proportional to the limiter particle flux according to chemical erosion. The iterated yields for these amounts of

power losses are quite high ($Y_C = 12\%$, $Y_O = 6\%$). Fixing these yields and a stepwise increase of density results in a radiative instability around $n_{LCFS} \approx 8 \cdot 10^{18}$ m^{-3} and $n_{LCFS} \approx 1 \cdot 10^{19}$ m^{-3} for O and C, respectively.

(8) Poor impurity screening: a high fraction of power losses from intrinsic and extrinsic impurities occurs within LCFS.

It is shown, that limiter plasmas feature a bad screening of the confinement against impurities. In particular, impurities recycled or sourced on the limiter are mostly released into the confinement and cause substantial power losses. However, efficient edge cooling and reduction of limiter heat loads require impurities to be concentrated at the LCFS.

(9) Neon is an efficient upstream radiator, Nitrogen cools the rear SOL.

It is shown that Neon radiates at higher temperatures and has a high recycling coefficient. This allows for homogeneous cooling, but the power losses occur mostly within the LCFS. Nitrogen is shown to radiate rather locally and deeper in the SOL.

(10) Enhanced impurity radiation can reduce heat and particle fluxes.

The downstream heat and particle fluxes can be reduced if good upstream radiators are in use. Dissipation of energy can ideally result in a reduction of the load maxima and an increase of the heat flux channel width λ_q. This is demonstrated clearly with Neon.

(11) Experiment and modeling show good agreement concerning heat flux patterns and fundamental transport characteristics.

Direct comparisons with experimental measurements, in particular, IR camera measurements, Bolometer and Langmuir probes allowed to validate the discussed trends qualitatively. Combination of the modeling database with the 3D model enables synthetic reconstruction of the signals and

then the propagation of the local measurements into a 3D information. Initial comparisons showed a quite good qualitative agreement of measured and modeled heat load distributions. Temperature measurements confirmed effects of radiation cooling. Further analysis is ongoing.

Chapter 4

Analysis of island divertor plasmas

4.1 Characterization of heat and particle fluxes in island divertor configurations

4.1.1 Link between divertor and limiter configurations

The central aspects of the limiter geometry were explored previously to asses the general properties of the 3D plasma edge transport and in particular the effects of impurities which is of relevance for radiative edge cooling at W7-X. In this chapter, the island divertor is analyzed along the same line, but the depth of analysis in each step is less fundamental. Instead, it is aspired to transfer the key findings on (a) magnetic edge geometry (b) main plasma transport (c) limiter and divertor target heat and particle deposition and (d) radiative edge cooling by intrinsic and seeded impurities. This analysis stimulated and guided by the limiter results has enabled to design specific experiments, and initial results are discussed at the end to link this numerical study to the actual experimental exploration which is commencing as this thesis is being written.

4.1.2 Geometric properties of 5/5 island divertor scenarios

The W7-X island divertor configurations are geometrically fundamentally different from the limiter configurations. A Poincaré plot of the vacuum magnetic field line structure of the 'standard divertor configuration' (SDC) at a toroidal cross section ($\phi = 12.3°$) is shown in figure 4.1(a). The $5/5$ islands are present in the boundary and intersect with the divertor plates (solid black lines).

The resulting SOL is defined by the open field lines. These field lines are shown in the target-to-target connection lengths (L_C) distributions in figure 4.1(b) in a logarithmic representation. The separatrix, which distinguishes the island domain from the closed flux surface domain of the plasma core, consists of open field lines of lengths of lengths $O(1km)$ (yellow→white). The island consists of L_C $O(100m)$ (orange). In the far SOL, deep in the divertor shadows and near the pumping gaps (remote volume beyond the island X-points) the connection lengths are $O(1m)$ – $O(10m)$ (black→blue). This outer domain is regarding the length scale similar to the initial limiter configuration or typical tokamak configurations.

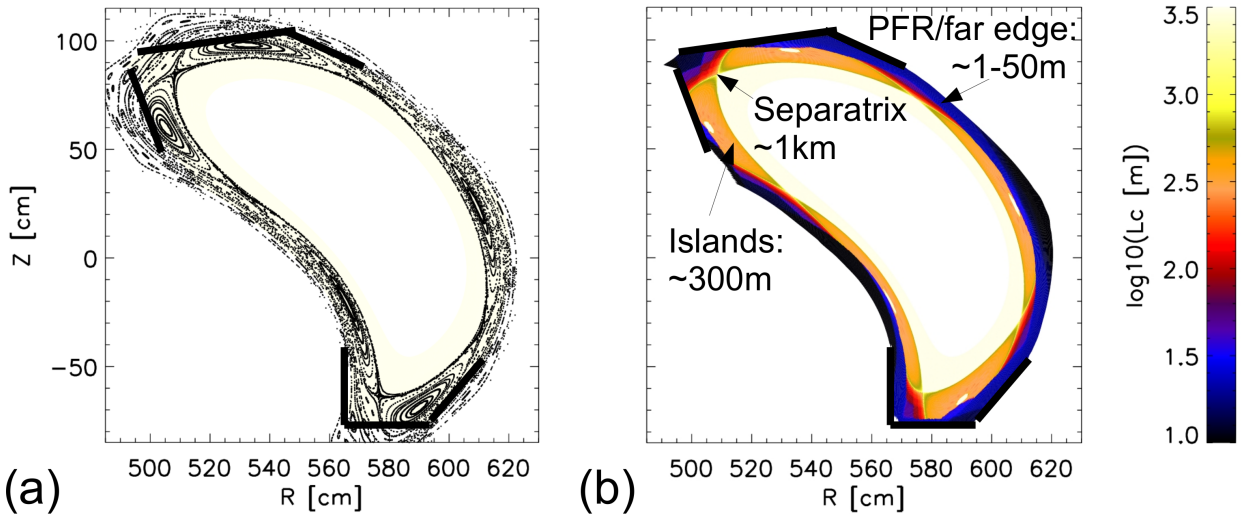

Figure 4.1 The standard divertor configuration (SDC). (a) Poincaré plot of the vacuum field at $\phi_{tor} = 12.3°$ cross section. (b) Target-to-target connection lengths plot at the same location.

Inside of the islands, a region exists in which the divertor target plates do not intersect the island flux surfaces. These regions are the O-points, and inside of these, infinite L_C (white) are found because the field lines never actually reach a target surface. In the initial limiter configuration, the averaged length of the parallel transport channels had a length of L_C ≈50m, which is similar to a tokamak SOL (without RMPs). In the island divertor this length scale, which defines the parallel loss channel due to the interaction with the parallel plasma gradients, is L_C ≈200m. During the

longer parallel path towards the targets cross-field transport can be more effective compared to the limiter case due to the longer path lengths on which radial diffusion can occur (e.g., $\lambda_n \propto \sqrt{(}L_C)$, see section 2.2.1). The island divertor obeys, in general, a larger perpendicular to parallel transport ratio for heat and particles.

A sketch of the main properties of the heat and particle transport is shown in figure 4.2. Ideally, heat and particles are sourced from the core domain and fuel the SOL across the separatrix as indicated by $\Gamma_\perp$ and $q_\perp$, respectively. Within the SOL, which mostly consists of the magnetic islands, heat and particles are guided within the fast parallel transport channels along open field lines towards the divertor targets, aka down-stream location. This is indicated by $\Gamma_\parallel$ and $q_\parallel$, respectively. However, during the relatively long parallel transport heat and particles may also perform further cross-field diffusion ($\Gamma_\perp$, $q_\perp$) within the SOL. In contrast to the previous (standard) limiter scenario, the effective perpendicular transport within the island SOL does also include a component from parallel transport in the radial direction. This parallel transport in radial direction occurs because the field lines orbit around the island O-point until they hit the target. In other words: the islands create an effective radial heat and particle loss channel by fast parallel transport.

When the particles eventually reach the divertor targets, they get recycled. This is indicated as Γ_{rec} in figure 4.2. The neutrals are released back into the SOL and define a particle source. Furthermore, erosion processes cause the release of impurities, which is indicated by Γ_{imp}. One notices that the island SOL width in figure 4.2 is locally ≈5-10 cm. Ideally, this domain will allow for good screening of impurities and efficient heat and particle exhaust. The five solid black lines beyond the downstream divertor target represent the versatile gas injection system. It is the same system used for impurity seeding during limiter scenarios. Although it is mounted at the same location, its meaning has changed concerning the magnetic SOL geometry. The impurities are injected through the divertor plates and thereby start at the downstream location. To perform

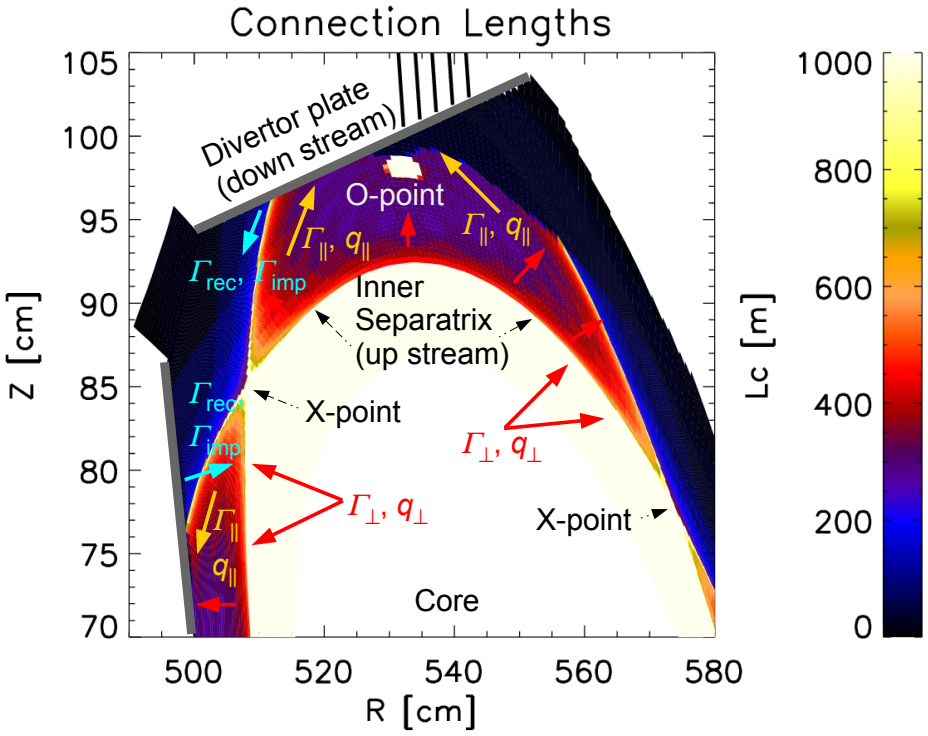

Figure 4.2 Sketch of heat and particle transport in the island divertor geometry.

upstream seeding, the neutral impurities would have to be released at the separatrix (ideally above the island O-point).

4.1.3 Radial transport within the divertor island

A significant change of the radial transport characteristics in the island divertor is expected when compared to the limiter scenario, because of the radial component of the parallel transport due to the internal shear of the magnetic islands. This drives effectively radial transport along open field lines in addition to the diffusive cross-field transport. In the situation of good flux surfaces in the previous limiter configuration, the radial transport was of purely diffusive nature. However, this magnetic jump step is effective for radial transport only in case the radial positions are connected

along field lines on a typical parallel gradient lengths scale ($\lambda_{\nabla_\parallel} \leq L_C$), because only with such a parallel gradient significant heat and particle transport can occur.

The radial distribution of plasma parameter within in the island is considered for one example shown in figure 4.3. A scenario close to initial experimental conditions with upstream density $n_{up} = 1 \cdot 10^{19}$ m^{-3} set near the separatrix, $P = 2.5$ MW and $D_\perp = 0.5$ m^{2}s^{-1} is considered. Radial profiles are sampled according to the five actual observation domains covered by the helium beam spectroscopy. This diagnostic resolved the outer half of the divertor island - from its O- towards the X-point - right in front of the divertor plate, and hence the according to observation can provide detailed insight into the radial transport across the island. These lines of sight (LoS) are labeled in the geometry plot in figure 4.3(a) as 'LoS1-5' according to the order of the injection tubes (5 being at the O-point). The 2D density and electron temperature distribution are shown in figure 4.3(b) and (c). Comparing figure 4.3(a) and (b) shows that the downstream density at the target peaks at the locations of the strike lines near the pumping gap. The temperature is higher at the strike lines as well.

The five radial profiles - starting at the divertor plate and going perpendicular inwards - of L_C, n_e and T_e according to 'LoS5-1' are plotted in figure 4.3(d-f). Although 'LoS4' (green) and 'LoS5' (magenta) cross the island O-point of very long to infinite L_C this has no significant effect on the profile shape of density and temperature for the transport conditions assumed. Estimation of density gradient lengths based on the simple SOL reveals: $\lambda_n = \sqrt{\frac{L_C D_\perp}{0.5cs}}$ ≈2.7 cm.

Temperature and density decay by one order of magnitude from the separatrix inward towards the divertor target plate. The decay is faster in the region of short L_C ($O(1-10m)$) and slower within the main island domain with $L_C \approx O(100m)$. The main island domain has a local width of w_i ≈6 cm. The cross-field profiles within the island are established through the whole set of perpendicular and parallel transport channels introduced in the previous section.

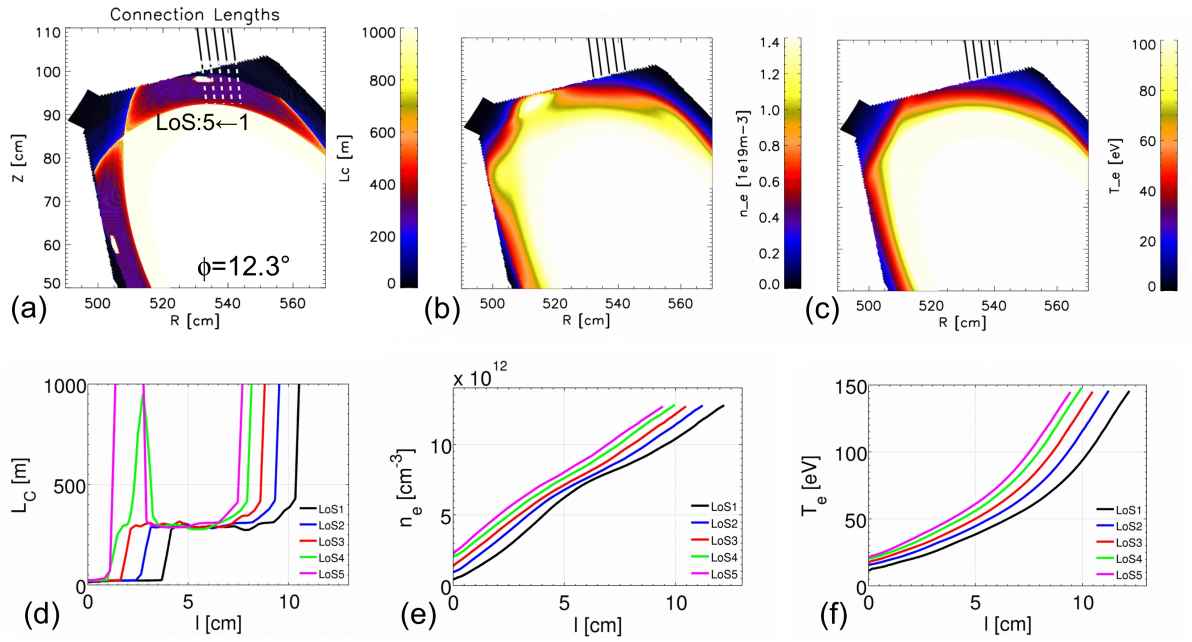

Figure 4.3 Island profiles accessible by He beam. (a) Lines of Sights (LoS) within the island gemoetry. (b) 2D n_e profile. (c) 2D T_e profile. (d) L_C-profiles along LoS. (e) n_e-profiles. (f) T_e-profiles

For particle and momentum transport one may estimate the parallel and perpendicular transport time scales as [6]

$$\tau_{\parallel} = \frac{L_{\parallel}}{V_{\parallel}} \approx \frac{\Delta x}{\Theta V_{\parallel}} \tag{4.1}$$

$$\tau_{\perp} = \frac{\Delta x^2}{D_{\perp}} \tag{4.2}$$

where $0.5L_C = L_{\parallel} = \Delta x \Theta^{-1}$, $\Theta \approx r_i \frac{d\iota}{dr}$, Δx is the radial width of the island and $V_{\parallel} = Mc_s$ is the parallel velocity. For W7-X standard island divertor configurations $\Theta \approx 0.001$. From this it follows that $\tau_{\parallel}/\tau_{\perp} = \frac{2D_{\perp}}{\Delta x \Theta V_{\parallel}}$. With $V_{\parallel} \approx c_s = 7 \cdot 10^4 - 1.2 \cdot 10^5 \mathrm{ms}^{-1}$ one obtains a ratio of 0.13-0.24. The parallel transport dominates in this regime and determines thereby the shape of the radial profiles.

The existence of parallel temperature gradients can be estimated based on the collisionality [4]:

$$\nu_e^* = \frac{10^{-16} n_{up} L}{T_{e,up}^2} > 15 \tag{4.3}$$

With the the T_e =80eV and $n_{up} = 10^{13}$ m^{-3} and $L = 150$m one obtains ν_e^* ≈23. This means that parallel gradients for electron heat transport exist within the main island domain and even more along the much longer separatrix flux tubes.

To identify the temperature regime, where parallel conductive heat flux dominates over the perpendicular one, the following relation is used[6, 4]:

$$T_e > \left(\frac{\chi_{\perp,e} n_e}{\Theta^2 \kappa_e} \right)^{\frac{2}{5}} \tag{4.4}$$

with $\kappa_e = 1.25 \cdot 10^{22}$(mseV$^{2.5}$). This requires $T_e > 17$eV and is satisfied in most of the island domain with the given input parameter $n_e = n_{up}$, Θ and $\chi_{\perp,e} = 3D_\perp = 1.5$ m^{2}s^{-1}.

This measurement in front of the divertor target plate is now compared to a similar assessment of the radial profiles at the position in the midplane of the device, 90 degrees away toroidally. This is also the location of a fast Langmuir probe system.

Profiles at this position were extracted for the same scenario at the probe location and shown in figure 4.4. The local island L_C and the fast probe path are sketched in figure 4.4(a). The connection lengths along the profile are shown in figure 4.4(b). Densities and electron and ion temperatures are shown in figure 4.4(c) and (d). The width of the main island domain along the profile path is w_i ≈4 cm due to compression of magnetic field structure. The fast probe covers similar domain as the 'LoS1' in case of the He beam. The profile shapes are similar but radially compressed - as expected due to the magnetic shaping, i.e., flux surface compression - in case of the fast probe. Due to internal island shear, a representation in magnetic coordinates is not possible at this point.

These profiles show that the main island domain geometry consists of mostly L_C ≈300m. The island O-point does not significantly change the local transport behavior which indicates that

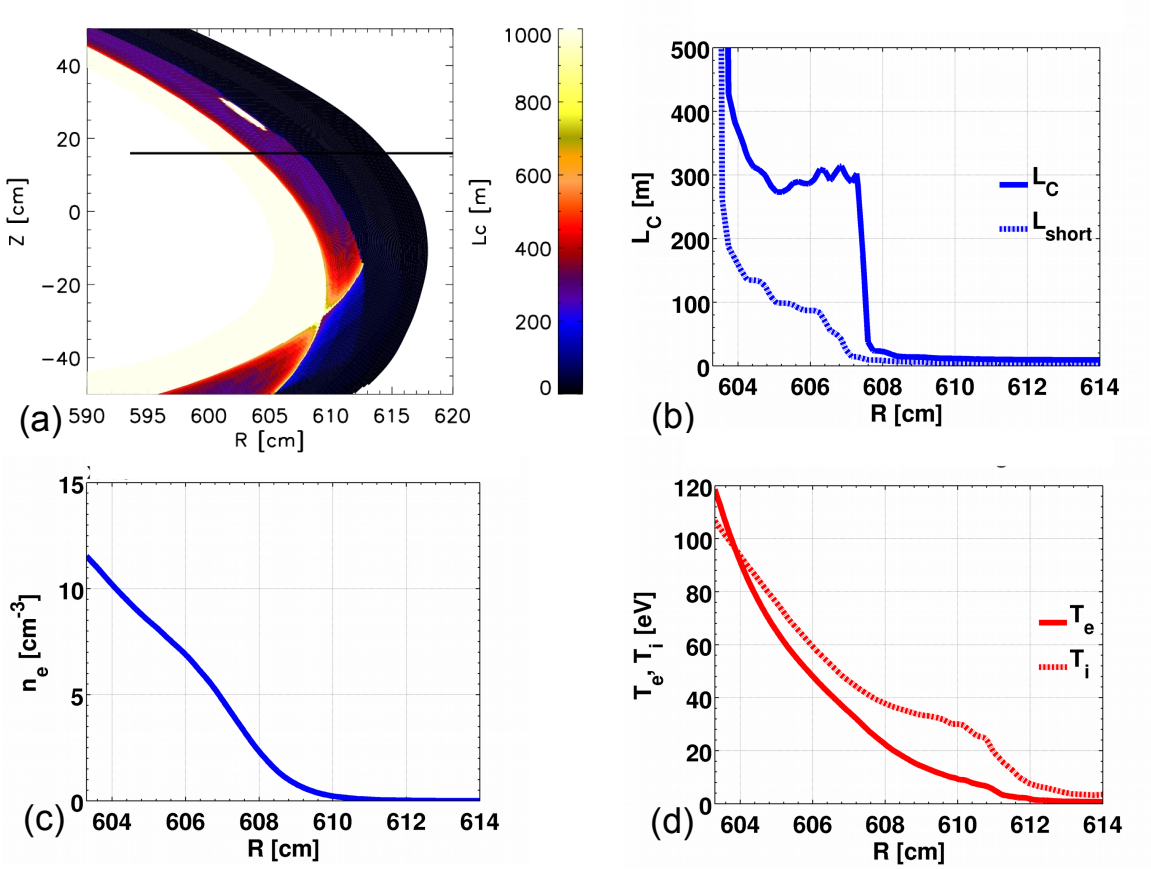

Figure 4.4 Radial profiles at the fast probe position (a) Fast probe path. (b) Shortest and target-to-target connection lengths. (c) n_e-profile. (d) $T_{e,i}$-profiles (solid, dashed).

diffusive processes play a more significant role. The profiles decay faster in the outer shadow region of short L_C.

4.1.4 Parallel transport within the divertor island

The parallel transport within the island is considered, analogous to the limiter discussion, by plotting the parallel profiles along open magnetic field lines within the islands. This explorative modeling is conducted including carbon as an intrinsically sputtered impurity, based on a fixed radiative power fraction. The actual sputtering yield is iteratively adjusted to match this value.

The following modeling parameters are chosen as a representative scenario: $n_{up} = 1 \cdot 10^{19}$ m^{-3}, $P = 2.5$ MW and $D_{\perp} = 0.5$ m^{2}s^{-1}. Carbon influxes are established according to a fixed power loss fraction of $f_{rad,C}$ =20%.

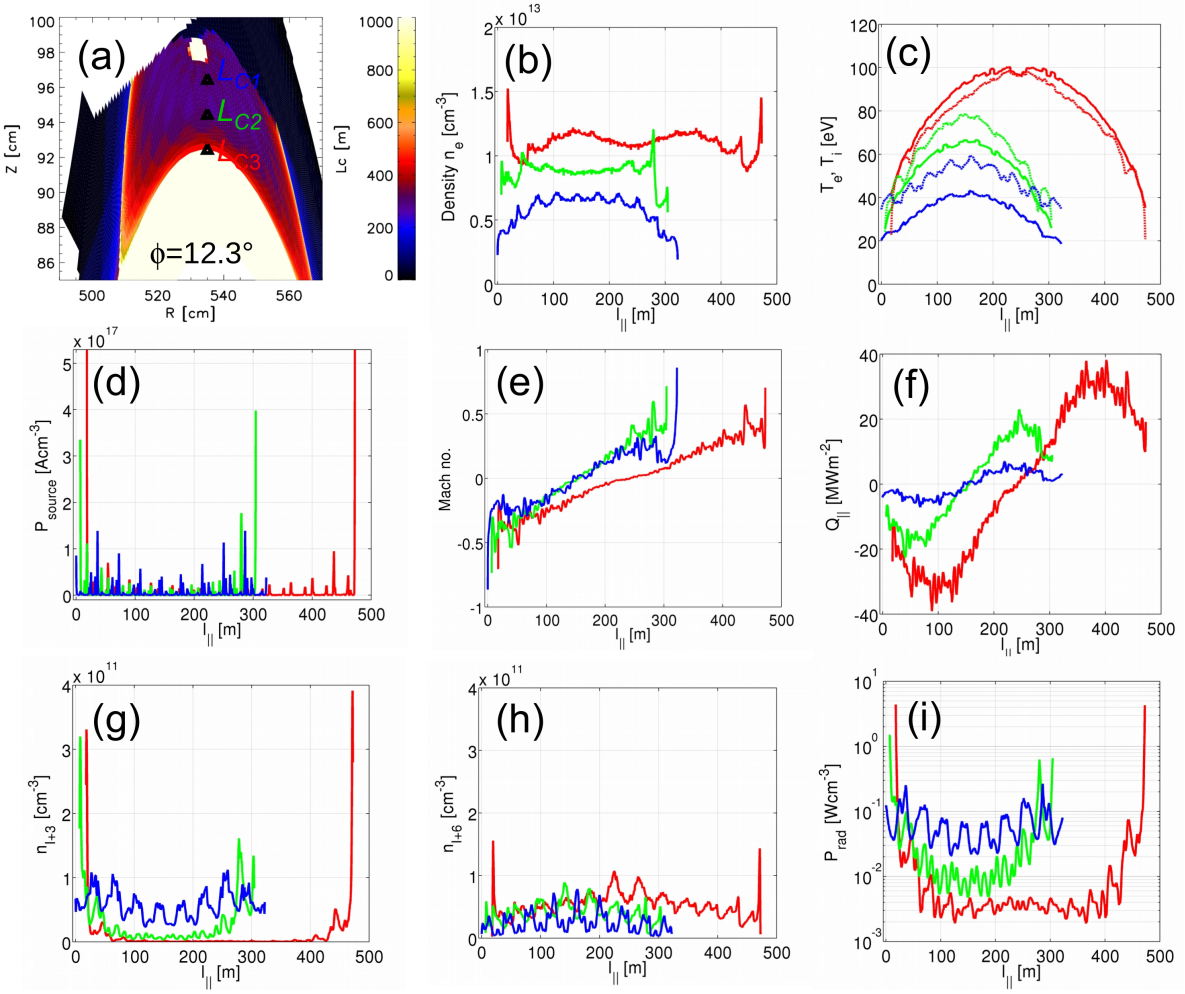

Figure 4.5 Parallel transport within the island. (a) 2D L_C profile: black triangles mark start position of 3 field lines ($L_{C_{1,2,3}}$). (b) Parallel n_e-profile. (c) Parallel T_e-profiles (solid) and T_i-profiles (dashed). (d) Parallel particle source profiles S_p. (e) Parallel Mach number profiles M. (f) Parallel heat flux profiles $Q_{\parallel}$. (g) Parallel C^{+3} density profiles. (h) Parallel C^{+6} density profiles. (i) Parallel profiles of total carbon radiation $P_{rad,C}$.

The parallel profiles are plotted within the open field line domain of the island, which represents the heterogeneous SOL in the island divertor geometry - contrary to the island O-point and also to

the closed flux surface domain deeper inside. The black triangle symbols mark the start positions of the three field lines in figure 4.5(a) at $\phi = 12.3°$. The first field line is chosen close to the separatrix at $(R, Z) = (535.0, 92.5)$ cm. Two other field lines are chosen by vertically shifting the Z-component by ΔZ =2 cm closer to the island O-point. The field lines are then followed in both toroidal directions until they hit a target. The parallel profiles labeled as L_{C_1}, L_{C_2} and L_{C_3} in figure 4.5(a). The density n_e, electron and ion temperature $T_{e,i}$, the particle source S_p, the Mach number M, the heat flux $Q_\parallel$, the carbon ion densities n_{I+3} and n_{I+6} and the total carbon radiation $P_{rad,C}$ are shown in figure 4.5(b-i). Blue, green and red correspond to L_{C_1} ≈322.17m, L_{C_2} ≈297.62m and L_{C_3} ≈454.78m. The plots indicate that the upstream positions are located at the center of the respective profiles where the temperatures reach their maximum peaking (figure 4.5(b)) and the Mach number and parallel heat fluxes (figure 4.5(d)) show stagnation ($M = 0$, $Q_\parallel = 0$). The ends of the profiles again represent the downstream location at the divertor target plate.

The profiles of the field line more in-depth in the island (L_{C_1}) shows a parallel density gradient with a drop towards the target. The profile close to the separatrix shows the opposite effect, i.e., an increase of the density at the downstream position. This is due to the strong local particle source and fueling from the separatrix (see also 2D density profile in figure 4.3(e)).

The magnetic flux tubes of field lines close to the separatrix have the longest connection lengths, and hence they have a larger areal surface towards the steeper gradient region towards the interior, where a higher level of particle flux enters. Therefore, island flux tubes close to the separatrix are stronger fueled by cross-field transport and reach the highest densities and temperatures (figure 4.3(b) and (c),red). The temperature profiles show the existence of parallel temperature gradients according to $\nu_e^* > 15$ (equation 4.3, figure 4.3(c)).

The Mach number M and even more the parallel heat fluxes $Q_\parallel$ (figure 4.5(e) and (f)) show in case of the field line close to the separatrix first some acceleration and de-acceleration near the downstream position due to friction with neutrals and density build up in the vicinity of strong

particle sources (figure 4.5(d)). The carbon impurities with lower charge states are mostly concentrated downstream as shown for main radiator C^{+3} in figure 4.5(g), while the carbon impurities with higher charge states increase rather towards upstream, as shown for C^{+6} in figure 4.5(h). The total radiative power losses by C occur accordingly close to the target (figure 4.5(i)).

The oscillations, in particular in the density profiles, are correlated to the oscillations of S_p in figure 4.5(d). These peaks occur once a field line passes a strong particle source close to a divertor target.

4.1.5 Optimization of island SOL geometry for high performance configurations

Based on this essential analysis of transport properties in the island divertor and the link to the impurity and radiation distribution, an attempt was made to investigate in how far the optimization of core transport aspects impacts the edge magnetic geometry. This analysis is based on an increased mirror term in the plasma equilibrium, which reduces the bootstrap current at a moderate increase of the effective ripple [5]. The critical aspect of such optimizations is to maintain edge stability, which means keeping the island divertor performance unaffected. The magnetic boundary is very sensitive to magnetic perturbations due to its low-shear and the fact that a low order resonance (m/n=5/5) is used to form the magnetic divertor structure. These magnetic perturbations are induced by currents caused by magnetic equilibrium effects, which, e.g., arise during plasma pressure ramp up. In particular, the net toroidal current I_{tor} ($O(10\text{kA})$) evolves due to decaying self-inductance on finite times scales and saturates to a non-zero bootstrap current I_{BSC}, which can alter the edge geometry:

$$I_{tor} = I_{BSC}\left(1 - e^{-\frac{t}{\tau_{L/R}}}\right) \tag{4.5}$$

The changes arise on the time scale of the shielding current decay time, the L/R-time, which is given by the ratio of plasma inductance L to the plasma resistance R. During long pulse high performance plasmas it is predicted to be $\tau_{L/R} \approx 20 - 40\text{s}$ [114].

Other response currents are the Pfirsch-Schlüter current and the diamagnetic current which evolve on time scales of the change of ∇p ($\sim$ energy confinement time$\sim$200ms for W7-X). It was predicted that during the build-up time of these currents these changes cause shifts of the strike lines along the divertor plates towards the edges at the divertor pumping gaps where the limits of 2-5 MWm^{-2} can be exceeded [115]. Therefore strategies need to be developed to mitigate potentially harmful effects for the high performance, steady-state scenarios at W7-X. A sophisticated approach

is to drive counter currents by the electron cyclotron current drive (ECCD) to compensate residual bootstrap currents and thereby maintain the magnetic edge structure[116]. This method is difficult because it requires active control of the ι-profile and the current drive efficiency reduces at high plasma densities.

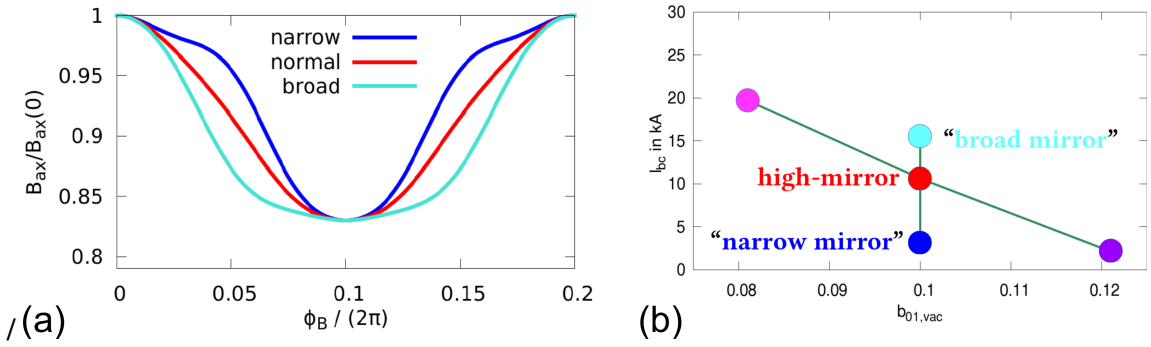

Figure 4.6 (a) Toroidal magnetic mirror field for Narrow High Mirror NHM (blue), High Mirror (HM) (red) and Broad Mirror (cyan). (b) Bootstrap currents I_{bc} of different higher mirror configurations [16].

The island divertor configuration space is relatively large [5]. Therefore, it is possible to counteract equilibrium states of the plasma which, as stated before, may cause an overload of unprotected and less cooled divertor components. The high mirror configuration (HM) features reduced bootstrap currents when compared to the standard divertor configuration (SDC) and hence has the advantage of stable island geometry. Taking advantage of this significant degree of freedom in configuration space, further optimization was undertaken to optimize the high mirror configuration concerning its MHD properties and moreover with respect to its SOL geometry [16]. The new, so-called 'narrow high mirror' (NHM) configuration, has the advantages of minimal bootstrap current and SOL geometry similar to the Standard Divertor Configuration (SDC).

The normalized magnetic mirror fields and the bootstrap currents of three high mirror configurations are shown in figure 4.6(a) and (b). The narrow high mirror configuration (NHM, blue)

features a narrower shape of the toroidal mirror field compared to the normal high mirror configuration (red) and a broad mirror configuration (cyan) (figure 4.6(a)). The bootstrap currents for a reference scenario with $n_e = 7.5 \cdot 10^{19}$ m^{-3} and $P = 5$ MW (X2, off-axis)[16] are shown in figure 4.6(b). The NHM features the smallest bootstrap current for several reference scenarios.

The connection lengths of SDC, HM, and NHM, are calculated and shown in figure 4.7(a-c). The islands SOL geometry of SDC and NHM are very similar. The islands SOL width of HM and NHM are slightly increased compared to the SDC. The HM is cut deeper by the divertor plates compared to the SDC and the NHM. The HM features no closed field line domain at the island O-point. This is because more part of the islands is scraped off by the divertor targets. The NHM is shown in figure 4.7(c). It is very similar to the SDC regarding the edge geometry.

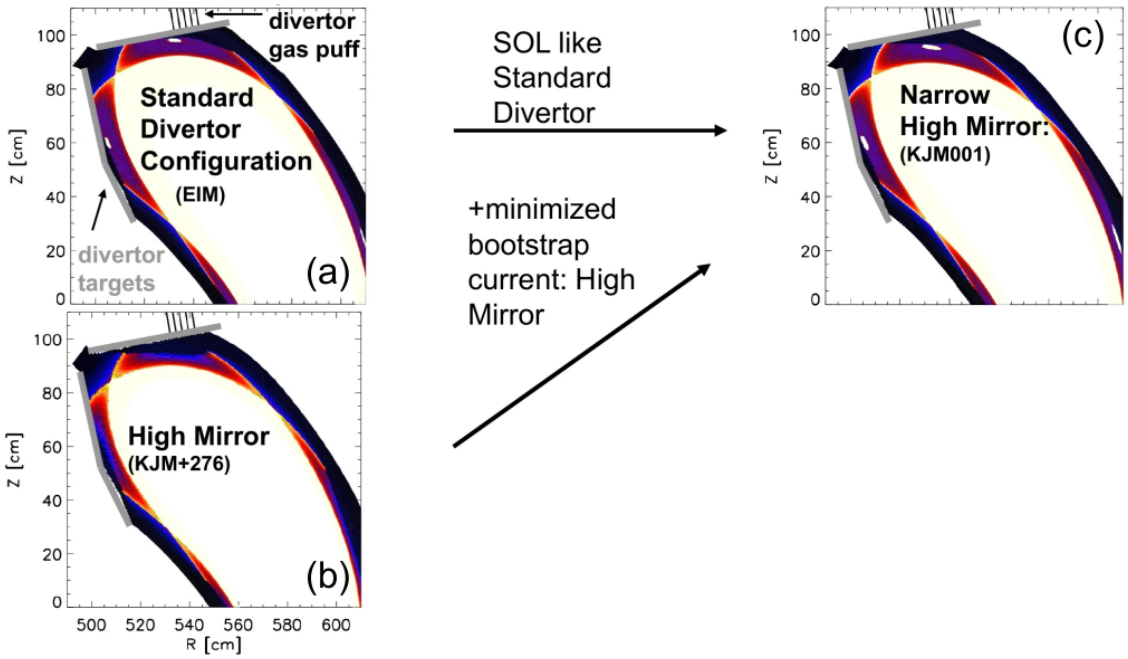

Figure 4.7 Differences in the edge magnetic structure between (a) Standard Divertor Configuration (SDC), (b) High Mirror (HM) and (c) Narrow High Mirror Configuration (NHM) in SOL geometry at $\phi = 12.3°$. (d) Bootstrap current of different higher mirror configurations [17].

This exploration of the configuration space for improved edge island geometry stability on its own was an important finding, demonstrating that there is still lots of capacity of configuration optimization and that core and edge can be optimized almost independently.

Another approach is to install additional target elements (scraper elements) partly shadowing the divertor pumping gaps [52]. The drawback of this approach is that the scraper element might act as a strong additional impurity source and will reduce the pumping efficiency. Due to these potential drawbacks and uncertainties, it is crucial to explore additional means of power load mitigation. Radiative edge cooling could become such an additional or even alternative means to mitigate the impact of bootstrap currents changing the strike line patterns avoiding the drawbacks of the approaches sketched before.

4.1.6 Heat and particle loads in the island divertor

Comparing the divertor heat and particle flux characteristics for different configurations with and without radiative edge cooling is necessary. Defining appropriate metrics for the analysis of heat and particle exhaust in the variable 3D SOL structure and on the 3D shaped discrete divertor targets is a challenge. A separation of heat and particle loads on different targets is desired due to their capacity to handle specific amounts of deposited heat and particle fluxes. Furthermore, localized peak maxima have to be identified.

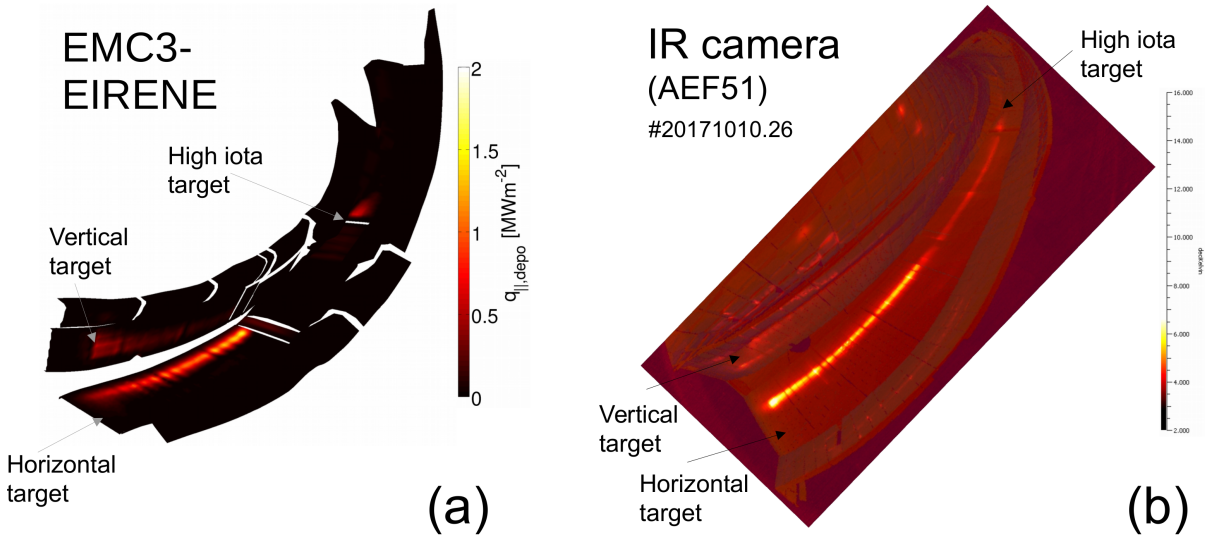

Figure 4.8 Comparison of modeled divertor heat flux and IR temperature measurement in the standard island divertor configuration. (a) Heat flux mapping from 3D modeling. (b) IR measurement of surface temperatures [18].

The heat transport was modeled for the standard divertor configuration with EMC3-EIRENE for the assumption of $n_{up} = 1 \cdot 10^{19}$ m^{-3}, $D_\perp = 0.5$ m^{2}s^{-1}, $\chi_{\perp,e,i} = 3D_\perp$ and $P = 2.5$ MW. A comparison of the mapping of the modeled heat flux onto the divertor targets and the experimentally measured heat deposited onto the divertor with an IR camera is shown in figure 4.8(a) and

(b). The modeling and measurement show good agreement. Most of the heat is deposited on the horizontal target in both modeling and measurement.

The relations between the local magnetic field, the divertor plate geometry, and the deposited heat fluxes are resolved in figure 4.9. In figure 4.9(a) the mapping of $q_{\parallel,d}$ onto the divertor targets is shown again in the divertor volume. The red dots represent a Poincaré plot of the vacuum magnetic field was calculated at $\phi = 12.3°$ for the SOL domain only. The yellow dots highlight the island separatrix. One notices that the main heat stripes distribute around the location of the island separatrix, which features corresponds to a domain with L_C $O(1km - 10km)$. The intensity of the heat stripes decays towards the island O-points. In the standard divertor configuration $q_{\parallel,d}$ is mostly concentrated on the horizontal divertor plate. A profile of $q_{\parallel,d}$ is extracted along the horizontal plate (in poloidal direction) $\phi = 12.3°$ as indicated by the arrow and the coordinate l_{Target} in figure 4.9(a). The 1D profiles of $q_{\parallel,d}$ is plotted in figure 4.9(b) (black dashed line) together with a corresponding heat flux profile obtained from the experimental IR measurement and calculations with the THEODOR code[104] (red). The profiles cover the full domain from the edge of the divertor plate at the pumping gap ($l_{Target} = 0$ cm) to the opposite end at ($l_{Target} \approx 60$ cm). The maximum of heat flux occurs at the separatrix location (Target location $l = 0$ cm). The decay of $q_{\parallel,d}$ is according to the modeling steeper towards the pumping gap due to the shorter connection lengths and flatter within the island due to the longer L_C and the strong poloidal magnetic component of the parallel transport. However, these decays are difficult to estimate from these initial experimental data due to the sensitivity of the profiles to field imperfections, surface layers, details of the local surface geometry or evolving currents.

Taking advantage of the discretization of the divertor geometry allows a statistical analysis of heat and particle loads. The indexing and labeling is shown in figure 4.10 for one scenario in the narrow high mirror configuration with $n_{up} = 2 \cdot 10^{18}$ m^{-3}, $P = 8$ MW, $D_\perp = 0.5$ m^{2}s^{-1} and $\chi_{\perp,e,i} = 3D_\perp$. The horizontal (16), vertical (17) components receive most of the heat and particle

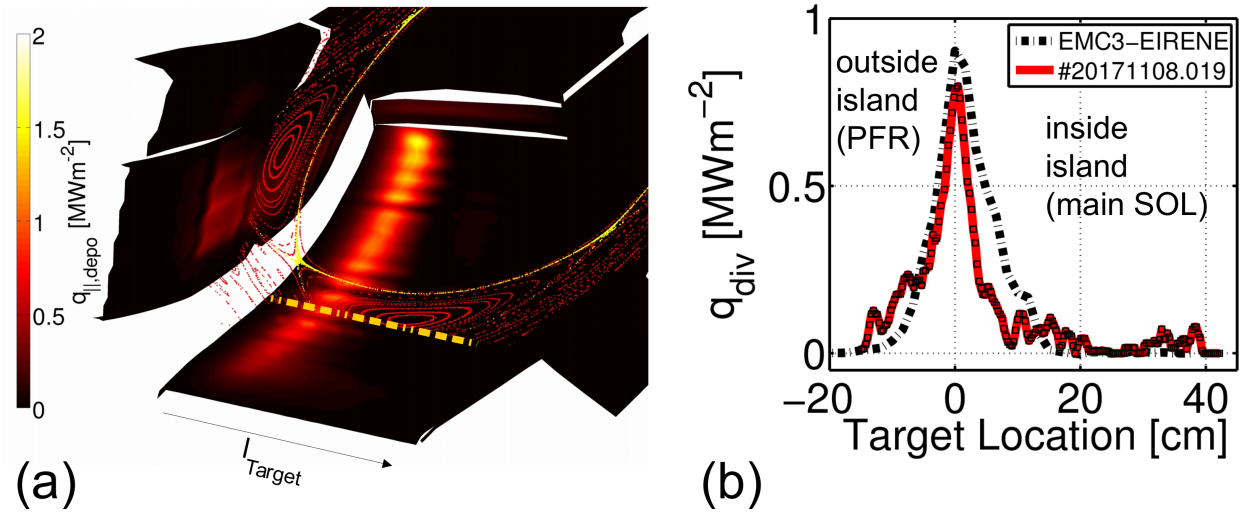

Figure 4.9 Sketch of heat island divertor geometry and resulting heat transport. (a) Heat flux mapping from modeling with Poincaré plot at $\phi_{tor} = 12.3°$. (b) Comparison of modeled and measured heat fluxes on the horizontal target [18].

loads as depicted and shown in the following for various scenarios. Furthermore, loads to the high iota target (15) are remarkable.

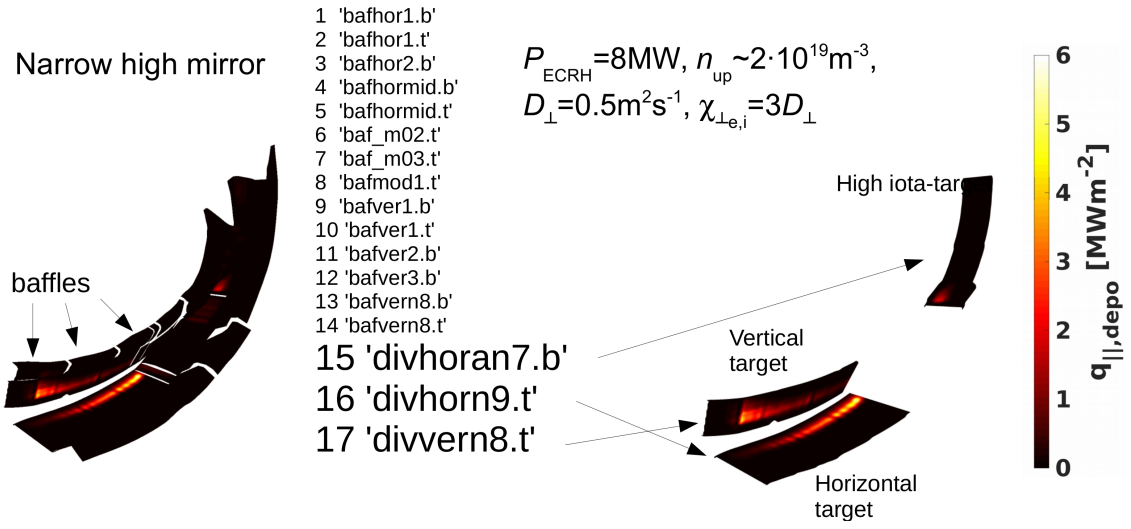

Figure 4.10 Divertor targets. Most heat and particle loads on horizontal and vertical target in standard and narrow high mirror divertor configuration.

A key question now is in how far this change of the edge topology as a consequence of the plasma equilibrium optimization towards low equilibrium currents and hence good edge stability is indeed an improvement for the divertor operation.

The question remains in how far the edge geometry optimization of the high mirror configuration was successful. As a measure of success one takes the similarity of heat and particle fluxes on various target elements is assessed.

It is desired that the optimized NHM configuration feature similar load distributions as the SDC configuration. For this purpose, several scans of the main plasma parameters were performed.

The first scenario considered was based on $n_{sx} = 2 \cdot 10^{19}$ m^{-3}, $D_{\perp} = 0.5$ m^{2}s^{-1}, P =8 MW. Simulations with these boundary conditions and input parameters were performed in both, SDC and NHM. The resulting deposited heat fluxes q_{depo} are depicted in figure 4.11 for both configurations including a comparison to the experimentally measured heat flux distributions by infra-red (IR) imaging. The heat load patterns are very similar. Significant heat loads on horizontal and vertical targets can be seen and minor loads on the high iota target. The loads on horizontal and vertical target correspond to the strike line locations. The mapping already indicates that in NHM the vertical target receives more and the horizontal target receives less load compared to the SDC. The experimental IR camera measurement is shown to confirm the general patterns of the strike lines in the two configurations qualitatively. A quantitative reproduction of the heat fluxes is impossible at this time due to limitations of the measurement of the radiated power as well as local plasma edge parameters (exact matching of plasma parameters is not attempted here).

Various scans were performed in both configurations. The particle and heat loads on the divertor targets are calculated for a density scan and shown in figure 4.12 for the narrow high mirror configuration. Impurities were neglected at this point. The deposited particle fluxes $\Gamma_{\parallel,depo}$ increase in wetted area and intensity with rising density. The heat stripes q_{depo} increase in width, but

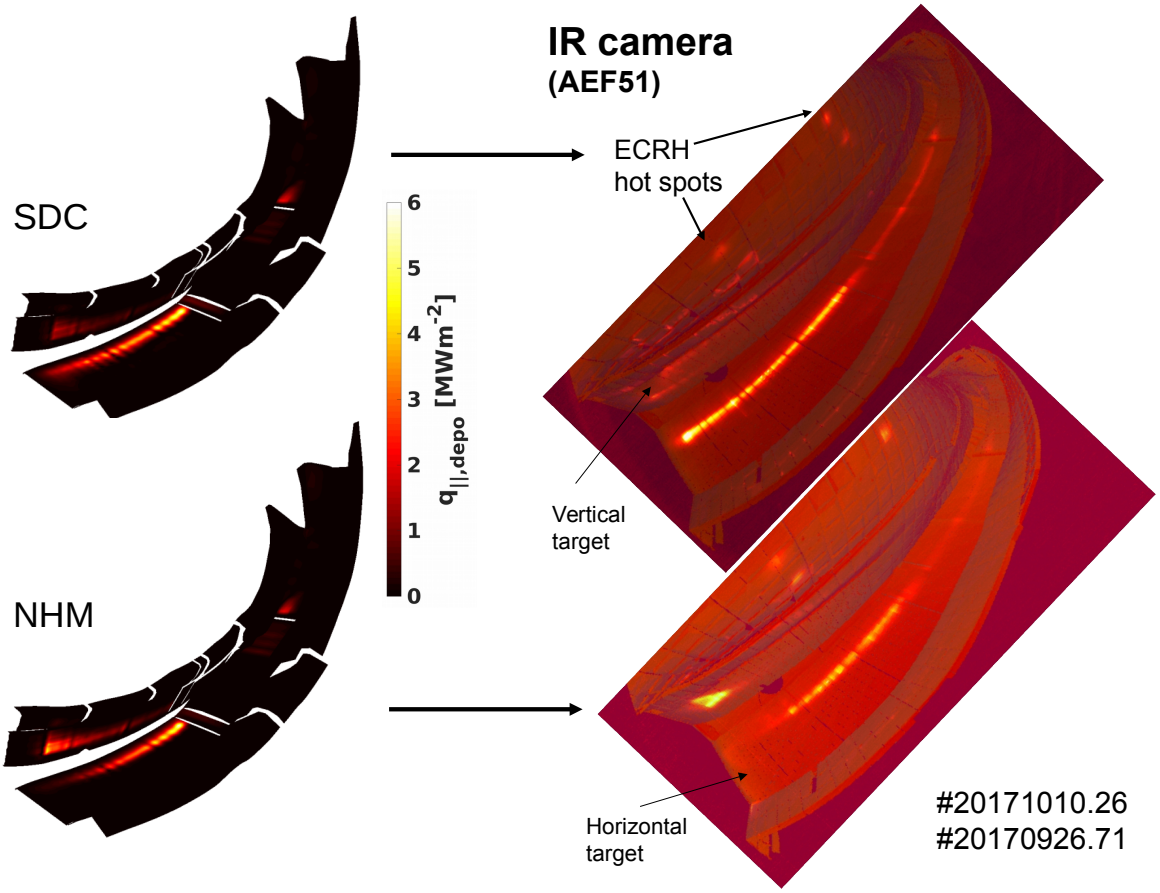

Figure 4.11 Comparison of deposited heat fluxes q_{depo} in standard divertor configuration (SDC) and narrow high mirror configuration (NHM) in modeling and experiment.

decrease in intensity. The latter is mostly due to power dilution with rising energy carrying number of particles.

The heat and particle loads are analyzed component-wise by calculating the integral heat loads Q_{T_j} and particle loads Γ_{T_j}:

$$Q_{T_j} = \int q_{\parallel,depo} dA_{T_j} \tag{4.6}$$

$$\Gamma_{T_j} = \int \Gamma_{\parallel,depo} dA_{T_j} \tag{4.7}$$

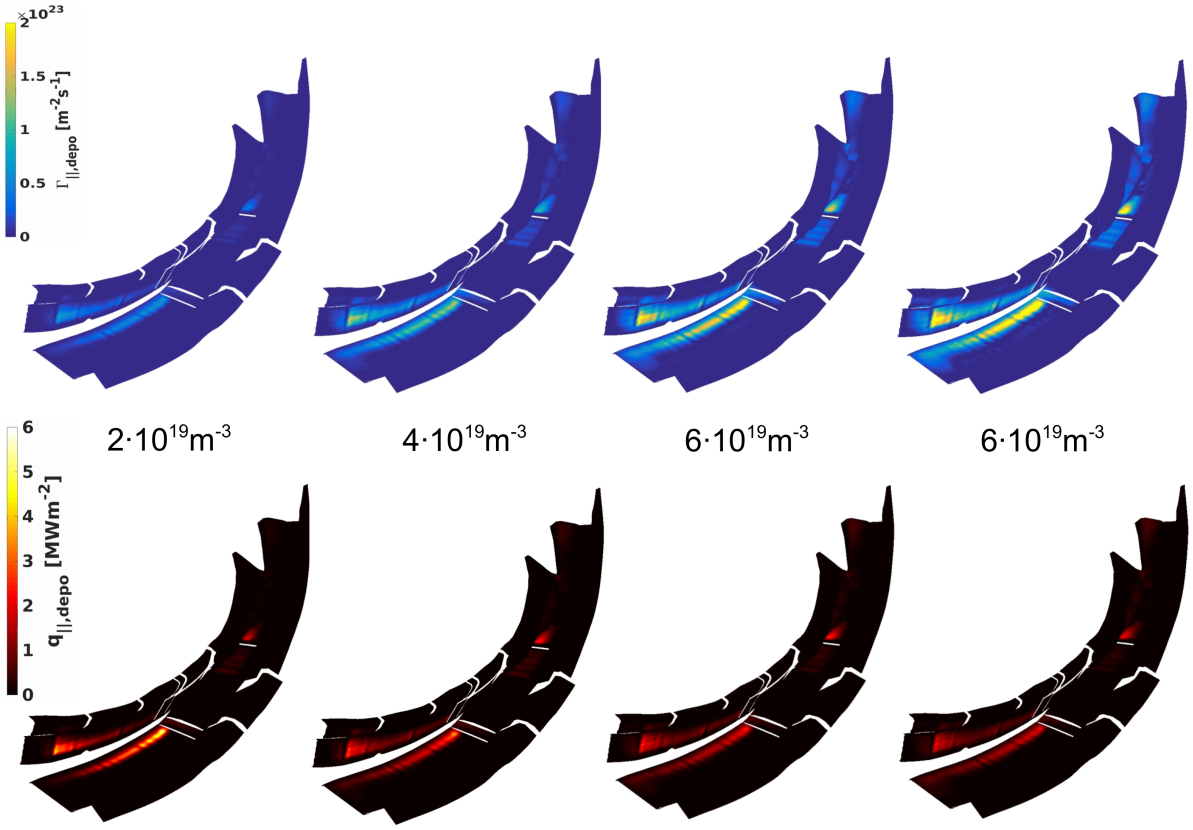

Figure 4.12 Effects of rising density on distribution of effective particle (top) and heat (bottom) loads in narrow high mirror configuration.

where dA_{T_j} is the surface area for each target component T_j. The component-wise distribution of these total loads is shown in figure 4.13 for the density scan in the NHM. It shows clearly an increase of the integral particle load $\Gamma_{\parallel,depo}$ (blue symbols) on horizontal (16) and vertical (17) components by roughly a factor of 5-6 with increasing density, while the heat flux stays almost unaffected. This points towards a uniform distribution between the mostly loaded target components and the scaling of downstream flux with upstream density suggest a high recycling regime in both configurations. The integral heat loads (red symbols) slightly decrease with rising density.

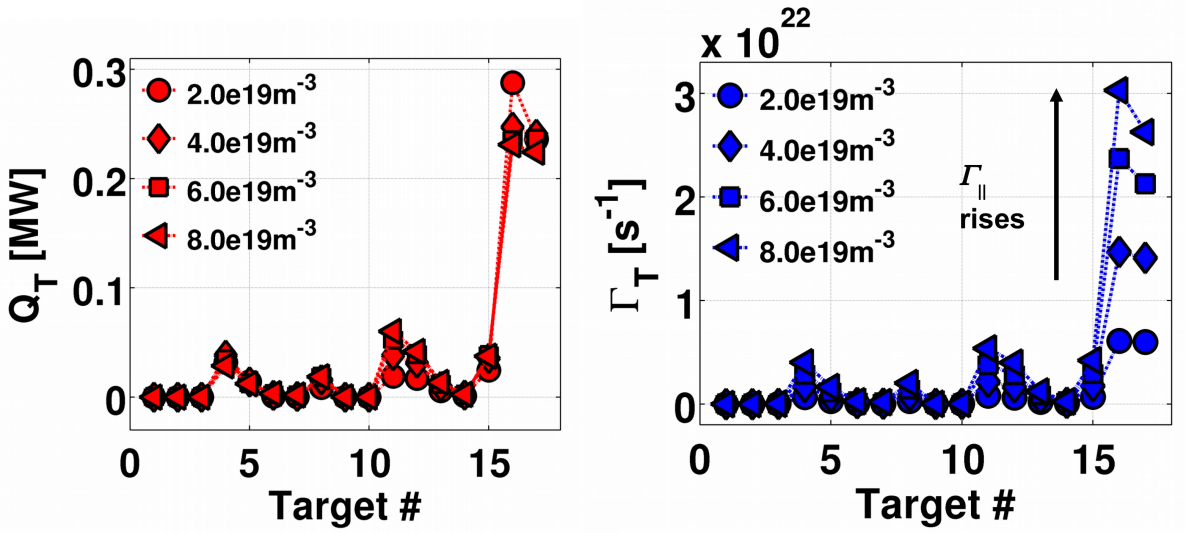

Figure 4.13 Component-wise distribution of integrated heat (red) and particle (blue) loads on divertor targets.

The relative component-wise distributions of heat and particle loads are a more insightful for comparison of different configurations:

$$q_{T_j}[\%] = \frac{Q_{T_j}}{\Sigma_j Q_{T_j}} \tag{4.8}$$

$$\gamma_{T_j}[\%] = \frac{\Gamma_{T_j}}{\Sigma_j \Gamma_{T_j}} \tag{4.9}$$

The resulting fractional heat and particle load distributions for the density scan ($2 - 8 \cdot 10^{19}$ m^{-3}) are shown in figure 4.14 for both configurations. Here, it becomes clear that most heat and particle loads are concentrated on the horizontal target in the standard divertor configuration. The heat and particle load distributions (q_{T_j} and γ_{T_j}) may vary between 65% and 40% for low and high densities. The heat and particle loads to the vertical target scatter around 25% for SDC. In the narrow high mirror configuration, the load distributions scatter around 40% on the horizontal and around 35% on the vertical target. The vertical target is less resistive against any loads compared

to the horizontal target. Yet, this optimization is an advancement to the original high mirror configuration were the load distributions (60% load onto the vertical target) are almost reversed to the standard configuration.

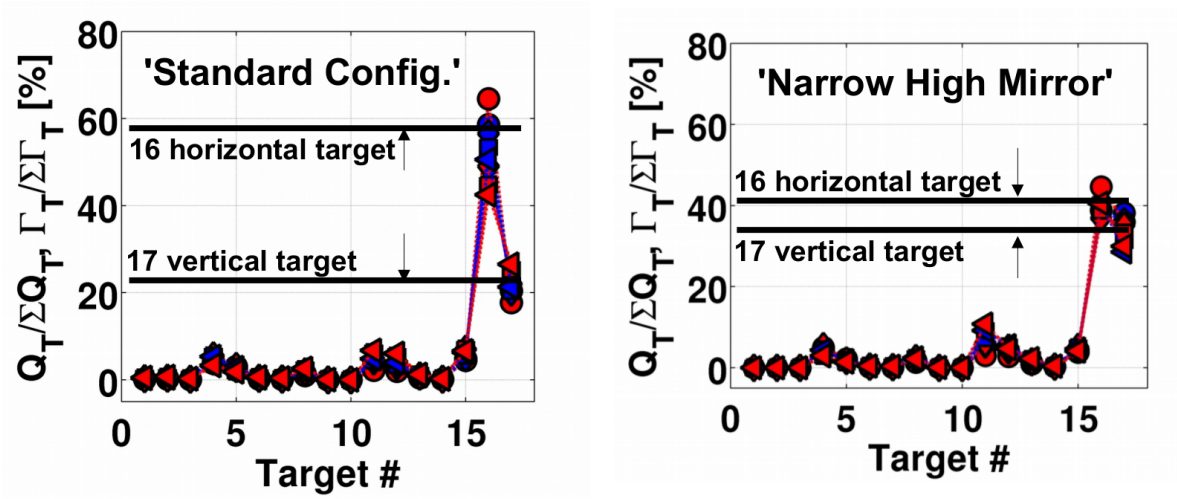

Figure 4.14 Relative component-wise distribution $[\%]$ of integrated heat (red) and particle (blue) loads on divertor targets for SDC and NHM.

These results show that the adjustment of the edge geometry allows for a more evenly redistribution of heat and particle loads between different divertor components. Density variation may result in changes of the relative heat and particle load distributions due to enhanced cross-field transport. In the standard configuration, the relative heat load onto the horizontal target may reduce by 20% in the range of densities considered.

The characteristic scaling of downstream parameters at the divertor plates with upstream densities at the border of the confined plasma region allows a more global view on the transport behavior. The downstream densities n_d, recycling fluxes Φ_{REC}, electron and ion temperatures $T_{ed,id}$ are shown in figure 4.15 (a-c) for the SDC.

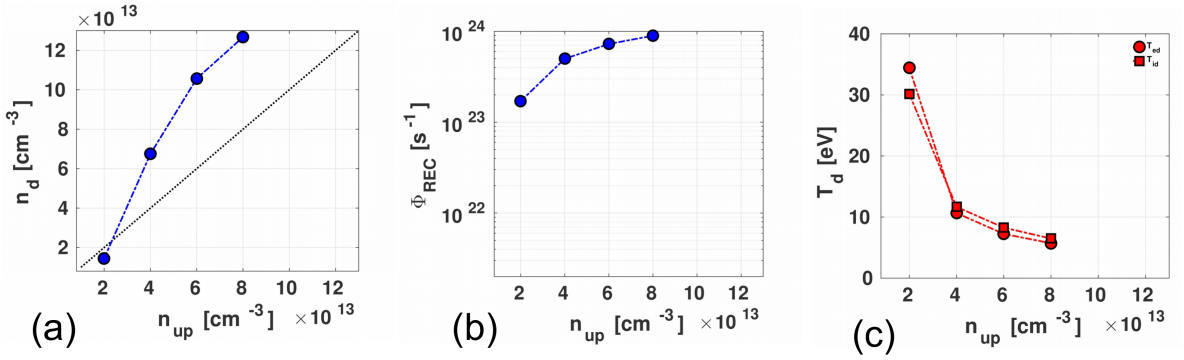

Figure 4.15 Global divertor transport for (a) downstream densities n_d, (b) recycling fluxes Φ_{REC}, (c) electron and ion temperatures $T_{ed,id}$ for the SDC.

This relatively coarse scan covers mostly the high recycling regime. Impurities are neglected at this point but would change the evolution of these profiles significantly. In particular earlier onset of detachment is expected due to additional energy dissipation by impurity line radiation. These results are close to those shown in figure 12 in [117] for the standard configuration ($I_{CC} = 0$). The high recycling regime is predicted for W7-X, but not for W7-AS or LHD. In the latter case viscous-transport induced momentum loss from counter-streaming flows to prevent high recycling, while this effect is suppressed in W7-X due to the large island sizes. These results represent the reference situation of a pure hydrogen plasma without additional power losses by the effects of impurities. However, the introduction of impurities may change this transport characteristic significantly.

4.2 Radiative power exhaust in the island divertor

4.2.1 Impurity forces balance in the island divertor

To characterize the impurity transport regime the leading terms of the impurity force balance are calculated for typical island divertor experiments conducted. The upstream density is chosen to be $n_{up} = 1 \cdot 10^{19}$ m^{-3} with $D_\perp = 0.5$ m^{2}s^{-1} and $\chi_{\perp,e,i} = 3D_\perp$. Low and medium and high power scenarios are considered with P =2.5, 5.0 and 10 MW. Carbon sourcing by sputtering is set to always achieve $P_{rad,C} = 0.5$ MW, only the distribution force balance, carbon density and radiation distributions are of interest here.

The impurity force balance and their dominating terms are calculated according to equation 2.21. The impurity flows caused by friction force F_{fr} and the ion thermal force F_{i-th} and the resulting flow caused by their balance ΔF are depicted in figure 4.16 (left, center and right) for low, medium and high power (top, center, and bottom). In the case with $P = 2.5$ MW, the ion thermal force is weak, and the impurity flow is determined by the friction of the main plasma flow ($\Delta F \approx F_{fr}$). In the case of $P = 5$ MW, the flow induced by the ion thermal force is increased, but the friction force still dominates the resulting flow. In case of highest power ($P = 10MW$) the thermal force is significantly enhanced and causes even a reversal of impurity flows in parts of the main SOL and at the upstream position. However, the friction force is still dominant at the downstream location at the targets.

The resulting distributions of the force balance, impurity concentration, and radiated power are averaged in poloidal and toroidal direction and shown as 1D profiles in figure 4.17 for low, medium and high heating power (black, blue and red solid lines). The discontinuities in the profiles are a result of the effective radial coordinate computed based on the surfaces of the computational grid which is adjusted to match with the internal separatrix and as much as possible also with the outer separatrix. The relevant aspect here is to distinguish between island SOL and confinement and to

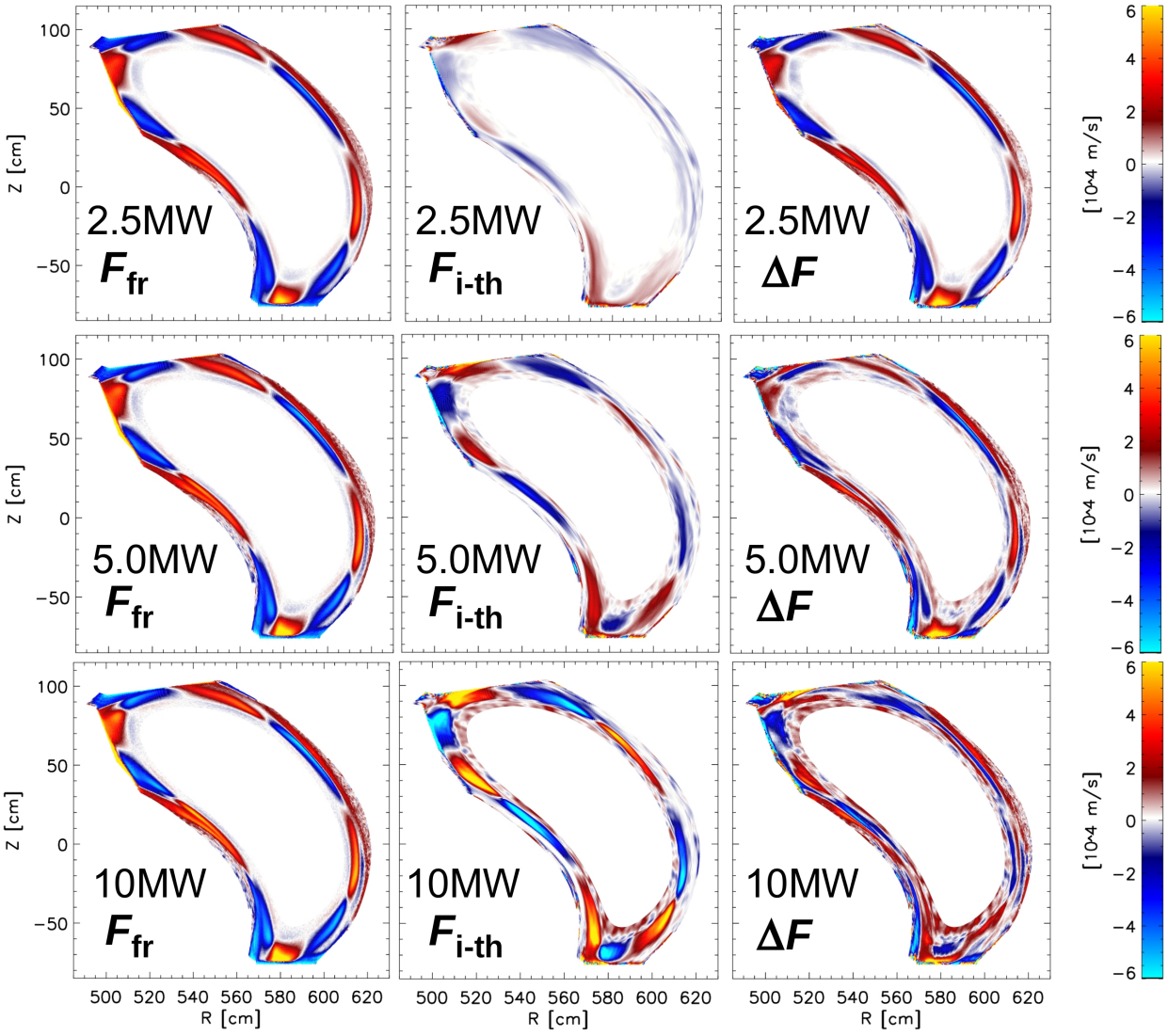

Figure 4.16 2D distribution of main terms of impurity force balance for low, medium and high power scenario.

identify the averaged force ratios and relative changes in the radial impurity distribution between different heating power scenarios.

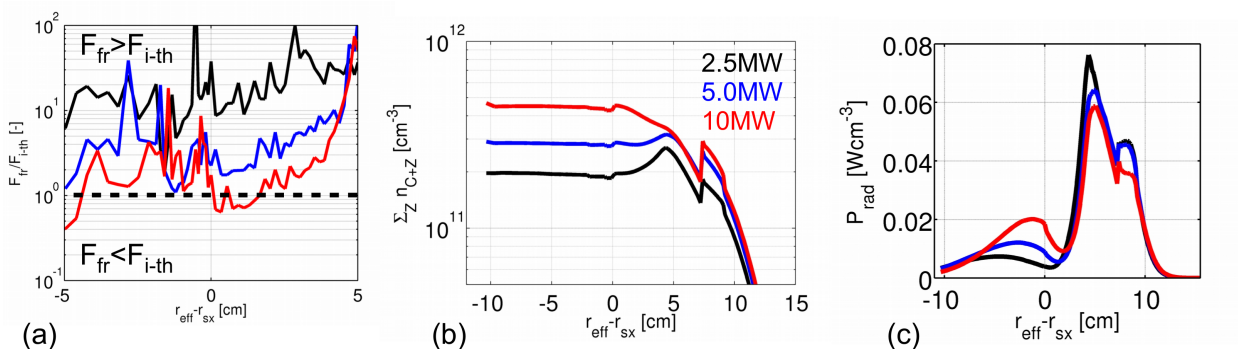

Figure 4.17 Analysis of radial carbon impurity distributions for P =2.5, 5.0 and 10 MW. (a) Ratio of friction to ion-thermal force: $\frac{F_{fr}}{F_{i-th}}$, (b) total carbon impurity concentrations. (c) Total carbon impurity line emission.

The radial distribution of the ratios of friction to ion-thermal force, $\frac{F_{fr}}{F_{i-th}}$ are depicted in 4.17(a). The black dashed line marks the position where both forces are equal separating regimes with dominating friction force (top) and ion-thermal force (bottom). Only the domain in the main transport region is depicted where significant changes of the ratio may occur.

The radial distribution of the total carbon impurity density is shown in figure 4.17(b) and the resulting total impurity radiation distributions are shown in figure The radial distribution of the total carbon impurity density is shown in figure 4.17(c).

It is generally stated that friction force dominates the SOL impurity transport in island divertor configurations. With increasing heating power the thermal forces may enhance. This is demonstrated with this scan of input power. Only in the scenario with highest heating power (10 MW) a significant decrease of the averaged force ratio is found with values of $\frac{F_{fr}}{F_{i-th}} < 1$ near the separatrix, that is close to the upstream position. However, the impurities considered are released downstream by sputtering (or gas puff in case of seeding). The maxima of the total carbon impurity densities

are located within the SOL for low and medium heating power. In case of $P = 10$ MW, this impurity density maximum occurs within the SOL close to the separatrix (see figure 4.17(b)), but is only marginal. Transition to a thermal force regime and inward flow of impurities at higher power is indicated.

However, the total carbon radiation is for all heating scenarios concentrated in the SOL, and their maxima shift only marginally. A slight increase of power losses within the confinement occurs with increasing heating power (see figure 4.17(b)). The fractions of total power losses within the confinement for the three scenarios are 8%, 14%, and 21%, respectively.

This analysis confirms that the friction force dominates the impurity force balance in most scenarios. In particular, the friction force is dominant near the targets at the downstream location due to the acceleration of plasma flows to ion sound speed. Only in very hot plasma domains, the ion-thermal force may become effective.

A comparison of the modeled intrinsic edge radiation and experiment ($\#20171108.029$) for the standard divertor configuration is shown in figure 4.18. The experimental camera view is tangential through the triangular cross section. It is focused on CIII(465nm) for Coherence Imaging Spectroscopy (CIS). The line radiation for the same wavelengths is calculated from the EMC3-EIRENE modeling for the scenario with $f_{rad,C} = 20\%$ by using PEC coefficients from the ADAS database. High-intensity radiation in the divertor is observed in both experiment and modeling. The radiation structures are sharper in the modeling. The level of anomalous transport determines the width of the radiating layer. A better matching broader radiation layer might be established by increasing $D_\perp$. These results are used to refine the analysis of flow measurements with a synthetic CIS diagnostic. The first application to W7-X flows is reported in [118]. For now, carbon lines are mostly used to determine flow structures and parallel velocities. Later, emission of different impurities might be considered as well.

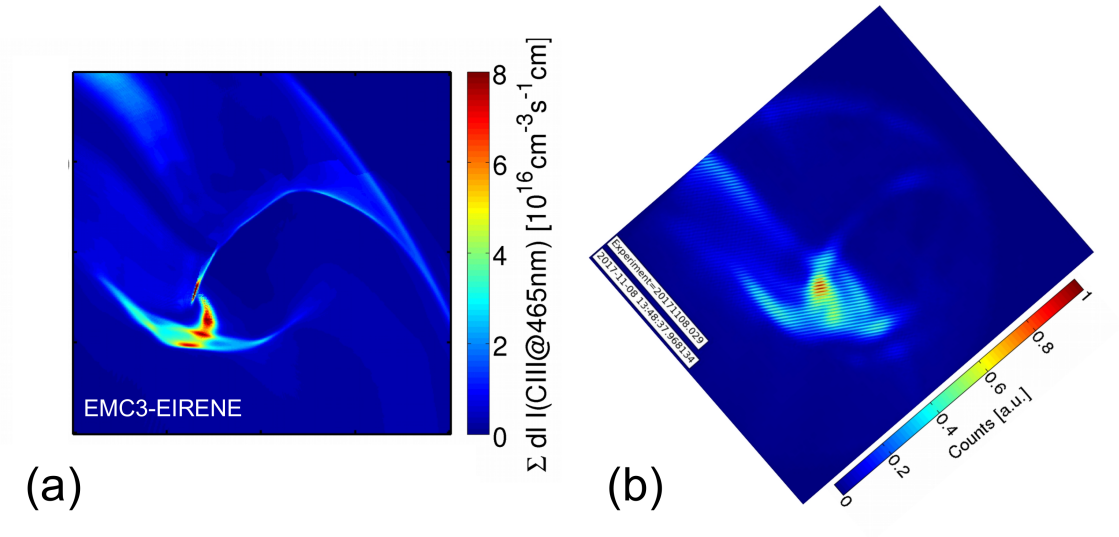

Figure 4.18 Comparison of carbon line emission (a) EMC3-EIRENE by use of synthetic camera and (b) experiment (CIS, courtesy of V. Perseo).

The modeled carbon radiation is also compared in the triangular cross-section with 2D tomographic reconstruction from bolometer data for a typical island divertor plasma. The modeled total carbon radiation distribution is shown in figure 4.19(a) and the experimental measurement of P_{rad} is shown in figure 4.19(b). Despite uncertainties in the radial and poloidal distribution within the tomographic reconstruction, the main feature of a general asymmetry in the radiation on the inboard and the outboard side predicted by EMC3-EIRENE modeling is found in the measurement. This asymmetry was observed at W7-AS as well and is generally explained with the higher heating power entering the SOL at the outboard side [50, 4]. As in the limiter case, the closer toroidal distance of the inboard island to the next neighboring divertor targets may enhance this effect.

In summary, the friction forces are dominant in the island divertor scenarios considered. Only in relatively high power scenarios the ion-thermal force may be increased in the main plasma transport domain and drag impurities towards the upstream position at the separatrix. Losses from intrinsic carbon radiation are expected to occur mostly in the SOL in any case. A maximum of 20%

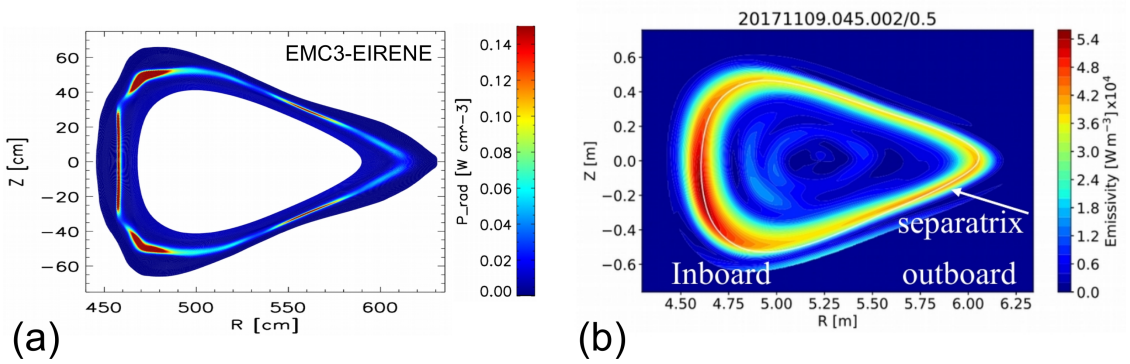

Figure 4.19 Comparison of total carbon radiation between (a) modeling with EMC3-EIRENE and (b) experiment (bolometer, courtesy of D. Zhang).

of the total losses may occur within the separatrix in the high power scenario. Experimental measurements of carbon line emission with video diagnostics and measurements of the total radiation with bolometer confirm the general features of the radiation distribution predicted by modeling.

4.2.2 Radiative power exhaust in island seeding scenarios

For the characterization of radiative power exhaust, a comparison between intrinsic and seeded impurity species is made equivalent to the limiter scenarios discussed in previous sections. Input parameters were chosen based on initial data from Thomson scattering for according to the typical performance of island divertor scenarios initially realized.

A reference scenario in the standard divertor configuration is calculated with upstream density $n_{up} = 1 \cdot 10^{19}$ m^{-3}, input power of $P = 2.5$ MW, $D_\perp = 0.5$ m^{2}s^{-1} and $\chi_{\perp,i,e} = 3D_\perp$. Next, four scenarios with three different impurity species are modeled. The impurity fluxes are calculated iteratively for intrinsic carbon and extrinsic nitrogen and neon by setting the total power losses P_{rad} as input parameter for the energy sink in the energy balance equation (equation 2.11).

In the first case, intrinsic radiative losses from eroded carbon are assumed to be $P_{rad,C} = 0.5$ MW, which corresponds to $f_{rad,C} = 20\%$ for comparison with the seeding scenarios. An

enhanced power loss of $P_{rad,N,Ne} = 1$ MW is assumed for the extrinsic N and Ne impurities, which corresponds to a power loss fraction of $f_{rad,N,Ne} = 40\%$ for both species.

Carbon is assumed to be eroded from the divertor targets and scaled with the recycling flux. Radiative losses from nitrogen and neon seeding are modeled differently. First, both neon and nitrogen are assumed to have $zero$ recycling and sourced only from the gas valve used in the experiment. An additional scenario is implemented assuming that neon is a fully recycling species and therefore sourced from all divertor plates in contact with the plasma. This scenario serves as an approximation for recycling of neon after termination of the injection. The treatment is analogous to the impurity sourcing in the previously discussed limiter scenarios.

The resulting total impurity radiation distributions of the different impurity species and sourcing scenarios are shown in figure 4.20(a-d) in the divertor region at a toroidal cross section at $\phi_{tor} = 12.3°$. The white dotted line represents a Poincaré plot of the island separatrix.

The rather low loss fraction of $f_{rad,C} = 20\%$ is assumed to be emitted by eroded carbon in attached lower radiation scenarios. The resulting total power distribution is shown in figure 4.20(a). The radiation is located close to the divertor target where the island separatrix intersects with the plate. The resulting total power loss distributions are shown for the situation during the injection of neon and nitrogen in figure 4.20(b) and (c). The Ne an N radiation are still well confined in the center of the islands and peaks in the SOL. The modeling would correspond to a simultaneous gas puff with the complete set of divertor gas boxes in all ten divertor units. In the current experiments only two divertors connected by the same island are symmetrically equipped with gas injection system.

The power loss distribution indicates that a dominant localized radiation in the island is expected only for the case of a low recycling species in the current experimental setup. The trapping of the radiation inside of the island is caused by confinement of the impurities injected, which requires a gas inlet set up matching with the stellarator symmetry of the configuration.

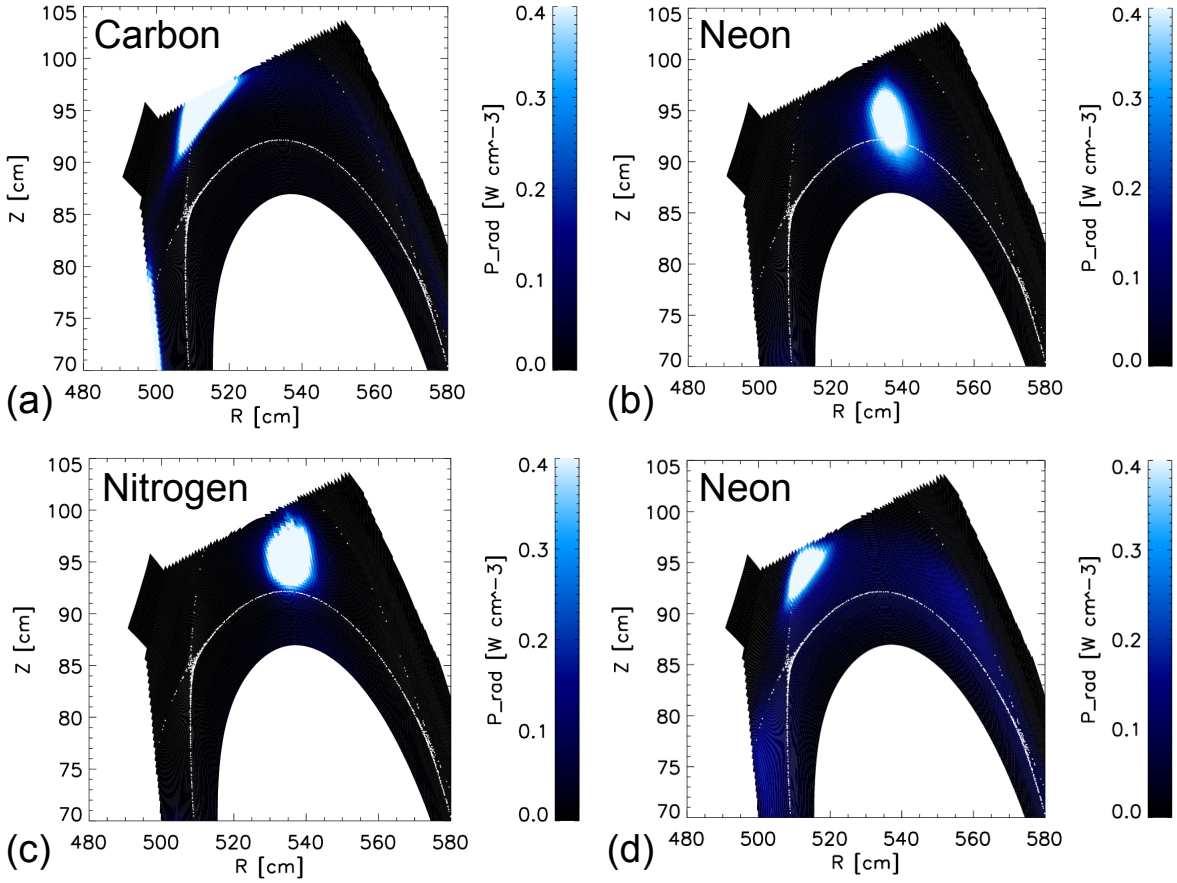

Figure 4.20 Radiation scenarios: (a) Carbon erosion: $f_{rad,C} = 20\%$, (b) Ne seeding without recycling: $f_{rad,Ne} = 40\%$, (c) N_2 seeding without recycling: $f_{rad,N} = 40\%$, (d) Ne recycling: $f_{rad,Ne} = 40\%$.

In case of seeded, non-recycling neon and nitrogen, the peak radiation is located near the source at the island O-point (compare 4.20(b) and (c)).

The assumption of full recycling of neon, realized by scaling the neon influx with the recycling flux, establishes a relatively homogeneous radiative mantle with radiation peaks near the strike lines as shown in figure 4.20(d). The neon radiation is concentrated within the island SOL.

In case of eroded carbon and recycled neon, which is technically treated equal by scaling the recycling flux with a yield factor, the impurity source and peak radiation is located at the strike line location and thereby also closer to the X-point (compare figure 4.20(a) and (d)).

The modeling suggests retention of power losses within the island SOL for any of the considered impurity species and radiation scenarios. The poloidal distribution may vary depending on the source location and recycling properties.

The scenario with $f_{rad,C} = 20\%$ requires an carbon influx of $\Gamma_C \approx 5 \cdot 10^{21}\mathrm{s}^{-1}$ corresponding to an erosion yield of $Y_C \approx 8.6\%$. For $f_{rad,Ne,N} = 40\%$ impurity influxes of $\Gamma_{Ne} \approx 1.1 \cdot 10^{21}\mathrm{s}^{-1}$ and $\Gamma_N \approx 2 \cdot 10^{21}\mathrm{s}^{-1}$ are required in case of seeding (see figure 4.20(b) and (c)) which corresponds to the yields $Y_{Ne} \approx 2.2\%$ and $Y_N \approx 3.9\%$. Ne requires almost a factor of two less particles compared N in order to achieve the same power loss fraction.

In case of Ne recycling after the puff fluxes of $\Gamma_{Ne} \approx 2.5 \cdot 10^{21}\mathrm{s}^{-1}$ which corresponds to a yield of $Y_{Ne} \approx 4.6\%$ (see figure 4.20(b)). This Ne flux is higher than the flux required during the puff situation discussed previously. Sourcing from the main recycling region appears to be less efficient concerning the particle rate. This may be a result of the strong friction force near the separatrix which drags the recycled particles down the target again. The flow friction is reduced in the island center due to the viscous friction between the counter streaming flows (see flows from friction force F_{fr} in figure fig:Impforcediv2D in section 4.2.1).

To distinguish radiation patterns expected based on high and low recycling properties neon line emission of low and higher charge states (NeII and NeVIII) is calculated for the low radiation scenario discussed previously. The results are shown in figure 4.21. In case of zero recycling, the video diagnostic or CIS should show radiating bundles only. In the case of high recycling, the edge radiation is distributed more homogeneously. The results indicate that observation of such structures may provide an additional indication of low and high recycling behavior of seeded impurities.

In summary, the choice of the primary radiator, intrinsic or extrinsic, low or high recycling can result in significant changes in plasma transport for comparable radiation scenarios. The intrinsic carbon source has an ideal cooling potential for reduction of downstream temperatures. However, it

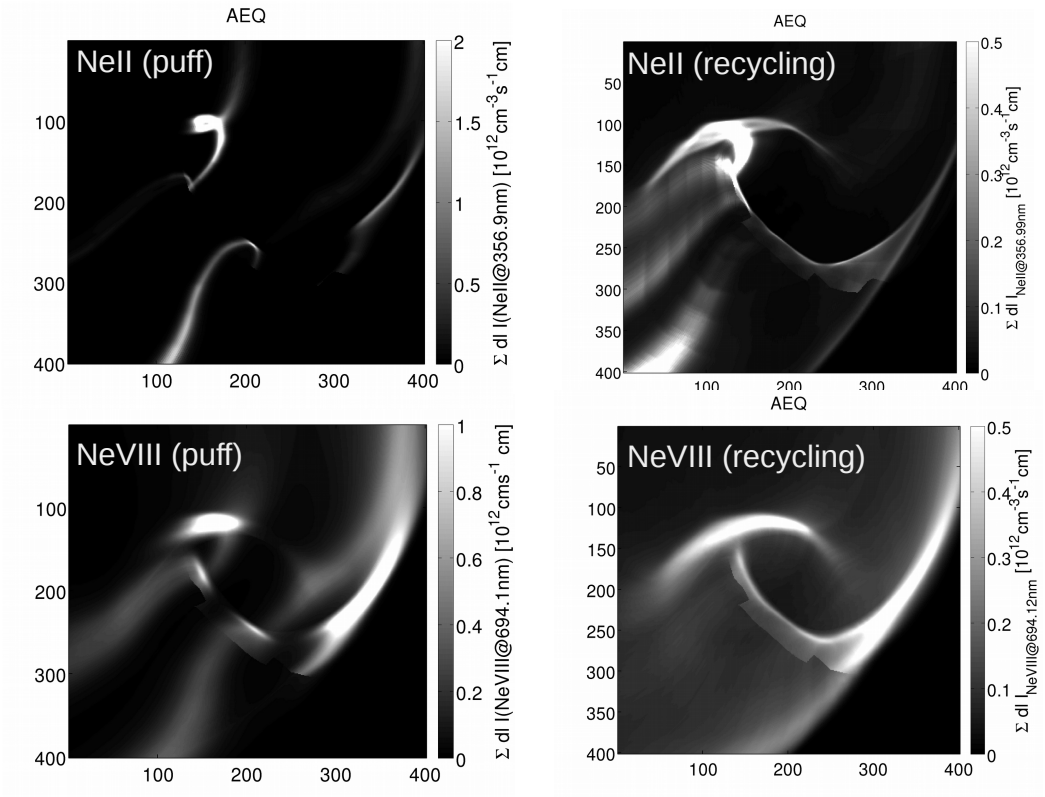

Figure 4.21 Comparison of Neon line emission of low and higher ionization states (NeII vs NeVIII) assuming no recycling and full recycling in the standard island divertor configuration.

requires too high impurity fluxes in low-performance scenarios and cannot be controlled directly. It may be compared with extrinsic high recycling seeding gases since chemical erosion and recycling may both allow for relatively uniform power dissipation in the edge. However, neon will radiate at higher temperatures and therefore facilitate X-point cooling. Nitrogen, under the assumption of zero recycling, features very localized cooling near the source region. The divertor gas box allows mostly for O-point seeding in the standard divertor configuration.

4.2.3 Impact of impurity seeding on divertor heat fluxes

The divertor heat fluxes have been calculated for the scenarios with neon and nitrogen seeding discussed in the previous section 4.2.2. Local heat flux profiles are averaged in the toroidal direction along the horizontal target which receives the major fraction of the loads. The heat flux profiles of reference scenario without impurities and the scenarios with neon and nitrogen for $f_{rad} = 40\%$ are shown in figure 4.22(a) and (b). The black curves represent the reference scenario. The scenarios with Ne seeding and recycling are shown in blue and red in figure 4.22(a). In both cases, the maximum heat flux profile reduces from $q_{\parallel,div} \approx 0.8$ MWm^{-2} to 0.5 and 0.45 MWm^{-2} which corresponds almost to the fraction of power losses.

The scenario with nitrogen seeding is shown in 4.22(b). The maximum of the averaged heat load drops here to $q_{\parallel,div} \approx 0.55$ MWm^{-2} which indicates that the stronger localization of power losses from nitrogen is slightly less efficient for cooling the main strike line location compared to neon.

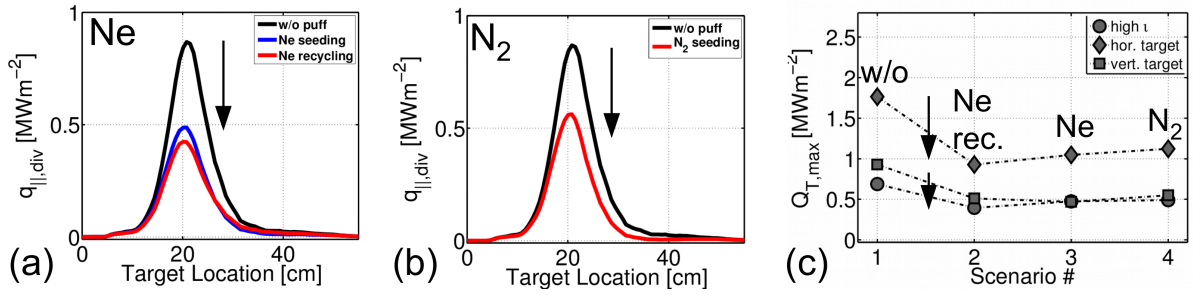

Figure 4.22 Divertor heat fluxes: (a) Neon seeding and recycling. (b) Nitrogen seeding. (c) Overview of heat fluxes on high ι, horizontal and vertical target for scenarios without and with Ne and N seeding.

A comparison of cooling effects on the maximum heat fluxes is shown in figure 4.22(c) for the horizontal target (diamonds), the high ι target (circles) and the vertical target (squares). Scenario 1 corresponds to the reference scenario without impurities, and scenario 2-3 represent Ne seeding,

Ne recycling, and N seeding, respectively. The most substantial reduction of maximum loads on the divertors is found for neon sourced or recycled at the strike line location on the horizontal target.

An analysis of the effectiveness of cooling dependent on the source location in a high power scenario is provided in the next section.

4.2.4 Comparison of seeding on source locations

The optimal source location for impurity seeding is crucial for optimization of power exhaust and potential re-design of gas inlet systems. A primary assessment was undertaken based on a comparison of four different source locations. Carbon only is considered in this first step since it is naturally released and may, on the other hand, be injected as methane through gas valves. For current experiments, a comparison between erosion and seeding through two divertor gas box valves and seeding through a manipulator valve close to the midplane (MPM) is tested. Furthermore, the gas species was varied for central island seeding. The results are shown in figure 4.23(a-e). The 2D distributions of $C + 3$ are plotted for seeding through Tube 4 and Tube 1, that is the center island and remotely in the domain of short L_C shadowed by the divertors (figure 4.23(a) and (b)). Furthermore, the distribution is shown for the case with erosion from the target (figure 4.23(d)). The input parameters and boundary conditions are kept equal between the different seeding and erosion scenarios. The power fraction is set to $f_{rad,C}$ =40% in all cases. The impurity flux or yield Y_C is considered to determine the efficiency in dependence on the source location. This is shown in figure 4.23(c). It turns out that the central island seeding is the most efficient source location to establish $f_{rad,C}$ =40% and erosion, on the other hand, is least efficient (compare black triangles in figure 4.23(c)). Recycling is neglected here, that is impurities get fully absorbed once they hit the wall. The efficiency should not only be evaluated based on the resulting impurity flux. At least the actual reduction of peak heat loads should be considered as well. Here, erosion-like sourcing

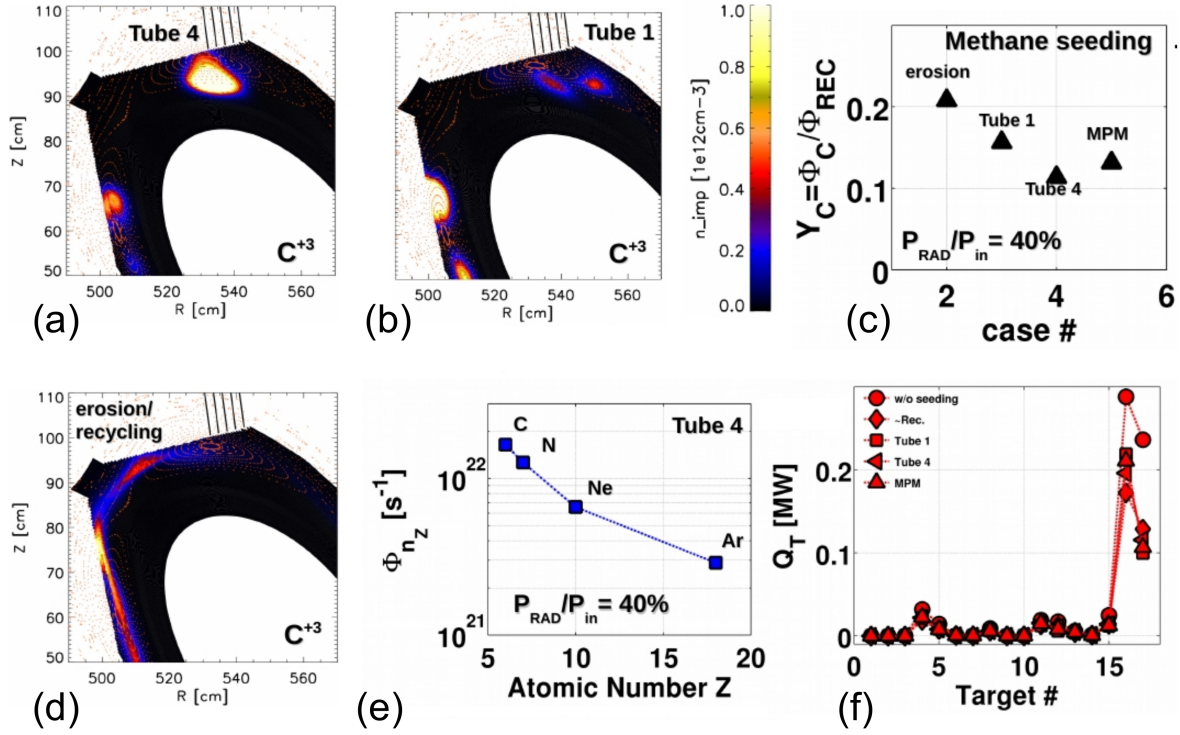

Figure 4.23 Efficiency of seeding depending on source locations and species. Carbon ion density distribution for C^{+3} resulting from (a) central island seeding and (b) seeding at the island boundary. (c) Comparison of Carbon Yields Y_C for fixed $f_{rad,C} = 40\%$ at various seeding locations. (d) Carbon ion density distribution for C^{+3} in case of sputtering. (d) Comparison of impurity fluxes for fixed $f_{rad} = 40\%$ for C, N, Ne, and Ar in case of central island seeding. (e) Total heat loads on the various divertor target components without seeding and in comparison between erosion (rec.), seeding at the island boundary, central island seeding, and seeding through the Multi-Purpose-Manipulator.

(see $C + 3$ density in figure 4.23(d)) provides the best result on the horizontal target (see figure 4.23(e)). However, seeding through Tube 1 is better for cooling at the vertical target (see figure 4.23(e)). In this case, the 2D distribution of the main radiator $C + 3$ shows a higher concentration at the vertical target (figure 4.23(b)). The findings indicate that low/non-recycling species need a more sophisticated arrangement of gas sources to address cooling of concerning hot spots. The

erosion-like sourcing is similar to recycling-like sourcing. In this case, cooling occurs near the domain with the highest particle and heat fluxes. However, a careful assessment of impurity source balances for scenarios of interest has to be taken into account as well.

Lastly, a comparison of seeding gases was performed for (atomic) Carbon, Nitrogen, Neon, and Argon in a scenario with central island seeding. Recycling is neglected even for the high recycling of noble gases. Under this simplification Neon and Argon are still confirmed to be more efficient radiators compared to Carbon and Nitrogen (see figure 4.23(d)).

4.2.5 Impurity seeding in different island geometries

The additional island control coils allow for a change of island geometry. In the standard island divertor configuration, the island control coils are used to increase the width w_i of the islands and to decrease the connection lengths L_C. An additional magnetic configuration with full control coil current, $I_{cc} = 2.5$kA has been implemented in order to study the effects of changing edge geometry on radiative power exhaust with impurities.

The connection length profiles the standard island divertor geometries with $I_{cc} = 0$kA and with $I_{cc} = 2.5$kA are shown in figure 4.24(a) and (b) in the divertor region in a toroidal cross section at $\phi_{tor} = 12.3°$. In case of full increased w_i the separatrix is shifted ≈2 cm inwards. The connection lengths reduce by a factor of ≈ 0.6 on average.

A comparison of plasma transport between these two configurations is made concerning the effects of changing island geometry on radiation and impurity exhaust. For this purpose the boundary conditions are set in both configuration to $n_{up} = 1 \cdot 10^{19}$ m^{-3} at the separatrix with an input power of $P = 2.5$ MW. Ne is sourced in both configurations with a flux of $\Gamma_{Ne} \approx 2.4 \cdot 10^{21}$s^{-1}.

The distribution of the total radiated Ne power is shown in figure 4.25(a) and (b) for $I_{cc} = 0$kA and $I_{cc} = 2.5$kA, respectively at toroidal location of $\phi_{tor} = 12.3°$. In the standard island divertor configuration with $I_{cc} = 0$kA the radiation distribution is poloidally more homogeneous

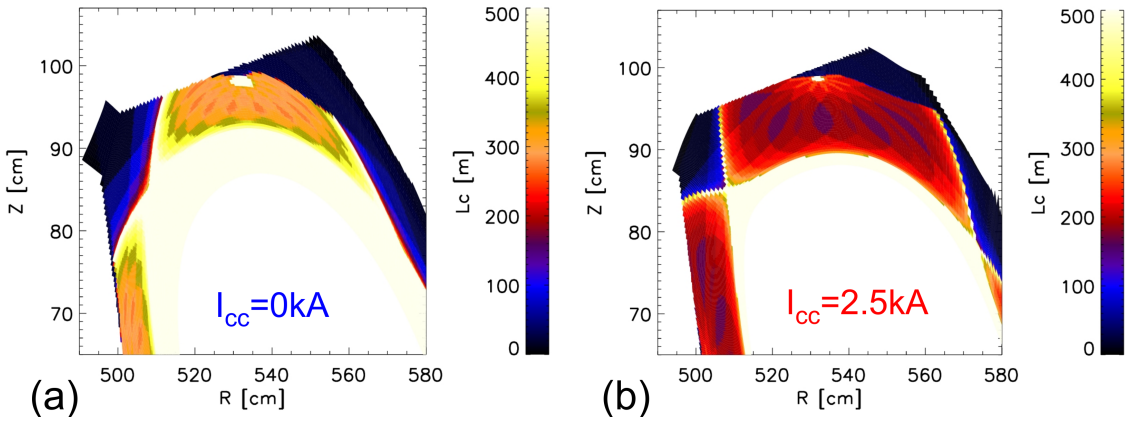

Figure 4.24 Connection length profiles for the standard island divertor configuration with (a) $I_{cc} = 0$kA and (b) $I_{cc} = 2.5$kA.

(figure 4.25(a)) compared to the case of the increased islands where the distribution shows stronger concentration of the radiation at the high intensity spots (figure 4.25(b)).

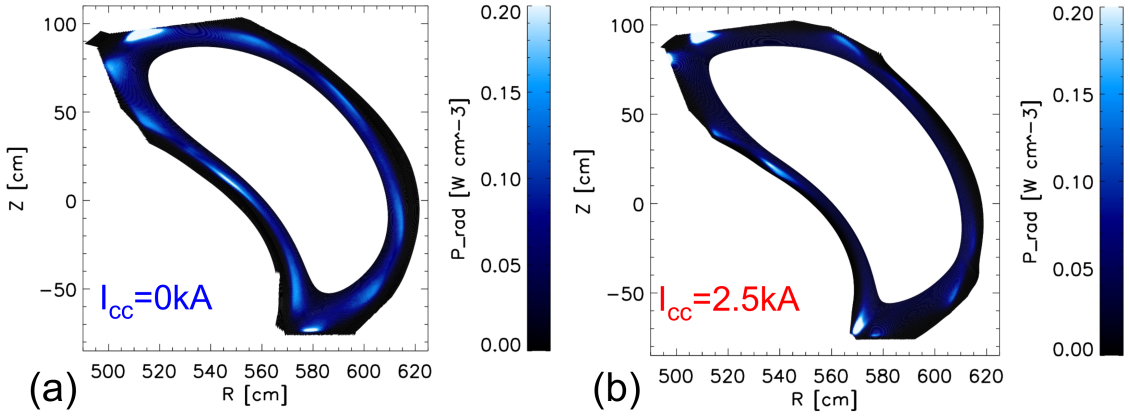

Figure 4.25 Distribution of total Ne radiation for the standard island divertor configuration with (a) $I_{cc} = 0$kA and (b) $I_{cc} = 2.5$kA.

This indicates a substantial impact on impurity transport and will be analyzed in the following based on a single reservoir particle balance approach applied to the volume of the whole simulation domains (V_{sim}) of the two configurations. Integration of neon impurity ion densities over the

simulation volume and assuming constant densities within the core domain gives the total number of particles:

$$N_{Ne} = \int_{V_{sim}} \Sigma_Z n_{Ne+Z} dV \tag{4.10}$$

The total numbers obtained are $N_{Ne} = 8.4 \cdot 10^{18}$ and $N_{Ne} = 4.8 \cdot 10^{18}$ for $I_{cc} = 0$kA and $I_{cc} = 2.5$kA, respectively. A particle residence time $\tau_{p,Ne}$ can be estimated based on the following particle balance equation:

$$\frac{dN_{Ne}}{dt} = \Gamma_{Ne} - \frac{N_{Ne}}{\tau_{p,Ne}} \tag{4.11}$$

In steady state one has $\frac{dN_{Ne}}{dt} = 0$ and therefore:

$$\tau_{p,Ne} = \frac{N_{Ne}}{\Gamma_{Ne}} \tag{4.12}$$

With this simple particle balance approach, one obtains based on the fixed input Γ_{Ne} and the calculated N_{Ne} two different time constants from 3D modeling for the two configurations. It turns out that the residence time drops from $\tau_{p,Ne} = 3.5$ms to $\tau_{p,Ne} = 2$ms with increased island size and decreased L_C. This is expected to be a result mostly due to the acceleration of the neon particle exhaust as a consequence of the reduced L_C, because the particle residence time generally scales like $\tau_p \propto \frac{L_C}{c_S}$.

This simplified approach may under experimental conditions interfere with a change of background plasma properties in response to the change of magnetic island structure as well.

In summary, the results show the feasibility of active control of radiative exhaust and radiation distribution by the island control coils which will be of importance for the control and optimization high radiation and detachment scenarios in future high-performance operation.

4.2.6 Anticipation of equilibrium effects on SOL geometry

Based on the current knowledge and recent studies the proposal is to perform further exploration of radiative edge cooling in the 3D field geometry of Wendelstein 7-X. The particular focus will be on the standard scenario, and the high mirror scenario since those are expected to be the most attractive scenarios for high-performance operation from the geometric point of view (small changes of the edge topology because Shafranov shift and bootstrap currents remain small) [50]. Here, it is of strong interest to benchmark also equilibrium cases. For the future scenarios approaching the L/R time, some equilibrium response might change the edge topology and should be taken into account by advanced means. The HINT code can serve as a predictive tool to asses how the generic trends of impurity transport are affected by exemplarily equilibrium effects.

The change of the magnetic edge topology covers effects potentially featuring the transition from relatively smooth nested island surfaces to stochastization of the vicinity of the islands as visible in the full Poincaré plots. Other significant effects may arise from the transition from fully opened islands to cases where the island field lines are only partly opened and a core of nested flux surfaces around the island O-point remains. That is, within the strongly reduced configuration space there is still a lot of potential effects that might change the magnetic edge topology to be addressed by equilibrium calculations provided by HINT.

The results of this study can serve as a preparation to address the issue of possible overloading of the edges of the divertor pumping gaps through use of mimic configurations which are designed to simulate the impact of bootstrap current effects on the edge topology [52]. Furthermore, some effort related to gas inlet optimization for impurity seeding is an important topic since the very complex 3D topology of stellarators is prone to strong impurity trapping within helical flux tubes connected with the respective impurity source. Further subtopics might address the resolution of uncertainties related to the physics models of the sputtering physic and the collisional-radiative

modeling. These topics are beyond the scope of this study, but they will be addressed if findings in the before mentioned studies will point to particularly interesting features in these directions.

In few examples β-effects were taken into account. For this purpose solutions provided by the 3D magnetohydrodynamic (MHD) equilibrium solver HINT [88] code were considered. An example how β effects might change the edge topology is shown in figure 4.26. On the left side, the connection lengths profile combined with a Poincaré plot of the vacuum high mirror configuration is shown. Here the edge features fixed clear, structured main islands and minor resonances which will eventually be opened by the divertor and baffle target plates defining the SOL. A stochastic layer can be found rather in the very edge. On the right side, a corresponding combination of connection lengths and Poincaré plot is shown for the high mirror for a case with $\beta = 3\%$. The full magnetic field represented by the Poincaré plot features a high degree of ergodization. The island separatrices have vanished. The islands and the last closed flux surface change shape. The open field line domain represented by the connection lengths L_C does not show ergodized structures but has a rather regular structure. The main geometric changes are a reduction of L_C and an increase of island SOL widths. This reduces the $^{\perp}/_{\parallel}$ transport ratios and thereby defines the most relevant configuration changes relevant to the EMC3-EIRENE model (in future upgrades changes of mirror ratios may also introduce change due to varying drift effects [73].

The potential impact on divertor loads is shown in figure 4.27 for a comparison between vacuum high mirror and high mirror with $\beta = 3\%$. The change of edge geometry results in a shift of strike lines and redistribution of power loads. The statistics show a slightly beneficial effect of the $\beta = 3\%$ induced changes since the vertical target becomes relieved while the horizontal target receives more load. However, the impact on neutral compression will have to be carefully assessed since the main fraction of the recycling zone on the horizontal target moves away from the pumping gap.

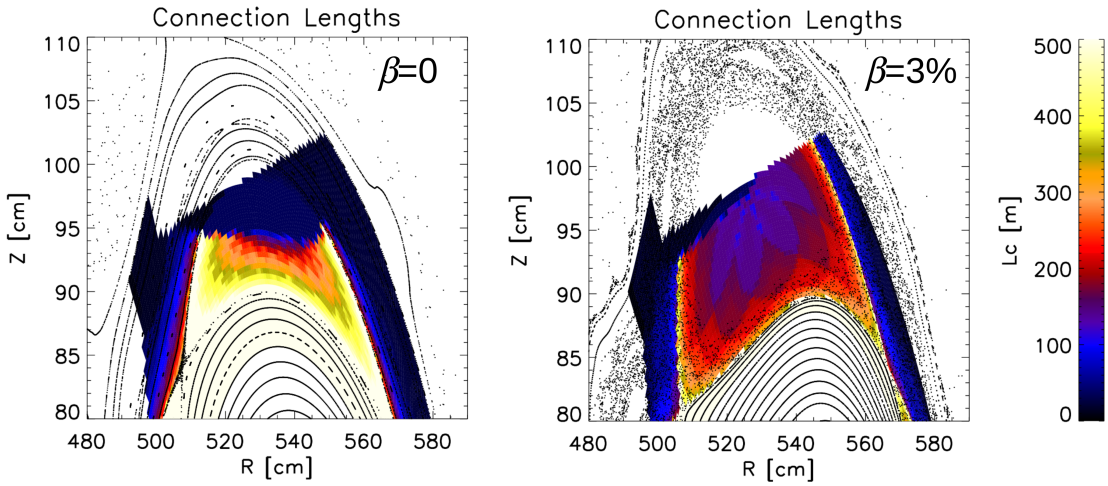

Figure 4.26 Change of divertor geometry can be seen in connection lengths plots overlayed with Poincaré plots for high mirror configuration. Left: vacuum approach. Right: equilibrium $\beta = 3\%$ by HINT.

The geometrical changes and its impact on PSI resulting from these β-effects are from modeling point of view to a large extent equivalent to very similar geometry changes induced by application of island control coils (see section 4.2.5). Therefore results from previously discussed experiments may serve as an approximation as far they recover the shortening of L_C and increase of island widths.

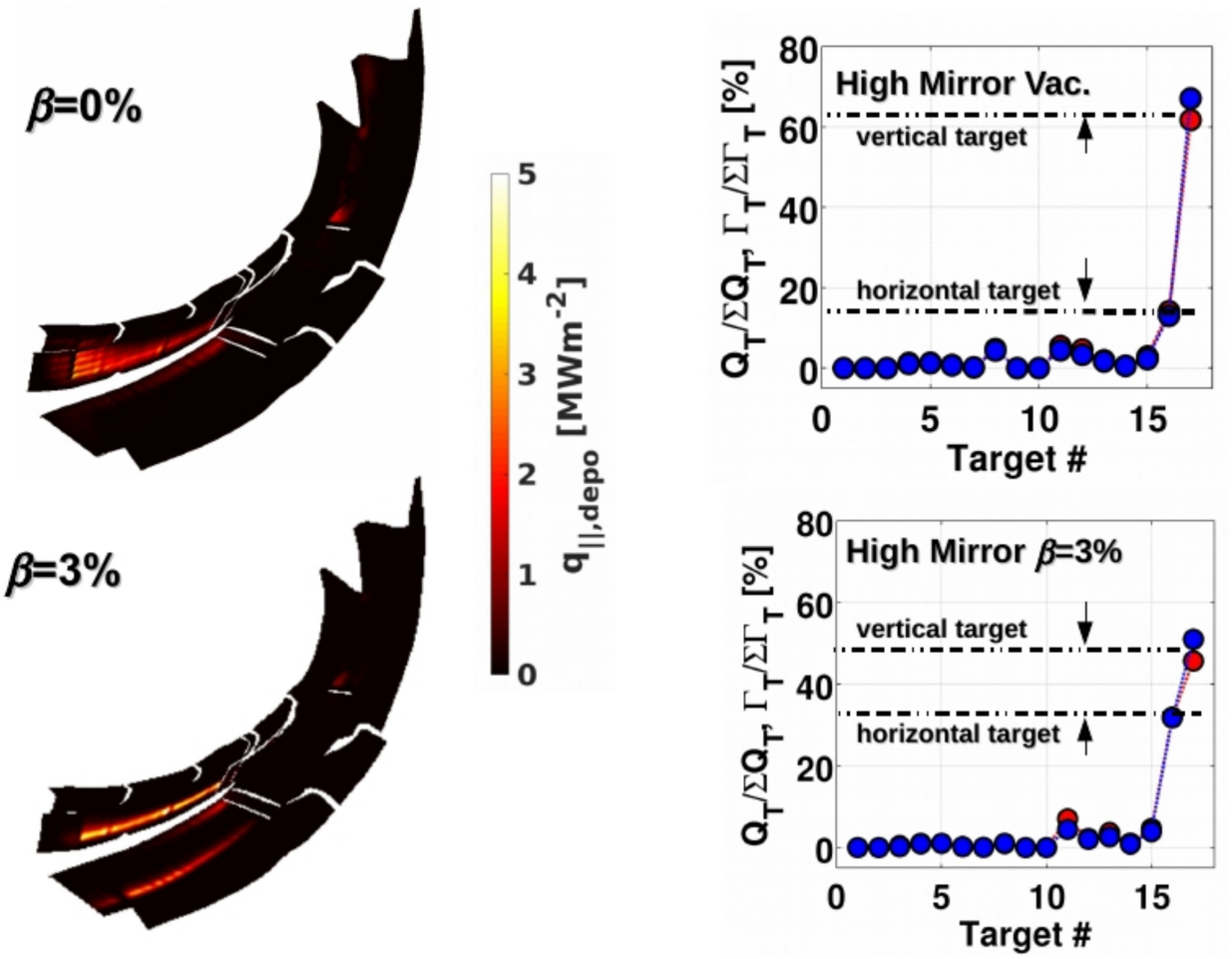

Figure 4.27 Impact of finite plasma β on divertor fluxes for High Mirror Configuration[17]

4.2.7 First radiative power exhaust experiments in the island divertor

4.2.7.1 Remote seeding

First experiments with neon seeding were conducted in the island divertor configuration to study the feasibility of power load mitigation by radiative power exhaust. Neon was injected through a valve (BG023 in the AEO31 port). The pressure was 1bar and in consecutive discharges, the valve opening time was increased as such: $\tau_{Ne,inj.} \approx$ 10 ms, 20 ms, 40 ms, and 80 ms. In the last case, the discharge suffered radiative instability and collapsed.

The overview of the time evolution of main plasma parameter is shown for discharge 20171102.048 with the highest neon influx before the radiative collapse in figure 4.28(a). The ECRH power is 2.9 MW. The feed-forward fueling causes a density peak at the beginning of the discharge. After equilibration to $\int n_e dl \approx 1.7 \cdot 10^{19}$ m^{-3} neon is injected at $t - t_1$ =0.7 s (as indicated by a dashed line in figure 4.28(a)). The total radiated power measured with the bolometer was enhanced by a factor of up to $\approx$ 2.5 in case of 20171102.048. The diamagnetic energy W_{dia} and the energy confinement times τ_E shown in the bottom plots of figure 4.28(a) indicate an only marginal effect on confinement electron temperatures and no confinement degradation even in this case with the highest radiation (an increase of P_{rad} by a factor of 4)

A drop of edge electron temperature from T_e $\approx$100eV to 50eV was measured with divertor Langmuir probes at the strike line for the highest radiation scenario.

The time evolution of locally measured divertor peak heat fluxes is shown for the successive increase of Ne influxes in figure 4.28(b). The reference heat flux without neon seeding is shown in black (20171102.044). The peak heat fluxes with increasing Ne influxes are shown in blue, green and red for discharges 20171102.045, 20171102.047 and 20171102.048. The maximum peak heat flux ($q_{div,max} = 2$ MWm^{-2}) shown drops in correlation to the enhanced power losses by roughly a factor of 0.5. The drop of heat fluxes is shown for a spatial profile (time averaged over Δt $\approx$1.5s after Ne injection) on a horizontal divertor target in figure 4.28(c) in the same color coding.

TThis first experiments with a neon influx scan demonstrated the feasibility of substantial edge P_{rad} enhancement and reduction of power loads onto the divertor. It also demonstrated the feasibility of a sustained radiative power exhaust after termination of the Ne injection due to the high recycling coefficient of this noble gas on the carbon divertor targets. Furthermore, these experiments indicate that the island divertor in principle allows for a more stable and controlled radiative power exhaust than the limiter.

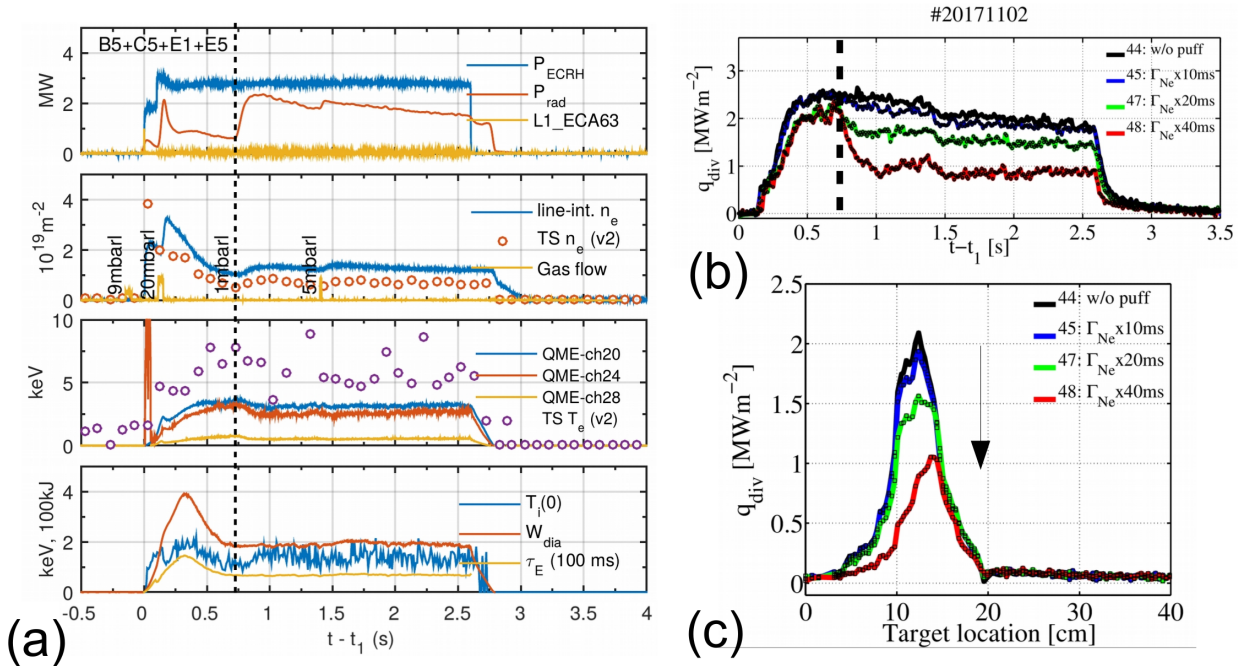

Figure 4.28 Overview of first neon seeding experiment [18].

4.2.7.2 Central island seeding of neon and nitrogen

Two scenarios with neon and nitrogen seeding in the standard island divertor configuration were realized (20171207.045 and 20171207.048). It should be mentioned that these experiments were performed in a reversed field configuration. The respective impurity species were injected near the island $O-$point.

First the scenario with seeding of Ne into the island (20171207.045) is shown in figure 4.29. The overview of main discharge parameters is shown in figure 4.29(a). The ECRH power is 2.9 MW. Improved feedback-controlled fueling allows for a relatively stationary line averaged density of $\int n_e dl = 1.8 \cdot 10^{19}\mathrm{m}^{-3}$. The Ne injection starts at $t - t_1$ =3 s and lasts for $\tau_{Ne,inj.}$ =200 ms (indicated by dashed lines in figure 4.29). The gas box pressure was 100mbar. With a flux rate of $\phi_{Ne} = 5 \cdot 10^{14}$ mbar^{-1}ms^{-1} one obtains a Ne flux of $\Gamma_{Ne} = 5 \cdot 10^{19}$ s^{-1}. The line averaged density

increases slightly by 10% in response to the seeding. The total radiation increases by almost a factor of 2, while energy confinement is not degraded ($\Delta W_{dia} \approx 0$, $\Delta \tau_E \approx 0$).

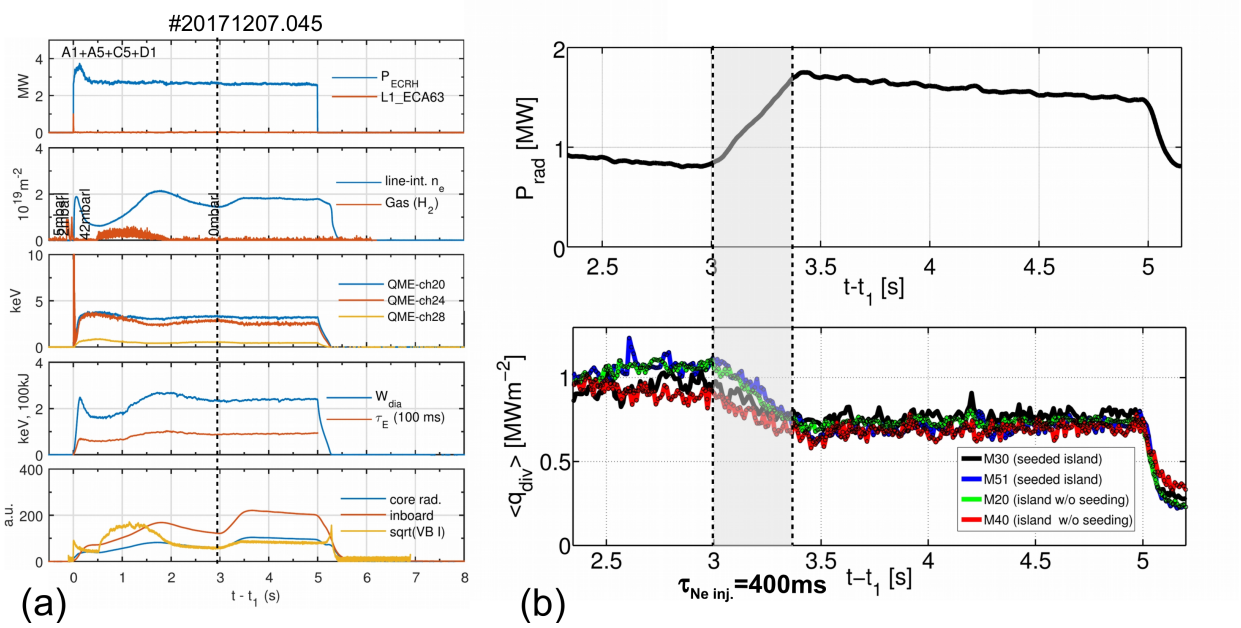

Figure 4.29 (a) Overview of central neon seeding experiment. (b) Time evolution of P_{rad} (top) and divertor peak heat fluxes $q_{\parallel,div}$ (bottom) [18].

The time evolution of P_{rad} measured with the bolometer and the divertor heat flux profiles on the horizontal divertor targets measured by IR cameras are compared in figure 4.29 (b) (top and bottom). The radiation increases by almost a factor of two. A drop of heat fluxes by $30-40\%$ after termination of the 400ms Ne injection is seen. The enhanced radiation decays only slowly over seconds, and the divertor heat fluxes increase only slowly and marginally after the end of Ne injection. Neon was injected only through a single divertor gas box valve into the island center at one toroidal location. However, a drop of heat fluxes is measured on horizontal targets connected to the seeded and the unseeded island as well.

In a second scenario N_2 was injected at the same location into the island (20171207.048). The overview of the main plasma parameter is shown in figure 4.30(a). The ECRH power was 2 MW.

The line average density $\int n_e dl \approx 1.6 \cdot 10^{19}$ m^{-3}. Nitrogen is injected at $t - t_1 = 3$ s for 270 ms and at $t - t_1$ =4.5 s for 50 ms (indicated by dashed lines). The nitrogen particle flux rate is $\Gamma_N \approx 2 \cdot 10^{20}$ s^{-1}.

The line averaged density is increased by 20% in response to the N_2 injection. The edge radiation is enhanced by 40%. The energy confinement properties remain constant in response to the impurity seeding. The electron temperature T_e measured with the Helium beam in the seeded island and the heat fluxes on the divertors connected to the seeded island are shown in figure 4.30(b) (top and bottom). The time evolution of is shown for channels 1, 9, 5 and 13 which correspond to increasing radial distance from the horizontal target towards the separatrix (indicated by the arrow labeled with r_{eff}). The error bars plotted for the T_e measurements are total uncertainties, which include the actual measurement uncertainty in the order of 5-8 eV and also the systematic uncertainty from the collisional-radiative model used for analysis of the line ratio values measured on He line emission[119].

Both T_e and $q_{div,max}$ show a drop in response to the N_2 injection, but also a relatively fast recovery almost over the same time scale as the injection time O(100 ms) in correlation with the response of P_{rad} shown in figure 4.30(a). Similarly, a fast drop and recovery occurs during the second short N_2 injection $t - t_1$ =4.5 s.

This scenario demonstrates that nitrogen allows for radiative power exhaust without confinement degradation, but generally features a fast recovery of plasma parameters after termination of the puff. This is in agreement with measurements made during the experiments in the limiter configuration and suggests low recycling on graphite walls.

The comparison of neon and nitrogen seeding shows that neon is a more efficient radiator, because stronger radiative exhaust ($\frac{\Delta P_{rad,N2}}{\Delta P_{rad,Ne}} \approx 0.4$) was achieved with less particles ($\frac{\int \Gamma_{N2} d\tau}{\int \Gamma_{Ne} d\tau}$ ≈2.7). This is certainly due to the higher number of energy levels of Ne atoms compared to N atoms

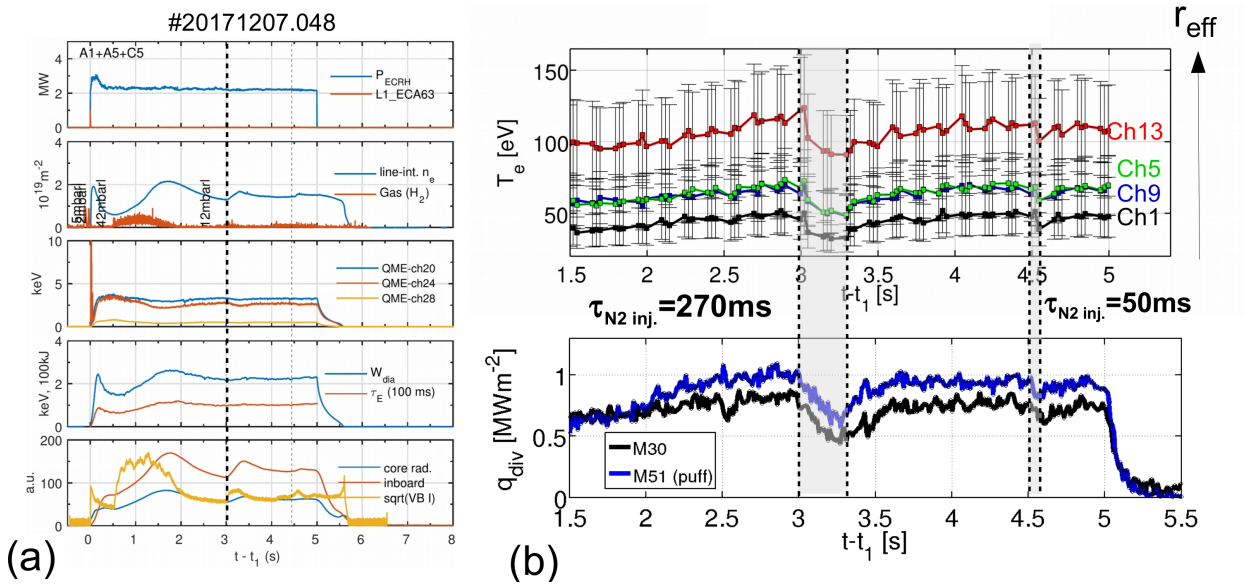

Figure 4.30 (a) Overview of central neon seeding experiment. (b) Time evolution of P_{rad} (top) and divertor peak heat fluxes $q_{\parallel,div}$ (bottom) [18].

($Z = 10$ vs. $Z = 7$). Furthermore, nitrogen will have a lower residence time due to its low recycling on the graphite walls and therefore requires a higher influx to sustain a certain level of line emission.

Both radiators suggest allowing for edge cooling and reduction of divertor heat loads without degradation of energy confinement. Effects on sputtering and symmetry of cooling will be a matter of further analysis and are beyond the scope of the presented work.

4.2.7.3 Seeding in different island geometries

The island SOL geometry is an important parameter determining the transport of seeded impurities and eventually the optimization of radiative power exhaust and detachment scenarios with impurity seeding. The island SOL geometry was manipulated with the island control coils experimentally. Application of full control coil current I_{CC} =2.5 kA increases the shear of the island, causes ergodization in the vacuum plot and increases the width of the SOL.

A sketch of the vacuum Poincaré Plot is shown in figure 4.31 (a). The ergodization does not affect the open field line domain, and the L_C rather shorten by a factor 0.5. Here, the effect on the time evolution of Bolometer P_{rad} is of interest. The total radiation is compared between standard island divertor configuration with I_{CC} =0 kA (blue) and with manipulated island geometry with I_{CC} =2.5 kA (red). Here, feed forward fueling is used and therefore the discharge needed some time to equilibrate. Neon is injected at $t - t_1$ =0.7 s. The effective time decay τ_{Prad} is obtained by fitting the Bolometer time signals in both configurations. One obtains $\tau_{Prad} = 547$ms for I_{CC} =0 kA and $\tau_{Prad} = 237$ ms for I_{CC} =2.5 kA.

These results indicate a faster decay in the configuration with I_{CC} =2.5kA. This may be in correlation to faster impurity exhaust due to shortening of L_C and improved impurity screening. However, a more refined analysis based on further experimental data maybe require in order to exclude also the influence of changes of main plasma parameters on the evolution of the total radiated power.

These scenarios will furthermore be investigated with 3D modeling. The manipulation of island geometry may to some extent allow to simulate effects of β induced changes of the edge island as discussed in the next section.

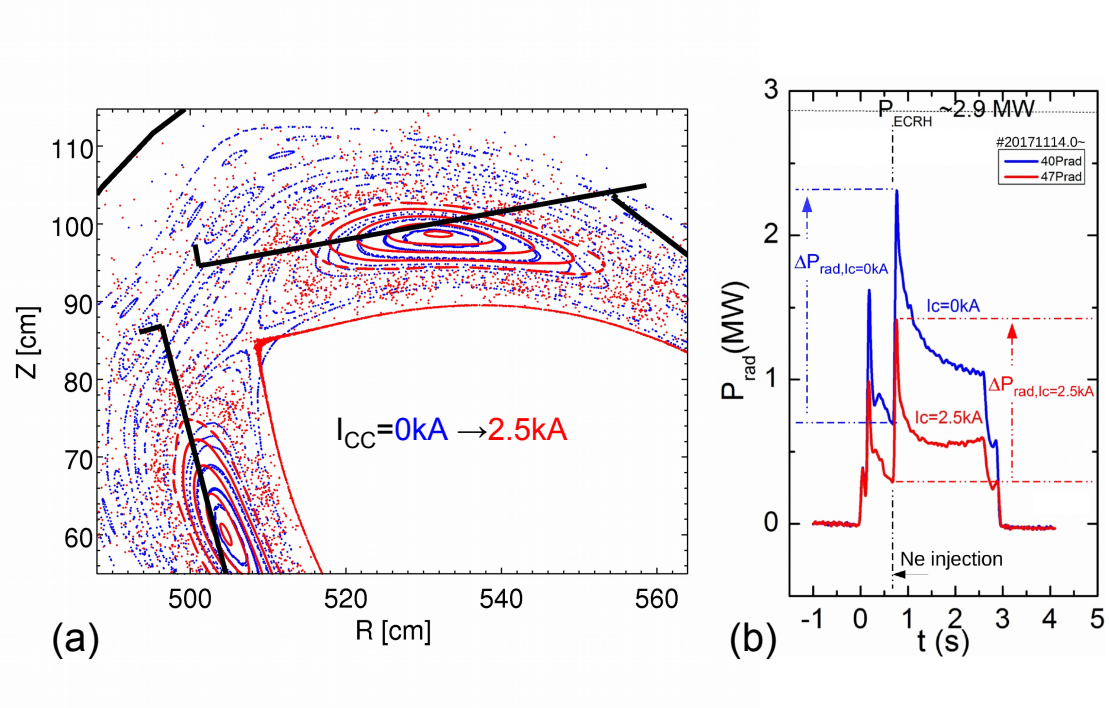

Figure 4.31 Variation of island SOL geometry. (a) Poincaré plot of vacuum magnetic field for $I_{CC} = 0$ (blue) vs $I_{CC} = 2.5$ kA (red). (b) $P_{rad}(t)$ for $I_{CC} = 0$ (blue) vs $I_{CC} = 2.5$ kA (red)

4.3 Summary for island divertor scenarios

Predictive modeling served for a basic assessment of the main plasma transport properties of the standard configuration and geometrically similar configurations such as the narrow high mirror configurations. The formation of islands in the SOL separates the recycling and impurity source from the confinement region. This is beneficial for impurity screening and exhaust, but may be disadvantageous for fueling and refueling.

The connection lengths are increased by a factor of 10 compared to the limiter configuration. Due to the long parallel path lengths diffusive transport may play a more significant role, that is

the $^{\perp}/_{\parallel}$-transport ratio is increased. The analysis of local profiles is more complicated compared to the limiter SOL due to the shear within the edge islands.

A simple SOL cannot hold anymore due to the additional weight of cross-field transport, additional particle sources and moreover the higher collisionality and existence of parallel temperature gradients within the island SOL. Divertor heat and particle loads were discussed for the two main divertor configurations of interest. A major concern is the optimization of the steering and exhaust of heat fluxes. It was demonstrated that the narrow high mirror configuration features a more even distribution of heat and particle fluxes on the main divertor targets, although its SOL geometry is very similar to the one of the standard divertor configuration.

Modeling demonstrates that impurity seeding can be used to dissipate power in island divertor scenarios. The recycling behavior and source locations altogether may determine the effectiveness of radiative power exhaust.

Experiments have been conducted based on preparation by modeling. Enhancement of P_{rad} and reduction of heat fluxes was demonstrated experimentally without degradation of energy confinement. Effects of island geometry changes have been investigated experimentally by application of control coils. These geometry effects are compared with β induced changes of the edge geometry.

The preliminary experimental findings need to be investigated further. Modeling will be adjusted to recover and interpret the main experimental findings and inform next step experiments towards radiative power exhaust in high-performance scenarios and detachment optimization.

The link to the results obtained in the limiter configuration, more detailed conclusions, and future work will be provided in the next section.

Chapter 5

Conclusions and outlook

A first-time study of plasma and impurity edge transport properties with the focus on heat flux characteristics and controlled radiative power exhaust at W7-X was presented. The assessment of two fundamentally different magnetic configurations - the limiter and the island divertor - allowed to investigate generic aspects of the edge transport and its dependence on the edge magnetic structure. Within this first time investigation of power exhaust by line radiation od impurities, the impurity transport, and the resulting radiation distributions have been investigated for carbon as main intrinsic impurities and for actively injected impurities, namely nitrogen and neon.

5.1 Conclusions for limiter scenarios

In the investigation of the startup limiter scenario, it was found that the scrape-off layer consists of three well-separated magnetic flux channels. The limiters create an open field line domain which is concerning the parallel length and the nested flux surface structure within the boundary vacuum field similar to tokamaks (averaged target-to-target connection lengths $< L_C >\approx$50 m). Therefore the plasma transport and heat flux characteristics have been assessed according to the simple scrape-off layer model and typical exponential decay relations used for the SOL domain within tokamaks.

The limiters created an open field line domain which consists of three types of magnetic flux bundles, $L_C = 36$ m, $L_C = 43$ m and $L_C = 79$ m, which corresponds to 1,1.2 and 2.2 toroidal test particle orbits around the device[7].

It is shown, that heat and particle fluxes are governed by the 3D flux tube geometry, and they feature some characteristic differences depending on the connection length of the SOL channel considered. Most noticeably, the longer flux tubes receive more heat and particles across the LCFS and therefore feature higher pressure and downstream heat and particle loads.

The magnetic flux tubes connect from a given poloidal plane with specific connection length towards the limiter. The path along the shortest connection length undergoes the highest level of plasma acceleration, and hence, counterstreaming ion flows are established in the modeling because adjacent flux tubes connect into the opposite toroidal direction on the shortest parallel length scale [7].

One challenge of stellarators with a low order rational surface at the edge is the high sensitivity of the boundary magnetic structure to changes of the value of the magnetic shear at the edge quantified by the ι value. For the limiter campaign, it was shown that within a change of $\Delta\iota \approx 5\%$ the main characteristics of the plasma edge transport is relatively insensitive. This was applied to change plasma core transport characteristics[95]. Although the poloidal distribution of connection lengths is changed, the general feature of three different types of connection lengths is maintained. The ratio of parallel to perpendicular transport is not changed due to this geometry change.

The modeling shows maximum deposited heat and particle loads (q_{depo}, Γ_{depo}) always in the domain of the longest flux tubes ($L_C = 79$ m). This was confirmed with IR camera measurements [9, 10].

The experimentally realized conditions of limiter plasmas were found to be characterized by low electron collisionality ($\nu_e^* < 5$) and dominantly convective heat transport. The parallel temperature gradients in the limiter SOL flux channels remain small, even under high density conditions with emerging downstream sources. It was shown that for these conditions and in the 3D edge geometry of the limiter configuration, an analysis of the 3D modeling results based on the simple

SOL model can be conducted. In this simple model, a generally isothermal SOL with ionization source located within the LCFS is assumed.

The analysis of the 1D radial profiles obtained from full 3D modeling provides strong support that the decay of main plasma parameter and in particular the downstream parallel heat flux follows mostly the scaling for L_C and diffusive transport predicted by the simple SOL:

$$\lambda_q \propto \lambda_n \propto \sqrt{D_\perp L_C} \tag{5.1}$$

Radial plasma profiles in longer flux tubes show a slower decay than those in short ones. Plasma decay in long and short magnetic flux tubes does scale exactly by $\sqrt{2}$ due to their 3D helical shape and due to the details of the heat and particle exchange between neighboring radially overlapping transport channels [9].

A density scan revealed that the limiter remains in linear low recycling regime for $n_{LCFS} = 1{\cdot}10^{18} - 1.6{\cdot}10^{19}$ m^{-3}. A transition to higher collisionality regime can be established and introduce parallel temperature gradients. It also causes the distribution of the available energy influx into the domain across more particles, which yields reduced temperature and an increase of dilution of energy at fixed input power and an increase of the widths of the deposited heat fluxes $\lambda_{q,depo}$.

It is found that the power losses by line emission of intrinsic impurities reduce temperatures and heat flux levels. It is shown, that the limiter releases impurities mostly into the confinement region. In this case, impurities radiate mostly in the confinement domain and only $\approx 25\%$ power losses occur in the SOL. An estimation of the yields for oxygen and carbon based on the experimentally measured total radiated power suggests relatively high chemical erosion yields of 6% and 12%, respectively. These yields define in the modeling a radiative density limit between $n_{LCFS} = 6 - 8 \cdot 10^{18}$ m^{-3} for oxygen or $n_{LCFS} = 8 - 10 \cdot 10^{18}$ m^{-3} for carbon at an input power of $P = 2$ MW.

For actively injected impurities, the recycling assumptions for nitrogen and neon as active gas species were found to be an important input for the modeling.

Nitrogen seeding under the assumption of zero recycling is found to radiate deeper in the main SOL. Thereby, heat fluxes may still be reduced at the maximum peak location. Yet, the radial temperature gradient is increased and thereby λ_q decreases. This may indicate a disadvantage of N_2 as coolant gas.

For neon, a case with seeding and zero recycling is compared with a case with full recycling (sourcing from the limiter only). In both cases, neon features a radiation distribution peaking in the confinement. The ratio of SOL to total power losses, $\frac{P_{rad,SOL}}{P_{rad,tot}}$, is in this cases $\approx 21\%$ for seeding and $\approx 8\%$ for recycling. This indicates that recycling of Ne may enhance the fraction of power losses in confinement.

Experiments during the limiter campaign suggest low recycling for nitrogen and high recycling for neon in agreement observations at LHD [48].

It is found by modeling, that limiter heat fluxes can principally be reduced in a controlled way with additional impurity seeding. Nitrogen and moreover neon are more effective radiators than the wall material carbon. Neon allows for a spatially more homogeneous heat flux reduction since its cooling function has maxima at higher temperatures, and it may also distribute more evenly at the core-SOL interface due to its high recycling properties. These characteristic radiation patterns are also recovered by comparing synthetically reproduced experimental radiation patterns from video diagnostics.

The analysis of this comparably well structured but still fully 3D plasma edge geometry of the limiter configuration enabled to identify important generic trends for the edge plasma transport and the radiation distribution. A similar overview of the analysis results for the island divertor configurations is presented in the next section.

5.2 Conclusions for divertor scenarios

A comparative study to the limiter configuration has been performed with the central goal to explore the heat fluxes and capability for radiative edge cooling in island divertor scenarios. This involved a similar basic characterization of the plasma transport and based on that, the investigation of the impurity transport to understand radiation distributions. Matching the limiter configuration study, also for the island divertor carbon was considered as an intrinsic impurity, and then N_2 and Ne as actively injected impurities were investigated.

First, the main geometric properties of the island divertor were investigated. Island divertor scenarios feature around the inner separatrix connection lengths of several kilometers, within the island volume $L_C \approx 300$ m and in the remote SOL and private flux region several 10 m down to several meters. This means that the resulting level of total perpendicular flux driven by cross-field transport can be enhanced when compared to the limiter configuration due to the relatively long L_C in the main island SOL.

The plasma edge for the configurations investigated is formed by a $5/5$ resonance, which results in five island bands, which each connect two of the ten divertor modules at a distance of 180 degrees toroidally. It was shown that these island bands represent transport channels for efficient exhaust of heat and particles. They feature a dedicated perpendicular transport internal to the island domain. On the one hand, they allow for diffusive flux across the relatively long connection lengths. Furthermore, the islands feature an additional projection of parallel transport in the radial direction internally, because of the magnetic shear. This establishes a direct connection from the upstream location at the separatrix to the downstream location at the divertor plates within the island.

To evaluate the ratio of perpendicular to parallel transport in the long L_C island domain, typically the parallel heat conductivity is compared to the perpendicular one. In the initial density

scenarios, this analysis applied to the modeling results suggests still strong parallel conductive transport compared to the perpendicular one. For an upstream density of $n_{up} = 1 \cdot 10^{19}$ m^{-3}, $D_{\perp} = 0.5$ m^{2}s^{-1} and input power of $P = 2.5$ MW it is shown that the parallel heat conduction dominates within the island already for $T_e > 17$ eV (see equation 2.44).

This basic analysis shows that the island acts as a magnetic flux bundle dominating the SOL, which, however, features a sub-confinement domain due to the internal flux surfaces and hence a more complex SOL transport physics background applies than seen for the limiter scenarios.

Analysis of local island divertor plasma profiles shows flattening in the density profile. For the input parameter as mentioned above, one finds still a substantial role of parallel transport compared to the perpendicular one. Therefore the flattening effect is related to the strong parallel transport through the island.

Analysis of the parallel profiles along open field lines within the island confirms the existence of parallel density and temperature gradients. Parallel transport guided by magnetic field lines within the island near the separatrix feature the highest temperature gradients since they are closest to the edge-core interface at the upstream position. These parallel gradients are driving the effective parallel transport recovered in the comparison to the perpendicular part before. Hence, the density increases downstream in the parallel profiles of field lines close to the separatrix, because of the strong recycling and particle source at the strike line location.

The sensitivity of the plasma transport on the magnetic edge structure was investigated by studying for the first time the newly designed 'narrow high mirror configuration'. This configuration minimizes the expected bootstrap current and hence offers a path to a stable edge geometry during the bootstrap current ramp up during long pulse high-performance discharges.

Parameter scans between both configurations show similar global scaling of upstream to downstream transport. As in the increased ι limiter configuration, the global geometric features of the standard divertor configuration are maintained in the 'narrow high mirror' configuration (which

was the goal). However, in the 3D modeling, it is seen that a shift of strike lines such that the vertical divertor plates receive more integral heat and particle loads than the horizontal target plates.

IR measurement confirmed the shift of the divertor heat flux pattern according to the predictions by modeling.

A critical element of divertor analysis is the recycling regime. This was studied in detail elsewhere, but qualitative comparisons in this thesis show that the general; recycling behavior is not affected drastically by the configuration change, other than a more homogeneous distribution of the heat and particle fluxes.

This basic study of the edge magnetic structure and the general transport characteristics then allowed to address impurity transport and the radiation distribution. Low radiative power exhaust scenarios have been modeled for prescribed power loss fractions of either 20% in case of carbon or 40% in case of nitrogen seeding and neon sourcing.

Eroded carbon and neon sourced according to the particle flux distribution show localization of the radiation near the strike lines. Nitrogen radiation, under the assumption of zero recycling, shows strong accumulation within the island.

Major features of the radiation and flow patterns have been investigated and recovered by synthetic diagnostics [120, 118]. Bolometer measurements confirmed the asymmetry between the inboard and outboard radiation intensity predicted by EMC3-EIRENE modeling.

It is shown that the strongest mitigation of critical target heat loads can be achieved with impurities coupled to the recycling flux on the divertor targets (according to erosion or recycling of impurities). However, it is less efficient concerning the required impurity fluxes realizing a prescribed power loss fraction of 40% compared to the same impurity species sourced from the seeding location. Comparison of different coolant gases shows that Neon and Argon are due to their cooling potentials the most efficient radiators to realize a prescribed power loss fraction of 40%.

Modeling of the standard island divertor configuration with increased islands and reduced L_C. The application of full control coil current ($I_{CC} = 2.5$ kA) results in a reduction of connection lengths by a factor of 0.6 similar to higher β scenarios. A drop and concentration in the radiation distribution is found for similar boundary conditions and equal neon influx. A single reservoir particle balance analysis suggest enhanced exhaust of impurities based on a reduced particle residence time $\tau_{p,Ne}$. This indicates the feasibility of fine adjustment of impurity transport and radiative exhaust by the island geometry.

Impurity seeding experiments have been designed and conducted based on initial 3D modeling data and based on the impurity fluxes used during the limiter campaign. First neon seeding experiments showed the feasibility of heat flux reduction while maintaining core energy confinement for scenarios with $P_{ECRH} = 2.5 - 2.9$ MW at upstream densities of $n_e \approx 1 - 1.8 \cdot 10^{19}$ m^{-3}. The first analysis of heat flux data from IR cameras and electron temperatures obtained from helium beam measurements suggests cooling in clear correlation to the radiation enhancement.

Neon and nitrogen seeding experiments have shown different time evolutions of P_{rad} and temperature related plasma parameters. Radiation enhancement by neon injection is sustained at a high level and decays over seconds after termination of the puff. Nitrogen shows fast drop of radiation and recovery of heat fluxes and temperatures after the injection over the time scale of the puff duration (O(100 ms)). This suggests high recycling for Ne and low recycling for N_2. Neon was found to be a more effective radiator than nitrogen.

In a further experiment, the edge magnetic geometry has been changed by island control coils. A faster drop of total radiated power in time is estimated based on an effective time decay τ_{Prad} in the experiment with $I_{CC} = 2.5$ kA and reduced L_C. This faster decay of radiation is assumed to be correlated to a reduced particle dwell time of Neon predicted by EMC3-EIRENE modeling. This experiment demonstrated the possibility of controlling the edge impurity transport and radiation

exhaust with the island geometry which is of importance in future impurity seeded detachment scenarios.

The effect of the remaining equilibrium change for increasing plasma pressure will be a result of a growing Shafranov shift. Such equilibrium effects are considered for one example for the high mirror configuration with $\beta = 3\%$ generated with the 3D MHD HINT Code. It is shown that these equilibrium scenarios are geometrically very similar to the geometry established by the island control experiments.

5.3 Future work and further enhancements identified in this study

In the following remaining topics and open questions are briefly discussed based on the results which were obtained so far. Most of these aspects were identified for further detailed studies and not necessarily within the scope of the present thesis.

Due to the limitations of edge diagnostics during the limiter configuration rather global studies concerning energy and particle confinement, power balance and study of general physics aspects are recommended. Contributions from wall recycling and erosion should be discussed based on a simplified wall geometry.

A particular topic to be addressed is the MARFE phenomenon studied observed within various limiter scenarios [113]. Here, an analysis was initiated in the present study but needs an extension of the simulation domain and careful treatment of the core boundary conditions and impurity transport.

The intrinsic carbon was modeled based on an effective sputtering yield. This yield defined an impurity flux scaled with the recycling flux, which is a reasonable assumption mostly for chemical sputtering and erosion. The general approach is to perform sensitivity analysis for the transport of impurities concerning the yield factor (e.g., 0.5-10$\%$) and the kinetic start energy (e.g., determined

by the surface temperature). However, more sophisticated models for physical sputtering, self-sputtering, and models including the effects of surface roughness exist and should be implemented.

The two limiter magnetic field configurations considered in this study were based on ideal coil geometries. However, due to electromagnetic forces, the coils changed their shape and slightly decreased the rotational transform. This can cause a shift of the 5/6 islands in the confinement region closer to the limiter into the particle source region. Comparing cases with islands in the confinement domain close to the limiter and further away might show a significant change in the particle confinement times. For comparisons with experimental measurements, in particular, IR, the re-distribution of limiter heat loads would be the topic of interest.

The limiter configuration is an ideal geometry for benchmark and comparisons between different 3D, 2D, and 1D modeling. Its relatively simple flux tube and flux surface geometry allow for a definition of magnetic coordinates and more sophisticated characterization of different low and high collisionality regimes.

The limiter configuration should be compared to divertor scenarios and divertor-limiter configurations for a more general and consistent comparison of these two concepts. The limiter field configurations may be proposed for experiments to study its main transport and PSI effects during divertor-limiter scenarios established during bootstrap current evolution in high-performance scenarios.

The role of anomalous cross-field transport may need more attention. Measurements with He beam spectroscopy suggest relatively flat island profiles even in low density divertor scenarios. A detailed comparison of modeling and various edge diagnostics with a focus on density, temperature, heat flux and particle flux measurements would be required to provide an estimation of actual $D_\perp$ and $\chi_\perp$ and identify potential additional wall sources which might contribute to an increase in decay of plasma edge parameters.

The analysis of impurity seeding experiments needs first further adjustment based on the ongoing analysis of experimental data. The modeling needs to informed by accurate surveys of the intrinsic impurity content to determine power losses from the intrinsic source.

Modeling of limiter and divertor scenarios has previously shown that faster parallel transport can be more effective within shorter transport channels. This major geometric feature will be investigated by modeling in more detail, soon. These experiments and related analysis by 3D modeling will contribute to the physics topic of stabilization and control of high radiative detached island divertor scenarios.

An update of the model towards more self-consistent recycling or self-sputtering is encouraged to simulate the full cycle establishing the final distribution of high recycling impurities.

Comparisons with equilibrium reconstruction by V3FIT or even use of grids based on magnetic fields recovered by V3FIT should be used to allow for best approximation of experimental edge geometry.

A systematic assessment of detachment by nitrogen and neon is desired since it will inform experiment proposals. Control of detachment by impurity seeding may become more relevant in future scenarios with tungsten wall coating or by complete replacement of graphite targets by all metal targets.

Several of these items for the divertor configuration will be addressed by experiments in the upcoming second part of the first island divertor campaign. The framework of modeling results and the basics studies conducted in this thesis will serve as a basis for the planning, execution, and analysis of these experiments.

LIST OF REFERENCES

[1] A. Kallenbach, M. Balden, R. Dux, T. Eich, C. Giroud, A. Huber, G.P. Maddison, M. Mayer, K. McCormick, R. Neu, T.W. Petrie, T. Ptterich, J. Rapp, M.L. Reinke, K. Schmid, J. Schweinzer, and S. Wolfe. Plasma surface interactions in impurity seeded plasmas. *Journal of Nuclear Materials*, 415(1, Supplement):S19 – S26, 2011. Proceedings of the 19th International Conference on Plasma-Surface Interactions in Controlled Fusion.

[2] G. Grieger, C. Beidler, E. Harmeyer, W. Lotz, J. Kisslinger, P. Merkel, J. Nührenberg, F. Rau, E. Strumberger, and H. Wobig. Modular Stellarator Reactors and Plans for Wendelstein 7-X. *Fusion Technology*, 21(3):1767–1778, 1992.

[3] Y. Feng. On the emc3-eirene code. *Seminar talk*.

[4] P. C. Stangeby. *The Plasma Boundary of Magnetic Fusion Devices*. Plasma Physics Series. Nicki Dennis, 2000.

[5] J Geiger, C D Beidler, Y Feng, H Maaberg, N B Marushchenko, and Y Turkin. Physics in the magnetic configuration space of w7-x. *Plasma Physics and Controlled Fusion*, 57(1):014004, 2015.

[6] Y. Feng, F. Sardei, P. Grigull, K. McCormick, J. Kisslinger, and D. Reiter. Physics of island divertors as highlighted by the example of w7-as. *Nuclear Fusion*, 46(8):807, 2006.

[7] F. Effenberg, Y. Feng, O. Schmitz, H. Frerichs, S.A. Bozhenkov, H. Hlbe, R. Knig, M. Krychowiak, T. Sunn Pedersen, D. Reiter, L. Stephey, and W7-X Team. Numerical investigation of plasma edge transport and limiter heat fluxes in wendelstein 7-x startup plasmas with emc3-eirene. *Nuclear Fusion*, 57(3):036021, 2017.

[8] F. Effenberg, Y. Feng, O. Schmitz, H. Frerichs, S. Bozhenkov, J. Geiger, H. Niemann, M. Jakubowski, R. König, M. Krychowiak, T. S. Pedersen, D. Reiter, L. Stephey, and G. Wurden. 3-D Modeling of Edge Transport and Plasma Surface Interactions for Wendelstein 7-X Startup Plasmas, 2016.

[9] F. Effenberg, Y. Feng, O. Schmitz, S. A. Bozhenkov, H. Frerichs, J. Geiger, H. Hölbe, M. Jakubowski, R. König, M. Krychowiak, H. Niemann, T. S. Pedersen, D. Reiter, L. Stephey, G. A. Wurden, and W7-X Team. 3-D Modeling of Heat Transport in Wendelstein 7-X Startup Plasmas with EMC3-EIRENE. Kyoto, 2016.

[10] G.A. Wurden, C. Biedermann, F. Effenberg, M. Jakubowski, H. Niemann, L. Stephey, S. Bozhenkov, S. Brezinsek, J. Fellinger, B. Cannas, F. Pisano, S. Marsen, H.P. Laqua, R. Knig, O. Schmitz, J.H. Harris, E.A. Unterberg, and the W7-X Team. Limiter observations during w7-x first plasmas. *Nuclear Fusion*, 57(5):056036, 2017.

[11] H. Niemann, F. Effenberg, M. Jakubowski, R. König, T. S. Pedersen, G. Wurden, and Max Planck Society W7-X Team, Max Planck Institute for Plasma Physics. Power loads and fall-off lengths in the limiter and divertor phase of Wendelstein 7-X, 2017.

[12] H. Niemann, A. Ali, P. Drewelow, F. Effenberg, M. Jakubowski, R. König, F. Pisano, A. Puig Sitjes, T. S. Pedersen, G. Wurden, and Max Planck Society W7-X Team, Max Planck Institute for Plasma Physics. Power loads in the scrape-off layer of Wendelstein 7-X, 2017.

[13] L. Stephey, A. Bader, F. Eenberg, O. Schmitz, G. A. Wurden, D. T. Anderson, F. S. B. Anderson, C. Biedermann, A. Dinklage, H. Frerichs, J. Geiger, J. Harris, R. Konig, M. Kornejew, P. Krychowiak, J. Lore, E. A. Unterberg, and the W7-X team. Control of neutral particle fueling and exhaust by edge topology optimization in Wendelstein 7-X and HSX. In American Physical Society, editor, *58th Annual Meeting of the APS Division of Plasma Physics* , volume 61 of *Bulletin of the American Physical Society*, San Jose, 2016.

[14] M. Krychowiak, A. Adnan, A. Alonso, T. Andreeva, J. Baldzuhn, T. Barbui, M. Beurskens, W. Biel, C. Biedermann, B. D. Blackwell, H. S. Bosch, S. Bozhenkov, R. Brakel, T. Bruer, B. Brotas de Carvalho, R. Burhenn, B. Buttenschn, A. Cappa, G. Cseh, A. Czarnecka, A. Dinklage, P. Drews, A. Dzikowicka, F. Effenberg, M. Endler, V. Erckmann, T. Estrada, O. Ford, T. Fornal, H. Frerichs, G. Fuchert, J. Geiger, O. Grulke, J. H. Harris, H. J. Hartfu, D. Hartmann, D. Hathiramani, M. Hirsch, U. Hfel, S. Jaboski, M. W. Jakubowski, J. Kaczmarczyk, T. Klinger, S. Klose, J. Knauer, G. Kocsis, R. Knig, P. Kornejew, A. Krmer-Flecken, N. Krawczyk, T. Kremeyer, I. Ksiek, M. Kubkowska, A. Langenberg, H. P. Laqua, M. Laux, S. Lazerson, Y. Liang, S. C. Liu, A. Lorenz, A. O. Marchuk, S. Marsen, V. Moncada, D. Naujoks, H. Neilson, O. Neubauer, U. Neuner, H. Niemann, J. W. Oosterbeek, M. Otte, N. Pablant, E. Pasch, T. Sunn Pedersen, F. Pisano, K. Rahbarnia, L. Ry, O. Schmitz, S. Schmuck, W. Schneider, T. Schrder, H. Schuhmacher, B. Schweer, B. Standley, T. Stange, L. Stephey, J. Svensson, T. Szabolics, T. Szepesi, H. Thomsen, J.-M. Travere, H. Trimino Mora, H. Tsuchiya, G. M. Weir, U. Wenzel, A. Werner, B. Wiegel, T. Windisch, R. Wolf, G. A. Wurden, D. Zhang, A. Zimbal, S. Zoletnik, and W7-X Team. Overview of diagnostic performance and results for the first operation phase in wendelstein 7-x (invited). *Review of Scientific Instruments*, 87(11), 2016.

[15] T. Barbui, F. Effenberg, O. Schmitz, M. Krychowiak, R. König, S. Klose, D. Zhang, J.M. Muñoz Burgos, P. Drews, Y. Liang, S. Liu, O. Neubauer, A. Terra, B. Schweer, and B.D. Blackwell. Local temperature effects in the helical scrape-off layer of startup plasmas at Wendelstein 7-X due to N seeding. In American Physical Society, editor, *58th Annual Meeting of the APS Division of Plasma Physics* , volume 61 of *Bulletin of the American Physical Society*, San Jose, 2016.

[16] J. Geiger, C. D. Beidler, Y. Feng, N. B. Marushchenko, Y. Turkin, and Max Planck Society W7-X Team, Max Planck Institute for Plasma Physics. Plasma Equilibrium and core confinement on W7-X with an island divertor, 2017.

[17] F. Effenberg, Y. Feng, H. Frerichs, O. Schmitz, T. Barbui, J. Geiger, M. Jakubowski, R. König, M. Krychowiak, H. Niemann, T. S. Pedersen, Y. Suzuki, G.A. Wurden, and Max Planck Society W7-X Team, Max Planck Institute for Plasma Physics. 3D Numerical Analysis of Radiative Edge Cooling in Wendelstein 7-X Island Divertor Scenarios. In American Physical Society, editor, *59th Annual Meeting of the APS Division of Plasma Physics* , volume 62 of *Bulletin of the American Physical Society*, Milwaukee, WI, 2017.

[18] F. Effenberg, S. Brezinsek, Y. Feng, M. Jakubowski, R. König, M. Krychowiak, O. Schmitz, A. Ali, T. Barbui, C. Biedermann, S. A. Bozhenkov, P. Drewelow, H. Frerichs, Y. Gao, J. Geiger, G. Kocsis, H. Niemann, T. S. Pedersen, A. Puig Sitjes, Y. Suzuki, T. Szepesi, U. Wenzel, V. Winters, G. A. Wurden, D. Zhang, and Max Planck Society W7-X Team, Max Planck Institute for Plasma Physics. Exploration of Radiative Edge Cooling in the Island Divertor at Wendelstein 7-X, 2017.

[19] Tim Abram and Sue Ion. Generation-iv nuclear power: A review of the state of the science. *Energy Policy*, 36(12):4323 – 4330, 2008. Foresight Sustainable Energy Management and the Built Environment Project.

[20] Giorgio Locatelli, Mauro Mancini, and Nicola Todeschini. Generation iv nuclear reactors: Current status and future prospects. *Energy Policy*, 61:1503 – 1520, 2013.

[21] Pushker A. Kharecha and James E. Hansen. Prevented Mortality and Greenhouse Gas Emissions from Historical and Projected Nuclear Power. *Environmental Science & Technology*, 47(9):4889–4895, 2013. PMID: 23495839.

[22] J.R. Gilleland, Yu.A. Sokolov, K. Tomabechi, and R. Toschi. Iter: Concept definition. *Nuclear Fusion*, 29(7):1191, 1989.

[23] R Aymar, P Barabaschi, and Y Shimomura. The iter design. *Plasma Physics and Controlled Fusion*, 44(5):519, 2002.

[24] J. F. Santarius and B. G. Logan, editors. *Generic magnetic fusion rocket model*, June 1993.

[25] G. A. Wurden, T. E. Weber, P. J. Turchi, P. B. Parks, T. E. Evans, S. A. Cohen, J. T. Cassibry, and E. M. Campbell. A new vision for fusion energy research: Fusion rocket engines for planetary defense. *Journal of Fusion Energy*, 35(1):123–133, Feb 2016.

[26] A D Sakharov. *Fizika Plazmy i Problema Upravlyaemykh Termoyadernykh Reaktsii (Plasma Physics and the Problem of Controlled Thermonuclear Reactions)*, 1:20, 1958.

[27] Lyman Spitzer Jr. The stellarator concept. *The Physics of Fluids*, 1(4):253–264, 1958.

[28] Allen H. Boozer. What is a stellarator? *Physics of Plasmas*, 5(5):1647–1655, 1998.

[29] J D Lawson. Some criteria for a power producing thermonuclear reactor. *Proceedings of the Physical Society. Section B*, 70(1):6, 1957.

[30] T. Eich, B. Sieglin, A. Scarabosio, W. Fundamenski, R. J. Goldston, and A. Herrmann. Inter-ELM Power Decay Length for JET and ASDEX Upgrade: Measurement and Comparison with Heuristic Drift-Based Model. *Phys. Rev. Lett.*, 107:215001, Nov 2011.

[31] R.J. Goldston. Heuristic drift-based model of the power scrape-off width in low-gas-puff H-mode tokamaks. *Nuclear Fusion*, 52(1):013009, 2012.

[32] H. Zohm, C. Angioni, E. Fable, G. Federici, G. Gantenbein, T. Hartmann, K. Lackner, E. Poli, L. Porte, O. Sauter, G. Tardini, D. Ward, and M. Wischmeier. On the physics guidelines for a tokamak demo. *Nuclear Fusion*, 53(7):073019, 2013.

[33] G. Federici, R. Kemp, D. Ward, C. Bachmann, T. Franke, S. Gonzalez, C. Lowry, M. Gadomska, J. Harman, B. Meszaros, C. Morlock, F. Romanelli, and R. Wenninger. Overview of eu demo design and r&d activities. *Fusion Engineering and Design*, 89(7):882 – 889, 2014. Proceedings of the 11th International Symposium on Fusion Nuclear Technology-11 (ISFNT-11) Barcelona, Spain, 15-20 September, 2013.

[34] R. Wenninger, R. Albanese, R. Ambrosino, F. Arbeiter, J. Aubert, C. Bachmann, L. Barbato, T. Barrett, M. Beckers, W. Biel, L. Boccaccini, D. Carralero, D. Coster, T. Eich, A. Fasoli, G. Federici, M. Firdaouss, J. Graves, J. Horacek, M. Kovari, S. Lanthaler, V. Loschiavo, C. Lowry, H. Lux, G. Maddaluno, F. Maviglia, R. Mitteau, R. Neu, D. Pfefferle, K. Schmid, M. Siccinio, B. Sieglin, C. Silva, A. Snicker, F. Subba, J. Varje, and H. Zohm. The demo wall load challenge. *Nuclear Fusion*, 57(4):046002, 2017.

[35] A Gallo, N Fedorczak, S Elmore, R Maurizio, H Reimerdes, C Theiler, C K Tsui, J A Boedo, M Faitsch, H Bufferand, G Ciraolo, D Galassi, P Ghendrih, M Valentinuzzi, P Tamain, the EUROfusion MST1 team, and the TCV team. Impact of the plasma geometry on divertor power exhaust: experimental evidence from tcv and simulations with soledge2d and tokam3x. *Plasma Physics and Controlled Fusion*, 60(1):014007, 2018.

[36] U. Samm, G. Bertschinger, P. Bogen, J. D. Hey, E. Hintz, L. Konen, Y. T. Lie, A. Pospieszczyk, D. Rusbuldt, R. P. Schorn, B. Schweer, M. Tokar, and B. Unterberg. Radiative edges under control by impurity fluxes. *Plasma Physics and Controlled Fusion*, 35(SB):B167, 1993.

[37] A.M. Messiaen, J. Ongena, U. Samm, B. Unterberg, P.E. Vandenplas, G. Van Oost, G. Van Wassenhove, J. Winter, D. Boucher, P. Dumortier, F. Durodie, H.G. Esser, H. Euringer, B. Giesen, E. Hintz, M. Lochter, M.Z. Tokar, G.H. Wolf, G. Fuchs, D.L. Hillis, F. Hoenen, P. Huttemann, R. Koch, L. Konen, H.R. Koslowski, A. Kramer-Flecken, D. Pettiaux, A. Pospieszczyk, B. Schweer, H. Soltwisch, G. Telesca, R. Uhlemann, R. van Nieuwenhove, M. Vervier, G. Waidmann, and R.R. Weynants. Improved confinement with edge radiative cooling at high densities and high heating power in textor. *Nuclear Fusion*, 34(6):825, 1994.

[38] G. Telesca, H.A. Claassen, P. Franz, A.M. Messiaen, J. Ongena, J. Rapp, U. Samm, N. Schoon, B. Schweer, M.Z. Tokar', B. Unterberg, and G. Van Oost. Scaling of radiated power to plasma contamination for neon seeded discharges on boronized TEXTOR-94. *Journal of Nuclear Materials*, 241-243:853–856, 1997.

[39] J. Rapp, P. Monier-Garbet, G.F. Matthews, R. Sartori, P. Andrew, P. Dumortier, T. Eich, W. Fundamenski, M. von Hellermann, J. Hogan, L.C. Ingesson, S. Jachmich, H.R. Koslowski, A. Loarte, G. Maddison, D.C. McDonald, A. Messiaen, J. Ongena, V. Parail, V. Philipps, G. Saibene, B. Unterberg, and JET EFDA Contributors. Reduction of divertor heat load in JET ELMy H-modes using impurity seeding techniques. *Nuclear Fusion*, 44(2):312, 2004.

[40] A Kallenbach, M Bernert, R Dux, L Casali, T Eich, L Giannone, A Herrmann, R McDermott, A Mlynek, H W Mller, F Reimold, J Schweinzer, M Sertoli, G Tardini, W Treutterer, E Viezzer, R Wenninger, M Wischmeier, and the ASDEX Upgrade Team. Impurity seeding for tokamak power exhaust: from present devices via iter to demo. *Plasma Physics and Controlled Fusion*, 55(12):124041, 2013.

[41] M.L. Reinke, J.W. Hughes, A. Loarte, D. Brunner, I.H. Hutchinson, B. LaBombard, J. Payne, and J.L. Terry. Effect of N2, Ne and Ar seeding on Alcator C-Mod H-mode confinement. *Journal of Nuclear Materials*, 415(1, Supplement):S340 – S344, 2011. Proceedings of the 19th International Conference on Plasma-Surface Interactions in Controlled Fusion.

[42] G.P. Maddison, C. Giroud, G.K. McCormick, J.A. Alonso, B. Alper, G. Arnoux, P.C. da Silva Aresta Belo, M.N.A. Beurskens, A. Boboc, S. Brezinsek, I. Coffey, S. Devaux, T. Eich, W. Fundamenski, D. Harting, A. Huber, S. Jachmich, I. Jenkins, E. Joffrin, M.A.H. Kempenaars, M. Lehnen, T. Loarer, P.J. Lomas, A.G. Meigs, P.D. Morgan, V. Riccardo, F.G. Rimini, M.F. Stamp, G. Telesca, H. Thomsen, and JET EFDA contributors. Moderation of divertor heat loads by fuelling and impurity seeding in well-confined ELMy H-mode plasmas on JET. *Nuclear Fusion*, 51(4):042001, 2011.

[43] J. D. Lore, M. L. Reinke, D. Brunner, B. LaBombard, B. Lipschultz, J. Terry, R. A. Pitts, and Y. Feng. Three-dimensional simulation of H-mode plasmas with localized divertor impurity injection on Alcator C-Mod using the edge transport code EMC3-EIRENE. *Physics of Plasmas*, 22(5):056106, 2015.

[44] M. Bernert, M. Wischmeier, A. Huber, F. Reimold, B. Lipschultz, C. Lowry, S. Brezinsek, R. Dux, T. Eich, A. Kallenbach, A. Lebschy, C. Maggi, R. McDermott, T. Pütterich, and S. Wiesen. Power exhaust by SOL and pedestal radiation at ASDEX Upgrade and JET. *Nuclear Materials and Energy*, 12:111–118, 2017. Proceedings of the 22nd International Conference on Plasma Surface Interactions 2016, 22nd PSI.

[45] M. Kobayashi, S. Masuzaki, I. Yamada, Y. Narushima, C. Suzuki, N. Tamura, B.J. Peterson, S. Morita, C.F. Dong, N. Ohno, S. Yoshimura, Y. Feng, M. Goto, K. Sato, T. Akiyama, K. Tanaka, and the LHD experiment group. Control of 3D edge radiation structure with resonant magnetic perturbation fields applied to the stochastic layer and stabilization of radiative divertor plasma in LHD. *Nuclear Fusion*, 53(9):093032, 2013.

[46] K. Mukai, S. Masuzaki, B.J. Peterson, T. Akiyama, M. Kobayashi, C. Suzuki, H. Tanaka, S.N. Pandya, R. Sano, G. Motojima, N. Ohno, T. Morisaki, I. Murakami, J. Miyazawa, N. Tamura, S. Yoshimura, I. Yamada, R. Yasuhara, H. Funaba, and K. Tanaka. Development of impurity seeding and radiation enhancement in the helical divertor of lhd. *Nuclear Fusion*, 55(8):083016, 2015.

[47] T. Morisaki, K. Oyama, N. Tamura, S. Masuzaki, T. Akiyama, G. Motojima, J. Miyazawa, B.J. Peterson, N. Ohno, and H. Yamada. Radiated power distributions in impurity-seeded plasmas in LHD. *Journal of Nuclear Materials*, 463:640 – 643, 2015. 21Proceedings of the 21st International Conference on Plasma-Surface Interactions in Controlled Fusion Devices Kanazawa, Japan May 26-30, 2014.

[48] H. Tanaka, G. Kawamura, S. Masuzaki, M. Kobayashi, T. Akiyama, B.J. Peterson, K. Mukai, R. Sano, S.Y. Dai, R. Sakamoto, T. Morisaki, and N. Ohno. Toroidally symmetric/asymmetric effect on the divertor flux due to neon/nitrogen seeding in lhd. *Nuclear Materials and Energy*, 12:241 – 246, 2017. Proceedings of the 22nd International Conference on Plasma Surface Interactions 2016, 22nd PSI.

[49] G.F. Matthews. Plasma detachment from divertor targets and limiters. *Journal of Nuclear Materials*, 220-222:104 – 116, 1995. Plasma-Surface Interactions in Controlled Fusion Devices.

[50] Y. Feng, C.D. Beidler, J. Geiger, P. Helander, H. Hlbe, H. Maassberg, Y. Turkin, D. Reiter, and W7-X Team. On the w7-x divertor performance under detached conditions. *Nuclear Fusion*, 56(12):126011, 2016.

[51] J Geiger, R C Wolf, C Beidler, A Cardella, E Chlechowitz, V Erckmann, G Gantenbein, D Hathiramani, M Hirsch, W Kasparek, J Kilinger, R Knig, P Kornejew, H P Laqua, C Lechte, J Lore, A Lumsdaine, H Maaberg, N B Marushchenko, G Michel, M Otte, A Peacock, T Sunn Pedersen, M Thumm, Y Turkin, A Werner, D Zhang, and the W7-X Team. Aspects of steady-state operation of the wendelstein 7-x stellarator. *Plasma Physics and Controlled Fusion*, 55(1):014006, 2013.

[52] H. Hölbe, T. Sunn Pedersen, J. Geiger, S. Bozhenkov, R. König, Y. Feng, J. Lore, A. Lumsdaine, and the Wendelstein 7-X Team. Access to edge scenarios for testing a scraper element in early operation phases of Wendelstein 7-X. *Nuclear Fusion*, 56(2):026015, 2016.

[53] Y. Feng. Up-scaling the island divertor along the w7-stellarator line. *Journal of Nuclear Materials*, 438, Supplement:S497 – S500, 2013. Proceedings of the 20th International Conference on Plasma-Surface Interactions in Controlled Fusion Devices.

[54] F Warmer, C D Beidler, A Dinklage, R Wolf, and The W7-X Team. From w7-x to a helias fusion power plant: motivation and options for an intermediate-step burning-plasma stellarator. *Plasma Physics and Controlled Fusion*, 58(7):074006, 2016.

[55] Y Suzuki and J Geiger. Impact of nonlinear 3d equilibrium response on edge topology and divertor heat load in wendelstein 7-x. *Plasma Physics and Controlled Fusion*, 58(6):064004, 2016.

[56] C.C. Hegna. Healing of magnetic islands in stellarators by plasma flow. *Nuclear Fusion*, 51(11):113017, 2011.

[57] D.A. Spong, S.P. Hirshman, L.A. Berry, J.F. Lyon, R.H. Fowler, D.J. Strickler, M.J. Cole, B.N. Nelson, D.E. Williamson, A.S. Ware, D. Alban, R. Snchez, G.Y. Fu, D.A. Monticello, W.H. Miner, and P.M. Valanju. Physics issues of compact drift optimized stellarators. *Nuclear Fusion*, 41(6):711, 2001.

[58] Jong-Kyu Park and Nikolas C. Logan. Self-consistent perturbed equilibrium with neoclassical toroidal torque in tokamaks. *Physics of Plasmas*, 24(3):032505, 2017.

[59] M. Kobayashi, Y. Xu, K. Ida, Y. Corre, Y. Feng, O. Schmitz, H. Frerichs, F.L. Tabares, T.E. Evans, J.W. Coenen, Y. Liang, A. Bader, K. Itoh, H. Yamada, Ph. Ghendrih, G. Ciraolo, D. Tafalla, A. Lopez-Fraguas, H.Y. Guo, Z.Y. Cui, D. Reiter, N. Asakura, U. Wenzel, S. Morita, N. Ohno, B.J. Peterson, and S. Masuzaki. 3D effects of edge magnetic field configuration on divertor/scrape-off layer transport and optimization possibilities for a future reactor. *Nuclear Fusion*, 55(10):104021, 2015.

[60] Bibhu Prasad Sahoo, Devendra Sharma, Ratneshwar Jha, and Yhe Feng. 3d monte-carlo study of toroidally discontinuous limiter sol configurations of aditya tokamak. *Physics of Plasmas*, 24(8):082505, 2017.

[61] Steven Marcinko and Davide Curreli. Numerical characterization of the edge transport conditions and limiter fluxes of the hidra stellarator. *Physics of Plasmas*, 25(2):022507, 2018.

[62] G. Grieger and I. Milch. Das Fusionsexperiment WENDELSTEIN 7-X. *Physik Journal*, 49(11):1001–1005, 1993.

[63] J. Nührenberg, W. Lotz, P. Merkel, C. Nührenberg, U. Schwenn, E. Strumberger, and T. Hayashi. Overview on Wendelstein 7-X Theory. *Fusion Technology*, 27:71–78, 1995.

[64] G. Grieger, W. Lotz, P. Merkel, J. Nhrenberg, J. Sapper, E. Strumberger, H. Wobig, R. Burhenn, V. Erckmann, U. Gasparino, L. Giannone, H. J. Hartfuss, R. Jaenicke, G. Khner, H. Ringler, A. Weller, F. Wagner, the W7X Team, and the W7AS Team. Physics optimization of stellarators. *Physics of Fluids B*, 4(7), 1992.

[65] H. Renner, E. Strumberger, J. Kisslinger, J. Nhrenberg, and H. Wobig. Boundary modelling of the stellarator wendelstein 7-x. *Journal of Nuclear Materials*, 241:946 – 949, 1997.

[66] S. Bozhenkov, F. Effenberg, Y. Feng, J. Geiger, D. A. Hartmann, H. Hölbe, T. S. Pedersen, and R. C. Wolf. Limiter for the early operation phase of W7-X. In S. Ratynskaia, P. Mantica, A. Benuzzi-Mounaix, G. Dilecce, R. Bingham, M. Hirsch, B. Kemnitz, and T. Klinger, editors, *41st EPS Conference on Plasma Physics*, volume 38F of *Europhysics Conference Abstracts (ECA)*, Berlin, 2014.

[67] T. Sunn Pedersen, T. Andreeva, H.-S. Bosch, S. Bozhenkov, F. Effenberg, M. Endler, Y. Feng, D.A. Gates, J. Geiger, D. Hartmann, H. Hölbe, M. Jakubowski, R. König, H.P. Laqua, S. Lazerson, M. Otte, M. Preynas, O. Schmitz, T. Stange, Y. Turkin, and the W7-X Team. Plans for the first plasma operation of Wendelstein 7-X. *Nuclear Fusion*, 55(12):126001, 2015.

[68] Y. Feng, F. Sardei, and J. Kisslinger. 3D Fluid Modelling of the Edge Plasma by Means of a Monte Carlo Technique. *Journal of Nuclear Materials*, 266-269:812–818, 1999.

[69] D. Reiter. Randschicht-Konfiguration von Tokamaks: Entwicklung und Anwendung stochastischer Modelle zur Beschreibung des Neutralgastransports. *Technical Report Jül-1947*, 1984.

[70] Y. Feng, F. Sardei, J. Kisslinger, P. Grigull, K. McCormick, and D. Reiter. 3d edge modeling and island divertor physics. *Contributions to Plasma Physics*, 44(1-3):57–69, 2004.

[71] Y. Feng, H. Frerichs, M. Kobayashi, A. Bader, F. Effenberg, D. Harting, H. Hoelbe, J. Huang, G. Kawamura, J. D. Lore, T. Lunt, D. Reiter, O. Schmitz, and D. Sharma. Recent improvements in the emc3-eirene code. *Contributions to Plasma Physics*, 54(4-6):426–431, 2014.

[72] S. I. Braginskii. Transport Processes in a Plasma. *Reviews of Plasma Physics*, 1:205, 1965.

[73] Y. Feng. Recent progress in implementing exb drift in emc3-eirene. 2018.

[74] D. Reiter, M. Baelmans, and P. Börner. The EIRENE and B2-EIRENE codes. *Fusion Science and Technology*, 47:172 – 186, 2005. Record converted from VDB: 12.11.2012.

[75] Heinke Gerd Frerichs. Three-dimensional plasma transport in open chaotic magnetic fields : a computational assessment for tokamak edge layers. volume 4321 of *Berichte des Forschungszentrums Jlich*, pages VI, 179 S. : Ill., graph. Darst., Jlich, 2009. Forschungszentrum Jlich, Zentralbibliothek. Zsfassung in engl. und dt. Sprache; Aachen, Techn. Hochsch., Diss., 2010.

[76] P. C. Stangeby, J. A. Tagle, S. K. Erents, and C. Lowry. Measurements of the cross-field diffusion coefficient D Ł in the edge plasma of JET. *Plasma Physics and Controlled Fusion*, 30(12):1787, 1988.

[77] J. Roth, R. Preuss, W. Bohmeyer, S. Brezinsek, A. Cambe, E. Casarotto, R. Doerner, E. Gauthier, G. Federici, S. Higashijima, J. Hogan, A. Kallenbach, A. Kirschner, H. Kubo, J.M. Layet, T. Nakano, V. Philipps, A. Pospieszczyk, R. Pugno, R. Ruggiri, B. Schweer, G. Sergienko, and M. Stamp. Flux dependence of carbon chemical erosion by deuterium ions. *Nuclear Fusion*, 44(11):L21, 2004.

[78] W. Eckstein, J. Bohdansky, and J. Roth. Physical sputtering. *Nuclear Fusion*, (Suppl):51–61, 1991.

[79] Y. Feng, F. Sardei, J. Kisslinger, D. Reiter, and Yu. L. Igitkhanov. Numerical Studies on Impurity Transport in the W7-AS Island Divertor. In C. Silva, C. Varandas, and D. Campbell, editors, *28th EPS Conference on Controlled Fusion and Plasma Physics. Contributed Paper*, volume 25A of *ECA*, pages 1949–1952, Funchal, 2001. European Physical Society.

[80] Y. Feng, T. Lunt, F. Sardei, and X. Zha. Implicit coupling of impurity transport at the SOL-core interface. *Computer Physics Communications*, 184(6):1555 – 1561, 2013.

[81] H. P. Summers. *Atomic data and analysis structure: user manual*. Joint European Torus, Abingdon, 1994.

[82] H. Frerichs. 3d numerische parameterstudien zum verunreinigungstransport in textor-ded. *Diplomarbeit*.

[83] H. Frerichs, F. Effenberg, O. Schmitz, C. Biedermann, Y. Feng, M. Jakubowski, R. Knig, M. Krychowiak, J. Lore, H. Niemann, T. S. Pedersen, L. Stephey, and G. A. Wurden. Synthetic plasma edge diagnostics for emc3-eirene, highlighted for wendelstein 7-x. *Review of Scientific Instruments*, 87(11):11D441, 2016.

[84] H. Frerichs, F. Effenberg, Y. Feng, O. Schmitz, L. Stephey, D. Reiter, P. Brner, and The W7-X Team. Reconstruction of recycling flux from synthetic camera images, evaluated for the wendelstein 7-x startup limiter. *Nuclear Fusion*, 57(12):126022, 2017.

[85] Andreeva T., Kilinger J., and Wobig H. Characteristics of main configurations of wendelstein 7-x. *Problems of Atomic Science and Technology Series: Plasma Physics*.

[86] Y. Feng, F. Sardei, and J. Kisslinger. A simple highly accurate field-line mapping technique for three-dimensional monte carlo modeling of plasma edge transport. *Physics of Plasmas*, 12(5):052505, 2005.

[87] S.A. Bozhenkov, M.W. Jakubowski, H. Niemann, S.A. Lazerson, G.A. Wurden, C. Biedermann, G. Kocsis, R. Knig, F. Pisano, L. Stephey, T. Szepesi, U. Wenzel, T.S. Pedersen, R.C. Wolf, and W7-X Team. Effect of error field correction coils on w7-x limiter loads. *Nuclear Fusion*, 57(12):126030, 2017.

[88] Yasuhiro Suzuki, Noriyoshi Nakajima, Kiyomasa Watanabe, Yuji Nakamura, and Takaya Hayashi. Development and application of hint2 to helical system plasmas. *Nuclear Fusion*, 46(11):L19, 2006.

[89] James D. Hanson, Steven P. Hirshman, Stephen F. Knowlton, Lang L. Lao, Edward A. Lazarus, and John M. Shields. V3fit: a code for three-dimensional equilibrium reconstruction. *Nuclear Fusion*, 49(7):075031, 2009.

[90] J.C. Schmitt, J.N. Talmadge, and D.T. Anderson. Measurement of a helical pfirschschlter current with reduced magnitude in hsx. *Nuclear Fusion*, 53(8):082001, 2013.

[91] Feng Y., Sardei F., Kisslinger J., Grigull P., McCormick K., and Reiter D. 3d edge modeling and island divertor physics. *Contributions to Plasma Physics*, 44(13):57–69, 2004.

[92] Kobayashi M., Feng Y., Sardei F., Reiter D., Reiser D., and Finken K. H. Implementation of the emc3eirene code on textorded: accuracy and convergence study. *Contributions to Plasma Physics*, 44(13):25–30, 2004.

[93] Y. Feng, S. Bozhenkov, F. Effenberg, H. Hölbe, D. Reiter, and Y. Turkin. Neutral transport behavior expected for the first limiter plasmas in W7-X. In S. Ratynskaia, P. Mantica, A. Benuzzi-Mounaix, G. Dilecce, R. Bingham, M. Hirsch, B. Kemnitz, and T. Klinger, editors, *41st EPS Conference on Plasma Physics*, volume 38F of *Europhysics Conference Abstracts (ECA)*, Berlin, 2014.

[94] L. Stephey, A. Bader, F. Effenberg, O. Schmitz, G. A. Wurden, D. T. Anderson, F. S. B. Anderson, C. Biedermann, A. Dinklage, Y. Feng, H. Frerichs, G. Fuchert, J. Geiger, J. H. Harris, R. Knig, P. Kornejew, M. Krychowiak, J. D. Lore, E. A. Unterberg, and I. Waters. Impact of magnetic islands in the plasma edge on particle fueling and exhaust in the hsx and w7-x stellarators. *Physics of Plasmas*, 25(6):062501, 2018.

[95] A Dinklage, C D. Beidler, P Helander, Golo Fuchert, H Maaberg, K Rahbarnia, T Sunn Pedersen, Y Turkin, R C. Wolf, A Alonso, T Andreeva, Boyd Blackwell, S Bozhenkov, Birger Buttenschn, A Czarnecka, Florian Effenberg, Y Feng, Joachim Geiger, Matthias Hirsch, and David Zhang. Magnetic configuration effects on the Wendelstein 7-X stellarator. 05 2018.

[96] O. Schmitz, M.W. Jakubowski, H. Frerichs, D. Harting, M. Lehnen, B. Unterberg, S.S. Abduallaev, S. Brezinsek, I. Classen, T. Evans, Y. Feng, K.H. Finken, M. Kantor, D. Reiter, U. Samm, B. Schweer, G. Sergienko, G.W. Spakman, M. Tokar, E. Uzgel, R.C. Wolf, and the TEXTOR Team. Identification and analysis of transport domains in the stochastic boundary of TEXTOR-DED for different mode spectra. *Nuclear Fusion*, 48(2):024009, 2008.

[97] A. R. Akerson, A. Bader, C. C. Hegna, O. Schmitz, L. A. Stephey, D. T. Anderson, F. S. B. Anderson, and K. M. Likin. Three-dimensional scrape off layer transport in the helically symmetric experiment HSX. *Plasma Physics and Controlled Fusion*, 58(8):084002, 2016.

[98] Y. Feng, F. Sardei, P. Grigull, K. McCormick, L. Giannone, J. Kisslinger, D. Reiter, Y. Igitkhanov, and U. Wenzel. Modelling of island divertor physics and comparison to w7-as experimental results. *Journal of Nuclear Materials*, 313316:857 – 862, 2003. Plasma-Surface Interactions in Controlled Fusion Devices 15.

[99] L. Stephey. The effects of edge magnetic structure on particle fueling andexhaust in the hsx and w7-x stellarators. *PhD Thesis*, 2017.

[100] P.C. Stangeby. A three-dimensional analytic model for discrete limiters in ITER. *Nuclear Fusion*, 50(3):035013, 2010.

[101] P.C. Stangeby, C.S. Pitcher, and J.D. Elder. The nature of plasma fluxes to surfaces nearly tangential to the magnetic field. *Nuclear Fusion*, 32(12):2079, 1992.

[102] G. A. Wurden, L. A. Stephey, C. Biedermann, M. W. Jakubowski, J. P. Dunn, M. Gamradt, and W7-X Team. A high resolution ir/visible imaging system for the w7-x limiter. *Review of Scientific Instruments*, 87(11), 2016.

[103] H. Niemann, M. Jakubowski, F. Effenberg, R. König, T.S. Pedersen, G.A. Wurden, F. Pisano, and W7-X Team. Power loads in the limiter phase of Wendelstein 7-X. 2016.

[104] A. Herrmann and ASDEX Upgrade Team. Limitations for Divertor Heat Flux Calculations of Fast Events in Tokamaks. In C. Silva, C. Varandas, and D. Campbell, editors, *28th EPS Conference on Controlled Fusion and Plasma Physics. Contributed Paper*, volume 25A of *ECA*, pages 2109–2112, Funchal, 2001. European Physical Society.

[105] Samuel A. Lazerson, Matthias Otte, Marcin Jakubowski, Ben Israeli, Glen A. Wurden, Uwe Wenzel, Tamara Andreeva, Sergey Bozhenkov, Christoph Biedermann, Gbor Kocsis, Tams Szepesi, Joachim Geiger, Thomas Sunn Pedersen, David Gates, and The W7-X Team. Error field measurement, correction and heat flux balancing on wendelstein 7-x. *Nuclear Fusion*, 57(4):046026, 2017.

[106] L. Stephey, G. A. Wurden, O. Schmitz, H. Frerichs, F. Effenberg, C. Biedermann, J. Harris, R. Knig, P. Kornejew, M. Krychowiak, E. A. Unterberg, and W7-X Team. Spectroscopic imaging of limiter heat and particle fluxes and the resulting impurity sources during wendelstein 7-x startup plasmas. *Review of Scientific Instruments*, 87(11):11D606, 2016.

[107] V R Winters, S Brezinsek, F Effenberg, M Rasinski, O Schmitz, L Stephey, C Biedermann, C P Dhard, H Frerichs, J Harris, M Krychowiak, R Knig, T Sunn Pedersen, G A Wurden, and the W7-X team. Overview of the plasma-surface interaction on limiter surfaces in the startup campaign of wendelstein 7-x. *Physica Scripta*, 2017(T170):014050, 2017.

[108] C. Buelo, L. Stephey, F. S. B. Anderson, D. Eisert, and D. T. Anderson. Development of a 3-d visible limiter imaging system for the hsx stellarator. *Review of Scientific Instruments*, 88(12):123508, 2017.

[109] D. Zhang, R. Burhenn, B. Buttenschön, R. König, R. Laube, H. Jenszch, L. Giannone, M. Marquardt, H. Thomsen, A. Werner, A. Alonso, C. Biedermann, S. Bozhenkov, R. Brakel, A. Czarnecka, T. Fornal, G. Fuchert, O. Grulke, M. Hirsch, J. Knauer, M. Kubkowska, A. Langenberg, H. P. Laqua, M. Otte, N. Pablant, E. Pasch, K. Rahbarnia, T. Schröder, J. Svensson, U. Wenzel, G. A. Wurden, and Max Planck Society W7-X Team, Max Planck Institute for Plasma Physics. Investigation of the Radiative Power Loss in the Limiter Plasmas of W7-X. In P. Mantica, editor, *43rd EPS Conference on Plasma Physics*, volume 40A of *Europhysics Conference Abstracts (ECA)*, Leuven, 2016. European Physical Society. author: Giruzzi, G.; author: Fajardo, M.; author: Gans, T.; author: Poedts, S.; author: Vennekes, N.

[110] T. Barbui, M. Krychowiak, R. Knig, O. Schmitz, J. M. Muoz Burgos, B. Schweer, A. Terra, and W7-X Team. Feasibility of line-ratio spectroscopy on helium and neon as edge diagnostic tool for wendelstein 7-x. *Review of Scientific Instruments*, 87(11):11E554, 2016.

[111] R. König, J. Baldzuhn, W. Biel, C. Biedermann, H.S. Bosch, S. Bozhenkov, T. Bruer, B. Brotas de Carvalho, R. Burhenn, B. Buttenschön, G. Cseh, A. Czarnecka, M. Endler, V. Erckmann, T. Estrada, J. Geiger, O. Grulke, D. Hartmann, D. Hathiramani, M. Hirsch, S. Jabonski, M. Jakubowski, J. Kaczmarczyk, T. Klinger, S. Klose, G. Kocsis, P. Kornejew, A. Krmer-Flecken, T. Kremeyer, M. Krychowiak, M. Kubkowska, A. Langenberg, H. P. Laqua, M. Laux, Y. Liang, A. Lorenz, A.O. Marchuk, V. Moncada, O. Neubauer, U. Neuner, J.W. Oosterbeek, M. Otte, N. Pablant, E. Pasch, T.S. Pedersen, K. Rahbarnia, L. Ryc, O. Schmitz, W. Schneider, H. Schuhmacher, B. Schweer, T. Stange, H. Thomsen, J.-M. Travere, T. Szepesi, U. Wenzel, A. Werner, B. Wiegel, T. Windisch, R. Wolf, G.A. Wurden, D. Zhang, A. Zimbal, S. Zoletnik, and the W7-X Team. The Set of Diagnostics for the First Operation Campaign of the Wendelstein 7-X Stellarator. *Journal of Instrumentation*, 10(10):P10002, 2015.

[112] L Giannone, J Baldzuhn, R Burhenn, P Grigull, U Stroth, F Wagner, R Brakel, C Fuchs, H J Hartfuss, K McCormick, A Weller, C Wendland, NBI Team, ECRH Team, W7-AS Team, K Itoh, and S-I Itoh. Physics of the density limit in the w7-as stellarator. *Plasma Physics and Controlled Fusion*, 42(6):603, 2000.

[113] U. Wenzel, K. McCormick, D. Hildebrandt, S. Klose, D. Naujoks, and H. Thomsen. Experimental observation of Marfes in the W7-AS stellarator. *Plasma Physics and Controlled Fusion*, 44(10):L57–L62, 2002.

[114] J. Geiger, R. C. Wolf, C. Beidler, A. Cardella, E. Chlechowitz, V. Erckmann, G. Gantenbein, D. Hathiramani, M. Hirsch, W. Kasparek, J. Kilinger, R. Knig, P. Kornejew, H. P. Laqua, C. Lechte, J. Lore, A. Lumsdaine, H. Maaberg, N. B. Marushchenko, G. Michel, M. Otte, A. Peacock, T. Sunn Pedersen, M. Thumm, Y. Turkin, A. Werner, D. Zhang, and the W7-X Team. Aspects of steady-state operation of the Wendelstein 7-X stellarator. *Plasma Physics and Controlled Fusion*, 55(1):014006, 2013.

[115] Geiger J., Beidler C.D., Drevlak M., Maaberg H., Nhrenberg C., Suzuki Y., and Turkin Yu. Effects of net currents on the magnetic configuration of w7x. *Contributions to Plasma Physics*, 50(8):770–774.

[116] Yu Turkin, H Maaßberg, CD Beidler, J Geiger, and NB Marushchenko. Current control by eccd for w7-x. *Fusion science and technology*, 50(3):387–394, 2006.

[117] Y. Feng, J. Kisslinger, F. Sardei, and D. Reiter. EMC3/EIRENE Transport Modelling of the Island Divertor in W7-X. In P. Lalousis and S. Moustaizis, editors, *35th European Physical Society Conference on Plasma Physics and 10th International Workshop on Fast Ignition of Fusion Targets. Contributed Papers*, volume 32D of *ECA*, Hersonissos, Crete, 2008. European Physical Society.

[118] D Gradic, O P Ford, A Burckhart, F Effenberg, H Frerichs, R Knig, T Lunt, V Perseo, R C Wolf, ASDEX Upgrade Team, Wendelstein 7-X Team, and Eurofusion MST1 team. Doppler coherence imaging of divertor and sol flows in asdex upgrade and wendelstein 7-x. *Plasma Physics and Controlled Fusion*, 60(8):084007, 2018.

[119] O Schmitz, I L Beigman, L A Vainshtein, B Schweer, M Kantor, A Pospieszczyk, Y Xu, M Krychowiak, M Lehnen, U Samm, B Unterberg, and the TEXTOR team. Status of electron temperature and density measurement with beam emission spectroscopy on thermal helium at textor. *Plasma Physics and Controlled Fusion*, 50(11):115004, 2008.

[120] V. Perseo, R. König, O. Ford, D. Gradic, F. Effenberg, C. Biedermann, G. Kocsis, T. S. Pedersen, and Max Planck Society W7-X Team, Max Planck Institute for Plasma Physics. First results of the Coherence Imaging Spectroscopy Systems on Wendelstein 7-X, 2017.